Full-field multi-fidelity surrogate models for optimal design of turbomachines

Tariq Benamara

Par **Tariq BENAMARA**

Full-field multi-fidelity surrogate models for optimal design of turbomachines

Thèse présentée
pour l'obtention du grade
de Docteur de l'UTC

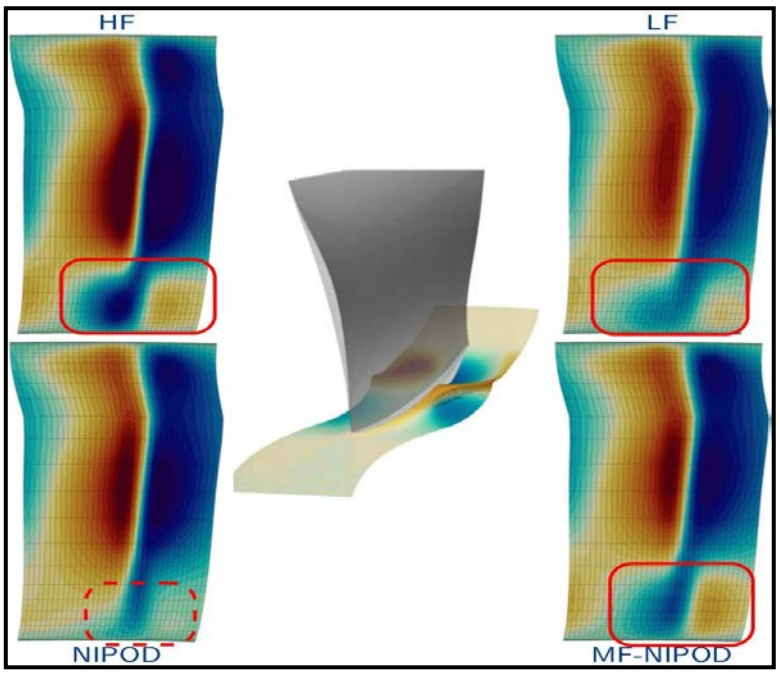

Soutenue le 7 juillet 2017
Spécialité : Mécanique Numérique : Unité de recherche en Mécanique - Laboratoire Roberval (FRE UTC - CNRS 2012)
D2368

Université de Technologie de Compiègne
École Doctorale
Sciences pour l'Ingénieur

T H È S E

En vue de l'obtention du grade de

Docteur
en Mécanique Numérique

de l' Université de Technologie de Compiègne

Soutenue le 7 Juillet 2017 par

Tariq Benamara

Full-field Multi-Fidelity Surrogate Models for Optimal Design of Turbomachines

Co-directeurs: Piotr Breitkopf (Laboratoire Roberval - UTC)
Caroline Sainvitu (Minamo Team - Cenaero)

Jury :

Président:	Pierre Duysinx	-	ULg
Rapporteurs:	Florian De Vuyst	-	CMLA - ENS Paris-Saclay
	Christian Gogu	-	Institut Clément Ader
Éxaminateur:	Emmanuel Le François	-	UTC
Invités:	Virgile Marguin	-	Safran Aircraft Engines
	Christian Rey	-	Safran Corporate Research Center
	Ingrid Lepot	-	Cenaero

I would like to dedicate this thesis to:
my father, Smaïl,
my mother, Nacera,
my loving wife, Ikram,
and my delightful children Sofia and Smaïl,

Remerciements

Après le long et laborieux chemin parcouru, vient maintenant la partie la plus naturelle de ce travail car ces trois dernières années auront été tout sauf un voyage solitaire. Il est donc temps pour moi de remercier toutes les personnes qui ont participé à la réussite de ce projet tant sur les plans technique qu'humain.

Mes premiers remerciements iront à mes co-directeur et co-directrice de thèse Pr. Piotr Breitkopf et Dr. Caroline Sainvitu pour leur encadrement tout au long de ces trois années. Merci à eux pour leur disponibilité (parfois lors de relectures dans des délais improbables) et pour avoir su trouver le juste équilibre entre liberté d'action et rappel de la direction et des priorités. Nos nombreuses discussions, et leurs remises en question répétées auront participé très largement à la réussite de ce projet.

Je tiens également à remercier les membres de mon jury de thèse pour avoir accepté d'évaluer mes travaux et pour les nombreuses questions et discussions sur les résultats présentés. Plus particulièrement Pr. Pierre Duysinx pour avoir assuré la présidence de ce jury, Dr. Christian Gogu et Pr. Florian De Vuyst pour avoir assuré la lourde tâche de rapporteurs, ainsi que Pr. Emmanuel Le François pour avoir accepté de relire également mon manuscrit et pour les conseils enrichissants prodigués lors de l'analyse de mes résultats numériques. Je remercie également Virgile Marguin et Pr. Christian Rey pour l'intérêt industriel qu'ils ont manifesté en acceptant de participer à ce jury. Enfin, je tiens particulièrement à remercier Dr. Ingrid Lepot pour avoir cru en mes capacités et avoir poussé ma candidature lors de la mise en place de ce sujet de thèse. Ses questions et remarques toujours pertinentes auront participé, tout au long de ces trois années, à la réussite de ce projet et à la mise en place et l'analyse du cas test industriel de cette thèse.

Comment pourrais-je oublier également les nombreuses questions addressées à Pr. Pierre Villon qui aura su tempérer mon optimisme débordant lorsque nécessaire, mais aussi raviver ma confiance et mon intérêt dans les justifications

mathématiques ponctuant ce manuscrit. Merci pour sa disponibilité et pour l'estime qu'il a toujours porté à mes questions et travaux, y compris lorsque je le dérangeais en congé avec des questions d'étudiant aux lacunes théoriques innombrables. Je profite de ces lignes pour remercier également mes collègues du laboratoire Roberval pour leur aide et avec qui j'ai pris plaisir à échanger, nommément Liang Xia, Liang Meng, Anna Madra, mais aussi Profs Catherine Vayssade, Pierre Feissel, Delphine Brancherie, Alain Rassineux pour ses précieux conseils en matière de formation et Brigitte Duch pour ses indications et rappels dans les différentes tâches administratives.

Je remercie également mes collègues de Cenaero (passés ou présents), tout d'abord Philippe Gueuzaine et Caroline Sainvitu pour m'avoir respectivement accepté au sein du laboratoire et intégré à l'équipe Minamo. Je remercie également mes compagnons de fortune et d'infortune dans l'équipe de développement, "Cha" Beauthier, "Chr" Dumeunier, "Paulo" Beaucaire et "Dédé" Chocat pour avoir rendu ces trois années agréables tant *in-situ* qu'à distance. Merci également pour vos encouragements dans les périodes les plus sombres de ces travaux et bien-entendu pour votre aide que ce soit pour comprendre comment la "constness" d'un attribut de classe virtuelle référencé par un pointeur intelligent pouvait créer une erreur de compilation trois fois par semaine passé 19h30, comprendre les subtilités des différentes méthodes d'optimisation découvertes au gré de ma recherche bibliographique ou encore m'expliquer et m'expliquer encore la différence entre optimisation robuste et fiabiliste... Il me serait également impossible d'oublier les différentes explications reçues (parfois tard le soir) sur l'écoulement dans les turbomachines, la CFD, la mécanique, l'art de la compilation, et bien d'autre sujets... Je souhaite donc saluer ici toutes les personnes (en m'excusant auprès de celles que j'oublierai) que j'ai dérangé par mes questions incessantes et qui ont toujours répondu avec le sourire : Farid Benyoucef, Ash Mahajan, Koen Hillewaert, Lieven Baert, Michaël Leborgne, Timothée Lonfils, Jean-François Thomas, Chloé Dumont, Pierre Schrooyen, Michel Rasquin, Nicolas Poletz, Danielle Coulon, Kevin Mailleux, Laurent Brognara... Enfin, je souhaite addresser un "tout grand merci" à mes collègues de Cenaero qui rendent les journées de travail très agréables et qui ont supporté mes plaintes incessantes parfois en pleine pause café : Eric Wyart, Benoit Wucher, Larbi Arbaoui, Olivier Pierard, Rebecca Nakhoul, Laurent Cadet, Jean-Pierre Lefèbvre, Florent Grisonnet, Séverine Quinet, Landry De Wulf, et Benoit Dompierre qui n'a parfois eu comme covoitureur qu'un loir ou qu'un râleur fustigeant son code ou (et) celui des autres...

Les financements octroyés par l'Association Nationale Recherche Technologie

et le groupe Safran ont permis le déroulement de cette thèse. Je souhaite remercier plus précisément l'ensemble de l'équipe méthodes de Safran Aircraft Engines pour les diverses interactions, et plus particulièrement Mickaël Meunier, Jean Coussirou et Abdelkader Otsmane pour leur encadrement respectif.

Certains professeurs ou encadrants ont laissé une empreinte particulière dans mon cursus universitaire, et m'ont implicitement ou explicitement guidés vers une thèse de doctorat. Je tiens ici à remercier certains d'entre eux, en commençant par rendre hommage au professeur Pierre Comte dont les cours passionnés et passionnant ont eu un impact certain sur mes choix de carrière. Je veux également remercier professeurs Jacques Borée, Eric Lamballais, Yves Gervais, Guillermo Paniagua, Jean-Camille Chassaing, et Arnaud Antkowiak.

Je remercie également mes amis qui se sont intéressés à mes discussions parfois déconnectées et ont prêté une oreille attentive à mes questionnements de thésard, plus particulièrement Fodhil Sidi-Moussa pour sa curiosité sans faille et nos nombreux échanges techniques, Erwan Audebert qui a osé se lancer dans la relecture d'un manuscrit en pleine ébauche, Bertrand M Bondo qui a relu consciencieusement mes articles avant soumission, et Mehdi Houhou qui m'a fait le plaisir de venir me supporter lors de ma soutenance.

Enfin je tiens ici à remercier ma famille sans qui ce travail n'aurait pas été possible. Je remercie tout d'abord mes parents pour leur soutien inconditionnel malgré des choix parfois "inexplicables". Avoir avec moi ma mère le jour de ma soutenance aura été source d'une joie sans limite. Enfin une pensée particulière pour ma femme Ikram qui m'a suivi et supporté dans cette aventure, ainsi que nos deux enfants Sofia et Smaïl. Ce travail n'aurait pas été possible sans son dévouement et je lui suis reconnaissant pour son soutien malgré toutes les contraintes que cela a pu engendrer. Je remercie également nos enfants pour m'avoir permis de garder le sens des priorités dans les moments les plus difficiles, et m'avoir gratifié de fous rires rafraichissants. Vous avoir avec moi le jour de ma soutenance en fera un souvenir inoubliable.

Lille, le 16 Octobre 2017, Tariq Benamara.

Abstract

Optimizing turbomachinery components stands as a real challenge despite recent advances in theoretical, experimental and High-Performance Computing (HPC) domains. This thesis introduces and validates optimization techniques assisted by full-field Multi-Fidelity Surrogate Models (MFSMs) based on Proper Orthogonal Decomposition (POD). The combination of POD and Multi-Fidelity Modeling (MFM) techniques allows to capture the evolution of dominant flow features with geometry modifications.

Two POD based multi-fidelity optimization methods are proposed. The first one consists in an enrichment strategy dedicated to Gappy-POD (GPOD) models. It is more suitable for instantaneous low-fidelity computations which makes it hardly tractable for aerodynamic design of turbomachines. This method is demonstrated on the flight domain study of a $2D$ airfoil from the literature.

The second methodology is based on a multi-fidelity extension to Non-Intrusive POD (NIPOD) models. This extension starts with a re-interpretation of the Constrained POD (CPOD) concept and allows to enrich the reduced space definition with abondant, albeit inaccurate, low-fidelity information.

In the second part of the thesis, a benchmark test case is introduced to test full-field multi-fidelity optimization methodologies on an example presenting features representative of turbomachinery problems. The predictability of the proposed Multi-Fidelity NIPOD (MFNIPOD) surrogate models is compared to classical surrogates from the literature on both analytical and industrial-scale applications. Finally, we employ the proposed tool to the shape optimization of a 1.5-stage booster and we compare the obtained results with standard state of the art approaches.

Résumé

L'optimisation des différents composants d'une turbomachine reste encore un sujet épineux, malgré les récentes avancées théoriques, expérimentales ou informatiques. Cette thèse propose et investigue des techniques d'optimisation assistées par méta-modèles vectoriels multi-fidélité basés sur la Décomposition aux Valeurs Propres (POD). Le couplage de la POD à des techniques de modélisation multi-fidélité permet de suivre l'évolution des structures dominantes de l'écoulement en réponse à des déformations géométriques.

Deux méthodes d'optimisation multi-fidélité basées sur la POD sont ici proposées. La première consiste en une stratégie d'enrichissement adaptée aux modèles multi-fidelité par Gappy-POD (GPOD). Celle-ci vise surtout des problèmes associés à des simulations basse-fidélité à coût de restitution négligeable, ce qui la rend difficilement utilisable pour la conception aérodynamique de turbomachines. Elle est néanmoins validée sur une étude du domaine de vol d'une aile $2D$ issue de la littérature.

La seconde méthodologie est basée sur une extension multi-fidèle des modèles par POD Non-Intrusive (NIPOD). Cette extension naît de la ré-interprétation du concept de POD Contrainte (CPOD) et permet l'enrichissement de l'espace réduit par ajout important d'information basse-fidélité approximative.

En seconde partie de cette thèse, un cas de validation est introduit pour valider les méthodologies d'optimisation vectorielle multi-fidélité. Cet exemple présente des caractéristiques représentatives des problèmes d'optimisation de turbomachines. La capacité de généralisation des méta-modèles par NIPOD multi-fidélité proposés est comparée, aussi bien sur cas analytique qu'industriel, à des techniques de méta-modélisation issues de la littérature. Enfin, nous utilisons la méthode développée au cours de cette thèse pour l'optimisation d'un étage et demi d'un compresseur basse-pression et comparons les résultats obtenus à des approches à l'état de l'art.

Contents

List of Figures

List of Tables

List of Notations

Abbreviations

General

e.g.	*exampli gratia* or "for example"
s.t.	subject to (for constraint definition)
w.r.t.	with respect to
HPC	High-Performance Computing
RAM	Random Access Memory
CPU	Central Processing Unit (usage time defining the evaluation cost)
UQ	Uncertainty Quantification
PDE	Partial Derivative Equation
CFD	Computational Fluid Dynamics
RANS	Reynold Averaged Navier-Stokes
LPC/T	Low-Pressure Compressor/Turbine
IGV/OGV	Inlet/Outlet Guide Vane

Optimization

MDO	Multi-Disciplinary Optimization
NLPP	Non-Linear Programming Problem
MOO	Multi-Objective Optimization
SOO	Single-Objective Optimization
DFO	Derivative Free Optimization
GBO	Gradient Based Optimization
SVM/R	Support Vector Machine/Regression
RBF(N)	Radial Basis Function (Network)
ANN	Artificial Neural Network
$\mathcal{GP}$	Gaussian Process
DA	Diffuse Approximation
(S/MF)DFSM	(Single-/Multi-Fidelity) Data Fitting Surrogate Model

GESM	Gradient Enhanced Surrogate Model
SMF/T	Surrogate Management Framework/Technique
TRMM	Trust Region Management Methodology
MFM	Multi-Fidelity Model / Modeling (depending on the context)
(MF)SBO	(Multi-Fidelity) Surrogate-Based Optimization
EGO	Efficient Global Optimization
SQP	Sequential Quadratic Programming
EA/O	Evolutionary Algorithm/Optimization
(MF)DoE	(Multi-Fidelity) Design of Experiments
S/MFSM	Single-/Multi-Fidelity Surrogate Model/Modeling
LHS	Latin Hypercube Sampling
LCVT	Latinized Centroidal Voronoï Tesselation
LOO	Leave One Out
ANOVA	ANalysis of VAriance

POD related acronyms

POD	Proper Orthogonal Decomposition
CPOD	Constrained POD
GPOD	Gappy POD
NIPOD	Non-Intrusive POD
NIROM	Non-Intrusive ROM
MFPOD	Multi-Fidelity POD
HMFPOD	hierarchised MFPOD
MFNIPOD	Multi-Fidelity NIPOD
HMFNIPOD	hierarchised MFNIPOD
ROM	Reduced Order Model
PCA	Principal Component Analysis
KLE	Karhunen-Loève Expansion
SVD	Singular Value Decomposition

Mathematical symbols

Remark: bold lower-case letters indicate vectors whereas bold capital letters indicate matrices. In case of scalar/vector/matrix with index or exponent, the font and case indicate the object type after index/exponent application (e.g. $\mathbf{v}_i$ calls the i-th vector $\mathbf{v}$ whereas y_i refers to the i-th component of vector $\mathbf{y}$).

M number of samples in a database
$\mathcal{D}$ design space

$\mathbf{S}$ $(n_H + n_L, M)$ sized matrix of concatenated full-field solutions
$\mathbf{Y}$ (n, M_H) sized matrix of high-fidelity full-field solutions
$\mathbf{Z}$ (n, M_L) sized matrix of low-fidelity full-field solutions
$\mathbf{s}$ (n_H+n_L) sized concatenated low- and high-fidelity full-field solution (snapshot)
$\mathbf{y}$ (n_H) sized high-fidelity full-field solution (snapshot)
$\mathbf{z}$ (n_L) sized low-fidelity full-field solution (snapshot)
m number of modes after truncation
n dimension of the output space described by $\boldsymbol{\chi}$
p dimension of the design space

Algebra

$I(\cdot)$	Integration function extracting the quantities of interest from a snapshot
$\mathbf{Im}\ \cdot$	Image or Span of the basis $\cdot$
$\mathbb{R}$	set of real numbers
$\mathbb{N}$	set of nonnegative integers
$[\![a, b]\!]$	list of integers between a and b in $\mathbb{N}$
$\mathbf{0}, \mathbf{0}, \overrightarrow{0}$	zero vector
$\mathbf{v}, \boldsymbol{v}, \overrightarrow{v}$	A vector variable
$\mathbf{A}, \boldsymbol{A}$	A matrix variable
$\mathbf{I}_d$	square identity matrix of dimension d
$\bar{\cdot}$	mean or centering vector
$\tilde{\cdot}$	approximate scalar or vector
$\lvert\cdot\rvert$	absolute value of a scalar
$\lVert\cdot\rVert$	vector or matrix norm
$\lVert\cdot\rVert_F$	vector or matrix Frobenius norm

Greek Letters

$\boldsymbol{\alpha}$	vector of POD coefficients
$\boldsymbol{\beta}$	vector of GPOD coefficients
$\boldsymbol{\chi}$	discretization of the numerical model yielding the "full-field" solutions
$\boldsymbol{\Phi}$	basis of single-fidelity proper orthogonal decomposition
$\boldsymbol{\Psi}$	basis of hierarchised multi-fidelity proper orthogonal decomposition
$\boldsymbol{\Phi}$	basis of multi-fidelity gappy proper orthogonal decomposition
ζ	a scalar quantity of interest
$\boldsymbol{\theta}$	vector of design parameters in $\mathbb{R}^p$
$\boldsymbol{\Theta}$	(p, M) sized matrix containing M vectors of design parameters in $\mathbb{R}^p$

Subscripts

H	High-fidelity

L	Low-fidelity
$\cdot i$	i-th column of a matrix

Superscripts

H	High-fidelity
L	Low-fidelity
$\perp$	matrix projection onto the high-fidelity POD basis
$\prime$	deviation from the mean or centering value $(\bar{\cdot})$
$\star$	optimal value
$\top$	matrix transpose operator

Aerodynamic notations

Remark: Aerodynamic notations are mostly used in the examples (Section 5.2 and Chapters 7, 8, and 9).

C_D	drag coefficient
C_L	lift coefficient
LE	blade Leading Edge
PS	blade Pressure Side
R	hub platform radius
SS	blade Suction Side
c	blade Chord length
s	hub pitch angle
y^+	dimensionless wall distance

Greek Letters

Π_{tot}	total-to-total pressure ratio
η_{is}	isentropic efficiency
ρe	dimensionless internal energy
ρu	1^{st} component of the dimensionless momentum
ρv	2^{nd} component of the dimensionless momentum
ρw	3^{rd} component of the dimensionless momentum
ρ	density

Chapter 1

Introduction

The research presented in this thesis, has been done in the frame of industry's growing interest for automated optimization techniques. Particularly, the present work is partly funded by the engine manufacturer Safran Aircraft Engines. This introduction will now provide the motivations behind this work, as well as an overview of the thesis's content.

1.1 Background and motivations

Many simulation-based optimization techniques have been developed and widely employed for the design of engineering systems. Among which, Multi-Disciplinary Optimization (MDO) has revealed itself a very effective tool for least-weight and high-performance designs, especially in aeronautics and aerospace engineering [I. Kroo et al., 1994; Peoples and Willcox, 2006], or turbomachinery design [Dornberger et al., 2000]. Most of the engineering design applications can be seen as numerical models of design variables $\boldsymbol{\theta}$ the designer has control over on one hand and state variables $\mathbf{y}(\boldsymbol{\theta})$ describing the physical state of the designed system on the other. The design problem is then formulated as the Non-Linear Programming Problem (NLPP):

$$\begin{aligned} \min_{\boldsymbol{\theta}} \quad & \mathcal{Y}\left(\boldsymbol{\theta}, \mathbf{y}(\boldsymbol{\theta})\right) \\ \text{s.t} \quad & \mathbf{c}\left(\boldsymbol{\theta}, \mathbf{y}(\boldsymbol{\theta})\right) \leq 0. \end{aligned} \tag{1.1}$$

The computational burden associated to the resolution of Problem 1.1 depends on many factors:

- the computational cost of the evaluation of $\mathbf{y}(\boldsymbol{\theta})$, $\mathcal{Y}\left(\boldsymbol{\theta}, \mathbf{y}(\boldsymbol{\theta})\right)$ and $\mathbf{c}\left(\boldsymbol{\theta}, \mathbf{y}(\boldsymbol{\theta})\right)$;
- the dimension of the design space $\boldsymbol{\theta}$;

- the order of dependence between $\boldsymbol{\theta}$ and $\mathbf{y}$.

These factors are addressed in the present work.

In the recent years, there is an increasing use of high-fidelity numerical models within MDO frameworks. Nevertheless, as observed in Giesing and Barthelemy, 1998, or more recently in Brezillon et al., 2012, solving MDO problems based on high-fidelity simulations can be very intricate. Many difficulties remain to be addressed such as

- the coupling of discipline dedicated high-fidelity solvers,
- the robustness of remeshing strategies for shape optimization,
- the computational burden hardly fitting the requirements in terms of number of evaluations, especially in high-dimensional design spaces.

To this end, Surrogate-Based Optimizations (SBOs) represent a class of optimization methodologies able to alleviate some of the aforementioned difficulties [Samad and K.-Y. Kim, 2009]. As soon as Derivative Free Optimization (DFO) is concerned, the main target of the designer is to find a gobal solution to the considered optimization problem. The main issue in using SBO in the context of global optimization in wide high-dimensional design spaces resides in the number of training samples required to reach acceptable discrepancy between the surrogate model and the "true" function of interest. Too small training samples could lead to a weak representation of the function to minimize or even introduce false optima [Mehmani et al., 2015]. In this regard, Multi-Fidelity Surrogate Modeling (MFSM) has become, in the past two decades, an active field of research within the MDO framework.

Whereas Multi-Fidelity Surrogate Models (MFSMs) are often referred to as hierarchised models and tagged as physics-based models, the large majority of Multi-Fidelity Modeling (MFM) techniques are "restrained" to the fusion of scalar data according to pre-defined kernel functions that are disconnected from the physical state of the optimized system. Keeping that in mind, and considering the increasing interest for Reduced Order Modeling (ROM) techniques able to determine the dominant physical features of the optimized system, one comes up naturally with the idea that building physics based MFSMs can pave the way towards SBO reaching high-precision requirements while keeping the computational burden affordable for industrial problems.

1.1.1 Motivation 1: Combine different levels of fidelity into MDO cycles

Traditionally in turbomachinery design, the design cycles involve sequential refinements of the considered product using simulation tools of increasing accuracy and costs. The first motivation of this work is to answer the need for surrogate models combining coarse and fine-simulations in order to integrate different levels of design in one conception step and make high-fidelity optimizations meet industrial requirements. In the case of turbomachinery design, the dimensionality of the optimizations engineers are running on a daily basis has been brought from less than 10 up to more than hundred variables in a few decades. In addition, the environmental and aircraft noise regulations now coerce aircraft engine manufacturers into fine tuning local and intricate physical phenomena early in their design cycles. This often involves taking into account flow features that are fully $3D$ and cannot be predicted by $2D$ or even quasi-$3D$ simulations [B. Chen and Yuan, 2008], resulting in high-fidelity computations taking up to tens of hours for each experiment and design point. Under these conditions, one can easily understand that observations made by Giesing and Barthelemy, 1998 and illustrated on Fig. 1.1 are at the heart of the first objective of this project.

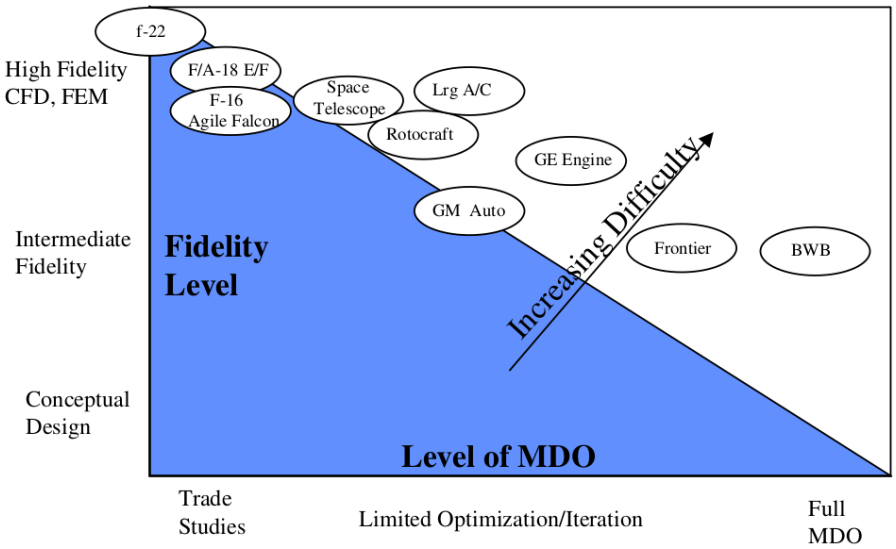

Figure 1.1: Distribution of Design Process Fidelity and Level of MDO [Giesing and Barthelemy, 1998].

We target here the development of MFSMs able to extract as much information as possible from "cheap" simulations to enable a wide exploration of high-dimensional design spaces. Several impediments have to be lifted before introduc-

ing MFSMs into industrially capable SBO software solutions. We give here an attempt to reduce the burden carried out in order to build the surrogate training databases. This involves either reducing the number of training points at a given fidelity or reduce the fidelity of the simulations while maintaining the precision of the surrogate model.

1.1.2 Motivation 2: Develop multi-level enrichment of full-field surrogate models

The second motivation of the thesis is to elaborate surrogate models able to capture the physics underlying the cost functions any optimization problem is working on (being objectives or constraints). We have this objective to respond designers calls for fast insight into the physical behavior of any experiment in the design space. By comparison to Data Fitting Surrogate Models (DFSMs), physics-based models should be able to build a fast estimate for the scalar quantities of interest of the optimization on the one hand, but also give the designer a rough idea on the physics associated to these estimated performances. Considering Proper Orthogonal Decomposition (POD) based models as best integrators of physics with respect to DFSMs, the target is, here, to propose a POD-based modeling technique coping with high-dimensional design spaces and costly evaluation tools. To this end, we attempt to create an improved POD-based surrogate model enriching sparse high-fidelity information with densely distributed low-fidelity data in the design space. As far as the author knows, this precise target has been enounced only by Mifsud, 2008; Mifsud, MacManus, et al., 2016 where both high- and low-fidelity information are fused together to construct the POD modal basis regardless of the level of precision of each training full-field simulation. In multi-fidelity modeling, a carefull attention has to be given to the correlation between low- and high-fidelity solutions to build an efficient methodology. Therefore, in order to soften the constraint on low- to high-fidelity correlation, we propose to tag the training snapshots with respect to their level of precision during the POD basis construction.

1.1.3 Motivation 3: Propose mulfi-fidelity optimization techniques

The last motivation of this thesis, but not the least, pertains to the efficient integration of the developed MFSMs into online optimization schemes with dedicated infill strategy. This is the cornerstone of any successfull industrial optimization. When dealing with design problems involving very expensive evaluation tools, one has to select the computed experiment parsimoniously. MFSMs are intended to

enlarge the amount of information used for the model training but trying to build computationally affordable models while ensuring a good precision in every interesting area of the design space is pointless as soon as no precise expert knowledge is available. To address this issue, an infill strategy and its associated ranking criterion are proposed. They are both adapted to full-field MFSMs. This last objective will pave the way towards efficient optimization of complex engineering systems. Finally, to demonstrate the reached situation within this thesis project, we target a challenging turbomachinery design.

1.2 Outline

In the current chapter, we have presented the motivations of this research investigating the extension of Reduced Order Models (ROMs) to the multi-fidelity paradigm. The second step targeted in this work is the coupling of full-field MFSMs with Evolutionary Algorithms (EAs) in dedicated SBO strategies and reduce the overall computational burden of turbomachinery design tasks. The work done in this thesis is naturally divided into two parts.

In Chapter 2, we start presenting literature related to the applications and developments proposed. Section 2.1 reviews the state of the art on aircraft engine and turbomachinery design. A short introduction to secondary flows in turbomachinery is given in Section 2.1.1. Sections 2.2 and 2.3 respectively review SBO techniques and MFSMs. After presenting a choice of ROMs used in the frame of SBOs in Section 2.4, we finally give literature on SBO applied to turbomachinery design in Section 2.5. Some rationales behind the strategies developed in this thesis conclude this chapter.

The first part describes the methodologies developed in this work. The second part pertains to the application of the developed methodology to an industrial-scale turbomachinery optimization problem. The remainder of the thesis is organised as follows:

Part I : Theoretical development and methodology

Chapter 3 primarily presents and re-interprets existing methodologies based on POD. Section 3.1 describes the POD and Non-Intrusive POD (NIPOD) methods, along with the chosen notations employed in the proposed extension. Engineering optimizations being usually defined with scalar quantities as objectives or contraints, the Constrained POD (CPOD) has been introduced to interpolate

these quantites despite non-zero truncation error. This technique is presented in Section 3.2 in order to detail the intellectual grounds of the proposed multi-fidelity extension. Finally, Gappy-POD (GPOD) is re-interpreted in Section 3.3.1 in order to propose a dedicated enrichment strategy in the coming chapters.

In Chapter 4, the multi-fidelity extension to NIPOD surrogate models is developed. The main contribution of this work is then theoretically developed in Section 4.1 yielding a hierarchised multi-fidelity extension to NIPOD models. The main steps of the proposed methodology are then wrapped up into algorithms detailed in Section 4.2 in order to help the interested reader implement the presented developments. Chapter 4 ends up with some preliminary conclusions highlighting the main differences with existing approaches.

The performance of a Multi-Fidelity SBO (MFSBO) framework highly depends on the capability of the method to smartly select the level of fidelity needed to maximize, at every iteration of the overall process, the computational cost to surrogate discrepancy reduction ratio. In order to ease the integration of the multi-fidelity GPOD method proposed by Toal, 2014 within an online SBO framework, Chapter 5 presents an infill strategy dedicated to this type of surrogates. The multi-fidelity methodology [Toal, 2014] is primarily described and reformulated. The GPOD approach [Everson and Sirovich, 1995] is also illustrated as being the grounds of the investigated multi-fidelity framework. A dedicated enrichment criterion, is then proposed and associated to an infill strategy summarized in the algorithm in Section 5.1. The proposed enrichment strategy is tested on the flight domain study of a transonic $2D$ airfoil. Some preliminary conclusions end up Chapter 5, as well as perspectives for infill strategies dedicated to full-field MFSMs as proposed in Chapter 4.

Part II : Industrial-scale surrogate modeling and optimization of aerodynamic performances

Chapter 6 presents the coupling of the proposed full-field MFSM developed in Chapter 4 within an evolutionary SBO scheme. To our best knowledge, no analytical example applicable to Multi-Fidelity NIPOD (MFNIPOD) surrogates is referenced in the literature. Therefore, an analytical $2D$-example carefully developed to represent key features of turbomachinery optimizations is introduced. The proposed MFSBO framework is then used to illustrate the interest of physics-based MFSBO. The chapter ends up with details on the implementation of the proposed multi-fidelity framework within a pre-existing single-fidelity SBO tool, and some preliminary conclusions.

In Chapter 7, the proposed industrial-scale application test case is introduced. It is derived from a previously published study and deals with the design of a multi-stage booster considering axial stacking and non-axisymmetric hub endwall deformations.

In Chapter 8, the predictability of the proposed multi-fidelity extension to POD based surrogate models is primarily assessed. The performed analysis is detailed in Section 8.1. Section 8.2 compares the single-fidelity POD and Multi-Fidelity POD (MFPOD) bases in order to quantify the improvement allowed by low-fidelity enhancement. In Section 8.3, the predictability of the proposed MFNIPOD model is compared to both existing single- and multi-fidelity techniques. This is done on the evaluation of the on-design isentropic efficiency (η_{is}) and pressure ratio (Π_{tot}) of the rotating row in the presented booster. Section 8.4 closes the chapter with a discussion on the choices made in order to perform MFSBOs.

Chapter 9 presents the results of Radial Basis Function Networks (RBFNs) and MFNIPOD assisted optimizations applied to the presented industrial application. As the chosen low-fidelity simulation is based on mesh coarsening of its high-fidelity counterpart, the impact of this coarsening is evaluated in Section 9.1 by performing two RBFN assited optimizations, respectively with low- and high-fidelity simulations. The presented MFSBO framework is then used in Section 9.2 to optimize the considered rotor blade, with carefull attention given to the impact of deformations on the aerodynamics of the machine. Section 9.3 closes the chapter with a discussion about the impact of the chosen simulation tool and some concluding remarks.

General Conclusions and perspectives on furture research terminate the thesis.

The research presented in Chapters 4, 6, and Part II gave rise to two full-size, peer-reviewed conference papers [Benamara, Breitkopf, Lepot, and Sainvitu, 2016b; Benamara, Breitkopf, Lepot, and Sainvitu, 2017], and a peer-reviewed research paper in *Structural and Multidisciplinary Optimization* [Benamara, Breitkopf, Lepot, Sainvitu, and Villon, 2017]. The content of Chapter 5 is mainly given in Benamara, Breitkopf, Lepot, and Sainvitu, 2016a.

Chapter 2

Literature review

In this chapter, we present literature related to the coming developments and the proposed industrial-scale application. Even though the targeted optimization techniques can be applied to a wide range of engineering systems, the present thesis takes root in the competitiveness of aircraft engine manufacturing domain. Therefore, it seems relevant to present shortly this targeted application first in Section 2.1. Section 2.1.1 introduces literature dealing with secondary flows in turbomachines and particularly low-pressure compressors, main focus of this study. Then, Sections 2.2, 2.3 and 2.4 respectively review Surrogate-Based Optimization (SBO) methods, conventional Multi-Fidelity Surrogate Models (MFSMs), and a choice of Reduced Order Models (ROMs) with their application. In Section 2.5 turbomachinery optimizations using SBO techniques are reviewed. Finally, Section 2.6 concludes the chapter with the selected orientations for this research and their underlying rationales.

2.1 Aircraft engine and turbomachinery design

Following the definition given by Gorla and Khan, 2003, a "*Turbomachinery is a device in which energy transfer occurs between a flowing fluid and a rotating element due to dynamic action, and results in a change in pressure and momentum of the fluid*". In axial machines, the rotating element (or rotor) is composed of several rows of rotating blades and is acting together with inserted static rows of blades composing the stator. Each couple of adjacent stator and rotor rows consists in a stage as illustrated by the red mark on Fig. 2.1b. Figure 2.1 shows a classical turbofan mainly composed of:

1. Fan : ensuring almost 80% of modern engines thrust;

2. Compressor : increasing both total pressure and temperature of the air passing through the engine core;

3. Combustor : burning the mixture fuel-compressed air to initiate gas acceleration;

4. Turbine : transfering kinetic energy to the engine shaft causing the compressor's spin;

5. Exhaust nozzle : mixing hot and fresh bypass air downstream the engine while limiting its noise emission.

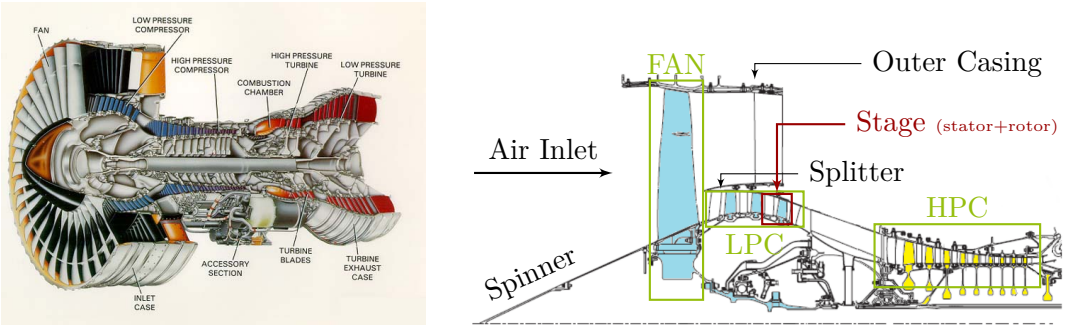

(a) Cut view of the PW4000 aircraft engine

(b) Fan and compressor core of the CFM56-5A turbofan [Piscopo, 2013]

Figure 2.1: View of civil aircraft engine.

The stages, mentioned earlier, compose the low- and high-pressure compressors on one hand and turbines on the other. The reader interested in more detailed information on Turbofan propulsion is referred to El-Sayed, 2008.

According to Meher-Homji, 2000, the birth of turbojet engines is located between 1920 and 1930 and resulted in Sir Frank Whittle's patent for jet engine. Three periods can be distinguished in nineteen century's evolution of turbomachinery design. Before mid-1900's, computational power was too low to consider numerical models higher in precision than 1D approximations. For this reason, engine designs were largely based on experiment and driven by strong asumptions, explaining relatively low performances. Between 1950 and 1980, 2D "through-flow-calculation" became the dominating method for turbomachinery design [X. D. Wang, 2010]. After 1980's, the increase in computational power made turbomachinery studies affordable via newly developed Reynolds Averaged Navier-Stokes (RANS) simulations and their associated turbulence models. As mentioned by X. D. Wang, 2010, the Computational Fluid Dynamics (CFD)

simulations used for turbomachinery design "*developed from 2D to 3D, from planar cascade to annular cascade, from single blade passage to whole ring, from single stage to multi-stages*". The switch from $2D$ to $3D$ computations allowed a better control over the blades design, as reported in Dang and Isgro, 1995; Dang, Damle, et al., 2000. The increase in fidelity is directly correlated to an important increase in the modern engines performance, as illustrated on Fig. 2.2. For a review on the application of CFD for turbomachinery design, the reader is referred to Denton and Dawes, 1998 and Pinto et al., 2016.

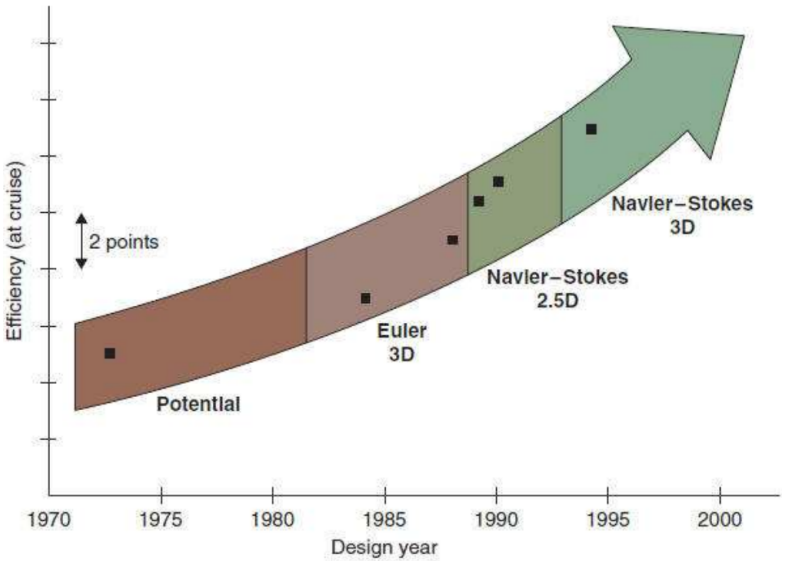

Figure 2.2: Impact of CFD on SNECMA fan performance, over a period of 30 years (from Escuret et al., 1998; X. D. Wang, 2010)

In their review article, Pinto et al., 2016 investigate the computational methods involved in aerodynamic study for turbomachinery. They come to the conclusion that high-fidelity CFD numerical methods have reached a maturity allowing their daily use in engineering offices. The predictive capability of these methods enables the restriction of undesired features in the machine like strong secondary flows in turbines or corner separations in compressors. They also highlight the present trend to move from steady state single stage simulations to multistage and unsteady predictions. They finally emphasize the associated computational limitations, as unsteady computations tend to be conflicting with usual numbers of evaluations required in any optimization campaign. Page et al., 2015 give an overview of high-fidelity based turbomachinery automated design and optimization.

2.1.1 Secondary flows in turbomachines

In the recent years, the reduction of both weight and size of axial aircraft compressors has led to high stage loadings. This tends to increase the cross flow intensity as well as three dimensional separation phenomena. Figure 2.3 shows the expected secondary structures in axial turbomachinery. These structures mainly appear due to the interaction between the boundary layer with the Leading Edge (LE) of the blade.

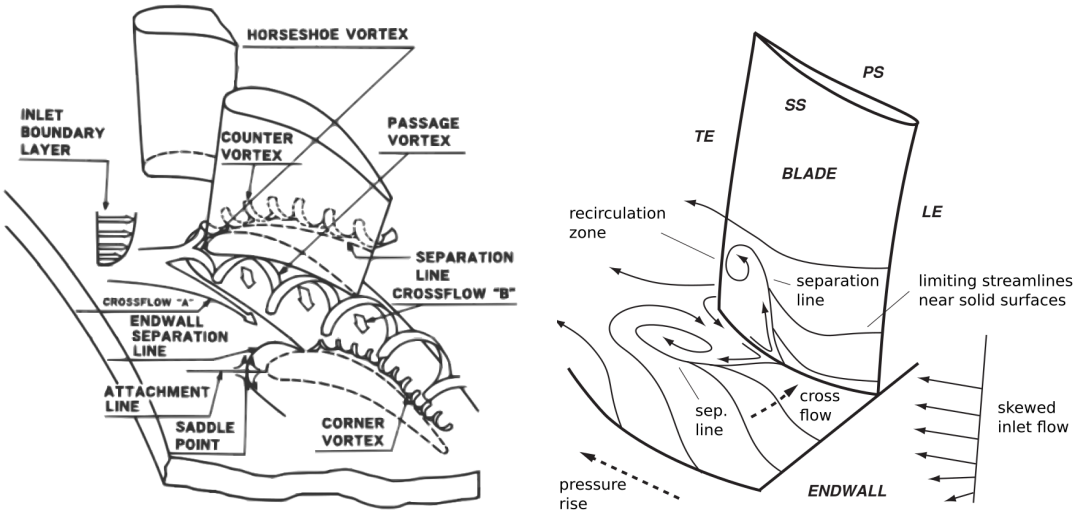

(a) Secondary flow in a turbine (from Takeishi et al., 1990)

(b) Formation of hub-corner stall with separation lines (from Lei et al., 2008)

Figure 2.3: Secondary flows in axial turbomachinery.

Most of the literature on secondary flows in axial turbomachinery is dealing with turbines [Denton, 1993; Langston, 2001] as the amplitude of the observed structures is increased by higher thickness to chord ratios (mainly due to turbine internal cooling constraints), and their impact on the global performances of the machine is strenghtened by the flow acceleration accross the passage. The increase in static pressure in the near-LE stagnating point creates a descending / ascending flow impacting the low-momentum boundary layer on the hub / casing endwall. In the hub vicinity, the radial velocity gradient induces a vortex filament upstream of the rotor LE [Levchenya et al., 2010] that rolls up into the horseshoe vortex when skirting the blade LE (see Fig. 2.3a and Reising, 2011). Another overwhelming secondary flow occurs in the blade channel and is known as hub or casing passage vortices. In the low-momentum boundary layer on the bounding walls of the passage, the equilibrium streamlines are overturned yielding a cross

flow going from the Pressure Side (PS) to the Suction Side (SS) of adjacent blades [Colombo, 2011, Chapter 1 - Section 3]. Two spiralling motions are thus originated and result in counter-rotating passage vortices that can also be linked to the corner vortex onset as they impact the boundary-layer on the blade surface. Depending on the inlet massflow rate at the considered operating point, the PS leg of the horseshoe vortex can cross over the passage and further complexify the passage vortex structure on one hand and interact with the SS leg of the horseshoe vortex from the adjacent blade on the other, as illustrated on Fig. 2.3a.

The secondary flows in turbine and compressor rotors are slightly different even if the structures remain equivalent. Firstly, the turning observed in compressors is usually far below its turbine design counterpart despite an increase in the turning accross compressor blade rows in the last decades. Secondly, the fluid being accelerated accross the turbine stages, the secondary structures are stretched and their rotating kinetic energy is increased. Therefore, designs that delay the development of hub vortices are improving the turbine efficiency simply by reducing the impact of flow acceleration on the secondary flows. In compressor design, this streching is not observable as the mean axial velocity is reduced accross the compressor stages. On the contrary, the diffusion is responsible for an increased mixing of the vortices with the main stream in the passage. Another phenomenon called "three-dimensional separation" is also observed in highly loaded compressor stages [Colombo, 2011, Chapter 1 - Section 4]. This phenomenon occurs when the low momentum fluid in the boundary layer, going from PS to SS of adjacent blades, intersects the low momentum fluid on the suction surface hub corner and can be further induced by a descending flow on the blade surface [Gbadebo et al., 2005]. As illustrated on Fig. 2.3b, the cross flow between PS and SS of adjacent blades triggers the seperation of the fluid. This phenomenon can be further induced by shock-boundary layer interaction in the case of high turnings revealing locally supersonic hub sections.

2.2 Surrogate Based Optimization

Simulation-based optimization has proven to be an efficient tool to explore large design spaces and target important improvements in performances while keeping the design cycle duration within acceptable limits. Nevertheless, the involved computational burden is often shown to be prohibitive for complex industrial applications [Pinto et al., 2016]. In this section, we give an overview of different attempts of industrial optimizations involving SBO techniques aiming at drastically reducing the number of costly evaluations by substituting an approximate

to the high-fidelity computational model. For complete review on the subject, the reader is referred to Keane and Nair, 2005; Queipo et al., 2005; Eldred and Dunlavy, 2006; Forrester, Sóbester, et al., 2007; Forrester, Sóbester, et al., 2008; Forrester and Keane, 2009; Koziel and Ogurtsov, 2014 or Viana et al., 2014.

The SBO paradigm is known to be an efficient approach to optimize cost functions estimated from computationally expensive computer codes [Queipo et al., 2005; Forrester and Keane, 2009]. The main idea is to replace the direct optimization by an iterative process involving the creation, the optimization and the update of a reasonably accurate analytical representation of the cost function that is tractable for extensive evaluation [Koziel and X.-S. Yang, 2011, Chapter 3]. Conceptually speaking, the SBO procedure can be summarized as follows:

1. Generate the initial surrogate model trained on an *a priori* sampling of the high-fidelity model,
2. Obtain an approximate solution to Problem 1.1 by optimizing the surrogate,
3. Evaluate the high-fidelity solution of the approximate optimum,
4. Update the surrogate model with the new high-fidelity point(s),
5. Stop the process if the arbitrary terminating conditions are met or go to step 2.

This sequence's inner loop (steps 2 to 4) can be formulated as an iterative procedure, as in Queipo et al., 2005; Koziel, Bandler, et al., 2006; Koziel and X.-S. Yang, 2011:

$$\boldsymbol{\theta}^{\star(i+1)} = \arg\min_{\boldsymbol{\theta}} \tilde{\mathcal{Y}}^{(i)}\left(\boldsymbol{\theta}, \mathbf{y}\boldsymbol{\theta}\right)) \quad \text{s.t} \quad \tilde{\mathbf{c}}^{(i)}\left(\boldsymbol{\theta}, \mathbf{y}(\boldsymbol{\theta})\right) \leq 0. \tag{2.1}$$

2.2.1 Provably convergent surrogate model management techniques

The optimization subproblem solved at iteration (i) can be associated to a trust-region constraint $\Delta^{(i)}$. Depending on the order of consistency of the surrogate model in the trust region surrounding the current optimum, the sequence of subproblems optima is provably convergent as demonstrated in Alexandrov, Dennis, et al., 1998. Being based upon zero- or first-order consistent surrogate models, the SBO strategy can target the optimization of the surrogate of the original objective or an associated merit function, potentially integrating the original constraints of the problem [Eldred and Dunlavy, 2006]. As part of the large class

of SBO methods, we can mention the Approximation Model Management Optimization (AMMO) by Alexandrov and R. M. Lewis, 2001, and the Surrogate Management Framework (SMF) of Booker et al., 1999 or Torczon and Trosset, 1998 associated to "pattern search" [Torczon, 1997] Derivative Free Optimizations (DFOs) that are more suited to first-order consistent models.

2.2.2 Gradient Based Optimization

Gradient Based Optimization (GBO) is often linked with direct optimization where a local search algorithm is based on the first-order derivative and eventually on the Hessian of the objective function. As mentioned earlier, this kind of strategy is untractable for industrial optimization problems associated to expensive evaluation tools. Nevertheless, we can integrate new types of surrogate modeling related methodologies into the class of GBOs:

- SBO techniques based on Gradient Enhanced Surrogate Models (GESMs) [Giannakoglou et al., 2006; Laurenceau and Sagaut, 2008; Han, Görtz, et al., 2013; Zimmermann, 2013; L. T. Leifsson et al., 2016; C. Song et al., 2016]
- GBO methods sped up with the approximate gradient of the surrogate model [Peri and Tinti, 2012; Bellary and Samad, 2014; Bahamonde et al., 2016].

2.2.3 Evolutionary Algorithm based optimization

Another class of SBO strategies that originated in the mid-1980's [Grefenstette and Fitzpatrick, 1985] and gained in popularity within the last two decades pertains to surrogate assisted Evolutionary Algorithms (EAs). According to Jin, 2011, SMFs for fitness evaluation are divided into individual-based [Jin, Olhofer, et al., 2000; Jin, Olhofer, et al., 2002; Ong et al., 2003; Branke and Schmidt, 2005], generation-based [Ratle, 1998; Bull, 1999; Jin, Olhofer, et al., 2002; Lim et al., 2006] and population-based [Hamza and Saitou, 2012; Gong et al., 2015] categories. The basic asumption these techniques are built on is that the surrogate model is accurate enough to support the whole optimization process supposedly yielding a global or near-optimal solution. This kind of Surrogate Management Technique (SMT) is often referred to as off-line surrogate based Evolutionary Optimization (EO) [Redmond and Parker, 1996; Bull, 1999; Greenman and Roth, 1999]. Nevertheless this strategy can lead to false optima as illustrated in Jin, Olhofer, et al., 2000. As opposed to previous type of SBO strategies, in that case, the construction of a model management method is much more complicated, and

no proof of convergence is yet associated to this class of techniques [Ong et al., 2003]. To cope with this issue, more recent developments usually involve online strategies [Pierret and Van den Braembussche, 1999; Branke and Schmidt, 2005; Emmerich et al., 2006]. For a complete overview on surrogate assisted EOs, the reader is referred to Jin, 2005; Jin, 2011.

2.3 Multi-fidelity surrogate modeling

The "multi-fidelity" terminology covers a wide range of concepts and is also referred to as "variable-fidelity" or "multi-level". Our main focus in this section are surrogate models fusion techniques combining precise, albeit costly, high-fidelity data with abondant, yet less accurate, lower-fidelity data. Nevertheless, it is worth mentioning other strategies combining multiple fidelity codes in a different way. For example, Burton and Hajela, 2003; Choi, Alonso, and I. M. Kroo, 2005; Choi, Alonso, I. M. Kroo, and Wintzer, 2008; Choi, Alonso, and I. M. Kroo, 2009; G. Singh and Grandhi, 2010 propose to restrain the use of high-fidelity simulations to configurations poorly predicted by the low-fidelity code. Rodríguez et al., 2001 and Peherstorfer et al., 2016 narrow down the search area by low-fidelity exploration before increasing the precision in a second phase restricted to a smaller design space.

Multi-fidelity strategies can be found in many disciplines with varying levels of fidelity and relation between low- and high-fidelity simulations. According to Fernández-Godino et al., 2016, the fidelity levels relation can be of three different types:

- complex compared to simplified mathematical model
  - modified differential equations : inviscid Euler / viscous RANS
  - linearization by boundary conditions or geometry simplification
- precise compared to coarse mathematical simulation
  - fine compared to coarsened discretization
  - converged compared to semi-converged computation
- experimental data compared to modeled physics

The idea of fusing information obtained from different fidelity simulation codes targeting similar physical phenomena has been discussed since the early 90's. One

possibility that originally emerged is the concept of additive or multiplicative correction. In this framework, a low-fidelity surrogate model (trained from a large number of samples) is corrected by the addition or scaling of a correction determined from reliable, yet sparse, high-fidelity information [Keane and Nair, 2005]. In the case of low-fidelity computations affordable for extensive evaluation, the correction can be applied directly on the low-fidelity solution, as proposed in Toal, 2014.

2.3.1 Corrective multi-fidelity surrogate models

On Fig. 2.4, we propose a synthetic view of the corrective multi-fidelity approach [Balabanov et al., 1998; Keane, 2012; Perdikaris et al., 2015].

The model (Fig. 2.4) is an additive correction, but this scheme could be easily applied to multiplicative or linear (also called "comprehensive" in Fernández-Godino et al., 2016) models [Keane, 2012; Perdikaris et al., 2015]. Lets consider two different simulation codes giving access to full-field solutions $\mathbf{y}$ and $\mathbf{z}$ at two different levels of accuracy. Stating $I(\cdot)$ the integration function yielding the performance indicators of the designed industrial product from its low- or high-fidelity full-field response, Fig. 2.4 illustrates the data flow map in corrective MFSMs. From two nested sets (HF locations evaluated at both HF and LF level) of low- ($\mathbf{z}$) and high-fidelity ($\mathbf{y}$) samples, the performance indicator ζ is computed respectively at low- (ζ_L) and high-fidelity (ζ_H) levels. A Data Fitting Surrogate Model (DFSM) $\tilde{\zeta}_L$ is built from all the low-fidelity information as well as a bridge function $\tilde{\zeta}_{H-L}$ (or $\tilde{\zeta}_{H/L}$). The fused surrogate model $\tilde{\zeta}$ is then obtained by sumation (or multiplication) of $\tilde{\zeta}_L$ with the scaling function. Depending on the expected accuracy and the type of constitutive Single-Fidelity Surrogate Models (SFSMs) $\tilde{\zeta}_L$ and $\tilde{\zeta}_{H-L}$, some hyper-parameters can be tuned to increase the generalization ability of $\tilde{\zeta}$.

Many multi-fidelity frameworks presented in the literature involve additive corrections where the scaling function (Fig. 2.4) hyper-parameters are not influenced by the low-fidelity model training or *vice versa* [Haftka, 1991; Balabanov et al., 1998; R. Lewis and Nash, 2000; Choi, Alonso, I. M. Kroo, and Wintzer, 2008]. The multiplicative correction framework is even more present in the literature than its additive analogue [Chang et al., 1993; Alexandrov, R. M. Lewis, et al., 2000; Alexandrov, Nielsen, et al., 2000; Madsen and Langthjem, 2001]. Being additive, multiplicative or linear correction, the bridge function can ensure a first- [Alexandrov, Nielsen, et al., 2000] or second-order correction [Gano et al., 2004; Eldred, Giunta, et al., 2004]. Concerning linear or comprehensive

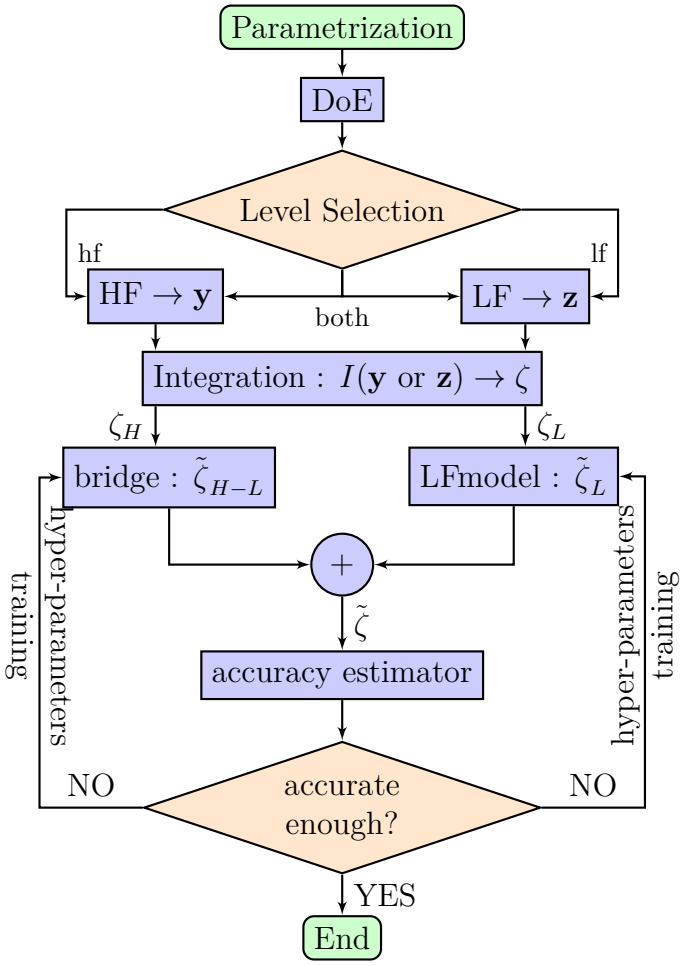

Figure 2.4: "Classical" additive multi-fidelity framework for scalar quantities [Balabanov et al., 1998; Perdikaris et al., 2015].

corrections, the scaling term can be non-constant as in Qian and J. C. F. Wu, 2008, even though most of the referenced methods define it as constant [Keane, 2012; Perdikaris et al., 2015].

As demonstrated by Fernández-Godino et al., 2016, after a 20$^{\text{th}}$ century dominated by deterministic multi-fidelity approaches, more recent researches tend to show the rise of "non-deterministic" methods, like Kriging [Kleijnen, 2009] and more specifically co-Kriging [Forrester, Sóbester, et al., 2007] based methodologies which received a growing interest since the seminal publication of Kennedy and O'Hagan, 2000.

2.3.2 Co-Kriging related methods

Numerous references propose to use the co-Kriging method or one of its related methodologies in SBO, Uncertainty Quantification (UQ) or design space exploration. Detailed information about the technique implementation are given, for example, in Kennedy and O'Hagan, 2000; Forrester, Sóbester, et al., 2008; Nava et al., 2010. The reader interested in application of this MFSM technique is also referred to Forrester, Sóbester, et al., 2007; Han, Zimmermann, et al., 2010; Zimmermann and Han, 2010; Kuya et al., 2011; Toal and Keane, 2011; Goh et al., 2013; Huang et al., 2013; Biehler et al., 2015 as non-exhaustive list.

The co-Kriging method [D. E. Myers, 1982; Kennedy and O'Hagan, 2000] is, like its single-fidelity Kriging [Krige, 1951; Matheron, 1963] counterpart, known to be limited in terms of design space dimensionality and usually restrained to optimization problems up to 10 variables [B.-S. Kim et al., 2009]. This is due to its hyper-parameters sub-optimization cost exponentially increasing with the dimensionality [Bouhlel et al., 2016]. This restriction can be lifted by changing the predictor of the sub-optimization of Kriging's hyper-parameters or reducing their number by ROM [Bouhlel et al., 2016].

2.3.3 Radial Basis Function Network and Artificial Neural Network related methods

Another type of MFSM that scales better with the number of design parameters is that on Artificial Neural Network (ANN) and Radial Basis Function Network (RBFN) concepts. Apart from linear or comprehensive correction, the augmented dimensionality formulation is a technique allowing the fusion of multi-level information by integrating the level of fidelity as parameter for the surrogate model [Reisenthel, Love, et al., 2006; Reisenthel, Allen, et al., 2010; Mifsud, MacManus, et al., 2016]. In ANN based modeling, the integration of empirical or *a priori* knowledge proposed by F. Wang and Zhang, 1997 can be modified to combine low-fidelity information [Leary et al., 2003].

2.3.4 Space Mapping techniques

As mentioned by Fernández-Godino et al., 2016, another approach to multi-fidelity data fusion, as compared to corrective techniques, pertains to the mapping of the input variables as in the Space Mapping related techniques [Bandler, Biernacki, et al., 1994; Koziel and L. Leifsson, 2012; Bandler, Cheng, et al., 2004; Robinson et al., 2008], in order to obtain mapped multi-fidelity data sharing the same

variable-dimension.

2.4 Reduced Order Models

Full-field surrogate models using projection-based ROM techniques are either used as low-fidelity models to search locally for new design points [Eldred and Dunlavy, 2006; Bui-Thanh, Willcox, et al., 2008; Raissi, 2013], or to capture most impacting physical phenomena and the effect of parametric changes [Bui-Thanh, 2003; Kyriacou et al., 2014; Hamdaoui et al., 2013; Bahamonde et al., 2016]. Considering the first category, the comprehension of the effect of parametric changes on the full-field solution of the considered Partial Derivative Equation (PDE) is obtained at the cost of important invasiveness to the simulation code. Another disadvantage of these methods is the non-negligible cost of the low-fidelity full field solution, as noted by Eldred and Dunlavy, 2006. On the other hand, the projection of the system of PDEs onto the reduced basis offers an insight into relatively important parts of the physics involved in the modeled problem.

In the case of ROM based surrogate models appropriate for intensive interrogation, different techniques allow to use a reduced order basis without any intervention on the simulation code, regardless its level of fidelity. These techniques are most of the time related to Proper Orthogonal Decomposition (POD) [Kerschen et al., 2005]:

- Surrogate-POD [Mifsud, Shaw, et al., 2009]
- Shape manifold learning [Le Quilliec et al., 2015; Meng et al., 2016],
- Non-Intrusive ROMs (NIROMs) [Bistrian and Navon, 2016; Lin et al., 2016],
- Physics-based reduced-order approximation [Audouze et al., 2009],
- POD with Interpolation (PODI or POD+I, Bui-Thanh, 2003; Bui-Thanh, Damodaran, et al., 2004; Cao et al., 2016; Verveld et al., 2016),
- Non-Intrusive POD (NIPOD) [Guénot et al., 2011; Guénot et al., 2013; D. Xiao, Fang, et al., 2015; D. Xiao, P. Yang, Fang, Xiang, Pain, and Navon, 2016; D. Xiao, P. Yang, Fang, Xiang, Pain, Navon, and M. Chen, 2017].

In the solution to an unsteady aerodynamic problem proposed by D. Xiao, Fang, et al., 2015; D. Xiao, P. Yang, Fang, Xiang, Pain, and Navon, 2016; D. Xiao, P. Yang, Fang, Xiang, Pain, Navon, and M. Chen, 2017, the ROM evaluation

cost is increased by the need to compute the initial condition of the parametrized configuration. Once the reduced order basis is constructed, a recursive approach is used to approximate the reduced solution at any time t for the evaluated set of parameters. Parametrized RBFN surrogate models are built from the initial solution at $t = 0$ in order to determine the right reduced approximation at time t. NIROMs have been used in inverse problems, as in Ostrowski et al., 2008; Hamim and R. P. Singh, 2017; Bui-Thanh, Damodaran, et al., 2004.

To the best of the author knowledge, only a few techniques have been proposed to couple the computational alleviation brought by multi-fidelity techniques with the physical insight allowed by ROM approaches. We can however record two different techniques respectively associated to the multi-fidelity hierarchical framework [L. Leifsson and Koziel, 2010; Toal, 2014; L. Leifsson and Koziel, 2015; L. T. Leifsson et al., 2016], and the fusion related MFSM framework [Mifsud, 2008; Mifsud, MacManus, et al., 2016]. The approach presented in L. Leifsson and Koziel, 2010 is referenced as physics-based as a shape-preserving mapping is computed to correct a low-fidelity pressure distribution and predict its high-fidelity counterpart. In his article, Toal, 2014 proposes to build a reduced basis of the concatenation of low- and high-fidelity full-field solutions. Using the so-called "Gappy-POD" technique [Everson and Sirovich, 1995; Bui-Thanh, 2003], a high-fidelity prediction can be built upon any computed low-fidelity solution. On the other hand, the method proposed in Mifsud, 2008 and Mifsud, MacManus, et al., 2016 allows to construct a mixed reduced basis from both low- and high-fidelity solutions. The prediction of the full field solution associated to an unknown parametric configuration is obtained via augmented MFSMs linking the design space with the POD reduced space.

Figure 2.5 illustrates the dimensionality augmentation of the POD coefficient space in Mifsud, 2008. Once the variable-fidelity POD basis is built, all the training snapshots are projected onto the POD-based ROM yielding databases linking the position in the design space, the level of fidelity (ε on Fig. 2.5) and the position in the POD space. Single-Fidelity DFSMs (SFDFSMs) are constructed considering ε as an extra parameter in the design space. The prediction of the full-field solution of an unknown location in the design space is then obtained by evaluating the surrogate model with $\varepsilon = 1$ (evaluation of an approximate high-fidelity full-field solution) and multiplying the predicted vector of coefficients onto the basis vectors of the variable-fidelity POD-based ROM.

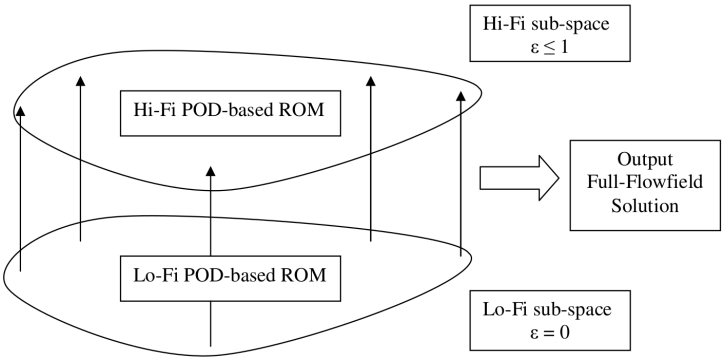

Figure 2.5: Schematic view of the "Variable-Fidelity POD-based ROM" (from Mifsud, 2008).

2.5 Surrogate Based Optimization in turbomachinery design

The application of SBO techniques to complex turbomachinery design has gained in popularity over the past decades, and numerous papers involved this kind of techniques in the shape design of different parts yielding increased efficiency.

Numerous references propose to treat turbomachinery related engineering designs via surrogate-assisted Multi-Objective Optimization (MOO) techniques such as:

- NSGA-II [Deb et al., 2002] as in Keskin et al., 2008; Cravero et al., 2012; Deng et al., 2013; Khalfallah et al., 2015; Wagner et al., 2015; Siddique et al., 2016,
- Differential Evolution (DE, Storn and Price, 1997) as in Mueller et al., 2012; De Maesschalck et al., 2013,
- other multi-objective optimization techniques as in Aulich and Siller, 2011; Schnell et al., 2012; Cremanns et al., 2016; Ma et al., 2016; Giovannini et al., 2016.

Other authors propose surrogate-based Single-Objective Optimization (SOO) tools with or without constraints management. Arsenyev et al., 2015; H. Wang et al., 2010; L. Song et al., 2016 respectively applied the Efficient Global Optimization (EGO) technique [D. R. Jones et al., 1998] to the shape design of a Low-Pressure Turbine (LPT), a LPT exhaust and a transonic axial compressor [Reid and Morre, 1978], while Ha and Kang, 2011; Lee et al., 2014;

Goulos et al., 2016 respectively applied Kriging assited EA or Search Pattern optimizations to the design of an exhaust for tonal noise reduction, the design of a turbine stage or a centrifugal compressor impeller. Talgorn et al., 2014 coupled the dynamic tree surrogate modeling algorithm [Taddy et al., 2011] with the Mesh Adaptive Direct Search algorithm (MADS, Audet and Dennis, 2006), and applied the proposed SBO strategy to the drag minimization of a simplified wing [Tribes et al., 2004] and the Multi-Disciplinary Optimization (MDO) of a supersonic business jet [Kodiyalam and Sobieski, 2001]. Other authors propose surrogate assisted EAs dealing with mixed variables [Baert et al., 2015], surrogate assisted co-evolutionary algorithms [P. Song et al., 2014], Kriging-assisted simulated annealing techniques [Qin et al., 2013], or a linear assembly of multiple surrogate models to support EA based optimization [Shahpar and Caloni, 2013].

Finally, hybrid techniques couple surrogate modeling with GBO techniques such as Sequential Quadratic Programming (SQP) [Queipo et al., 2005]. In their articles, J.-H. Kim and K.-Y. Kim, 2012 and Heo et al., 2016 compare Kriging [Krige, 1951; Matheron, 1963], RBFN [Bishop, 1995] and Response Surface Approximation (RSA) [R. Myers, 2016] assisted SQP. Samad, K.-Y. Kim, et al., 2006, Samad and K.-Y. Kim, 2008 propose to support SQP optimization with a selection/aggregation of multiple surrogates. Leveraging the gradient information obtained from an adjoint solver, Giannakoglou et al., 2006 applied gradient enhanced ANNs and RBFNs assisted EA to the optimization of $3D$ turbine and compressor cascades.

2.6 Conclusions

As shown in Section 2.5, a majority of SBO techniques used in turbomachinery design deals with DFSMs. The secondary flows introduced in Section 2.1.1 strongly impact the performances of designed machines. As stressed out by Filomeno Coelho et al., 2008, POD based models, with respect to DFSMs give valuable insight into the physics gouverning a system's response. Therefore we target the integration of POD based full-field surrogate models within SBO strategies.

In the mean time, as illustrated in Section 2.3, MFSMs frequently outperform their single-fidelity analogue. Consequently, we propose, in the remainder of this thesis, POD based MFSMs integrated into online enrichment or Multi-Fidelity SBO (MFSBO) techniques and their applications to aerodynamic design.

Part I

Theoretical development and methodology

Chapter 3

POD based methodologies

This chapter presents Proper Orthogonal Decomposition (POD) based methodologies re-interpreted in order to create and enrich full-field Multi-Fidelity Surrogate Models (MFSMs). We present firstly the Non-Intrusive POD (NIPOD) and its constitutive steps in Section 3.1. Section 3.2 summarizes the Constrained POD (CPOD) intially introduced by M. Xiao, Breitkopf, Filomeno Coelho, Knopf-Lenoir, Sidorkiewicz, et al., 2010; M. Xiao, Breitkopf, Filomeno Coelho, Knopf-Lenoir, Villon, et al., 2013; M. Xiao, Breitkopf, Filomeno Coelho, Villon, et al., 2014. Finally, Section 3.3 re-interprets the Gappy-POD (GPOD) for multi-fidelity data introduced by Toal, 2014 in order to enable the later development of a dedicated enrichment criterion.

3.1 Non-Intrusive POD

Also known as Karhunen-Loève Expansion (KLE), or Principal Component Analysis (PCA), POD was first introduced in the field of turbulence by Lumley, 1967. POD is widely used to capture the essential dynamics of the physical phenomenon under study from a set of full-field simulations within a lower dimensional space [Gogu et al., 2009]. Assuming only a few independent modes strongly impact the dynamics of the system, an important decrease in the computational cost of the solution can be obtained concessing few in terms of precision.

While the POD-Galerkin model reduction intends to project the set of Partial Derivative Equations (PDE) onto the subspace spanned by the "most energetic" modes, the NIPOD interpolates the relation between the design space $\mathcal{D} \subset \mathbb{R}^p$ and the reduced output space. This step enables the prediction of the physical response for any defined configuration in $\mathcal{D}$. This type of models are referred to as NIPOD [Guénot et al., 2011; Guénot et al., 2013; D. Xiao, Fang, et al., 2015],

"Galerkin-free" Reduced Order Models (ROMs) [Shinde et al., 2016], "surrogate" POD [Hamdaoui et al., 2013], or POD "with interpolation" (PODI) [Bui-Thanh, 2003; Cao et al., 2016].

3.1.1 Basics of POD

We consider a p-dimensional $\mathcal{D}$ and a "costly" evaluation function yielding high-fidelity (or, at least, precise enough) discretized solutions $\mathbf{y} \in \mathbb{R}^n$, where $n \gg p$. We also define $\boldsymbol{\theta} \in \mathbb{R}^p$ the vector of parameters associated to a given position in $\mathcal{D}$ and a computed solution $\mathbf{y}(\boldsymbol{\theta})$. Given a Design of Experiments (DoE) $\boldsymbol{\Theta}$ of M samples in $\mathcal{D}$, we define the column-dominant snapshot matrix $\mathbf{Y}$ containing the snapshots $\mathbf{y}_i(\boldsymbol{\theta}_i)\ \forall i \in [\![1, M]\!]$, and a centering snapshot $\bar{\mathbf{y}}$, usually taken as the mean vector $\bar{\mathbf{y}} := \dfrac{1}{M}\sum_{i=1}^{M}\mathbf{y}_i$. Following the formulation introduced in Raghavan et al., 2013, the POD procedure is presented as the best orthogonal projector for the vectors contained in the set of snapshots $\mathbf{Y}$.

Each snapshot $\mathbf{y}$ is considered as a point in an Euclidean affine space $\mathcal{E}$ on the vector space $E \in \mathbb{R}^n$ associated with:

1. the coordinate system $(O, \mathcal{B})$ where $\mathcal{B}$ is the canonical basis of E and O is a point chosen as origin (usually the mean snapshot $\bar{\mathbf{y}}$);
2. the usual inner product $\langle \mathbf{u}, \mathbf{v} \rangle$;
3. the usual norm $\|\mathbf{u}\|^2 = \langle \mathbf{u}, \mathbf{u} \rangle$.

The POD based ROM associated to the known vectors contained in $\mathbf{Y}'$ (where $\mathbf{Y}'_{\cdot i} := \mathbf{y}_i - \bar{\mathbf{y}}\ \forall i \in [\![1, M]\!]$) lies in the m-dimensional Euclidean affine subspace $\mathcal{F}$ which is at most M-dimensional, and far smaller than the output vector space dimension n ($O < m \leq M \ll n$). Let $\boldsymbol{\Phi} := [\boldsymbol{\phi}_1, \cdots, \boldsymbol{\phi}_m]$ be an orthonormal basis generating $\mathcal{F}$. We characterize the POD orthogonal projector $\langle \boldsymbol{\Phi}\boldsymbol{\Phi}^\top, \mathbf{y} - \bar{\mathbf{y}} \rangle : \mathcal{E} \to \mathcal{F}$ with the optimality and orthogonality conditions

$$\min_{\boldsymbol{\Phi}} \left(\left\| \left(\mathbf{I} - \boldsymbol{\Phi}\boldsymbol{\Phi}^\top \right) \mathbf{Y}' \right\|_F^2 \right), \text{ with } \boldsymbol{\Phi}^\top\boldsymbol{\Phi} = \mathbf{I}_m, \tag{3.1}$$

where $\|A\|_F^2 := tr(A^\top A)$ is the Frobenius norm, yielding $\boldsymbol{\Phi}$ the eigenmodes of the covariance matrix $\mathbf{Y}'\mathbf{Y}'^\top$.
By limiting the basis $\boldsymbol{\Phi}$ to the m most "energetic" modes, the reconstruction error

$$\epsilon(m) = 1 - \frac{\sum_{i=1}^{m} \lambda_i}{\sum_{j=1}^{M} \lambda_j}, \tag{3.2}$$

where $\boldsymbol{\lambda}$ is the vector of monotonically decreasing eigenvalues associated with the eigenvalue problem

$$\mathbf{Y'}\mathbf{Y'}^{\top}\boldsymbol{\phi}_i = \lambda_i \boldsymbol{\phi}_i. \tag{3.3}$$

Practically, following the "snapshots" method proposed by Sirovich, 1987, the basis $\boldsymbol{\Phi}$ is determined by Singular Value Decomposition (SVD) of the deviation matrix $\mathbf{Y'}$. For further information regarding the connections and equivalence between POD, PCA, KLE and SVD, one can refer to Liang et al., 2002. The reduced-order solution $\tilde{\mathbf{y}}(\boldsymbol{\theta}) \in \mathbb{R}^n$ may be written:

$$\tilde{\mathbf{y}}(\boldsymbol{\theta}) = \bar{\mathbf{y}} + \sum_{i=1}^{m} \boldsymbol{\phi}_i \alpha_i, \tag{3.4}$$

where α_i is the projection coefficient of the full-field solution $\mathbf{y}(\boldsymbol{\theta})$, of any vector of parameters $\boldsymbol{\theta} \in \mathcal{D}$, onto the i-th vector in the basis $\boldsymbol{\Phi}$.

3.1.2 Surrogates of the projection coefficients

NIPOD targets a fast evaluation of the full-field simulation by interpolating each of the projection coefficients $\alpha_i \ \forall i \in [\![1, m]\!]$, with respect to the position $\boldsymbol{\theta} \in \mathcal{D}$. The surrogate model for each of the projection coefficients $\tilde{\alpha}_i$ is constructed using a data fitting method such as:

- Polynomial Responses (RSMs) [Forrester, Sóbester, et al., 2008],
- Diffuse Approximations (DAs) [Nayroles et al., 1992; Breitkopf et al., 1998],
- Radial Basis Function Networks (RBFNs) [Bishop, 1995, Section 5],
- Support Vector Regressions (SVRs) [Smola and Schölkopf, 2004],
- Gaussian Processes ($\mathcal{GP}$s) [Rasmussen and Williams, 2006],
- Artificial Neural Networks (ANNs) [Bishop, 1995, Section 4].

In the present work, RBFNs are used to train the surrogate models of the projection coefficients. We denote $\mathbf{H}$ the matrix such that $h_{jk} = h_j\left(\|\boldsymbol{\theta}_k - \boldsymbol{\theta}_j\|^2, \sigma_j\right) \ \forall j, k \in [\![1, M]\!]^2$, with h_j the Radial Basis Functions (RBFs) composing the network and centered around the M training experiments. To ensure $\mathbf{H}$ is positive definite, we use non-conditionally invertible multi-quadric

$$h_j(\boldsymbol{\theta}, \sigma) = \sqrt{\frac{\|\boldsymbol{\theta} - \boldsymbol{\theta}_j\|^2}{\sigma^2} + 1}, \tag{3.5}$$

or Gaussian

$$h_j(\boldsymbol{\theta}, \sigma) = \exp\left(-\frac{\|\boldsymbol{\theta} - \boldsymbol{\theta}_j\|^2}{2\sigma^2}\right) \tag{3.6}$$

kernels. Denoting $\boldsymbol{\alpha}_i$ the "target" vector [Bishop, 1995, Chapter 5] of the projection coefficients of all the training snapshots onto the i-th mode of the basis $\boldsymbol{\Phi}$, ω_{ij} are the weights of the linear regression obtained by resolution of

$$\mathbf{H}\boldsymbol{\omega}_i = \boldsymbol{\alpha}_i. \tag{3.7}$$

The computation of the weight vector $\boldsymbol{\omega}_i$ associated to each dimension $i \in [\![1, m]\!]$ of the ROM, gives access to a fast estimation ($\tilde{\alpha}_i(\boldsymbol{\theta}) \approx \alpha_i(\boldsymbol{\theta})$) of the reduced-order solution in the POD space for any $\boldsymbol{\theta}$ in the design space $\mathcal{D}$:

$$\tilde{\alpha}_i(\boldsymbol{\theta}) = \sum_{j=1}^{M} \omega_j h_j\left(\|\boldsymbol{\theta} - \boldsymbol{\theta}_j\|_2, \sigma_j\right). \tag{3.8}$$

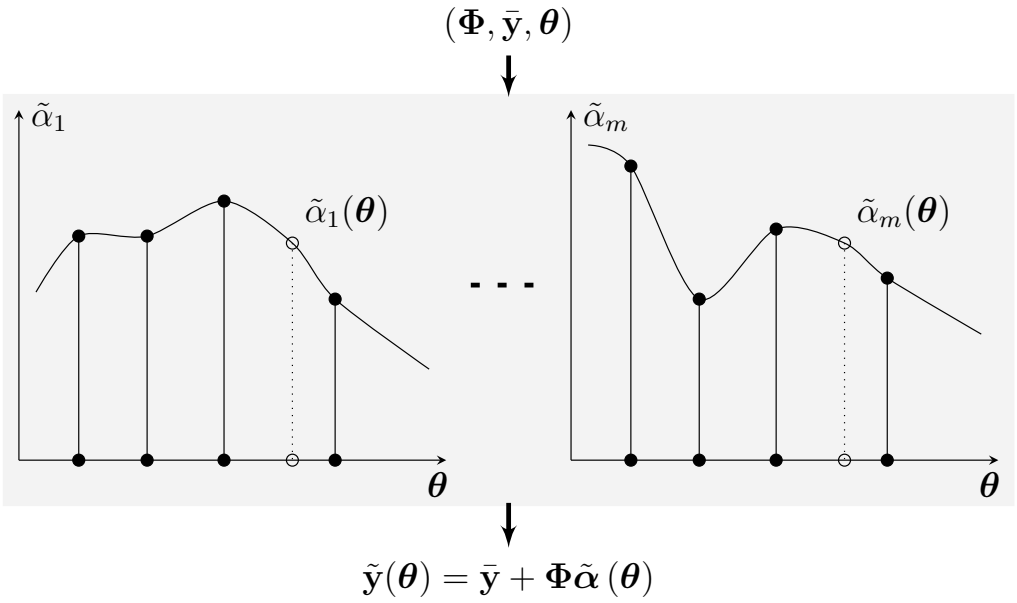

Figure 3.1: Illustration of the approximation procedure of the surrogate model.

Figure 3.1 illustrates the way the surrogate models of the projection coefficients ($\tilde{\alpha}_i(\boldsymbol{\theta})\ \forall\ i, \boldsymbol{\theta} \in [\![1, m]\!] \times \mathcal{D}$) give access to a fast evaluation of the full-field reduced solution $\tilde{\mathbf{y}}$ of any unknown location $\boldsymbol{\theta}$.

3.2 Constrained POD

As mentioned in Section 3.1.1, it is possible to reduce the dimension of the ROM built by POD conceding a sensible increase in the reconstruction error of the training full-field solutions. Equation 3.2 gives the reconstruction error depending on the number of dropped modes. In this matter, the storage of eigenmodes in descending order (with respect to their associated eigenvalues) given by the SVD technique is of first importance in order to limit the error mentioned above. Even though POD based surrogate models give access to the reduced full-field solution, classical optimization algorithms deal with scalar quantities of interest describing the objectives and constraints of the optimization problem. Therefore, an integration is performed on the full-field solution to obtain these quantities of interest ($I(\mathbf{y}$ or $\mathbf{z})$ on Fig. 2.4 and $I(\tilde{\mathbf{y}}^\star)$ on Fig. 4.1). The idea of CPOD has been introduced by M. Xiao, Breitkopf, Filomeno Coelho, Knopf-Lenoir, Villon, et al., 2013 in order to insure the precise estimation of the quantities of interest of all the training experiments while truncating the POD basis.

Two different approaches have been proposed in M. Xiao, Breitkopf, Filomeno Coelho, Knopf-Lenoir, Sidorkiewicz, et al., 2010 and M. Xiao, Breitkopf, Filomeno Coelho, Knopf-Lenoir, Villon, et al., 2013. The former one proposes to keep the POD basis $\mathbf{\Phi}$ unchanged (see Section 3.1.1), and to modify the way the projection coefficients are obtained from the full-field solutions. Usually, the coefficients database is obtained by projecting the full-field training snapshots onto the reduced basis $\mathbf{\Phi}$ which minimizes the full-field reconstruction error. This step is here modified to minimize this error constrained by the vectorial error of estimation of all the integral quantities. In the latter approach, the authors propose to modify the basis itself accounting for the impact of truncation on the prediction of the integral quantities.

As soon as all the quantities of interest for the optimization problem are linearly dependent on the full-field solution, one can express the integrations performed on the snapshots as constraints in the optimal linear subspace spanned by the constrained POD basis $\mathbf{\Psi}$. These constraints can be taken into account in the search for the optimal basis. We denote here the vector of integral quantities of interest $\mathbf{g}$ gathering objectives and constraints of the optimization problem together, and assemble the constraint matrix $\mathbf{G}$ puting the constraints associated to all the training experiments together. We characterize the constrained orthogonal projector $\left\langle \mathbf{\Psi}\mathbf{\Psi}^\top, \mathbf{y} - \bar{\mathbf{y}} \right\rangle \ : \ \mathcal{E} \to \mathcal{F}$ with the constrained optimality and orthogonality conditions

$$\begin{aligned} &\min_{\boldsymbol{\Psi}} \left(\left\| \left(\mathbf{I} - \boldsymbol{\Psi}\boldsymbol{\Psi}^\top \right) \mathbf{Y}' \right\|_F^2 \right), \\ \text{with} \quad &\boldsymbol{\Psi}^\top \boldsymbol{\Psi} = \mathbf{I}_m, \\ \text{and} \quad &\mathbf{G}^\top \boldsymbol{\Psi}\boldsymbol{\Psi}^\top \mathbf{Y}' = \mathbf{G}^\top \mathbf{Y}', \end{aligned} \tag{3.9}$$

where $\text{card}(\mathbf{g}) < m \ll M$ the number of training snapshots.
The constraint matrix $\mathbf{G}$ is decomposed thanks to QR-factorization

$$\mathbf{G} = [\mathbf{Q}_1 \ \mathbf{Q}_2] \left[\mathbf{R}_1 \ \mathbf{0} \right]^\top, \tag{3.10}$$

and the modes are sought in the orthogonal space spanned by $\mathbf{Q}_2$. It ensures the integral constraints to be satisfied before minimizing the full-field reconstruction error. To this end, the deviation matrix $\mathbf{Y}'$ is projected onto the orthogonal space $\mathbf{Y}_{\mathbf{Q}_2} = \mathbf{Q}_2^\top \mathbf{Y}'$ and the optimal basis for $\mathbf{Y}_{\mathbf{Q}_2}$ is obtained by SVD:

$$\mathbf{Y}_{\mathbf{Q}_2} = \mathbf{V}\mathbf{D}\mathbf{U}^\top. \tag{3.11}$$

Finally the constrained orthogonal basis is buit as

$$\boldsymbol{\Psi} = \left[\mathbf{Q}_1 \ \mathbf{Q}_2 \mathbf{V}_q \right], \tag{3.12}$$

where $\mathbf{V}_q$ stands for the matrix of q first columns of $\mathbf{V}$ such that $\text{card}(\mathbf{g}) + q = m$.

In Chapter 4, this methodology is re-interpreted to interpolate sparse high-fidelity information and approximate abondant low-fidelity data instead of focusing on integral quantities defined in the constraint matrix $\mathbf{G}$. The main difficulty is the centering technique mentioned in Section 4.1.1 that should now handle low- and high-fidelity mean vectors potentially lying in different vectorial spaces. This issue is detailed and lifted in Section 4.1.3.

3.3 Gappy POD-based multi-fidelity modeling

Initially introduced by Everson and Sirovich, 1995 in the context of image processing, the so-called "Gappy-POD" has been used in aerodynamics by Bui-Thanh, Damodaran, et al., 2004 especially for inverse design problems. The "gappy" denomination of this method comes from its ability to reconstruct missing information of a given vector or to fulfill the "gaps" in the corrupted data. In image processing domain, missing pixels is a problem engineers are confronted frequently with. In this frame, the GPOD procedure allows to build a matrix basis from complete images and to reconstruct the missing pixels of corrupted

material.

Following the introduction to POD in Section 3.1.1, this section presents the concept of POD associated to incomplete data. The mathematical notations given in Section 3.1 are, as far as possible, respected in this section. We start defining the term "multi-fidelity" as employed in Toal, 2014, and the associated snapshots in Section 3.3.1. GPOD is introduced in the context of Multi-Fidelity Modeling (MFM), as well as the mathematical definitions required for a dedicated enrichment criterion to be proposed in Section 5.1. This enrichment criterion aims at pointing out the surrogate low-accuracy areas. Its ability to detect and propose locations in the design space to explore in order to maximize the improvement of the model is compared against enrichment criteria from the literature on a $2D$ airfoil flight condition study.

3.3.1 Multi-fidelity modeling and associated Gappy-POD technique

The GPOD based MFSM, proposed in Toal, 2014, parametrizes the high-fidelity full-field solution by its low-fidelity counterpart, where other surrogate models usually tend to create a direct link between the design space and the output space. Following the respective definition of $\mathbf{z}$ and $\mathbf{y}$ as low- and high-fidelity full-field solutions, we construct the concatenated snapshot $\mathbf{s}$ obtained for any experiment $\boldsymbol{\theta}$ in the design space $\mathcal{D}$:

$$\mathbf{s}(\boldsymbol{\theta}) = \begin{pmatrix} z_1 \\ \vdots \\ z_{n_L} \\ \hline y_1 \\ \vdots \\ y_{n_H} \end{pmatrix} = \begin{pmatrix} \mathbf{z}(\boldsymbol{\theta}) \\ \hline \mathbf{y}(\boldsymbol{\theta}) \end{pmatrix}. \tag{3.13}$$

The term "multi-fidelity" is here understood in a different way than the definition stated in Chapter 4, where the discretized full-field low- and high-fidelity solutions have to share the same output space. In GPOD based Multi-Fidelity Surrogate Modeling (MFSM), two potentially different sizes n_L and n_H represent respectively the number of nodes in the low- and high-fidelity discretizations. We consider here a unique DoE $\boldsymbol{\Theta}$ of M points $\boldsymbol{\theta}_i$ in the design space $\mathcal{D}$, $\forall i \in [\![1, M]\!]$. The matrix of all multi-fidelity snapshots is denoted $\mathbf{S}$, by analogy with the high-fidelity matrix $\mathbf{Y}$ defined in Section 3.1.1. We also consider a centering snapshot $\bar{\mathbf{s}}$ and the deviation matrix $\mathbf{S}'$, such that its column vectors $\mathbf{s}'_i = \mathbf{s}_i - \bar{\mathbf{s}}$, $\forall i \in [\![1, M]\!]$. For the sake

of simplicity, we denote in this chapter $\mathbf{y}' = \mathbf{y} - \begin{pmatrix} \bar{s}_{n_L+1} \\ \vdots \\ \bar{s}_{n_L+n_H} \end{pmatrix}$, and $\mathbf{z}' = \mathbf{z} - \begin{pmatrix} \bar{s}_1 \\ \vdots \\ \bar{s}_{n_L} \end{pmatrix}$.

The GPOD procedure is based on the Singular Value Decomposition of the deviation matrix $\mathbf{S}'$. We call $\boldsymbol{\Phi}$ the orthonormal basis associated with the concatenated multi-fidelity subspace. The model reduction is performed by taking only the m "most energetic" modes of $\boldsymbol{\Phi}$, where $m \leq M$ as in Section 3.1.1. Given a location $\boldsymbol{\theta}$ in the design space $\mathcal{D}$, the estimation of the high-fidelity solution $\tilde{\mathbf{y}}(\boldsymbol{\theta})$ by GPOD is enabled by projecting the computed low-fidelity full-field solution $\mathbf{z}(\boldsymbol{\theta})$ onto the basis $\boldsymbol{\Phi}$. This is done in a step we call gappy-projection.

Let $\boldsymbol{\alpha} = \boldsymbol{\Phi}^\top \mathbf{s}'$ be the vector of the projection coefficients of $\mathbf{s}'$ onto the POD space, and denote $\mathcal{P}(\mathbf{s}') = \boldsymbol{\Phi}\boldsymbol{\Phi}^\top \mathbf{s}'$ the projector associated to the basis $\boldsymbol{\Phi}$. $\boldsymbol{\alpha}$ can be seen as the vector of coefficients minimizing the distance between $\mathbf{s}'$ and $\mathcal{P}(\mathbf{s}')$:

$$\boldsymbol{\alpha} = \underset{\boldsymbol{\alpha}^*}{\operatorname{argmin}} \left(\|\mathbf{s}' - \boldsymbol{\Phi}\boldsymbol{\alpha}^*\|^2 \right). \tag{3.14}$$

Gappy-POD as a predictor of high-fidelity data

The GPOD can be interpreted as the filtered projection of a vector onto the subspace spanned by the basis $\boldsymbol{\Phi}$. Once the $\boldsymbol{\Phi}$ basis built with a set of snapshots $\begin{pmatrix} \mathbf{z} \\ \mathbf{y} \end{pmatrix}$, we use the GPOD to predict high- from low-fidelity data [Toal, 2014]. Following [Bui-Thanh, Damodaran, et al., 2004], a mask vector associates 1 with low-fidelity and 0 with high-fidelity data. We start revisiting this formulation by introducing a projector $\mathcal{G}(\mathbf{s}') : \mathcal{E} \to \mathcal{E}$ allowing the same association

$$\mathcal{G}(\mathbf{s}') = \boldsymbol{\Gamma}\mathbf{s}',$$

$$\text{where } \boldsymbol{\Gamma} = \begin{pmatrix} \mathbf{I}_{n_L} & \mathbf{0} \\ \mathbf{0} & \mathbf{0} \end{pmatrix} \begin{matrix} \} \, n_L \\ \} \, n_H \end{matrix} \quad . \tag{3.15}$$
$$\qquad\qquad\qquad\qquad\quad \underbrace{\phantom{\mathbf{I}_{n_L}}}_{n_L} \; \underbrace{\phantom{\mathbf{0}}}_{n_H}$$

We now seek the best projection $\mathcal{P}_g = \boldsymbol{\Phi}\boldsymbol{\beta}$ of a filtered and centered snapshot $\boldsymbol{\Gamma}\mathbf{s}' = \begin{pmatrix} \mathbf{z}' \\ \mathbf{0} \end{pmatrix}$ by minimizing the functional

$$\mathcal{J}(\boldsymbol{\beta}) = \frac{1}{2}\|\boldsymbol{\Gamma}\mathbf{s}' - \boldsymbol{\Gamma}\boldsymbol{\Phi}\boldsymbol{\beta}\|^2, \;\; \boldsymbol{\beta} \in \mathbb{R}^m. \tag{3.16}$$

Using the idempotence property of $\mathcal{G} \Leftrightarrow \boldsymbol{\Gamma}\boldsymbol{\Gamma} = \boldsymbol{\Gamma}$, the diagonal property of $\boldsymbol{\Gamma}$ and the orthonormality of $\boldsymbol{\Phi}$, the minimization of $\mathcal{J}(\boldsymbol{\beta})$ yields

$$\boldsymbol{\beta} = \left(\boldsymbol{\Phi}^\top \boldsymbol{\Gamma} \boldsymbol{\Phi}\right)^{-1} \boldsymbol{\Phi}^\top \boldsymbol{\Gamma} \mathbf{s}'. \tag{3.17}$$

Let $\mathcal{H}$ be the projector associated with the diagonal matrix $\boldsymbol{\Upsilon} = \mathbf{I}_n - \boldsymbol{\Gamma}$, extracting the high-fidelity part $\boldsymbol{\Upsilon}\mathbf{s}' = \begin{pmatrix} \mathbf{0} \\ \mathbf{y}' \end{pmatrix}$. The GPOD operator [Toal, 2014] is referred to as $\mathcal{P}_t$ hereafter and is obtained by replacing $\boldsymbol{\Gamma}\boldsymbol{\Phi}\boldsymbol{\beta}$ with $\boldsymbol{\Gamma}\mathbf{s}'$ in the reconstructed snapshot:

$$\mathcal{P}_t(\mathbf{s}) = \boldsymbol{\Gamma}\mathbf{s} + \boldsymbol{\Upsilon}\left(\bar{\mathbf{s}} + \boldsymbol{\Phi}\boldsymbol{\beta}\right). \tag{3.18}$$

vector	notation	expression
centering snapshot	$\bar{\mathbf{s}} =$	$\frac{1}{M}\sum_{i=1}^{M} \mathbf{s}_i$
deviation snapshot	$\mathbf{s}' =$	$\mathbf{s} - \bar{\mathbf{s}}$
multi-fidelity snapshot	$\mathbf{s} =$	$\begin{pmatrix} \mathbf{z} \\ \mathbf{y} \end{pmatrix}$
low-fidelity data	$\boldsymbol{\Gamma}\mathbf{s} =$	$\begin{pmatrix} \mathbf{z} \\ \mathbf{0} \end{pmatrix}$
high-fidelity data	$\boldsymbol{\Upsilon}\mathbf{s} =$	$\begin{pmatrix} \mathbf{0} \\ \mathbf{y} \end{pmatrix}$
POD projection	$\mathcal{P}(\mathbf{s}) =$	$\bar{\mathbf{s}} + \boldsymbol{\Phi}\boldsymbol{\Phi}^\top \mathbf{s}'$
GPOD projection	$\mathcal{P}_g(\mathbf{s}) =$	$\bar{\mathbf{s}} + \boldsymbol{\Phi}\left(\boldsymbol{\Phi}^\top \boldsymbol{\Gamma} \boldsymbol{\Phi}\right)^{-1} \boldsymbol{\Phi}^\top \boldsymbol{\Gamma} \mathbf{s}'$
GPOD prediction [Toal, 2014]	$\mathcal{P}_t(\mathbf{s}) =$	$\boldsymbol{\Gamma}\mathbf{s} + \boldsymbol{\Upsilon}\mathcal{P}_g(\mathbf{s})$

Table 3.1: Multi-fidelity / POD notations.

The notations in Table 3.1 are used in the following sections. Note that $\boldsymbol{\Upsilon}\mathcal{P}_t(\mathbf{s}) = \boldsymbol{\Upsilon}\mathcal{P}_g(\mathbf{s})$ and $\boldsymbol{\Gamma}\mathcal{P}_t(\mathbf{s}) = \boldsymbol{\Gamma}\mathbf{s}$ by construction.

3.3.2 Illustration of the Gappy-projection operator

We give here a short illustration of the difference between full-field and gappy-projection. We consider the fonctional space defined by the linear combination of three Legendre's polynomials (namely $\mathcal{L}_2, \mathcal{L}_3,$ and $\mathcal{L}_5$). We select several combinations of this functional space as high-fidelity solutions $y_i(x) = \theta_1\mathcal{L}_2 + \theta_2\mathcal{L}_3 + \theta_3\mathcal{L}_5$, where $\theta_1 \in [-2, 2]$, $\theta_2 \in [-2, 2]$, $\theta_3 \in [-1, 2]$, and $i \in [\![1, M]\!]$. The associated low-fidelity snapshots are defined as $z_i(x) = y_i(x) - \theta_3\mathcal{L}_5$. In this case, we impose $n_L = n_H$ for simplicity, but the illustration would remain unchanged if not. We denote $\boldsymbol{\chi}$, the evenly distributed discretization of the real line between -1 and 1

with $n = n_H = n_L$ x-values, and $\boldsymbol{L}_k^{\boldsymbol{\chi}}$ the real-valued vector of the $\boldsymbol{\chi}$-discretized k^{th} Legendre's polynomial $\boldsymbol{L}_k^{\boldsymbol{\chi}} = [\mathcal{L}_k(\chi_1), \cdots, \mathcal{L}_k(\chi_n)]$. We also define a concatenated multi-fidelity snapshot $\mathbf{s} = \theta_1 \begin{pmatrix} \boldsymbol{L}_2^{\boldsymbol{\chi}} \\ \boldsymbol{L}_2^{\boldsymbol{\chi}} \end{pmatrix} + \theta_2 \begin{pmatrix} \boldsymbol{L}_3^{\boldsymbol{\chi}} \\ \boldsymbol{L}_3^{\boldsymbol{\chi}} \end{pmatrix} + \theta_3 \begin{pmatrix} \mathbf{0} \\ \boldsymbol{L}_5^{\boldsymbol{\chi}} \end{pmatrix}$.

We sample the $3D$ design space $\mathcal{D}$, such that all multi-fidelity experiments lie on a plane as illustrated on Fig. 3.2. The subspace spanned by the POD basis $\boldsymbol{\Phi}$ is represented by the plane denoted $\boldsymbol{\Phi}$ on Fig. 3.2. Considering the unknown location $\boldsymbol{\theta} \in \mathcal{D}$, Fig. 3.2 illustrates the different projections of the concatenated snapshot $\mathbf{s}$ realized typically by POD and GPOD. It is important to keep in mind that a POD projection requires to know the entire snapshot at both low- and high-fidelity levels. Therefore, this kind of projection is usually of no interest in the context of engineering optimization, and is only used to quantify the completeness of the subspace spanned by the POD basis with respect to the real output space of the problem at hand. The gappy-projection finds the point in Im $\boldsymbol{\Phi}$ minimizing the error in Eq. 3.16 as illustrated by the green point located on the minimum.

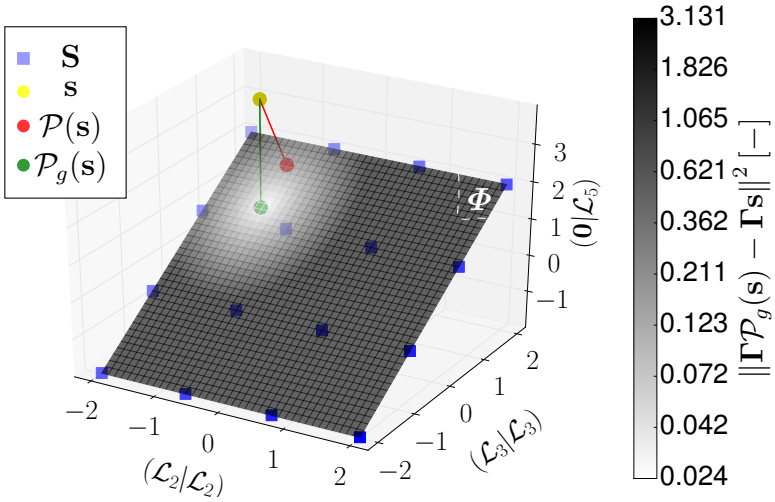

Figure 3.2: Comparison of classical and gappy-projection for an arbitrary snapshot outside the training ensemble of the multi-fidelity POD.

Figure 3.3 shows the low- and high-fidelity functions associated to the snapshot $\mathbf{s}$ illustrated on Fig. 3.2. We can also see the low- and high-fidelity parts of the POD projection and gappy-projection of the test vector $\mathbf{s}$. We can see that gappy-projection presents an error only on its high-fidelity part, whereas the POD projection presents an error for both parts. One can say that the gappy-projection is better adapted to the low-fidelity vector than the POD projection as no con-

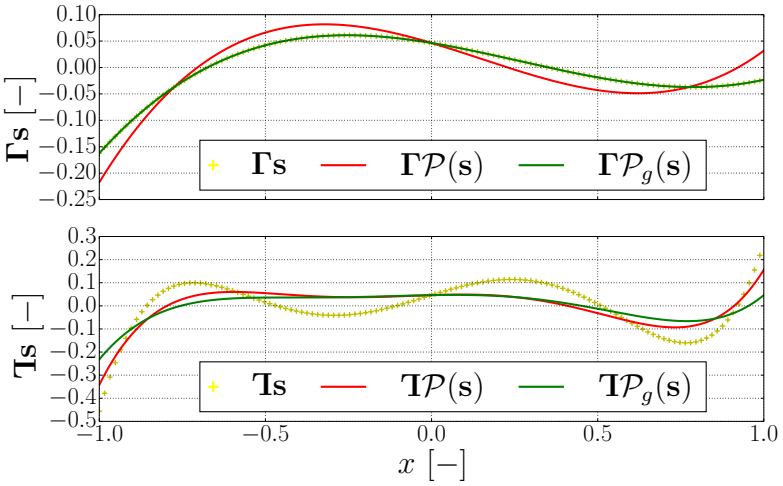

Figure 3.3: Low- and high-fidelity solutions with their classical and gappy-projection.

straint on the high-fidelity representation is applied. We can also see that the error of the POD projection is lower when considering the high-fidelity part of the vector.

Chapter 4

Multi-Fidelity POD based model

This chapter introduces the Hierarchised Multi-Fidelity POD (HMFPOD) based surrogate model developed in this research. It settles the mathematical derivations and numerical implementation of the proposed multi-fidelity extension to Non-Intrusive POD (NIPOD) based surrogate models and gives the mathematical notations employed in subsequent chapters. The training data is hierarchised with respect to the level of precision of each experiment, which constitutes the main contribution of the present work. The developed surrogate model is composed of two main ingredients:

1. multi-fidelity extension for Proper Orthogonal Decomposition (POD) bases computation to improve the output space modeling,

2. multi-fidelity Data Fitting Surrogate Models (DFSMs) to improve the quality of the surrogate mapping between input and ROM spaces.

Concerning the multi-fidelity extension for POD bases, we re-interpret the Constrained POD (CPOD) [M. Xiao, Breitkopf, Filomeno Coelho, Knopf-Lenoir, Villon, et al., 2013; M. Xiao, Breitkopf, Filomeno Coelho, Villon, et al., 2014; D. Xiao, Fang, et al., 2015] concept to estimate from numerous low-fidelity samples the structures or patterns in the output space that high-fidelity samples alone were unable to illustrate. With regard to multi-fidelity DFSM of the mapping between input and ROM spaces, we employ either co-Kriging [Kennedy and O'Hagan, 2000] or additive correction based multi-fidelity Radial Basis Function Networks (RBFNs) [Balabanov et al., 1998].

The remainder of this chapter is organised as follows: Section 4.1 gives the mathematical definitions and derivations required for the Multi-Fidelity POD (MFPOD) basis enrichment. All the notations are conserved in the coming sections and chapters to help the reader identify the link between mathematical

development, algorithmic implementation and application. Section 4.2 presents step-by-step algorithms in order to handle multi-fidelity information and build multi-fidelity enhanced POD bases. Section 4.2.2 specifies the POD coefficients interpolation proposed for MFPOD based surrogate modeling. Finally, concluding remarks are given in Section 4.3.

4.1 Bi-level Proper Orthogonal Decomposition

This section introduces the mathematical principles involved in the enhancement of POD based models with multi-fidelity information. Two levels of fidelity are considered here but the extension to multiple levels of fidelity is suggested at the end of the section.

4.1.1 Concept introduction

We consider a design space $\mathcal{D}$ defined in Section 3.1.1 and two different simulations of a single physical phenomenon associated with different levels of accuracy. We assume the high- and low-fidelity solutions respectively known on M_H and M_L different locations in $\mathcal{D}$, resulting in snapshots $\mathbf{y}_1, \cdots, \mathbf{y}_{M_H}$, and $\mathbf{z}_1, \cdots, \mathbf{z}_{M_L}$. The low-fidelity solution assumed far cheaper than its high-fidelity counterpart to compute, we consider the case $M_H \ll M_L$.

The methodology is composed of the following steps:

1. Find the modal responses of the system at hand, as defined by the high-fidelity experiments (see Section 3.1.1),
2. Extract from the low-fidelity experiments the "motion" explained by previously determined high-fidelity modes,
3. Compute the part of modal responses, defined by the low-fidelity experiments, but missed by the known high-fidelity solutions,
4. Use the concatenated basis of all modal responses computed as hierarchised MFPOD basis.

By opposition to the corrective multi-fidelity framework illustrated on Fig. 2.4, in the proposed framework (Fig. 4.1), the modal functions associated to low-fidelity information ($\boldsymbol{\Xi}$ on Fig. 4.1) are directly dependent on their high-fidelity counterpart ($\boldsymbol{\Phi}^{\perp}$ on Fig. 4.1).

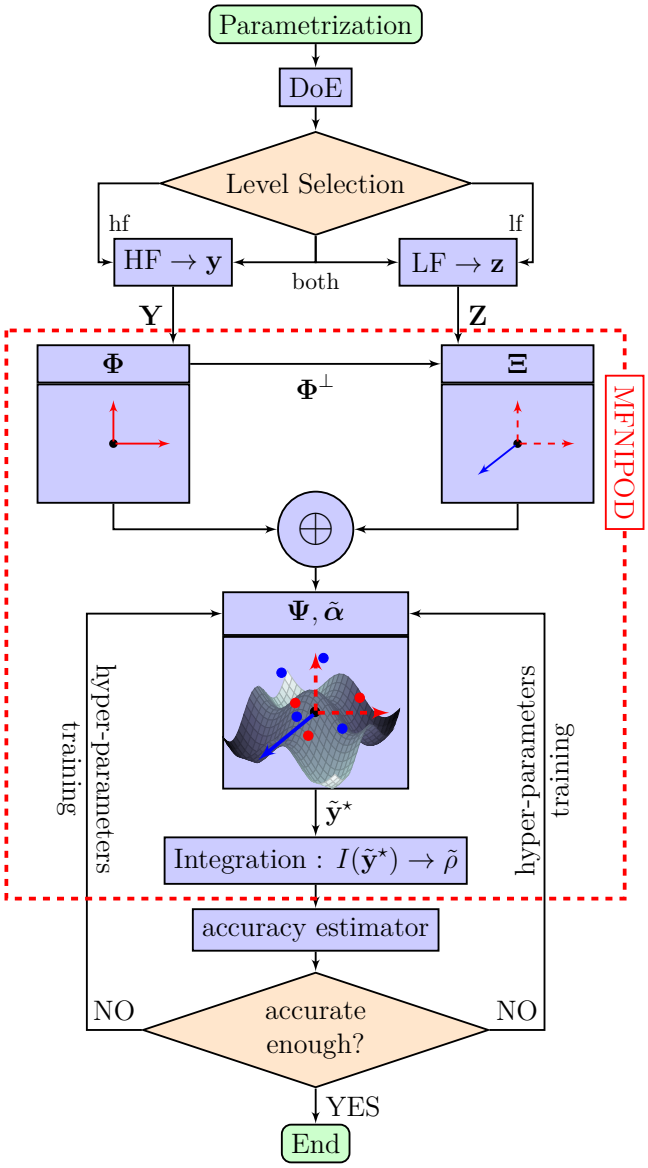

Figure 4.1: Proposed full-field hierarchised Multi-Fidelity NIPOD (MFNIPOD) framework.

All the notations on Fig. 4.1 are consistent with the definitions and derivations detailed in Sections 4.1.2, 4.1.3, and 4.2.

Without loss of generality, we assume hereafter, low- and high-fidelity simulations sharing the same mesh or resulting in equally sized solutions. In the case of different discretizations, a pre-processing step on the data $\mathbf{y}$ and $\mathbf{z}$ has to be

performed for the vectorial solutions to share the same output space, prerequisite for the proposed method to be applicable. Conceptually speaking, the aggregation of new modes, computed from low-fidelity snapshots, to enrich the output subspace obtained from high-fidelity requires all the modes to be equally sized. This compels automatically the user to ensure a low- to high-fidelity mesh consistency. For the sake of readability, we prefer referring to the different levels of code as the vectors $\mathbf{y}$ (high-fidelity) and $\mathbf{z}$ (low-fidelity) than using index notations such as $\{\mathbf{z}_1, \mathbf{z}_2, \cdots\}$ [Le Gratiet and Garnier, 2014], $\{\mathbf{z}(x, t_1), \mathbf{z}(x, t_2), \cdots\}$ [Kennedy and O'Hagan, 2000], or $\{\mathbf{y}_e, \mathbf{y}_c\}$ [Forrester, Sóbester, et al., 2008].

We want to define a subspace for all the computed solutions of the problem at hand. After computing the optimal subspace for the representation of sparse high-fidelity full-field solutions, we extend it considering the "cheap" information extracted from abondant low-fidelity snapshots. To cope with the multi-fidelity centering issue, we propose an automated strategy to determine the centering snapshot from the difference between low- and high-fidelity sets of snapshots. The completion of the multi-fidelity basis is obtained as explained in Sections 4.1.2 and 4.1.3.

4.1.2 High-fidelity decomposition and centering snapshot selection

We first seek an orthonormal basis $\mathbf{\Phi}$ for the M_H-dimensional subspace in $\mathbb{R}^n$ spanned by the high-fidelity snapshots $\mathbf{y}_i$ by minimizing

$$\mathrm{J}(\bar{\mathbf{y}}, \mathbf{\Phi}) = \frac{1}{2} \sum_{i=1}^{M_H} \|\mathbf{y}_i - \bar{\mathbf{y}} - \mathbf{\Phi}\mathbf{\Phi}^\top(\mathbf{y}_i - \bar{\mathbf{y}})\|^2. \tag{4.1}$$

In our case zero projection error is desirable on the high-fidelity snapshots, as legitimated by the hypothesis $M_H \ll M_L$ related to low- to high-fidelity simulation cost ratio. $\bar{\mathbf{y}}$ may be chosen as any vector satisfying

$$\mathbf{y}_i - \bar{\mathbf{y}} \in \mathrm{Im}\ \mathbf{\Phi}, \tag{4.2}$$

without any effect on the projection error (Eq. 4.1). Therefore, as no truncation will be performed on the basis $\mathbf{\Phi}$, we use the QR decomposition of the deviation high-fidelity matrix $\mathbf{Y}'$:

$$[\mathbf{Y}'] = [\mathbf{Q}_1 \mid \mathbf{Q}_2]\,[\mathbf{R}]\,, \tag{4.3}$$

where,

$$\mathbf{R} = \begin{pmatrix} & \mathbf{r} & \\ & M_H & \\ 0 & & n - M_H \end{pmatrix}.$$

We choose $\mathbf{\Phi} = \mathbf{Q}_1$ and look in $\text{span}(\mathbf{Q}_2)$ for the modes corresponding to the low-fidelity snapshots. The basis completion is sought in the subspace orthogonal to the centered snapshots in $\mathbf{Y}'$, also linked with the lower $(n - M_H \times M_H)$-null block of $\mathbf{R}$.

4.1.3 Low-fidelity enhancement

We assume a set of low-fidelity snapshots $\mathbf{z}_i,\ \forall i \in [\![1, M_L]\!]$ is available and stored in the matrix $\mathbf{Z}$. Stating the search of the optimal projection basis (denoted $\mathbf{\Psi}$ hereafter) and of the multi-fidelity centering snapshot $\bar{\mathbf{z}}$ for both low- and high-fidelity snapshots as a minimization problem, the global cost function can be written as

$$J(\bar{\mathbf{z}}, \mathbf{\Psi}) = \underbrace{\frac{1}{2}\sum_{i=1}^{M_H} \left\| \left(\mathbf{I} - \mathbf{\Psi}\mathbf{\Psi}^\top\right)(\mathbf{y}_i - \bar{\mathbf{z}}) \right\|_{\mathbb{R}^n}^2}_{\mathbf{T}_H} + \underbrace{\frac{1}{2}\sum_{i=1}^{M_L} \left\| \left(\mathbf{I} - \mathbf{\Psi}\mathbf{\Psi}^\top\right)(\mathbf{z}_i - \bar{\mathbf{z}}) \right\|_{\mathbb{R}^n}^2}_{\mathbf{T}_L}, \tag{4.4}$$

where we define the orthonormal basis

$$\mathbf{\Psi} = [\mathbf{\Phi} \mid \mathbf{\Xi}], \tag{4.5}$$

and

$$\bar{\mathbf{z}} = \bar{\mathbf{y}} + \mathbf{d} \tag{4.6}$$

with $\mathbf{d} \in \mathbb{R}^n$.
Knowing $\mathbf{\Phi}$, and $\bar{\mathbf{y}}$ (see Section 4.1.2), the minimized functional becomes

$$J(\bar{\mathbf{z}}, \mathbf{\Psi}) = \mathcal{J}(\mathbf{d}, \mathbf{\Xi}), \tag{4.7}$$

s.t

$$\mathbf{\Phi}^\top \mathbf{\Xi} = \mathbf{0}_{(M_H \times M_L)}, \tag{4.8}$$

$$\mathbf{\Xi}^\top \mathbf{\Xi} = \mathbf{I}_{M_L}. \tag{4.9}$$

Without any loss of generality, we impose $\mathbf{d} \in (\text{Im } \mathbf{\Phi})^{\perp}$, equivalent to

$$\mathbf{\Phi}^{\top}\mathbf{d} = \mathbf{0}_{(M_H \times 1)}. \tag{4.10}$$

For the sake of readability, we first develop the terms $\mathbf{T}_H$ and $\mathbf{T}_L$ in order to simplify the functionals $J(\bar{\mathbf{z}}, \mathbf{\Psi})$ and $\mathcal{J}(\mathbf{d}, \mathbf{\Xi})$.

Decomposition of $\mathbf{T}_H = \frac{1}{2}\sum_{i=1}^{M_H} \left\| \left(\mathbf{I} - \mathbf{\Psi}\mathbf{\Psi}^{\top}\right)(\mathbf{y}_i - \bar{\mathbf{z}}) \right\|^2_{\mathbb{R}^n}$

We use the definition in Eq. 4.6 to develop

$$\begin{aligned} \mathbf{T}_H &= \frac{1}{2}\sum_{i=1}^{M_H} \left\| \left(\mathbf{I} - \mathbf{\Psi}\mathbf{\Psi}^{\top}\right)(\mathbf{y}_i - \bar{\mathbf{y}} - \mathbf{d}) \right\|^2_{\mathbb{R}^n} \\ &= \frac{1}{2}\sum_{i=1}^{M_H} \left\| \left(\mathbf{I} - \mathbf{\Psi}\mathbf{\Psi}^{\top}\right)(\mathbf{y}_i - \bar{\mathbf{y}}) - \left(\mathbf{I} - \mathbf{\Psi}\mathbf{\Psi}^{\top}\right)\mathbf{d} \right\|^2_{\mathbb{R}^n}. \end{aligned} \tag{4.11}$$

Equation 4.2 gives $\mathbf{y}_i - \bar{\mathbf{y}} \in \text{Im}\mathbf{\Phi}$, with $\text{Im}\mathbf{\Phi} \subset \text{Im}\mathbf{\Psi}$ by construction (see Eq. 4.5), yielding

$$\left(\mathbf{I} - \mathbf{\Psi}\mathbf{\Psi}^{\top}\right)(\mathbf{y}_i - \bar{\mathbf{y}}) = \mathbf{0}. \tag{4.12}$$

By construction (Eq. 4.5),

$$\mathbf{\Psi}\mathbf{\Psi}^{\top} = \mathbf{\Phi}\mathbf{\Phi}^{\top} + \mathbf{\Xi}\mathbf{\Xi}^{\top}. \tag{4.13}$$

Considering the result in Eq. 4.12 on one hand, and the properties given in Equations 4.10 and 4.13 on the other yields the decomposition

$$\begin{aligned} \left(\mathbf{I} - \mathbf{\Psi}\mathbf{\Psi}^{\top}\right)(\mathbf{y}_i - \bar{\mathbf{z}}) &= \left(\mathbf{I} - \mathbf{\Psi}\mathbf{\Psi}^{\top}\right)(\mathbf{y}_i - \bar{\mathbf{y}}) - \left(\mathbf{I} - \mathbf{\Psi}\mathbf{\Psi}^{\top}\right)\mathbf{d} \\ &= -\left(\mathbf{I} - \mathbf{\Psi}\mathbf{\Psi}^{\top}\right)\mathbf{d} \\ &= -\left(\mathbf{I} - \mathbf{\Xi}\mathbf{\Xi}^{\top}\right)\mathbf{d} - \mathbf{\Phi}\mathbf{\Phi}^{\top}\mathbf{d} \\ &= -\left(\mathbf{I} - \mathbf{\Xi}\mathbf{\Xi}^{\top}\right)\mathbf{d}. \end{aligned} \tag{4.14}$$

Introducing this result into Eq. 4.4 reduces its first term to

$$\mathbf{T}_H = \frac{M_H}{2}\mathbf{d}^{\top}\left(\mathbf{I} - \mathbf{\Xi}\mathbf{\Xi}^{\top}\right)\mathbf{d}. \tag{4.15}$$

Decomposition of $\mathbf{T}_L = \frac{1}{2}\sum_{i=1}^{M_L} \left\| \left(\mathbf{I} - \boldsymbol{\Psi}\boldsymbol{\Psi}^\top\right)(\mathbf{z}_i - \bar{\mathbf{z}}) \right\|_{\mathbb{R}^n}^2$

We demonstrate hereafter $\left(\mathbf{I} - \boldsymbol{\Psi}\boldsymbol{\Psi}^\top\right)\left(\mathbf{I} - \boldsymbol{\Phi}\boldsymbol{\Phi}^\top\right) = \left(\mathbf{I} - \boldsymbol{\Psi}\boldsymbol{\Psi}^\top\right)$ to develop $\mathbf{T}_L$.

Considering Eq. 4.13, we develop

$$\left(\mathbf{I} - \boldsymbol{\Psi}\boldsymbol{\Psi}^\top\right)\left(\mathbf{I} - \boldsymbol{\Phi}\boldsymbol{\Phi}^\top\right) = \left(\mathbf{I} - \boldsymbol{\Phi}\boldsymbol{\Phi}^\top\right)\left(\mathbf{I} - \boldsymbol{\Phi}\boldsymbol{\Phi}^\top\right) - \boldsymbol{\Xi}\boldsymbol{\Xi}^\top\left(\mathbf{I} - \boldsymbol{\Phi}\boldsymbol{\Phi}^\top\right), \tag{4.16}$$

and use the orthonormality of $\boldsymbol{\Phi} \Rightarrow \boldsymbol{\Phi}^\top\boldsymbol{\Phi} = \mathbf{I}_{M_H}$ to write

$$\left(\mathbf{I} - \boldsymbol{\Psi}\boldsymbol{\Psi}^\top\right)\left(\mathbf{I} - \boldsymbol{\Phi}\boldsymbol{\Phi}^\top\right) = \mathbf{I} - \boldsymbol{\Phi}\boldsymbol{\Phi}^\top - \boldsymbol{\Xi}\boldsymbol{\Xi}^\top\left(\mathbf{I} - \boldsymbol{\Phi}\boldsymbol{\Phi}^\top\right). \tag{4.17}$$

Finally, taking Eq. 4.8 into account results in

$$\left(\mathbf{I} - \boldsymbol{\Psi}\boldsymbol{\Psi}^\top\right)\left(\mathbf{I} - \boldsymbol{\Phi}\boldsymbol{\Phi}^\top\right) = \left(\mathbf{I} - \boldsymbol{\Psi}\boldsymbol{\Psi}^\top\right). \tag{4.18}$$

We use Equations 4.2, 4.10, and 4.18 to simplify the inner term in $\mathbf{T}_L$:

$$\left(\mathbf{I} - \boldsymbol{\Psi}\boldsymbol{\Psi}^\top\right)(\mathbf{z}_i - \bar{\mathbf{z}}) = \left(\mathbf{I} - \boldsymbol{\Psi}\boldsymbol{\Psi}^\top\right)\left(\mathbf{I} - \boldsymbol{\Phi}\boldsymbol{\Phi}^\top\right)(\mathbf{z}_i - \mathbf{d}).$$

We also define

$$\mathbf{z}_i^\perp := \left(\mathbf{I} - \boldsymbol{\Phi}\boldsymbol{\Phi}^\top\right)\mathbf{z}_i, \tag{4.19}$$

and use Eq. 4.10 to further simplify the previous equation to

$$\left(\mathbf{I} - \boldsymbol{\Psi}\boldsymbol{\Psi}^\top\right)(\mathbf{z}_i - \bar{\mathbf{z}}) = \left(\mathbf{I} - \boldsymbol{\Psi}\boldsymbol{\Psi}^\top\right)\left(\mathbf{z}_i^\perp - \mathbf{d}\right). \tag{4.20}$$

Finally, taking into account that $\mathbf{z}_i^\perp \in (\text{Im }\boldsymbol{\Phi})^\perp \ \forall i \in [\![1, M_L]\!]$ by definition (see Eq. 4.19), and considering Equations 4.10, and 4.13 yields

$$\mathbf{T}_L = \frac{1}{2}\sum_{i=1}^{M_L} \left\| \left(\mathbf{I} - \boldsymbol{\Xi}\boldsymbol{\Xi}^\top\right)\left(\mathbf{z}_i^\perp - \mathbf{d}\right) \right\|_{\mathbb{R}^n}^2. \tag{4.21}$$

Optimality condition for $\mathcal{J}(\mathbf{d}, \boldsymbol{\Xi})$

To develop the optimality condition of $\mathcal{J}$, we first define the $\boldsymbol{\Phi}$-projected low-fidelity snapshots $\mathbf{z}_i^\perp$ and introduce the simplified $\mathbf{T}_H$ (Eq. 4.15) and $\mathbf{T}_L$ (Eq. 4.21) into Eq. 4.4, to obtain the reduced functional to minimize:

$$\mathcal{J}(\mathbf{d}, \boldsymbol{\Xi}) = \frac{M_H}{2}\mathbf{d}^\top\left(\mathbf{I} - \boldsymbol{\Xi}\boldsymbol{\Xi}^\top\right)\mathbf{d} + \frac{1}{2}\sum_{i=1}^{M_L}\left(\mathbf{z}_i^\perp - \mathbf{d}\right)^\top\left(\mathbf{I} - \boldsymbol{\Xi}\boldsymbol{\Xi}^\top\right)\left(\mathbf{z}_i^\perp - \mathbf{d}\right). \tag{4.22}$$

To satisfy the optimality condition on $\mathcal{J}(\mathbf{d}, \boldsymbol{\Xi})$, we now seek

$$\min_{\mathbf{d},\boldsymbol{\Xi}} \mathcal{J}\left(\mathbf{d}, \boldsymbol{\Xi}\right) = \min_{\boldsymbol{\Xi}} \left\{ \min_{\mathbf{d}} \mathcal{J}\left(\mathbf{d}, \boldsymbol{\Xi}\right) \right\}, \tag{4.23}$$

where $\mathbf{d} \in \mathbb{R}^n$, $\boldsymbol{\Phi}^\top \mathbf{d} = \mathbf{0}_{(M_H \times 1)}$, $\boldsymbol{\Xi}^\top \boldsymbol{\Xi} = \mathbf{I}_{M_L}$, and $\boldsymbol{\Phi}^\top \boldsymbol{\Xi} = \mathbf{0}_{(M_H \times M_L)}$.

The optimality of $\mathcal{J}\left(\mathbf{d}, \boldsymbol{\Xi}\right)$ w.r.t. $\mathbf{d}$ satisfies

$$\left\langle \frac{\partial \mathcal{J}}{\partial \mathbf{d}}, \delta \mathbf{d} \right\rangle = 0 \ \forall \ \delta \mathbf{d} \in Im\ \mathbf{Q}_2, \tag{4.24}$$

with

$$\left\langle \frac{\partial \mathcal{J}}{\partial \mathbf{d}}, \delta \mathbf{d} \right\rangle = -\delta \mathbf{d}^\top \left(\mathbf{I} - \boldsymbol{\Xi}\boldsymbol{\Xi}^\top \right) \left[\mathbf{d} - \frac{M_L \cdot \bar{\mathbf{z}^\perp}}{(M_H + M_L)} \right],$$

where $\bar{\mathbf{z}^\perp} = \dfrac{1}{M_H} \displaystyle\sum_{i=1}^{M_L} \mathbf{z}_i^\perp$.

The optimal $\mathbf{d}$ has to satisfy the condition $\mathbf{d}^\star - \dfrac{M_L \cdot \bar{\mathbf{z}^\perp}}{M_H + M_L} \in Im\ \boldsymbol{\Xi}$, which is possible as both $\mathbf{d}$ and $\mathbf{z}_i^\perp \in (Im\ \boldsymbol{\Phi})^\perp \ \forall\ i \in [\![1, M_L]\!]$.

For the sake of simplicity, we impose the solution to the sub-problem $\min_{\mathbf{d}} \mathcal{J}\left(\mathbf{d}, \boldsymbol{\Xi}\right)$ in Eq. 4.23 as

$$\mathbf{d}^\star = \frac{M_L}{M_H + M_L} \cdot \bar{\mathbf{z}^\perp}. \tag{4.25}$$

We also introduce,

$$\mathbf{z}_0^\perp = \left(\sqrt{M_H} + 1 \right) \mathbf{d}^\star, \tag{4.26}$$

such that the cost function $\mathcal{J}\left(\mathbf{d}^\star, \boldsymbol{\Xi}\right) := \mathscr{J}\left(\boldsymbol{\Xi}\right)$ is simplified as follows:

$$
\begin{aligned}
\mathscr{J}(\boldsymbol{\Xi}) &= \frac{M_H}{2}\mathbf{d}^{\star\top}\left(\mathbf{I}-\boldsymbol{\Xi}\boldsymbol{\Xi}^\top\right)\mathbf{d}^\star \\
&\quad+\frac{1}{2}\sum_{i=1}^{M_L}\left(\mathbf{z}_i^\perp-\mathbf{d}^\star\right)^\top\left(\mathbf{I}-\boldsymbol{\Xi}\boldsymbol{\Xi}^\top\right)\left(\mathbf{z}_i^\perp-\mathbf{d}^\star\right) \\
&= \frac{1}{2}\left(\sqrt{M_H}\mathbf{d}^{\star\top}\left(\mathbf{I}-\boldsymbol{\Xi}\boldsymbol{\Xi}^\top\right)\sqrt{M_H}\mathbf{d}^\star\right) \\
&\quad+\frac{1}{2}\sum_{i=1}^{M_L}\left(\mathbf{z}_i^\perp-\mathbf{d}^\star\right)^\top\left(\mathbf{I}-\boldsymbol{\Xi}\boldsymbol{\Xi}^\top\right)\left(\mathbf{z}_i^\perp-\mathbf{d}^\star\right) \\
&= \frac{1}{2}\left(\mathbf{z}_0^\perp-\mathbf{d}^\star\right)^\top\left(\mathbf{I}-\boldsymbol{\Xi}\boldsymbol{\Xi}^\top\right)\left(\mathbf{z}_0^\perp-\mathbf{d}^\star\right) \\
&\quad+\frac{1}{2}\sum_{i=1}^{M_L}\left(\mathbf{z}_i^\perp-\mathbf{d}^\star\right)^\top\left(\mathbf{I}-\boldsymbol{\Xi}\boldsymbol{\Xi}^\top\right)\left(\mathbf{z}_i^\perp-\mathbf{d}^\star\right) \\
&= \frac{1}{2}\sum_{i=0}^{M_L}\left(\mathbf{z}_i^\perp-\mathbf{d}^\star\right)^\top\left(\mathbf{I}-\boldsymbol{\Xi}\boldsymbol{\Xi}^\top\right)\left(\mathbf{z}_i^\perp-\mathbf{d}^\star\right).
\end{aligned}
\tag{4.27}
$$

To complete the basis $\boldsymbol{\Psi} = [\boldsymbol{\Phi} \mid \boldsymbol{\Xi}]$, we now seek $\boldsymbol{\Xi}$ satisfying the conditioned POD problem

$$
\begin{aligned}
\min_{\boldsymbol{\Xi}} \frac{1}{2}\sum_{i=0}^{M_L}\left(\mathbf{z}_i^\perp-\mathbf{d}^\star\right)^\top\left(\mathbf{I}-\boldsymbol{\Xi}\boldsymbol{\Xi}^\top\right)\left(\mathbf{z}_i^\perp-\mathbf{d}^\star\right), \\
\text{s.t} \\
\boldsymbol{\Xi}^\top\boldsymbol{\Xi} = \mathbf{I}_{m_L} \text{ with } m_L \leq M_L, \\
\boldsymbol{\Phi}^\top\boldsymbol{\Xi} = \mathbf{0}.
\end{aligned}
\tag{4.28}
$$

Problem 4.28 implies $\boldsymbol{\Xi} \in Im\ \mathbf{Q}_2 \Rightarrow \exists \mathbf{t},\ \boldsymbol{\Xi} = \boldsymbol{Q}_2\mathbf{t}$, where $\mathbf{Q}_2$ is the orthonormal basis given by the first QR-decomposition (Equation 4.3) spanning $(Im\ \boldsymbol{\Phi})^\perp$, and $\mathbf{t}$ is a $(n - M_H) \times m_L$ real-valued matrix. Keeping in mind the orthonormality of $\mathbf{Q}_2$, $\mathbf{Q}_2^\top\mathbf{Q}_2 = \mathbf{I}_{n-M_H}$ yields $\mathbf{t}^\top\mathbf{t} = \mathbf{t}^\top\mathbf{Q}_2^\top\mathbf{Q}_2\mathbf{t} = \boldsymbol{\Xi}^\top\boldsymbol{\Xi} = \mathbf{I}_{m_L}$.
One can notice that $\mathbf{z}_i^\perp - \mathbf{d}^\star \in Im\ \mathbf{Q}_2\ \forall\ i \in [\![0, M_L]\!]$, and introduce $\mathbf{u}_i \in \mathbb{R}^{(n-M_H)}$, such that $\mathbf{z}_i^\perp - \mathbf{d}^\star = \mathbf{Q}_2\mathbf{u}_i$.

By replacing $\boldsymbol{\Xi}$ and $\mathbf{z}_i^\perp - \mathbf{d}^\star$, respectively with $\mathbf{Q}_2\mathbf{t}$ and $\mathbf{Q}_2\mathbf{u}_i$ in Eq. 4.28, we obtain:

$$
\begin{aligned}
\left(\mathbf{z}_i^\perp-\mathbf{d}^\star\right)^\top\left(\mathbf{I}-\boldsymbol{\Xi}\boldsymbol{\Xi}^\top\right)\left(\mathbf{z}_i^\perp-\mathbf{d}^\star\right) &= \mathbf{u}_i^\top\mathbf{Q}_2^\top\left(\mathbf{I}-\mathbf{Q}_2\mathbf{t}\mathbf{t}^\top\mathbf{Q}_2^\top\right)\mathbf{Q}_2\mathbf{u}_i \\
&= \mathbf{u}_i^\top\mathbf{u}_i - \mathbf{u}_i^\top\mathbf{t}\mathbf{t}^\top\mathbf{u}_i \\
&= \mathbf{u}_i^\top\left(\mathbf{I}-\mathbf{t}\mathbf{t}^\top\right)\mathbf{u}_i.
\end{aligned}
\tag{4.29}
$$

The completion problem is therefore reduced to

$$\begin{aligned} &\min_{\mathbf{t}} \frac{1}{2} \sum_{i=0}^{M_L} \mathbf{u}_i^\top \left(\mathbf{I} - \mathbf{t}\mathbf{t}^\top \right) \mathbf{u}_i, \\ &\qquad\qquad \text{s.t} \\ &\mathbf{t}^\top \mathbf{t} = \mathbf{I}_{m_L} \text{ with } m_L \leq M_L, \end{aligned} \tag{4.30}$$

which is equivalent to a classical POD problem on $\mathbf{t}$, and can be solved by Singular Value Decomposition (SVD), m_L being the number of retained modes. We finally denote $\mathbf{t}^\star$ the solution of the aforementioned problem (Eq. 4.30).

To conclude this procedure, the resulting ROM is given by the couple $\bar{\mathbf{z}} = \bar{\mathbf{y}} + \mathbf{d}^\star$ (Equations 4.6 and 4.25), and $\mathbf{\Psi} = [\mathbf{\Phi} \mid \mathbf{Q}_2 \mathbf{t}^\star]$ from Equations 4.3 and 4.30, and is computed as follows:

$$\tilde{\mathbf{y}}(\boldsymbol{\theta}) = \left[\mathbf{\Psi}\mathbf{\Psi}^\top \left(\mathbf{y}(\boldsymbol{\theta}) - \bar{\mathbf{z}} \right) \right] + \bar{\mathbf{z}}. \tag{4.31}$$

4.2 Algorithmic implementation

In this section, algorithms are given in order to illustrate how the proposed methodology can be implemented practically. As already indicated, the hierarchised multi-fidelity reduced order surrogate model proposed in the present work is composed of two main ingredients that are linked to Algorithms 1 and 2.

4.2.1 Multi-fidelity hierarchised basis construction

We consider here two solvers of different levels of precision returning the vectorial solutions $\mathbf{z}$ and $\mathbf{y}$ for low- and high-fidelity respectively, and both lying in $\mathbb{R}^n$. To better illustrate the steps involved in the multi-fidelity reduction of the output space, we propose the algorithm below yielding the reduced basis $\mathbf{\Psi}$ leveraging sparse high-fidelity data as well as abondant low-fidelity information in the design space.

To sum up the presented developments, the proposed method enriches the sparse high-fidelity interpolating subspace with densely distributed low-fidelity information. The proposed algorithm yields a "hierarchised" MFPOD basis in the sense that the addition of $\mathbf{\Xi}$ basis does not introduce error in the reconstruction of high-fidelity snapshots.

Algorithm 1 MFPOD basis enhancement

Require: Training Design of Experiments (DoE) phase completion
- Training DoE $\boldsymbol{\Theta}^H$ of M_H points
  (Latinized Centroidal Voronoï Tesselation sampling, from Saka et al., 2007)
- Training DoE $\boldsymbol{\Theta}^L$ of M_L points $|M_L > M_H$
- Low-fidelity training set $\mathbf{Z}|\mathbf{Z}_{\cdot i} = \mathbf{z}(\boldsymbol{\Theta}^L_{\cdot i})\ \forall i \in [\![1, M_L]\!]$
- High-fidelity training set $\mathbf{Y}|\mathbf{Y}_{\cdot i} = \mathbf{y}(\boldsymbol{\Theta}^H_{\cdot i})\ \forall i \in [\![1, M_H]\!]$
- High-fidelity centering snapshot $\bar{\mathbf{y}}$

procedure HIGH-FIDELITY DATA DECOMPOSITION($\mathbf{Y}, \bar{\mathbf{y}}$)
  Center the high-fidelity data $\mathbf{Y}'$, $\mathbf{Y}'_{\cdot i} = \mathbf{Y}_{\cdot i} - \bar{\mathbf{y}}$
  Decompose (QR-algorithm) $\mathbf{Y}' = [\mathbf{Q}_1 \mid \mathbf{Q}_2]\,[\mathbf{R}]$
  Define $\boldsymbol{\Phi} := \mathbf{Q}_1$
  return $\boldsymbol{\Phi}, \mathbf{Q}_2$
end procedure

procedure LOW-FIDELITY COMPLETION($\mathbf{Z}, \bar{\mathbf{y}}, \boldsymbol{\Phi}, \mathbf{Q}_2$)
  Require: High-fidelity data decomposition $\rightarrow \boldsymbol{\Phi}, \mathbf{Q}_2$
  Project $\mathbf{Z}$ onto $(\text{Im}\ \boldsymbol{\Phi})^\perp$
    $\mathbf{Z}^\perp := \left(\mathbf{I} - \boldsymbol{\Phi}\boldsymbol{\Phi}^\top\right)\mathbf{Z}$
  Compute $\mathbf{d}^\star$ (Equation 4.25) and $\mathbf{z}_0^\perp$ (Equation 4.26)
  Enrich $\mathbf{Z}^\perp$ with $\mathbf{z}_0^\perp$
  Center the low-fidelity data around $\mathbf{d}^\star$
    $\mathbf{Z}^{\perp\prime}_{\cdot i} := \mathbf{Z}^\perp_{\cdot i} - \mathbf{d}^\star\ \forall\ i \in [\![0, M_L]\!]$
  Compute the $\mathbf{U}$ matrix
    $\mathbf{U} = \mathbf{Q}_2^\top \mathbf{Z}^{\perp\prime}$
  Compute $\boldsymbol{\Xi} = \mathbf{Q}_2\mathbf{t}^\star$ (see Eq. 4.30 and Section 4.1.3)
  Concatenate the ROM $\boldsymbol{\Psi} = [\boldsymbol{\Phi} \mid \boldsymbol{\Xi}]$, and $\bar{\mathbf{z}} = \bar{\mathbf{y}} + \mathbf{d}$
  return $\bar{\mathbf{z}}, \boldsymbol{\Psi}$
end procedure

4.2.2 Multi-fidelity surrogate models of the projection coefficients

Each training vector being associated to a single location in the design space $\mathcal{D} \subset \mathbb{R}^p$, NIPOD models are based on an approximate relation between the design space $\mathcal{D}$ and the POD space. While Section 4.1.1 introduced the methodology to enhance any POD basis with cheap information gathered from a low-fidelity representation of the physical phenomenon under study, this section (notations from Section 3.1 are respected) builds the NIPOD model allowing to predict the

full field high-fidelity solution in the reduced output space Im $\boldsymbol{\Psi}$ at virtually no additional cost.

By projecting the $\bar{\mathbf{z}}$-centered low- and high-fidelity training snapshots $\bar{\mathbf{Z}}$ and $\bar{\mathbf{Y}}$ onto the basis $\boldsymbol{\Psi}$, two databases of coefficients are built.

One surrogate model is trained for each dimension of the Reduced Order Model (ROM) itself. For MFNIPOD, the projection of low- and high-fidelity centered snapshots gives two databases of m-dimensional outputs, $\boldsymbol{\beta}_i = \boldsymbol{\Psi}^\top \bar{\mathbf{Z}}_{\cdot i}\ \forall i \in [\![1, M_L]\!]$ and $\boldsymbol{\alpha}_i = \boldsymbol{\Psi}^\top \bar{\mathbf{Y}}_{\cdot i}\ \forall i \in [\![1, M_H]\!]$. The framework presented on Fig. 2.4 is then used for the first m dimensions ($M_H \leq m \leq M_H + M_L$) of $\boldsymbol{\alpha}$ and $\boldsymbol{\beta}$, along with the experiment locations in the design space $\boldsymbol{\Theta}^H$ and $\boldsymbol{\Theta}^L$, to build m scalar multi-fidelity surrogate models, with α_j and β_j replacing respectively ζ_H and ζ_L on Fig. 2.4 $\forall j \in [\![1, m]\!]$. The construction of the resulting surrogate model is illustrated on Fig. 4.2 and summarized in Algorithm 2.

Algorithm 2 Multi-fidelity NIPOD construction

Require: Multi-fidelity POD basis enhancement $\rightarrow \bar{\mathbf{z}}, \boldsymbol{\Psi}$ (Algorithm 1)

1: **procedure** MULTI-FIDELITY NIPOD MODEL($\mathbf{Y}, \mathbf{Z}, \bar{\mathbf{z}}, \boldsymbol{\Psi}$)
2: Center the data
$\mathbf{Y}',\ \mathbf{Y}'_{\cdot i} = \mathbf{Y}_{\cdot i} - \bar{\mathbf{z}}$
$\mathbf{Z}',\ \mathbf{Z}'_{\cdot i} = \mathbf{Z}_{\cdot i} - \bar{\mathbf{z}}$
3: Compute the high-fidelity m-dimensional POD coefficients
$\boldsymbol{\alpha}_i = \boldsymbol{\Psi}^\top \mathbf{Y}'_{\cdot i}\ \forall i \in [\![1, M_H]\!]$
4: Compute the low-fidelity m-dimensional POD coefficients
$\boldsymbol{\beta}_i = \boldsymbol{\Psi}^\top \mathbf{Z}'_{\cdot i}\ \forall i \in [\![1, M_L]\!]$
5: Build m multi-fidelity surrogate models* from $\boldsymbol{\alpha}_{1,\cdots,M_H}$ and $\boldsymbol{\beta}_{1,\cdots,M_L}$
$\tilde{\boldsymbol{\alpha}}\ :\ \mathcal{D} \rightarrow \mathbb{R}^m$
$\boldsymbol{\theta} \rightarrow [\tilde{\alpha}_1(\boldsymbol{\theta}), \cdots, \tilde{\alpha}_m(\boldsymbol{\theta})]^\top$
6: **end procedure**

The surrogate models* mentioned in Algorithm 2 can be:

1. nested multi-level models $\leftarrow$ **Ensure:** $\boldsymbol{\Theta}^H \subset \boldsymbol{\Theta}^L$
   - co-Kriging
   - multi-fidelity nested RBFN
2. classical corrective models.

We call nested multi-level models, Multi-Fidelity Models (MFMs) within the fusion paradigm and based on a nested MFDoE. Theoretically, no restriction to interpolating surrogate models has to be made, but approximating the POD coefficients could have a non-negligible impact on the physical response prediction of known locations, especially for truncated ROMs.

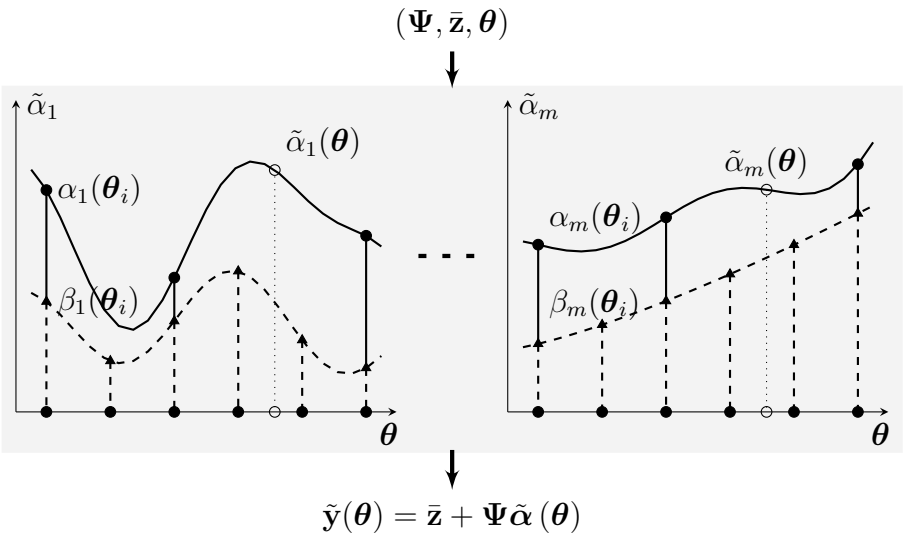

Figure 4.2: Illustration of the approximation procedure of the Multi-Fidelity Surrogate Model (MFSM).

The couple $(\tilde{\boldsymbol{\alpha}}(\boldsymbol{\theta}), \boldsymbol{\Psi})$ then gives access to an immediate prediction of the vectorial output of any new location $\boldsymbol{\theta} \in \mathcal{D}$, as detailed in Algorithm 3.

Algorithm 3 MFNIPOD prediction

Require: Choice of the ROM dimensionality m

1: **procedure** MFNIPOD PREDICTION
2: Predict the POD coefficients $\tilde{\alpha}_j(\boldsymbol{\theta})\ \forall j \in [\![1, m]\!] \mid \boldsymbol{\theta} \in \mathcal{D}$
3: Build the POD coordinate m-dimensional vector $\tilde{\boldsymbol{\alpha}}$
4: Evaluate the solution field $\tilde{\mathbf{y}}(\boldsymbol{\theta}) = \bar{\mathbf{z}} + \boldsymbol{\Psi}\tilde{\boldsymbol{\alpha}}$
5: **end procedure**

As mentioned earlier, the extension to multiple levels of fidelity ($m_f \geq 2$) is possible. In this case, the procedure called "low-fidelity completion" (Section 4.1.3) is repeated to add information from lower fidelity snapshot matrices.

This repetition gives a further enhanced basis, we denote $\mathbf{\Psi}$ for simplicity. Projecting all the centered snapshots onto $\mathbf{\Psi}$ yields m_f databases of coefficients used to train m_f-level surrogate models such as corrective RBFNs or m_f-levels co-Kriging.

4.3 Concluding remarks

In this chapter, we have developed a surrogate model fusing full-field information simulated at different levels of precision, and enabling the capture of more modal features composing the output space spanned throughout the design space exploration. The proposed technique interpolates sparse high-fidelity full-field solutions and takes low-fidelity snapshots to enrich the model in the unexplored areas of the design space or with features not experienced on high-fidelity.

In the *variable-fidelity* ROM introduced by Mifsud, MacManus, et al., 2016, all the information is concatenated in the deviation matrix $\mathbf{Y}'$ regardless of the level of precision which is only considered at the projection coefficient surrogate modeling step. The main difference in the methodology proposed in this chapter lies in the hierarchy conservancy between all the levels of fidelity involved in the training data sets.

Although the construction of a suitable surrogate model constitutes a fundamental stone of a Surrogate-Based Optimization (SBO) strategy, the integration of any surrogate model within the optimization loop and its effective operation together with an Evolutionary Algorithm (EA) reveals itself hard task. In the next chapter, we introduce an infill strategy dedicated to Gappy-POD (GPOD) based models as proposed by Toal, 2014. The developed HMFPOD is integrated into an Multi-Fidelity SBO (MFSBO) framework and tested on an analytical example, as well as on an industrial-scale problem in Part II.

Chapter 5

Enrichment criteria for GPOD surrogates

This chapter addresses the question of the infill strategy inherently related to any online Surrogate-Based Optimization (SBO) framework and its development towards efficient coupling with the surrogate and optimizer components. The computational effort required to reach an acceptable accuracy for the surrogate models involved in any SBO loop is unaffordable in many challenging industrial optimization problems. In addition, the reduction of design cycles duration and CPU budget limitations drive engineers to reduce the size of *a priori* Design of Experiments (DoE) and concentrate the computational effort in potentially interesting areas of the design space. In this situation, not only the performance of the optimizer or the predictability of the surrogate models are crucial but also their coupling via dedicated infill strategies. Therefore, we propose here an infill strategy and its associated enrichment criterion to further improve the Gappy-POD (GPOD) based Multi-Fidelity Surrogate Models (MFSMs) proposed by Toal, 2014.

As introduced in the literature review on Reduced Order Models (ROMs) in Section 2.4, the multi-fidelity methodology presented by Toal, 2014 intends to parametrize a high-fidelity solution by its low-fidelity counterpart. This method firstly builds a "multi-fidelity" subspace defined by all the experiments fusing low- and high-fidelity full-field solutions. For the GPOD based MFSM strategy, the low- and high-fidelity solutions are concatenated to form an extended solution snapshot. The subspace is then created according to a set of extended snapshots. Assuming the computational cost associated with the low-fidelity simulation is moderate enough to consider exploring the whole design space, a GPOD based MFSM estimates the lacking high-fidelity solution. By projecting the low-fidelity solution onto the subspace basis, the entire snapshot

is estimated. It then contains an approximate reconstruction of the low-fidelity solution and the prediction of its high-fidelity counterpart. We claim the gappy-reconstruction error of the low-fidelity full-field representation can indicate where the surrogate model lacks accuracy in the design space and drive the selection of new interesting points in an online SBO framework. This proposed error estimator is verified on a $2D$ aerodynamic test case taken from the literature.

In the case of engineering optimization, the less the high-fidelity solver is called the better. Therefore, the procedure presented in Toal, 2014 uses the gappy-projection to predict the high-fidelity full-field solution. However even if the gappy-projection is better adapted to the representation of the low-fidelity solution, the reconstruction error can be non-negligible. The gappy-reconstruction error on the low-fidelity solution is, in the case presented in Section 3.3.2 (see Fig 3.3), null for simplicity and readability purposes. We claim in the remainder that the quantifiable error (if the low-fidelity solution is computed) between the low-fidelity full-field solution and its gappy-reconstruction on $\boldsymbol{\Psi}$ is somehow related to the overall accuracy of the Proper Orthogonal Decomposition (POD) basis and can serve to detect low-accuracy areas, as soon as a good correlation between low- and high-fidelity is verified.

5.1 Gappy-POD enrichment criterion

As long as the low- and high-fidelity models are well correlated and the amount of available data is sufficient, it seems natural that GPOD and POD projections should be well correlated too. On the other hand, a large GPOD projection error foretells a lack of precision of the POD approximation in the considered area. The proposed error estimator δ (Eq. 5.1) is then based on the following hypothesis : if $\rho_{(\mathbf{z},\mathbf{y})}$ high $\forall \boldsymbol{\theta} \in \mathcal{D}$, then $\rho_{(\delta,\|\mathcal{P}(\mathbf{s})-\mathbf{s}\|^2)}$ high too, where $\rho_{(a,b)}$ stands for the correlation between two general variables so that $\rho_{(\mathbf{z},\mathbf{y})}$ pertains to the low- and high-fidelity solutions correlation. Setting an arbitrary case dependent threshold ϵ_{app} on δ allows for detecting areas of potential enrichment and results in an adaptive infill criterion associated with Algorithm 4, and used in Section 5.2.4.

It is important to keep in mind that the high-fidelity computations and so the projection $\mathcal{P}(\mathbf{s})$ are usually available on limited locations of the design space $\mathcal{D}$. On the contrary, the low-fidelity model has a computational cost enabling a more exhaustive simulation campaign over the design space. Therefore, we consider here a current snapshot $\mathbf{s}(\boldsymbol{\theta})$ only simulated with the low-fidelity model, and propose as criterion the maximization of the error estimator δ hereafter for the DoE enrichment procedure dedicated to multi-fidelity GPOD based surrogates:

$$\delta = \frac{\|\mathbf{\Gamma}\mathcal{P}_g(\mathbf{s}) - \mathbf{\Gamma}\mathbf{s}\|^2}{\|\mathbf{\Gamma}\mathbf{s}\|^2} \ . \tag{5.1}$$

The numerator $\|\mathbf{\Gamma}\mathcal{P}_g(\mathbf{s}) - \mathbf{\Gamma}\mathbf{s}\|^2$ can be seen as the norm of the low-fidelity difference between the GPOD projection $\mathcal{P}_g(\mathbf{s})$ and the GPOD prediction $\mathcal{P}_t(\mathbf{s})$ given the equality $\mathbf{\Gamma}\mathcal{P}_t(\mathbf{s}) = \mathbf{\Gamma}\mathbf{s}$.

5.1.1 Algorithm

Maximizing the error estimator δ (Eq. 5.1) indicates the areas where the low-fidelity GPOD reconstruction reveals high relative error with respect to the computed low-fidelity data itself. Algorithm 4 is proposed as a simple implementation of this error estimate associated with a stopping criterion within an adaptive sampling strategy involving MFSMs and potentially improving the exploitation/exploration balance of an online SBO. In the coming sections, the error estimator δ (Eq. 5.1) is referred to as enrichment criterion and linked to the stopping condition ϵ_{app}. In the context of multi-fidelity optimization, the low-fidelity solution is usually considered far cheaper than the high-fidelity simulation affording the designer to compute $\mathbf{z}$ on a large number of points in the design space $\mathcal{D}$.

Algorithm 4 DoE enrichment algorithm

Require: Training DoE phase completion + verification set availability
- Training DoE $\mathbf{\Theta}$ of M points (LCVT, Saka et al., 2007)
- Low-fidelity solution for the training set $\mathbf{z}(\boldsymbol{\theta})\ \forall \boldsymbol{\theta} \in \mathbf{\Theta}$
- High-fidelity solution for the training set $\mathbf{y}(\boldsymbol{\theta})\ \forall \boldsymbol{\theta} \in \mathbf{\Theta}$
- Multi-fidelity database $\mathbf{S} = \left[\begin{pmatrix}\mathbf{z}_1\\ \mathbf{y}_1\end{pmatrix}, \cdots, \begin{pmatrix}\mathbf{z}_M\\ \mathbf{y}_M\end{pmatrix}\right]$
- Basis $\boldsymbol{\Psi}$ associated with $\mathbf{S}$
- Verification set $\mathbf{\Theta}_v$ of V points, where $M \ll V \ll n$
- Low-fidelity solution on $\mathbf{\Theta}_v$
- Filtered multi-fidelity database $\mathbf{\Gamma S}_v$

Ensure: $\delta_{max} > \epsilon_{app}$, with $\bar{\delta}$ the metamodel of δ over the design space $\mathcal{D}$

1: **procedure** ADAPTIVE-DOE
2: **while** $\delta_{max} = \max_{\boldsymbol{\theta}\in\mathcal{D}} \bar{\delta}(\boldsymbol{\theta}) > \epsilon_{app}$ **do**
3: Compute $\delta(\boldsymbol{\theta})\ \forall \boldsymbol{\theta} \in \mathbf{\Theta}_v$ (Eq. 5.1)
4: Build a metamodel $\bar{\delta}$ over the design space $\mathcal{D}$
5: Search $\boldsymbol{\theta}_{next} = \operatorname{argmax}_{\boldsymbol{\theta}\in\mathcal{D}} \bar{\delta}(\boldsymbol{\theta})$
6: **if** $\boldsymbol{\theta}_{next} \notin \mathbf{\Theta}_v$ **then**
7: Compute $\mathbf{s}^L(\boldsymbol{\theta}_{next})$
8: **end if**

Compute $\mathbf{y}(\boldsymbol{\theta}_{next})$
Concatenate $\mathbf{s}(\boldsymbol{\theta}_{next}) = \begin{pmatrix} \mathbf{z}(\boldsymbol{\theta}_{next}) \\ \mathbf{y}(\boldsymbol{\theta}_{next}) \end{pmatrix}$
Update the POD basis $\boldsymbol{\Psi}$ with $\mathbf{s}(\boldsymbol{\theta}_{next})$ [Brand, 2006]
end while
end procedure

In the next section, we apply the proposed procedure on a $2D$ application test case pertaining to the flight domain study of a $2D$ airfoil. The selected test case allows for a fast low-fidelity computation in order to predict the missing high-fidelity solution and an easy illustration of all new locations suggested for enrichment by the proposed algorithm.

5.2 RAE2822 Application case

A usual application illustrating multi-fidelity approches deals with 2D airfoil optimization [Lopez Peña et al., 2012; L. Leifsson and Koziel, 2010; Luliano and Quagliarella, 2013; Filomeno Coelho et al., 2008]. We propose to use the panel theory as the low-fidelity model and a more expensive Reynolds Averaged Navier-Stokes (RANS) computation as the high-fidelity model. The multi-fidelity hierarchy considered in this application is linked to levels of physics. The addressed application is the air flow around the RAE2822 airfoil [Cook et al., 1979] illustrated on Fig. 5.1 under free stream conditions given in Table 5.1. The low-fidelity simulations are performed under potential flow hypothesis using the well documented panel code *Xfoil* [Drela, 1989] enabling viscous and compressibility corrections. The high-fidelity computations are performed using the 2D RANS solver *elsA* [Cambier et al., 2013].

The variations in free-stream Mach number (M_∞) are expected to induce appearance of shock waves for some points in the design space. These changes in the flow regime constitute the major difficulty to create a global surrogate model on the entire design space.

The low-fidelity experiments are performed on a mesh of 352 panels along the airfoil. Each simulation takes approximately one second to run on a workstation Intel Xeon 4x1.6GHz with 48 Go of RAM and gives access to the pressure distribution along the shape as well as the Lift Coefficient (C_L) and the Drag Coefficient (C_D). The high-fidelity computation is run on a 40 chord length (c) scaled C-H types structured mesh containing 47104 cells over 10000 iterations with

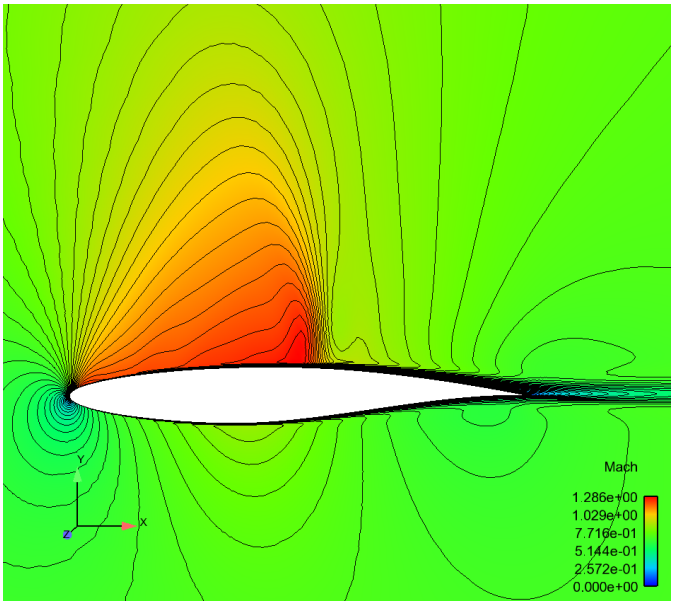

Figure 5.1: Mach number distribution around the airfoil RAE2822, study case 9 [Cook et al., 1979] : $\alpha_\infty = 2.79°$ and $M_\infty = 0.73$.

a Spalart-Allmaras turbulence model [Spalart and Allmaras, 1992] and a 3-level multigrid acceleration. We extract the static pressure distribution and the friction vector on the shape, the lift and drag coefficients as well as the temperature, pressure and velocity over the all domain. Each simulation takes approximately 15 minutes on 8 cores of Ivy Bridge Intel Xeon E5-2697(v2) processors with 1.8 Go of RAM allocated.

	variable	value	unit
heat capacity ratio	γ	1.4	$-$
gaz constant	r	287.053	$Jkg^{-1}K^{-1}$
temperature	T_∞	303.15	K
chord length	c	1.0	m
Reynolds number	$\mathcal{R}_e$	$6.5 \cdot 10^6$	$-$
Mach number	M_∞	$0.55 < M_\infty < 0.75$	$-$
angle of attack	α_∞	$-1. < \alpha_\infty < 3.5$	$°$

Table 5.1: Aerodynamic and free stream conditions.

We can expect the low-fidelity to fit the high-fidelity data concerning the pressure distribution but also to reveal a reduced precision of the drag coefficient for increased M_∞ and α_∞ because of missing friction information. This is due

to the enlarged part of pressure and friction induced drag in the area where the low-fidelity model lacks precision (shock waves development).

5.2.1 Multi-fidelity snapshots

To ensure a good agreement between low- and high-fidelity extractions, the low-fidelity mesh $\boldsymbol{\chi}^L$ generated by *Xfoil v6.1* is projected on the high-fidelity mesh $\boldsymbol{\chi}^H$ generated by *Autogrid v8r10.3*. The multi-fidelity snapshots are then built by concatenating the linear interpolation of the low-fidelity pressure $\widetilde{P}_s^L \in \mathbb{R}^{352}$ on $\boldsymbol{\chi}^H$, the skin distribution of high-fidelity pressure $P_s^H \in \mathbb{R}^{352}$ and the wall friction components $\tau_{p_x} \in \mathbb{R}^{352}$ and $\tau_{p_y} \in \mathbb{R}^{352}$,

$$\mathbf{s} = \begin{pmatrix} \mathbf{z} = \begin{pmatrix} \widetilde{P}_s^L \end{pmatrix} \\ \mathbf{y} = \begin{pmatrix} P_s^H \\ \tau_{p_x} \\ \tau_{p_y} \end{pmatrix} \end{pmatrix}. \tag{5.2}$$

In our case, each design point is taken in the $(M_\infty - \alpha_\infty)$-space $\mathcal{D} \subset \mathbb{R}^2$ $(p = 2)$. Therefore, the low- and high-fidelity meshes remain unchanged for all experiments. An intermediate mapping of each solution on a fixed reference grid should be operated to perform the "snapshot"-POD in the case of shape optimization [Quarteroni and Rozza, 2014, Chapter 4]. In complex industrial cases involving moving meshes, a specific attention has to be payed to the interpolation scheme [Fang et al., 2009].

5.2.2 Design of Experiments and POD initialization

The design space $\mathcal{D}$ being 2D, we choose to compute an initial DoE composed of 10 snapshots. The *a priori* sampling method is the Latinized Centroidal Voronoï Tesselation (LCVT) [Saka et al., 2007; Romero et al., 2006].

As shown on Fig. 5.2, only two points are populating the transonic region confined between the red line and the top-right corner of the figure. This leads to a poor definition of the transonic behavior in the snapshot matrix yielding reduced prediction capabilities of the model. In addition, the top-left corner corresponds to incidences bringing out brutal accelerations of the fluid in its path around the leading edge. This phenomenon is partially captured by the low-fidelity simulations whereas real shocks appearing for $M_\infty > 0.63$ are visible only on the high-fidelity solutions. Given the low density of samples (Fig. 5.2), no reduction is made on the POD basis $(m = M = 10)$, built from the snapshots matrix with substracted mean.

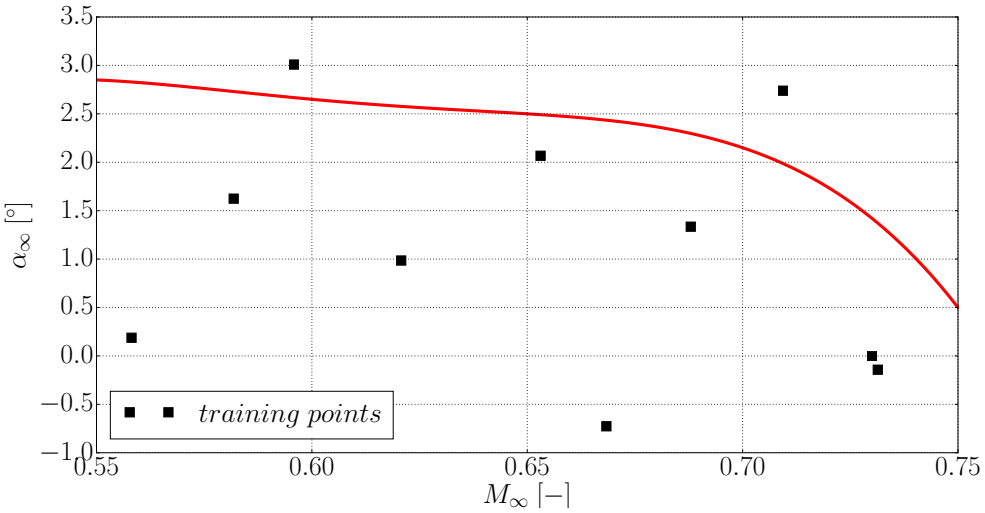

Figure 5.2: Initial samples repartition over $\mathcal{D}$ and delimitation between shocked and shock-free configurations.

5.2.3 Enrichment criterion

Figure 5.3 shows the correlation between three relative characteristic errors:

1. the high-fidelity relative error made by the POD projection of a complete snapshot $\sqrt{\dfrac{\|\mathbf{T}\mathcal{P}(\mathbf{s}) - \mathbf{T}\mathbf{s}\|^2}{\|\mathbf{T}\mathbf{s}\|^2}}$;
2. the high-fidelity relative error of the GPOD projection of a low-fidelity snapshot $\sqrt{\dfrac{\|\mathbf{T}\mathcal{P}_g(\mathbf{s}) - \mathbf{T}\mathbf{s}\|^2}{\|\mathbf{T}\mathbf{s}\|^2}}$;
3. the low-fidelity relative error of the GPOD projection of a low-fidelity snapshot $\sqrt{\dfrac{\|\mathbf{\Gamma}\mathcal{P}_g(\mathbf{s}) - \mathbf{\Gamma}\mathbf{s}\|^2}{\|\mathbf{\Gamma}\mathbf{s}\|^2}}$.

We propose to use this information to identify the areas of poor representativeness of the POD basis. The results illustrated on Fig. 5.3c represent the distribution of the δ criterion proposed in Section 5.1 over the design space $\mathcal{D}$. The multi-fidelity training points are shown as white squares, whereas the validation points supposed to be simulated only at the low-fidelity level are represented by circles colored according to the error value.

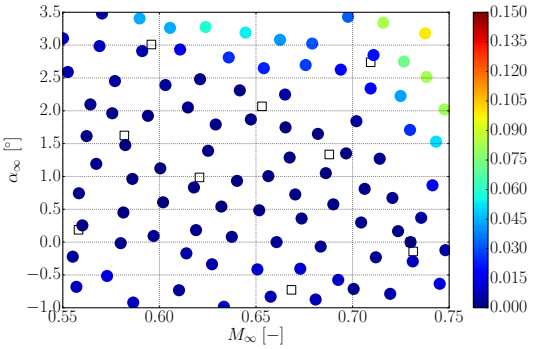

(a) Relative L_2 POD projection error on high-fidelity data $\sqrt{\frac{\|\mathbf{\Upsilon}\mathcal{P}(\mathbf{s})-\mathbf{\Upsilon}\mathbf{s}\|^2}{\|\mathbf{\Upsilon}\mathbf{s}\|^2}}$

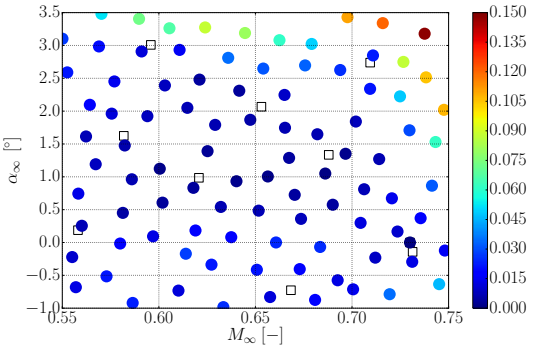

(b) Relative L_2 GPOD projection error on high-fidelity data $\sqrt{\frac{\|\mathbf{\Upsilon}\mathcal{P}_g(\mathbf{s})-\mathbf{\Upsilon}\mathbf{s}\|^2}{\|\mathbf{\Upsilon}\mathbf{s}\|^2}}$

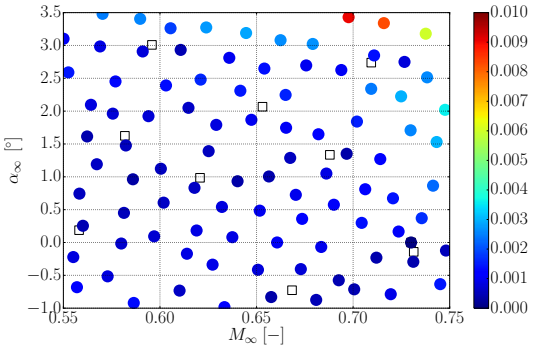

(c) Relative L_2 GPOD projection error on low-fidelity data $\sqrt{\frac{\|\mathbf{\Gamma}\mathcal{P}_g(\mathbf{s})-\mathbf{\Gamma}\mathbf{s}\|^2}{\|\mathbf{\Gamma}\mathbf{s}\|^2}}$

Figure 5.3: Comparison of POD and GPOD errors.

One can notice that the areas of high relative errors seem correlated to each other regardless of the chosen criterion $\frac{\|\mathbf{\Upsilon}\mathcal{P}(\mathbf{s}) - \mathbf{\Upsilon}\mathbf{s}\|^2}{\|\mathbf{\Upsilon}\mathbf{s}\|^2}$ (Fig. 5.3a), $\frac{\|\mathbf{\Upsilon}\mathcal{P}_g(\mathbf{s}) - \mathbf{\Upsilon}\mathbf{s}\|^2}{\|\mathbf{\Upsilon}\mathbf{s}\|^2}$ (Fig. 5.3b), or δ (Fig. 5.3c). Our previous hypothesis seems thus confirmed on this study case, even though the order of magnitude of the criterion δ if far lower than the orders of the two other errors.

5.2.4 Adaptive DoE procedure

The results presented are obtained by implementing Algorithm 4 except for its 4^{th} step (metamodeling of $\bar{\delta}$). Indeed, in our case, $\mathbf{\Theta}_v$ is rich enough (100 points

over a 2-D design space), to only use the additional DoE as potential enrichment locations such that the criterion δ is directly computed all over the sample set $\boldsymbol{\Theta}_v$.

In order to assess the efficiency of the enrichment criterion defined in Section 5.1, we propose to compare our approach with a cross-validation based method [Guénot et al., 2011; Guénot et al., 2013; Braconnier et al., 2011]. This method is based on an adapted *leave-one-out* (LOO) algorithm giving an estimation of the influence of a training snapshot on the POD basis (see Fig. 5.4). On Fig. 5.4a, one can see the evolution of the POD basis improvement coefficient [Braconnier et al., 2011] over the design space and notice the increase of its value for high M_∞ and α_∞ conditions. In Guénot et al., 2013, this coefficient is scaled by the distribution of distance to training points as shown on Fig. 5.4b.

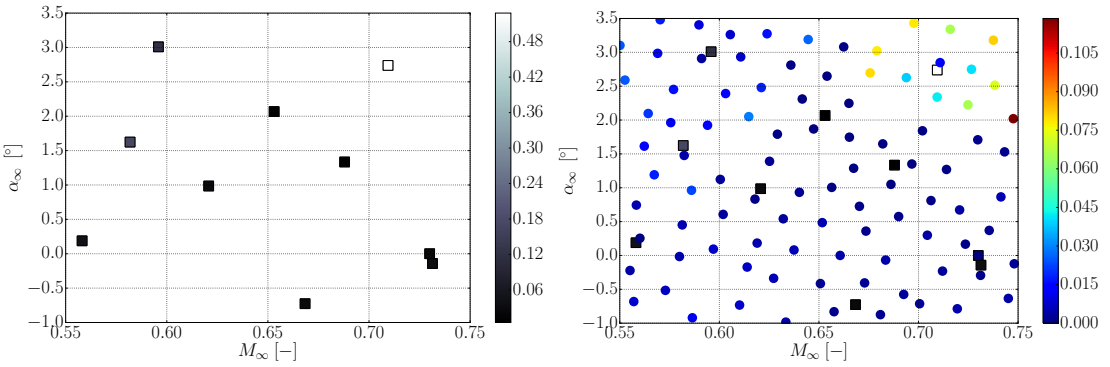

(a) POD basis improvement criterion (PBI) [Braconnier et al., 2011]

(b) Scaled POD basis improvement criterion (PBI^+) [Guénot et al., 2013]

Figure 5.4: Reference criteria.

As explained previously, the enrichment criterion in Guénot et al., 2013 considers a weighted distance between a new point $\boldsymbol{\theta} \in \mathcal{D}$ and the training database $\boldsymbol{\Theta} \in \mathcal{D}^M$. On the other hand, our criterion δ is based on the scaled GPOD projection error over the low-fidelity data as defined in Equation 5.1.

The two enrichment strategies based on both criteria [Guénot et al., 2013] and δ are illustrated on Fig. 5.5 where the squares are used for training the initial POD basis and 15 points are added (one at a time) according to the considered criterion. The selected points are highlighted by a color map associated with the current iteration number. One can notice that the two criteria both lead to the infill of the transonic regime ($M_\infty > 0.7$) first. After the first iterations (5 in this case), the PBI^+ criterion [Guénot et al., 2013] leads to the high α_∞ and low M_∞ area whereas the δ-criterion heads to the low α_∞ and high M_∞ region. These two

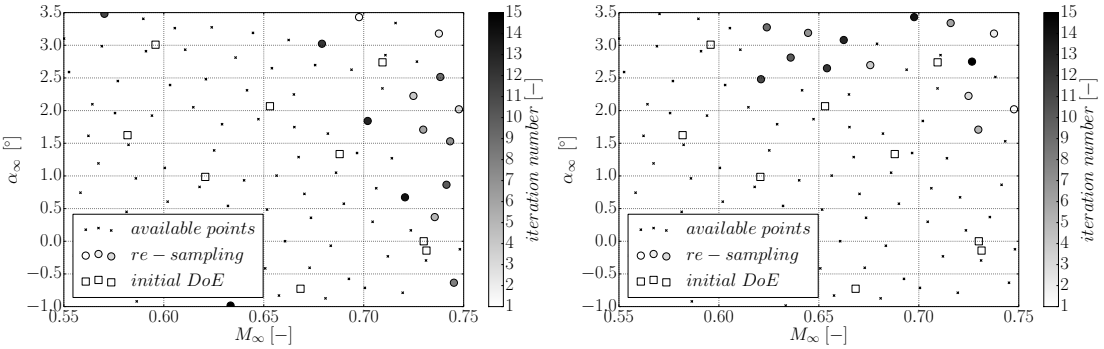

(a) GPOD criterion : $\max_{\mathbf{s}}(\delta)$

(b) POD basis improvement criterion (PBI$^+$) [Guénot et al., 2013]

Figure 5.5: Comparison of enrichment strategies.

regimes are supposed to reveal bad correlations between the low- and high-fidelity pressure distributions because of shocks appearance.

Figure 5.6 shows the low- (left) and high-fidelity (right) pressure distributions of the snapshots selected at iterations 1 to 3 for POD basis enrichment by the proposed δ-criterion. The illustrated points are connected to the poor precision area of the low-fidelity code. The computed pressure distribution is depicted by the blue solid curve while the POD and GPOD projections are respectively in red and green dotted curves. It is important to keep in mind the good agreement of low- and high-fidelity simulations hypothesis. In our case, the development of shocks tends to deteriorate the low-fidelity pressure distribution as shown on Figures 5.6a, 5.6b, and 5.6c (left column).

Indeed, the shocks are not predicted by the low-fidelity code, but a non-negligible noise appears in these regions increasing the GPOD projection error on the low-fidelity data. This increases the error δ and leads the proposed algorithm towards these areas.

At the same time, the PBI$^+$ criterion (Fig. 5.7) leads the algorithm towards the same region according to the space filling and the influence of each training snapshot on the POD basis (see Fig. 5.4).

Once again, the emergence of new patterns associated with shocked configurations incites the algorithm to add new points in the high M_∞ and α_∞ area. The former criterion [Guénot et al., 2013] is attracted to this region by the lack of shocked configurations in the initial training set while the proposed one δ is

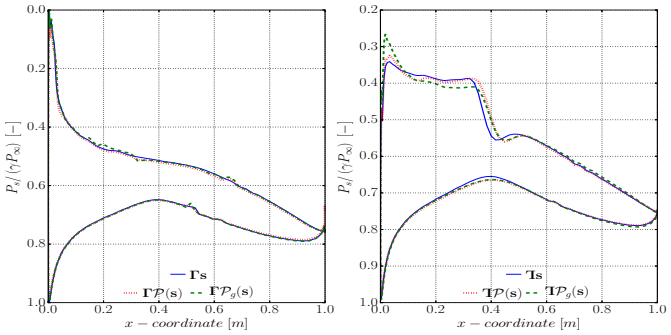

(a) Selected point at iteration 1 ($M_\infty = 0.698$, $\alpha_\infty = 3.430$)

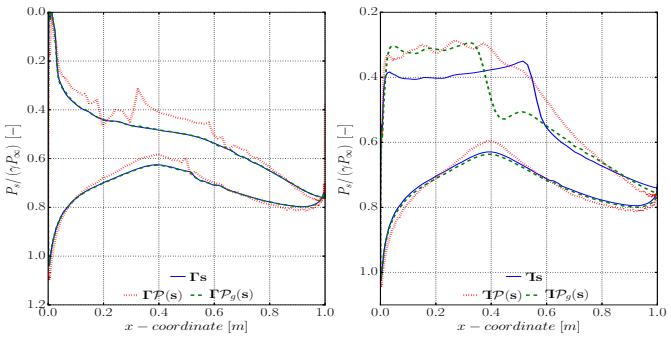

(b) Selected point at iteration 2 ($M_\infty = 0.738$, $\alpha_\infty = 3.179$)

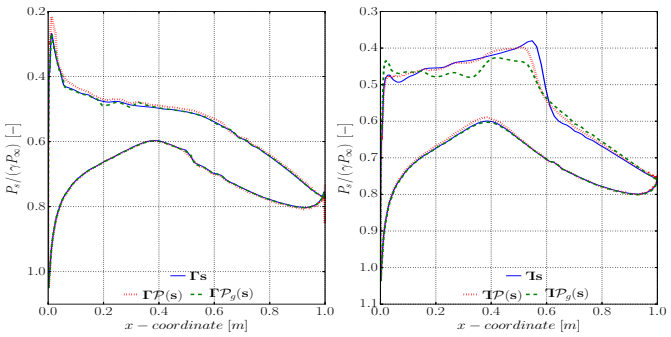

(c) Selected point at iteration 3 ($M_\infty = 0.748$, $\alpha_\infty = 2.020$)

Figure 5.6: Low-fidelity (left) and high-fidelity (right) pressure distributions of 3 enrichment points according to the proposed δ-criterion.

drawn because of the inaccuracy of the low-fidelity code in unadapted regions.

The mean and maximum projection errors over the design space can be analyzed along with the enrichment iterations for both criteria on Fig. 5.8. The magenta and green curves give the evolution of the error obtained with an enrichment driven (max value in the flight domain targeted) by the maximum

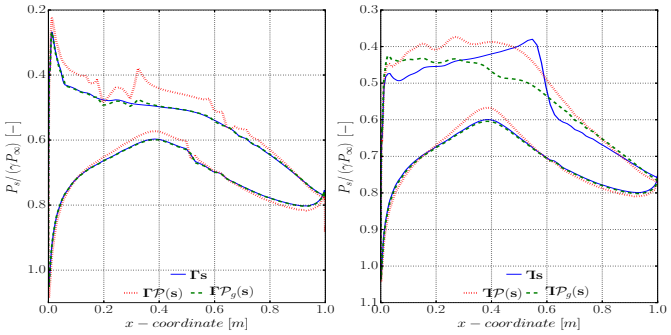

(a) Selected point at iteration 1 ($M_\infty = 0.748$, $\alpha_\infty = 2.020$)

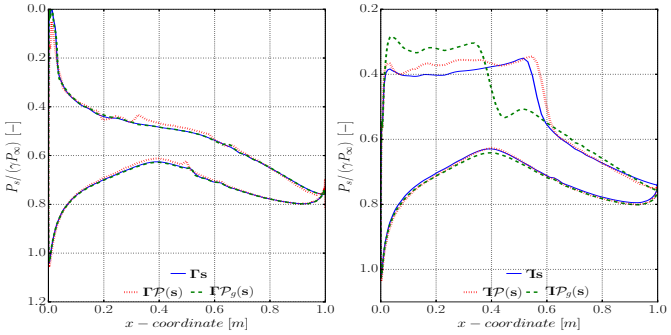

(b) Selected point at iteration 2 ($M_\infty = 0.738$, $\alpha_\infty = 3.179$)

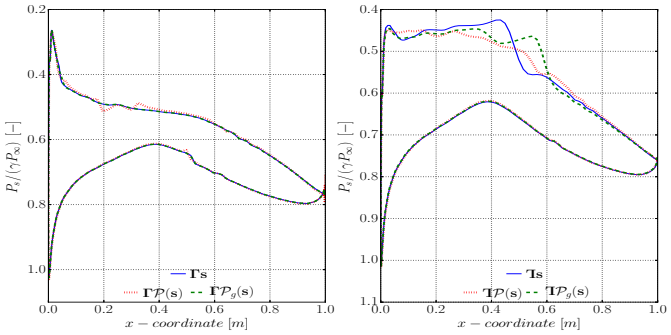

(c) Selected point at iteration 3 ($M_\infty = 0.725$, $\alpha_\infty = 2.224$)

Figure 5.7: Low-fidelity (left) and high-fidelity (right) pressure distributions of 3 enrichment points according to the PBI$^+$ criterion [Guénot et al., 2013].

uncertainty of a Kriging metamodel (denoted $\mathcal{GP}$ for Gaussian Process on Fig. 5.8) built over the two aerodynamic scalars C_D and C_L, usually interesting in the study of the flight domain. The global projection errors $\|\mathcal{P}(\mathbf{s}) - \mathbf{s}\|^2$ present the same trends (see Fig. 5.8b) regardless of the chosen criterion. On the contrary, the high-fidelity GPOD projection errors $\|\mathbf{\Upsilon}\mathcal{P}_g(\mathbf{s}) - \mathbf{\Upsilon s}\|^2$ (see Fig. 5.8a) reveal a real impact of the criterion at hand.

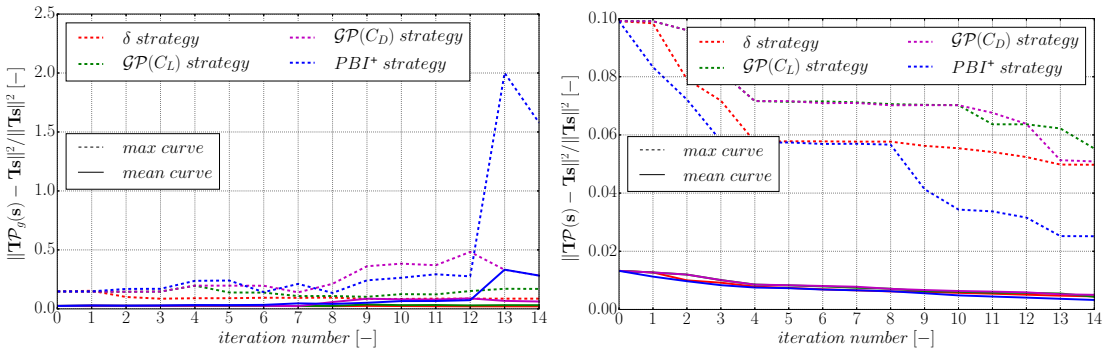

(a) GPOD projection of the high-fidelity data $\frac{\|\mathbf{I}\mathcal{P}_g(\mathbf{s})-\mathbf{I}\mathbf{s}\|^2}{\|\mathbf{I}\mathbf{s}\|^2}$

(b) POD projection of the high-fidelity data $\frac{\|\mathbf{I}\mathcal{P}(\mathbf{s})-\mathbf{I}\mathbf{s}\|^2}{\|\mathbf{I}\mathbf{s}\|^2}$

Figure 5.8: Comparison of the evolution of the mean (solid line) and maximal (dotted line) errors along iterations for the different enrichment strategies.

After the first iterations, the POD-based strategies diverge due to the lack of precision of the low-fidelity simulation. At the same time, the maximum uncertainty strategy remains stable but with a reduced efficiency compared to the proposed criterion and, as major drawback, its dependence to the variable the Kriging model is built on.

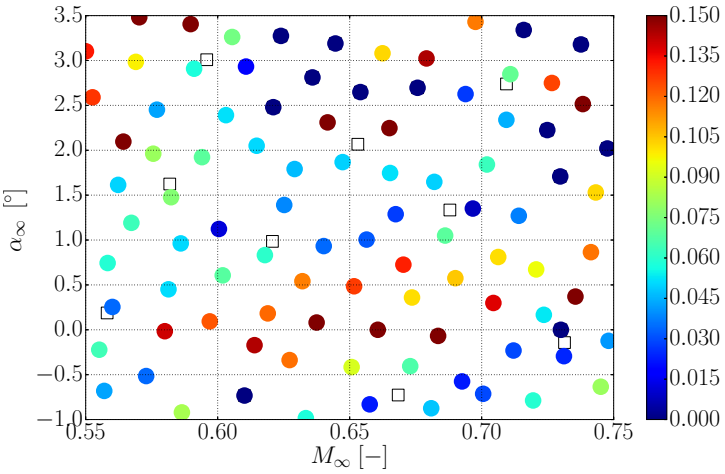

Figure 5.9: GPOD high-fidelity projection error $\sqrt{\frac{\|\mathbf{I}\mathcal{P}_g(\mathbf{s})-\mathbf{I}\mathbf{s}\|^2}{\|\mathbf{I}\mathbf{s}\|^2}}$ after 12 iterations of PBI$^+$ enrichment.

After several experiments in the high α_∞ and low M_∞ region are added by the PBI$^+$ strategy to the training set (iteration 13 on Fig. 5.8a), the high-fidelity error

of the GPOD projection is widely increased (see Fig. 5.9). These experiments correspond to high angle of attack and are typically associated with a poor prediction of the low-fidelity model as shown on Fig. 5.10.

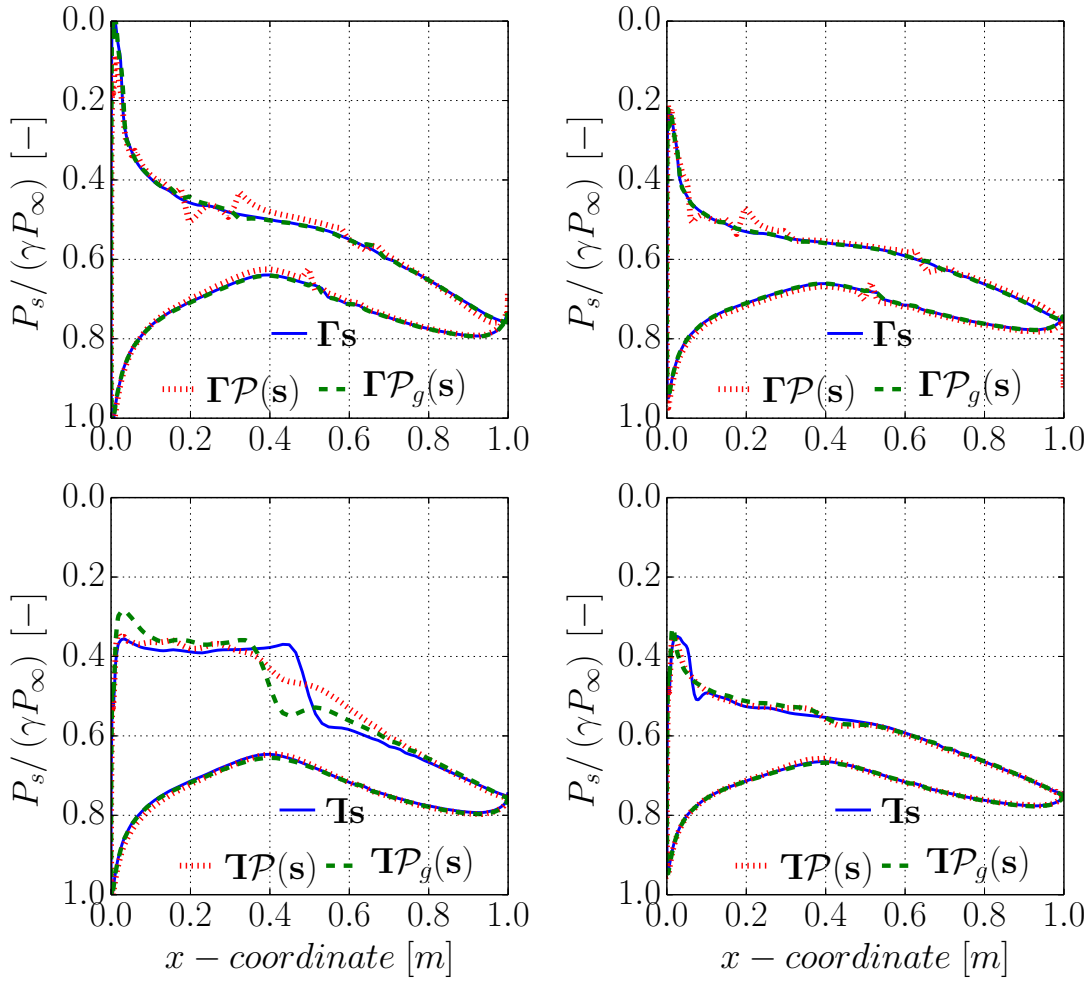

(a) Low- and high-fidelity pressure distribution at $\alpha_\infty = 3.34°$ and $M_\infty = 0.716$

(b) Low- and high-fidelity pressure distribution at $\alpha_\infty = 3.19°$ and $M_\infty = 0.645$

Figure 5.10: Pressure distribution of low-fidelity poorly simulated experiments.

Figure 5.10a illustrates the low- and high-fidelity pressure distributions computed for a design point with high M_∞ and high α_∞. One can see that the shock around 50% of the chord is observed only on the high-fidelity simulation while the pressure is increased just after the leading edge on the low-fidelity

solution.

As shown on Fig. 5.10b, the low M_∞ and high α_∞ area also presents an important lack of accuracy in the low-fidelity solution. The high-fidelity static pressure (2^{nd} row on Fig. 5.10b) suddenly increases around the leading edge of the airfoil whereas the low-fidelity solution presents a smoother evolution (1^{st} row on Fig. 5.10b). One can notice the similarity between the low-fidelity pressure distributions on Figures 5.10a and 5.10b coming from different regions in the design space. This confusion drives the GPOD projection unable to predict correctly the high-fidelity data from a low-fidelity simulation.

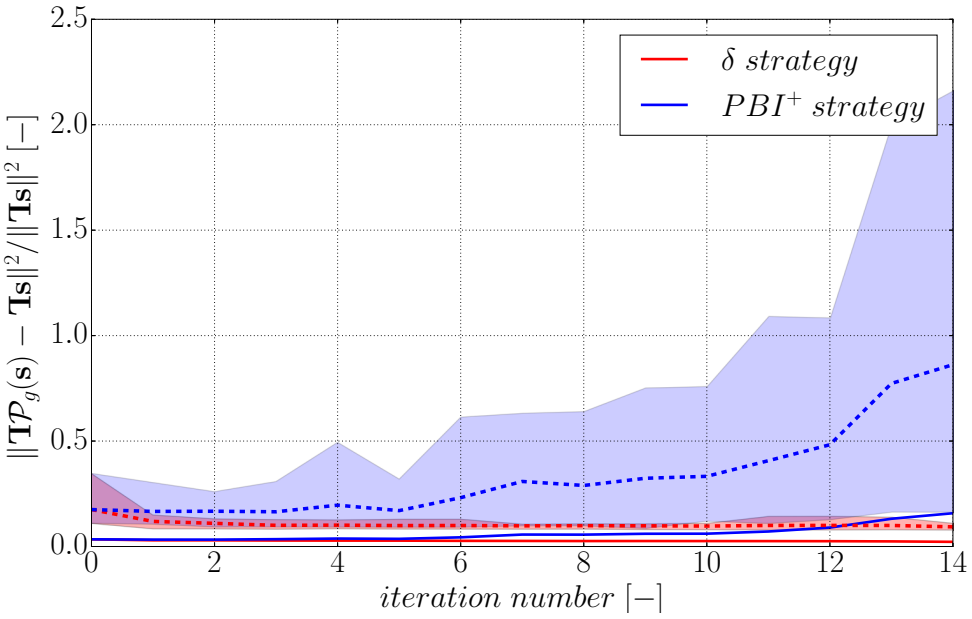

Figure 5.11: Influence of the random initialization of 10 initial DoE on the evolution of the GPOD prediction error of the high-fidelity data $\frac{\|\mathbf{T}\mathcal{P}_g(\mathbf{s})-\mathbf{T}\mathbf{s}\|^2}{\|\mathbf{T}\mathbf{s}\|^2}$ along with the enrichment strategy.

To assess the impact of randomness in DoE initialization, we built 10 different DoE with the LCVT sampling method and observed their impact on the enrichment locations chosen by each strategy. Figure 5.11 shows that the previous comments are verified for the 10 initial DoE available. The shaded areas correspond to the gap between the lowest and highest high-fidelity GPOD prediction error observed at each enrichment iteration. One can see that the shaded area associated with the δ strategy is very small compared to the blue shaded area

presenting the PBI$^+$ results. In addition, the mean and maximum level of GPOD prediction errror along with the enrichment iterations is much higher for the PBI$^+$ enrichment strategy. A converged statistical study of the impact of the initial DoE on the enrichment performances being unaffordable, we can argue from this last comparison that the proposed enrichment method outperforms the strategies from the literature and is robust with respect to the stochastic initial sampling.

5.3 Concluding remarks

The proposed enrichment criterion showed its capacity to detect the surrogate low-accuracy areas. We also highlighted the limits of a more "classical" enrichment criterion based on the impact of previously computed simulations on the subspace basis. As shown in the previous section, the criterion proposed in Braconnier et al., 2011 and Guénot et al., 2013 tends to add new simulations making the gappy-projector rapidly instable. The proposed one limited this behavior while targeting low-accuracy areas. Considering the presented capabilities of the proposed infill criterion, we claim the integration of this criterion into an infill strategy targeting the optimization of an integral quantity derived from the predicted high-fidelity information could be of first interest.

Nevertheless, one of the main drawbacks of the GPOD based Multi-Fidelity Surrogate Modeling (MFSM) as defined by Toal, 2014 is the hypothesis on the cost of the low-fidelity simulations. Indeed, to be affordable in an intensive Evolutionary Algorithm (EA) based optimization, the low-fidelity computational charge should be way smaller than usual appropriate low-fidelity models of complex engineering systems. This remark is especially well-founded in the turbomachinery application we target in this thesis.

Most of multi-fidelity applications consider low-fidelity CPU durations ranging from a few seconds up to tens of minutes, as compared to hours or day-scaled high-fidelity simulations. For this kind of applications, the surrogate models proposed in Section 4.1 are more satisfactory because of their very low evaluation cost, in the order of the millisecond on actual machines. Next chapter addresses the integration of such surrogate models into a Multi-Fidelity SBO (MFSBO) framework.

Part II

Industrial-scale surrogate modeling and optimization of aerodynamic performances

Chapter 6

Implementation of Multi-Fidelity NIPOD and analytical example

In this chapter we introduce an analytical example carefully built to exhibit typical features of aerodynamic optimization problems on one hand and to provide an insight on Multi-Fidelity SBOs (MFSBOs) on the other. This example allows to discuss in detail several issues such as fidelity levels correlation or constraints handling among others, and to compare methods without having to run time-consuming proprietary codes. The notations used in this chapter are made coherent with Chapters 3 and 4.

This chapter presents the introduction of the Multi-Fidelity POD (MFPOD) based surrogate models, proposed in Chapter 4, within a Surrogate-Based Optimization (SBO) framework. This is to alleviate the high-fidelity simulation-based optimization for engineering designs dilemma. As mentioned in Chapter 1, the computational burden associated to high-fidelity optimizations being unaffordable, we now integrate the Multi-Fidelity NIPOD (MFNIPOD) model into an Evolutionary Algorithm (EA) based optimization method.

Exploring the entire design space to determine the best configuration for a given optimization problem has become untractable for the considered number of parameters to vary at the same time. A solution to cope with this "curse of dimensionality" is to explore restricted areas (also called "search boxes") and narrow down or enlarge these search boxes as well as move their center. This solution can slightly accelerate the convergence towards interesting areas, being in terms of constraints satisfaction or objective minimization. Considering all the ingredients composing a surrogate based optimization, the real challenge is not only to improve all these ingredients separately but make them properly operate in concert in order to increase the performances of the overall SBO framework.

This chapter is organised as follows. Section 6.1 gives the major steps of an online MFSBO methodology. Then, Section 6.2 presents an analytical example illustrating the interest of the Multi-Fidelity Surrogate Model (MFSM) for a $2D$ constrained optimization problem targeting features that are representative of typical aerodynamical optimization problems. Section 6.3 gives information on the implementation of the proposed MFSMs into the SBO tool Minamo. An overview of the functionalities of the SBO methodology available in Minamo as well as the outline of the developments involved for the coupling of the proposed MFNIPOD surrogate models with the surrogate-assisted optimizer are presented in this section. Finally, some concluding remarks are given in Section 6.4. The industrial example addressing the scaling aspects of the proposed method is presented in the last chapters of this thesis (Chapters 7, 8, and 9).

6.1 Surrogate Based Optimization

The proposed process of SBO starts with the definition of the optimization problem in terms of parameters (design space $\mathcal{D} \subset \mathbb{R}^p$), objective $\mathcal{Y}$ and constraints $\mathbf{c}$ associated with multiple evaluation chains able to evaluate the quantities of interest at different levels of fidelity. The Design of Experiments (DoE) samples the $\mathcal{D}$ according to multi-fidelity sets of experiments $\mathbf{\Theta}^H$ and $\mathbf{\Theta}^L$ (see Alg. 1) that are respectively evaluated via high- and low-fidelity numerical models yielding the matrices $\mathbf{Y}$ and $\mathbf{Z}$ (see Fig. 4.1 and Algorithm 1) for Non-Intrusive POD (NIPOD) models, or the databases $\boldsymbol{\mathcal{Y}}$ and $\mathbf{C}$ for Data Fitting Surrogate Models (DFSMs). The SBO loop is then performed iteratively:

1. EA based optimization on the surrogate model (no accurate simulation is performed);
2. Evaluation of the most interesting point with both low- and high-fidelity simulation tools;
3. Enrichment of the training database with the new computations to improve the surrogate model's accuracy;
4. Stopping criterion.

As a first step towards smart integration of MFSMs into dedicated SBO strategies, we restrict the analysis in this section to online enrichment adding one evaluated point at each iteration either at the high-fidelity level for Single-Fidelity Surrogate Models (SFSMs) or at both low- and high-fidelity levels for the proposed

MFSMs.

In the next section, we illustrate the MFNIPOD based surrogates within an online SBO framework. No selection of the level of fidelity required for the evaluation of the enrichment points is performed. One location is estimated with both low- and high-fidelity solvers at each iteration.

6.2 Analytical example

To our best knowledge, no analytical test case presenting multi-fidelity and vectorial aspects is referenced in the literature. Therefore, we present in this section a 2D analytical optimization problem based on the multi-fidelity definitions proposed in Forrester, Sóbester, et al., 2008, Chapter.8 and Le Gratiet and Garnier, 2014. The notations used in this section respect, as far as possible, that of Sections 4.1.1 and 4.2. A carefull attention has been paid to make the proposed analytical example present typical features of aerodynamical optimizations. These features, a non-exhaustive list is given hereafter, concern either the objective or the constraint functions and are observable in the whole design space $\mathcal{D}$ or a part of it:

F-1 multi-modal functions : isentropic efficiency (η_{is})

F-2 multi-class functions as objectives or constraints :

- F-2.1 $\mathcal{C}^0$ class functions : chord relative shock location
- F-2.2 $\vdots$
- F-2.3 $\mathcal{C}^\infty$ class functions : mass or volume of the geometry

F-3 "plateau" like functions : blind probe after separation

F-4 highly correlated low- and high-fidelity functions : pressure ratio (Π_{tot})

F-5 poorly correlated low- and high-fidelity functions : η_{is} in presence of separation

6.2.1 Problem definition

We consider here a $2D$ design space $\mathcal{D} \subset \mathbb{R}^2$ such that each configuration in $\mathcal{D} = [4, 6] \times [10, 14]$ describes two continuous functions in $\mathbb{R}$ depending on $x \in [0, 1]$:

- Low-fidelity approximation

$$\begin{aligned} z_{\boldsymbol{\theta}}(x): \quad & \mathcal{D} \rightarrow \mathcal{F}_l\left(\mathbb{R}^{\{0,1\}}\right) \\ & \boldsymbol{\theta} \rightarrow \tfrac{1}{2}\left((6x-2)^2 \sin(\theta_2 x - 4)\right) + 10\left(x - \tfrac{1}{2}\right) - \theta_1 \end{aligned}, \tag{6.1}$$

- "High-fidelity" function

$$\begin{aligned} y_{\boldsymbol{\theta}}(x): \quad & \mathcal{D} \rightarrow \mathcal{F}_h\left(\mathbb{R}^{\{0,1\}}\right) \\ & \boldsymbol{\theta} \rightarrow \tfrac{1}{2}\left((6x-2)^2 \sin(\theta_2 x - 4)\right) + \sin\left(10\cos(\theta_1 x)\right) \end{aligned}. \tag{6.2}$$

We denote respectively $z_{\boldsymbol{\theta}}(x), y_{\boldsymbol{\theta}}(x)$, the instances of above functions for a given vector of parameters $\boldsymbol{\theta}$. Let also $f_{\boldsymbol{\theta}}(x)$ represent any function in either $\mathcal{F}_l\left(\mathbb{R}^{\{0,1\}}\right)$, or $\mathcal{F}_h\left(\mathbb{R}^{\{0,1\}}\right)$ regardless of the level of fidelity. Figures 6.1b and 6.1c show function instances obtained from Equations 6.1 and 6.2 throughout the design space according to the DoE on Fig. 6.1a.

Following notations in Problem 1.1, we define the arbitrary constrained optimization problem as follows:

$$\begin{aligned} & \text{minimize functional} \\ & \mathcal{Y}(\boldsymbol{\theta}, y_{\boldsymbol{\theta}}) = \min_{x\in[0,1]}\left(y_{\boldsymbol{\theta}}(x)\right), \\ & \text{s.t constraints} \\ c_1(\boldsymbol{\theta}, y_{\boldsymbol{\theta}}) = & \operatorname*{argmin}_{x\in[0,1]}\left(y_{\boldsymbol{\theta}}(x)\right) - 0.75 \leq 0, \\ c_2(\boldsymbol{\theta}, y_{\boldsymbol{\theta}}) = & \ 7.5 - \max_{x\in[0,1]}\left(y_{\boldsymbol{\theta}}(x)\right) \leq 0. \end{aligned} \tag{6.3}$$

The low-fidelity counterparts to $\mathcal{Y}$ and $\mathbf{c}$ are hereafter denoted $\mathcal{Y}_L(\boldsymbol{\theta}, z_{\boldsymbol{\theta}})$, $c_{1L}(\boldsymbol{\theta}, z_{\boldsymbol{\theta}})$ and $c_{2L}(\boldsymbol{\theta}, z_{\boldsymbol{\theta}})$. One can see, on Fig. 6.1b, the maximum value (▼) and the minimum position (▲) associated to each of the illustrated experiments. We can especially notice that despite the proximity of red and green points (Fig. 6.1a), the minimal locations (Fig. 6.1b) associated to these two points are slightly different. In addition, we can also observe that the low-fidelity formula (Eq. 6.1) tends to make the minimum position (argmin) insensitive to parameter modifications (all minima are located around 0.1 on Fig.6.1c and $\overrightarrow{\nabla}_{\boldsymbol{\theta}}(c_{1L}) \approx \overrightarrow{0}$). By comparing Figures 6.1b and 6.1c, we can also observe that the ordering of the illustrated experiments w.r.t. their maximum value is not consistent between low- and high-fidelity.

The low- and high-fidelity distributions of objective and constraints are illustrated on Fig. 6.2. One can observe that some features highlighted above are met on the objectives and constraints of Problem 6.3. For example the objective

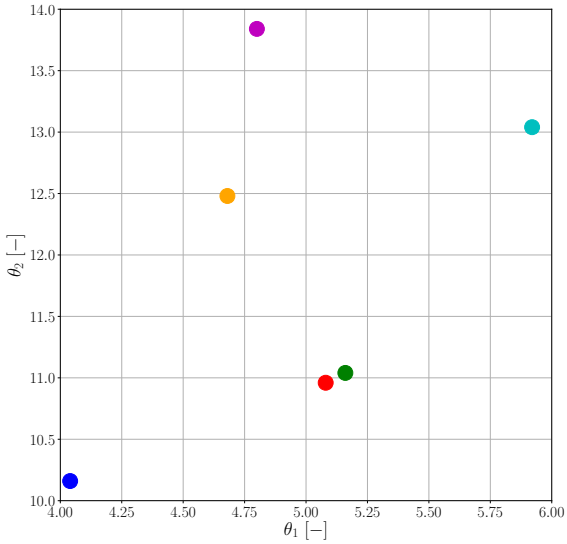

(a) Locations in $\mathcal{D}$

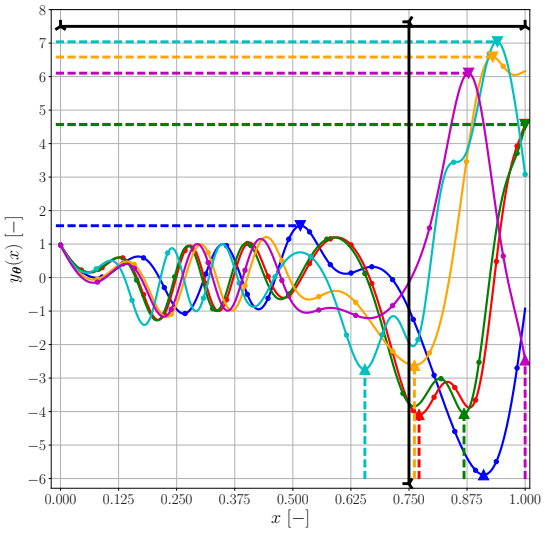

(b) High-fidelity snapshots

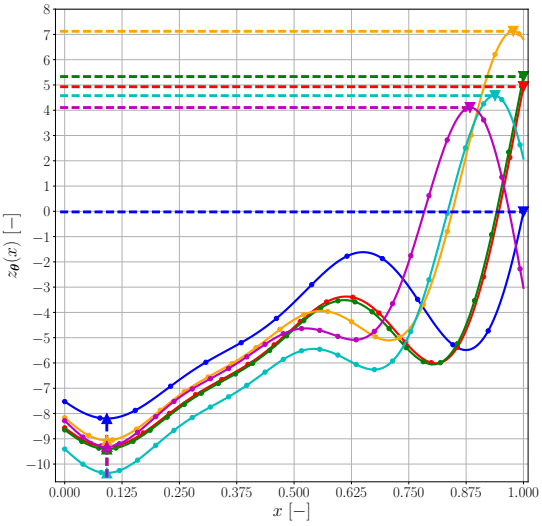

(c) Low-fidelity snapshots

Figure 6.1: Selection of 6 experiments in $\mathcal{D}$ and associated snapshots.

$\mathcal{Y}(\boldsymbol{\theta}, y_{\boldsymbol{\theta}})$ and the constraint $c_2(\boldsymbol{\theta}, y_{\boldsymbol{\theta}})$ are clearly multi-modal (Feature F-1), as illustrated on Figures 6.2a and 6.2c. The high-fidelity constraint $c_1(\boldsymbol{\theta}, y_{\boldsymbol{\theta}})$ presents discontinuities in its derivative (Feature F-2.1) because of brutal modification of the position of the minimum value. The low-fidelity functions seem of $\mathcal{C}^\infty$-class (Feature F-2.3) and present relatively weak correlations with respect to their high-fidelity counterparts as mentioned in Feature F-5. Particularly, a "plateau" is observable on the top area of Fig. 6.2b, representative of high-fidelity func-

tions with a global minimum at $x = 1$. The low-fidelity constraint $c_{1L}(\boldsymbol{\theta}, z_{\boldsymbol{\theta}})$ is obviously constant in the whole design space and also representative of Feature F-3.

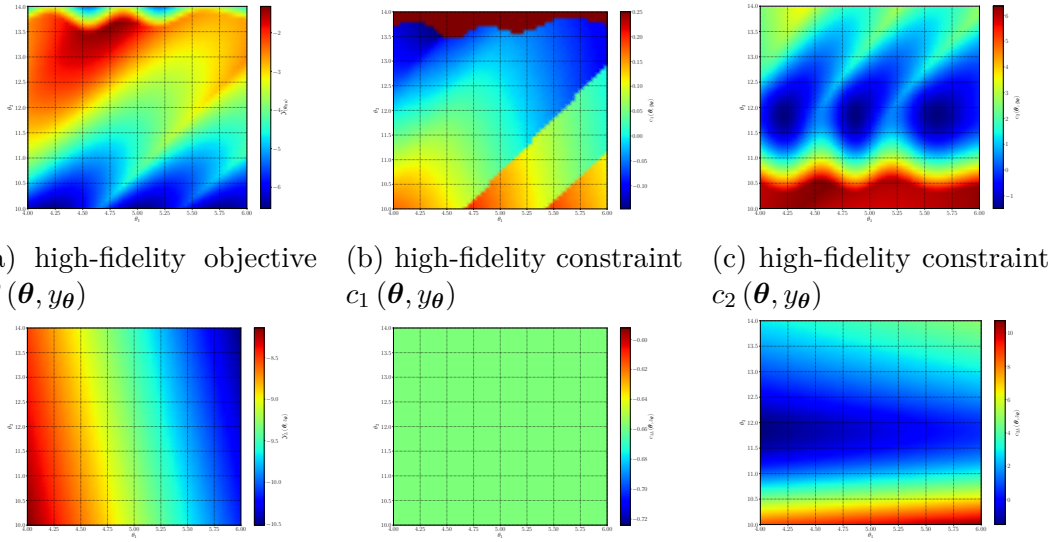

(a) high-fidelity objective $\mathcal{Y}(\boldsymbol{\theta}, y_{\boldsymbol{\theta}})$ (b) high-fidelity constraint $c_1(\boldsymbol{\theta}, y_{\boldsymbol{\theta}})$ (c) high-fidelity constraint $c_2(\boldsymbol{\theta}, y_{\boldsymbol{\theta}})$

(d) low-fidelity objective $\mathcal{Y}_L(\boldsymbol{\theta}, z_{\boldsymbol{\theta}})$ (e) low-fidelity constraint $c_{1L}(\boldsymbol{\theta}, z_{\boldsymbol{\theta}})$ (f) low-fidelity constraint $c_{2L}(\boldsymbol{\theta}, z_{\boldsymbol{\theta}})$

Figure 6.2: Comparison of high- (1st row) and low-fidelity (2nd row) distribution of the objective and constraints of Problem 6.3

Figure 6.3 presents the map of the optimization objective in the design space with both constraints represented by hatched areas.

One can see the discontinuities of the gradient of c_1 constraint (circled jump on Fig. 6.3) which is explainable by the appearance of new waves with large amplitude (gap between red and green points on Fig. 6.1) brutally changing the position of the function's minimum. It is noteworthy that the real optimum associated to the optimization problem 6.3 is located close to the intersection between the constraint boundaries, resulting in optimizations highly sensitive to the precision of the surrogates on constraints.

6.2.2 POD bases comparison

We start comparing the NIPOD and MFNIPOD bases associated with snapshots defined by the low- and high-fidelity functions discretized with 404 points evenly distributed on the $[0, 1]$ interval ($\boldsymbol{\chi} = \boldsymbol{\chi}_H = \boldsymbol{\chi}_L$). To do so, we first train a Proper Orthogonal Decomposition (POD) model with 2601 training samples evenly distributed in the design space $\mathcal{D}$ yielding a "perfect" hierarchised basis $\boldsymbol{B}^{\mathcal{F}}$ of

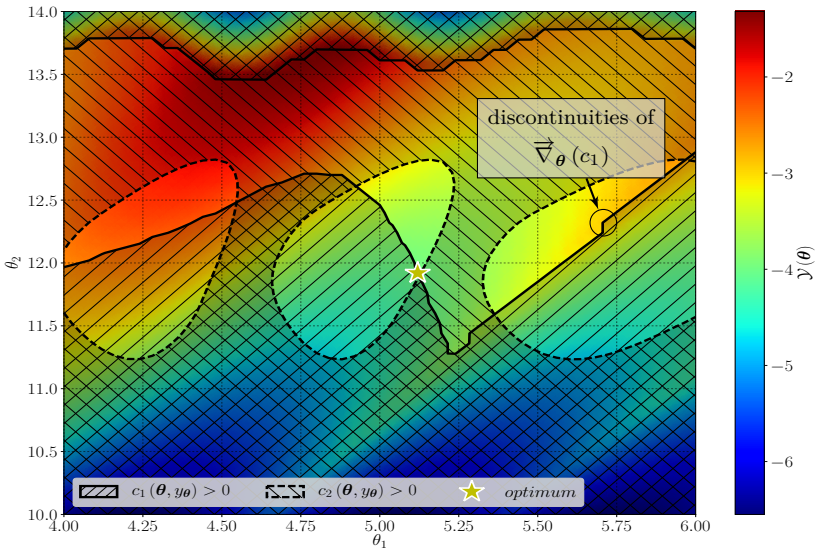

Figure 6.3: Distribution of high-fidelity minimal value (objective) in the design space with hatched constrained areas (see Problem 6.3).

the functional space $\mathcal{F}_h$ at hand. We therefore focus on the 25 first modes of this basis ordered according to decreasing singular values of the snapshot matrix, as the 25^{th} mode of this basis is associated to a relative eigenvalue lower than $1.e^{-8}$. Figure 6.4 shows the evolution of the L_2-norm of the projection of the 25 first modes of the ideal basis $\boldsymbol{B}^{\mathcal{F}}$ onto the orthogonal space of the bases $\boldsymbol{\Phi}$ and $\boldsymbol{\Psi}$ obtained respectively from single- and multi-fidelity POD approaches, as measured by $\dfrac{\boldsymbol{\lambda}_i}{\sum_j \boldsymbol{\lambda}_j} \left\| \left(\mathbf{I} - \tilde{\boldsymbol{B}} \tilde{\boldsymbol{B}}^{\top} \right) \boldsymbol{B}_i^{\mathcal{F}} \right\|^2$, where $\tilde{\boldsymbol{B}}$ is either $\boldsymbol{\Phi}$ or $\boldsymbol{\Psi}$, and $\boldsymbol{\lambda}$ is the vector of eigenvalues associated to $\boldsymbol{B}^{\mathcal{F}}$ in descending order. It is important to note that the lower the norm of the projection outside the modeled subspace, the better the model. We can see that the "lost" part of the real modes is almost always higher for the single-fidelity basis.

Table 6.1 gives the coefficients associated to the "cross"-projection of the first modes of the single- and multi-fidelity bases $\boldsymbol{\Phi}$ and $\boldsymbol{\Psi}$. By computing the scalar product of each mode in $\boldsymbol{\Phi}$ with each mode in $\boldsymbol{\Psi}$, we can evaluate the misalignment of the bases. The bases $\boldsymbol{\Phi}$ and $\boldsymbol{\Psi}$ are respectively trained with 6 high-fidelity samples for the former, and 10 low-fidelity experiments added to 4 high-fidelity samples for the latter. This ratio represents equivalent training costs considering an evaluation cost ratio of 20% between low- and high-fidelity evaluation chains.

One can see that the absolute diagonal coefficients (green cells) are close to unity (well correlated modes) for modes 1 et 2, but are fairly different afterwards. This remark is further confirmed by the presence of off-diagonal

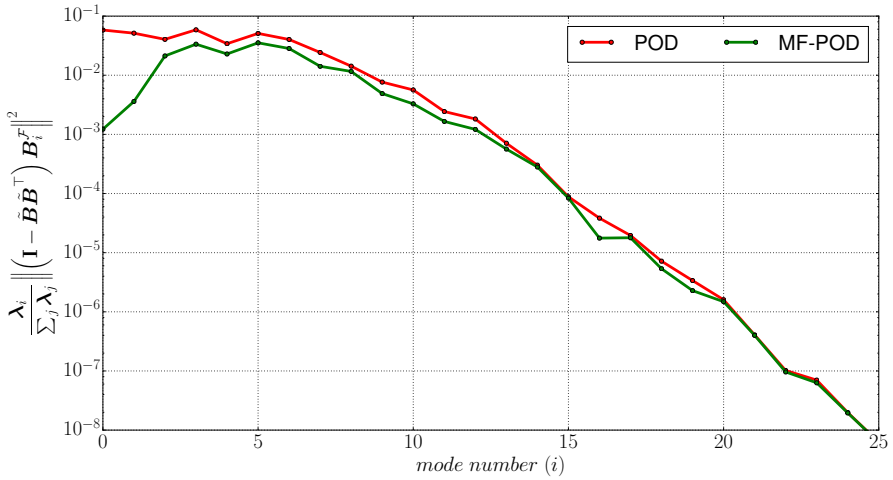

Figure 6.4: Comparison of single- and multi-fidelity POD bases w.r.t. to the 25 first modes of the ideal basis trained with 2601 evenly distributed snapshots.

ψ_i \ ϕ_j	1	2	3	4	5
1	0.9617	0.2557	0.0465	−0.0847	−0.0190
2	0.2362	−0.9402	0.2126	−0.0639	0.1048
3	−0.0420	−0.0403	−0.4575	−0.8783	0.1258
4	−0.0024	0.0016	0.0152	−0.0104	−0.0176
5	0.0040	−0.0080	−0.0268	0.0114	−0.0194
6	−0.0802	0.1842	0.5398	−0.1974	0.6176
7	−0.0382	0.0370	0.2435	−0.1507	−0.1676

Table 6.1: "Cross"-projection coefficients between $\mathbf{\Phi}$ and $\mathbf{\Psi}$.

non-zero terms (orange cells : $|\cdot| > 0.1$, red cells : $|\cdot| > 0.2$). It is important to keep in mind the orthonormality of each basis, $\mathbf{\Phi}$ on one hand, and $\mathbf{\Psi}$ on the other. Therefore, the projection coefficients are scaled between -1 and 1.

The modification introduced by low-fidelity enhancement now appears clearly from the "cross"-projections coefficients (Table 6.1), as well as the improvement of the output subspace representativeness (Fig. 6.4). As explained previously, once the output space is modeled by POD-based Reduced Order Model (ROM), NIPOD surrogates are built by "mapping" the design space to the modeled subspace. In

the coming section, we compare the predictivity of the proposed NIPOD surrogate model, and single-fidelity Radial Basis Function Networks (RBFNs) w.r.t. the objective and constraints of the optimization problem 6.3.

6.2.3 Surrogate modeling

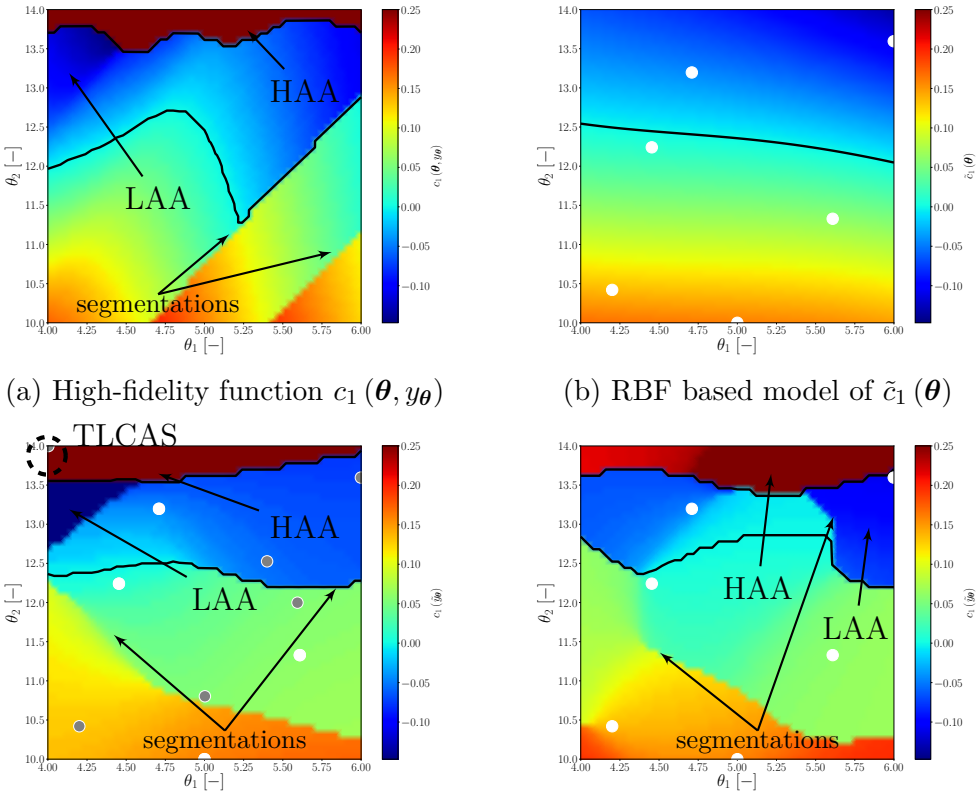

(a) High-fidelity function $c_1(\boldsymbol{\theta}, y_{\boldsymbol{\theta}})$

(b) RBF based model of $\tilde{c}_1(\boldsymbol{\theta})$

(c) Multi-fidelity NIPOD model $c_1(\tilde{y}_{\boldsymbol{\theta}})$

(d) Mono-fidelity NIPOD model $c_1(\tilde{y}_{\boldsymbol{\theta}})$

Figure 6.5: Comparison of modeled constraint w.r.t. high-fidelity (grey and white circles locating respectively low- and high-fidelity training samples, black line depicting $c_1 = 0$, HAA=high argmin area, LAA=low argmin area, TLCAS=top left corner added sample).

Figure 6.5 presents the distribution of c_1 in the design space. We can clearly see on the real distribution (Fig. 6.5a), that some discontinuities related, as explained before, to new waves arising (as illustrated by experiments red and green on Fig. 6.1) brutally in the design space. The space segmentation is observable on POD based models (Figures 6.5c and 6.5d) while impossible to capture by the Radial Basis Function (RBF) based model (Fig. 6.5b).

The main idea behind the proposed methodology is illustrated by the extension of the high $c_1\,(\tilde{y}_{\boldsymbol{\theta}})$ area on top of Figures 6.5c and 6.5d (HAA highlighted zone). Indeed, we previously observed that the low-fidelity function c_{1L} is not representative of its high-fidelity counterpart. To be more precise, the distribution of c_{1L} is constant everywhere in the design space. Nevertheless, we can see on Fig. 6.5c, that adding a low-fidelity training sample (TLCAS on Fig. 6.5c) on the top left corner of the design space makes the MFNIPOD model much more predictive of the HAA area w.r.t. the single-fidelity NIPOD model (Fig.6.5d). This behavior is due to the "activation" of a different pattern thanks to the multi-fidelity enrichment of the POD basis ($\boldsymbol{\Xi}$ in Section 4.1.3) and the improvement of the models on the POD projection coefficients ($\tilde{\boldsymbol{\alpha}}$ in Section 4.2.2) via low-fidelity information enhancement. Figure 6.6 shows the functions associated to the HAA area mentioned above. Adding the low-fidelity training sample (TLCAS) evidently improves the prediction in its surrounding area whereas its c_{1L} (circle on the dotted dark curve on Fig. 6.6) is clearly not representative of its high-fidelity analogue c_1 (filled circle on the solid dark curve on Fig. 6.6).

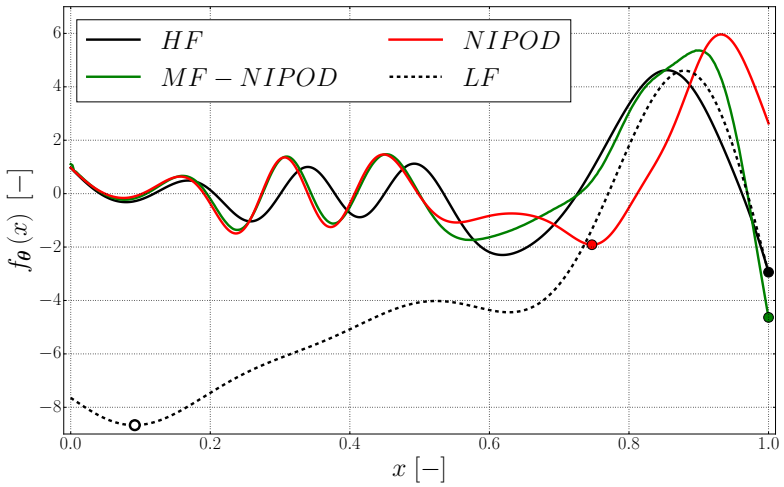

Figure 6.6: Comparison of computed (low- and high-fidelity) and modeled (NIPOD and MFNIPOD) functions for $\boldsymbol{\theta} = (\ 4.16\ ,\ 13.92\ )$, with minimum points highlighted by colored circles.

The capture of $\mathbf{c}_1$ constraint boundary (see Problem 6.3) remains better with the proposed methodology than both single-fidelity NIPOD and RBF-based models, even when the number of training samples increases. This last observation opens the door to optimizations trageting the correct feasibility area in the design space (as the feasible sub-space is shown non-convex on Fig. 6.3).

6.2.4 MFNIPOD assisted optimization

We can first evaluate the capacity offered by a MFNIPOD and a RBFN surrogate model (Fig. 6.5) to the EA in order to closely estimate the interesting zones in the design space. To this purpose, Fig. 6.7 shows the constrained design space as modeled by the surrogates trained at the end of the DoE phase.

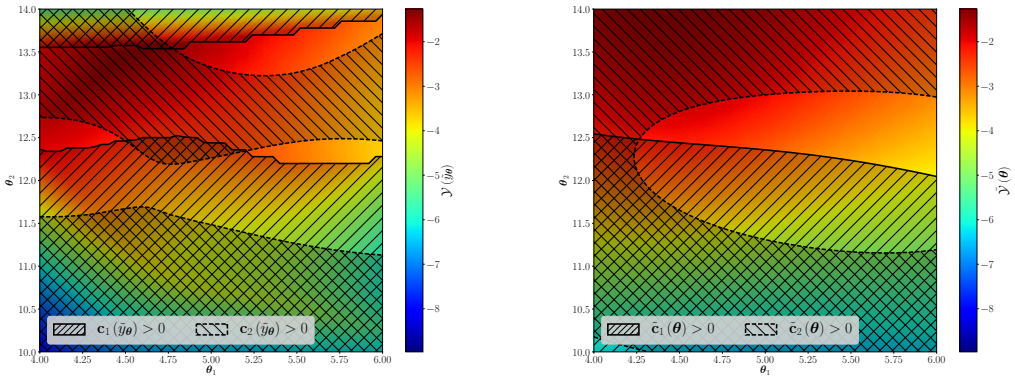

(a) MFNIPOD model ($\mathcal{Y}(\tilde{y}_{\boldsymbol{\theta}})$)

(b) RBFN SFSM ($\tilde{\mathcal{Y}}(\boldsymbol{\theta})$)

Figure 6.7: Comparison of two modeled search spaces after the DoE phase.

The maps on Fig. 6.7 have to be compared to the high-fidelity distribution (Fig. 6.3) to evaluate the accuracy given by each surrogate model to the optimizer. Considering that the EA always targets feasible points with respect to Problem 6.3, rapidly capturing the constraints boundaries is a key element for the SBO strategy. These maps and associated surrogate models are independently enriched for 20 iterations (one $\boldsymbol{\theta}$-location at each iteration), to compare the optimization efficiency associated to both RBFN and MFNIPOD surrogate models. Figure 6.8 shows the points added iteratively (point size increasing with the iteration number) by the two independent optimizations based either on RBFN or MFNIPOD surrogates. One can see that after the first iteration adding a point in the right feasible zone (MFNP1 on Fig. 6.8), the MFNIPOD assisted optimization targets the feasible area in the center of the design space and rapidly converges to the real constrained optimum of the presented problem. In the contrary, the successive RBF models are unable to capture the right feasible zone and keep on driving the EA towards the right zone of the design space (grey points on Fig. 6.8).

As every surrogate based optimization is highly dependent on the initial training samples, we performed 100 autonomous optimizations based on independently generated training ensembles. The number of training samples in the DoE phase is exactly conserved for all these parallel runs, as well as the number of enrichment

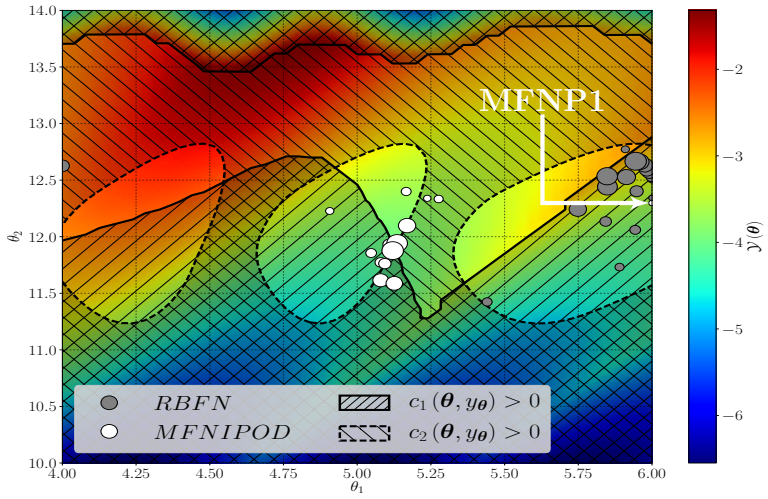

Figure 6.8: 20 first added new points during RBFN assisted (grey) and MFNIPOD assisted (white) independent optimizations.

points. Figure 6.9 shows the mean convergence and the related deviation of the optimum evolution with the number of iterations. The transparent areas represent the $\pm 1\sigma$ interval around the mean value of the sample of optima obtained in each independent optimization, bounded by the extreme values mesured in the samples. This correction explains why the decrease of the lower bound of the transparent areas is restricted to value higher than the known solution of Problem 6.3. The minimal value obtained with the MFNIPOD based surrogate modeling is lower than its RBF based counterpart.

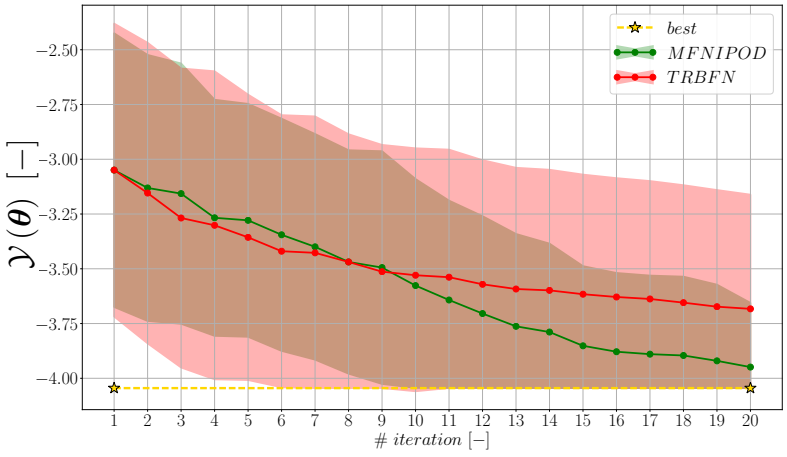

Figure 6.9: Convergence history of the optimum value (mean and standard-deviation) with the number of iterations during the optimization processes

In order to illustrate the convergence of the optimizations in the design space, we plot on Fig 6.10 the evolution of the distance between the best evaluated candidate (denoted $\boldsymbol{\theta}^*$) at iteration i and the optimal value satisfying Problem 6.3 (denoted $\boldsymbol{\theta}^\star$). We can see that this distance decreases along the optimization process assisted either by MFNIPOD or RBFN. The convergence rate seems higher in the case of MFNIPOD assisted optimizations because the central feasibility area on Fig. 6.3 is almost captured everytime by the MFNIPOD driven optimizations whereas, the RBFN driven optimizations often target the area on the right of the $2D$ map on Fig. 6.3.

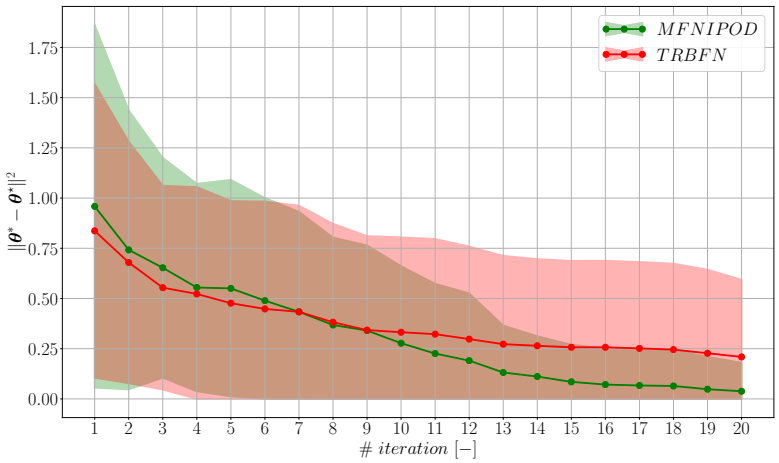

Figure 6.10: Evolution of the distance between the best candidate of i-th iteration and the optimal solution of Problem 6.3

6.3 Implementation

The chosen SBO framework is the optimization platform Minamo developed by Cenaero. Its last released version (2.7.1) integrates an EA strongly coupled with Single-Fidelity DFSMs (SFDFSMs) in an adaptive/online scheme. The available regressive models are Kriging [Krige, 1951; Matheron, 1963], RBFN [Bishop, 1995, Chapter 5] and its Leave One Out (LOO) [Rippa, 1999] optimized version. For binary responses, the Support Vector Machine (SVM) model [Cortes and Vapnik, 1995] is available and is for example used to cope with evaluation chain failures and detection of forbidden areas in the design space. The extension of this framework to multi-fidelity problems is illustrated on Fig. 6.11.

As mentioned earlier, the more accurate the surrogate model, the faster the convergence of the optimization process in interesting areas for the designer. This

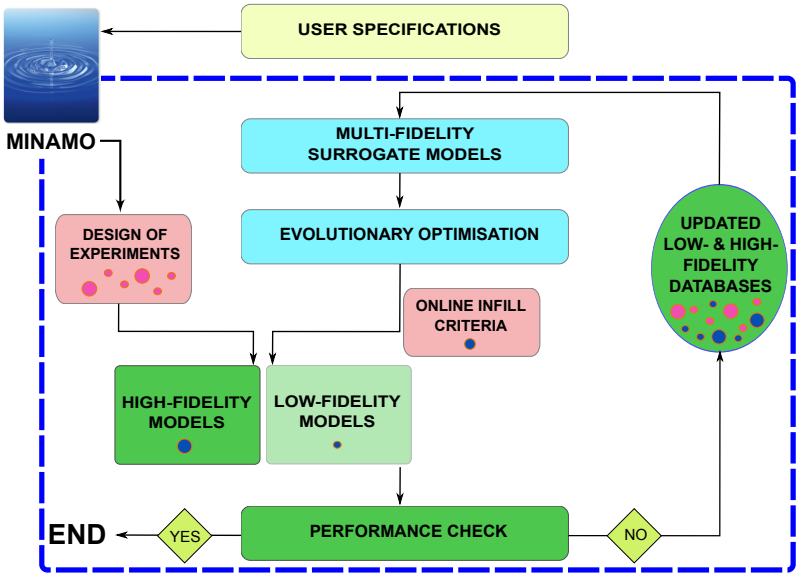

Figure 6.11: Integration of MFSBO procedure in MINAMO.

statement comes with two important facts an efficient SBO framework is built on. Firstly, ensuring the required accuracy of the surrogate model through the whole design space is untractable for complex industrial problems. Secondly, interaction between the parametrization and the constraints definition usually creates large zones in the design space associated to either failed computations or bad performances. The solution developed to cope with this issue is based on selection operators targeting "crash-free" areas in the design space dynamically modified by a dedicated strategy. This technique is inherited from the so-called Trust Region Management Methodologies (TRMMs) and automatically moves, and narrows down or enlarges the searching box, in which the surrogate model is built and the EA is working. Initially introduced by Sorensen, 1982 and Moré, 1983, the TRMMs estimate the size of the trustable surrogate region surrounding a high-fidelity estimated location in the design space. These methods inspired provably convergent "move-limit" strategies as in Alexandrov, Dennis, et al., 1998, which underlie the move-limit strategy implemented in MINAMO. Even though no proof of convergence is given when coupling zero-order surrogate models with an EA and a move-limit strategy, the ability to reduce or increase the size of the training and searching domains for the surrogate model construction and the EA optimization usually reduces significantly the number of calls to expensive high-fidelity simulations towards the areas of interest.

The implementation of MFSMs within MINAMO required the adaption of this scheme in order to manage multiple databases associated to each level of fidelity,

resulting in the MFSBO framework illustrated on Fig. 6.11. It is important to keep in mind that a more classical single-fidelity SBO design cycle is obtained by removing the low-fidelity model and updating the database only with one type of evaluator.

In our case, the shift from data regressive to full-field models also required to update the databases in order to handle and maintain high-dimensional snapshot solutions at multiple levels of fidelity that are linked to integrated scalar responses. Anticipating the important amount of data involved in Computational Fluid Dynamics (CFD) full-field solutions, as illustrated in the coming chapter, an efficient implementation within Minamo's kernel has been preferred to a weak coupling of external libraries. The test of the modified optimization platform is presented on an industrial-scale application in the remainder of this thesis.

6.4 Concluding remarks

The presented analytical problem is intended to model some key features of targeted turbomachinery applications. The proposed MFNIPOD coupled with EA outperformed more conventional RBFN assisted EA optimizations.

The interest for multi-fidelity increases with the ratio between low- and high-fidelity evaluation costs. The proposed benchmark allows to construct performance indicators by investigating the impact of an assumed CPU ratio on the convergence rate of the proposed methodology. On the other hand, a relevant cost ratio has to be associated to real engineering simulations to justify the sizes of the training ensembles and elaborate a multi-fidelity dedicated enrichment strategy.

We consider the interest of analytical benchmarks highly valuable for the estimation of performance of reduced order MFSBOs.

Nevertheless, mathematical examples can suffer from their apparent lack of representativeness. For instance, the chosen condensation (min, argmin and max functions such as in Section 6.2) can be representative of "plateau" like signals or other important features but may appear artificial as opposed to physics based integrations like efficiency computations in CFD or von Mises indicator in structural mechanics.

Next chapters are dedicated to the study and optimization of the performances of a Low-Pressure Compressor (LPC) in order to assess the reliability of the proposed model w.r.t. existing surrogates.

Chapter 7

$3D$-rotor case presentation

In this chapter, we present an industrial-scale application in order to evaluate the capacity of the surrogate models proposed in Section 4.1 to study and optimize a turbomachinery component, namely a Low-Pressure Compressor (LPC). The insight allowed by this kind of surrogate models is first assessed and compared to single-, and multi-fidelity Data Fitting Surrogate Models (DFSMs) as well as single-fidelity Non-Intrusive POD (NIPOD) models. Their integration into the Surrogate-Based Optimization (SBO) framework presented in Sections 6.1 and 6.3 is also tested on the constrained maximization of the isentropic efficiency η_{is} of an industrial 1.5-stage booster (illustrated in its engine environment on Fig. 7.1).

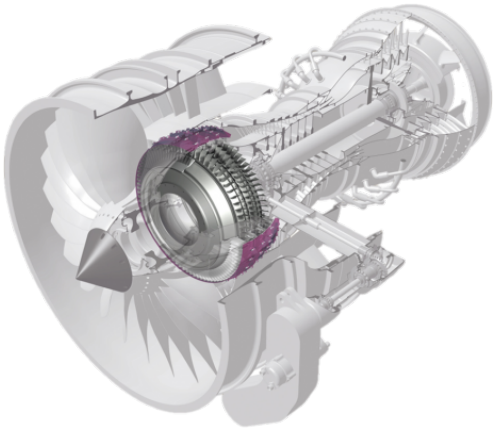

Figure 7.1: Safran Aero-Booster's engine with LPC highlighted (from Safran Aero Boosters, 2016).

Aerodynamic design of LPCs is of major interest and still stands as endeavor for engine manufacturers. The first constraint imposed to the compressor manufacturer is the total-to-total pressure ratio Π_{tot} observed between the inlet plane upstream the Inlet Guide Vane (IGV) and the outlet plane downstream the

Outlet Guide Vane (OGV). In addition to this pressure ratio achievement, the overall efficiency has to be maximized while ensuring the right stall margin at all flight conditions. The stall margin is the distance from an operating point to the line of separation between stable and unstable conditions in the compressor map [Rukavina, 1991, Chapter 1]. In reality, finding a design satisfying all the aforementioned conditions is very challenging for engineers.

The remainder of this chapter is structured as follows. Section 7.1 introduces the application with its technical challenges. Section 7.2 presents the chosen design space and illustrates the allowed modifications on the blade. The complete multi-fidelity evaluation chain at both low- and high-fidelity is presented in Section 7.3. Section 7.4, illustrates the Multi-Fidelity DoE (MFDoE) used to train and assess the surrogate's predictability.

The performance of the proposed Multi-Fidelity Models (MFMs) is assessed on the isentropic efficiency prediction of a $3D$ 1.5-stage LPC. The chosen test case is taken back from the SBO performed by Lepot et al., 2011 on the rotor R_1 of the 1.5-stage booster (see Fig. 7.2) initially designed by Safran Aero Boosters.

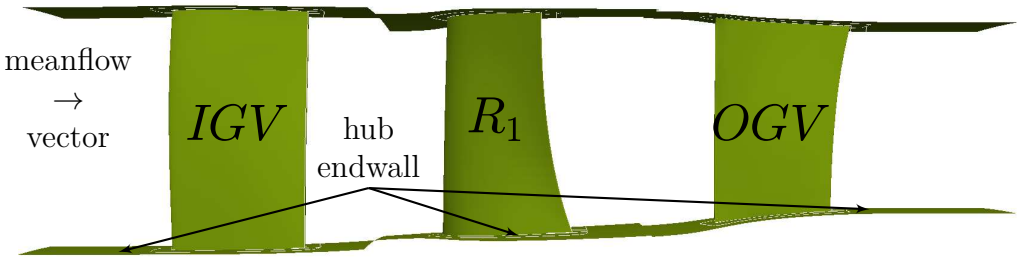

Figure 7.2: Throughout view of the computational domain.

7.1 Physical context

The reference design presents highly loaded hub sections on the rotor stage R_1. This implies high diffusion and shocked suction sides, as illustrated on Fig. 7.3.

Axisymmetric endwall contouring is a classical method to improve efficiency of highly loaded compressor designs [Hoeger et al., 2002; P. P. Chen et al., 2012; Kröger et al., 2011]. As mentioned in Lepot et al., 2011, the important

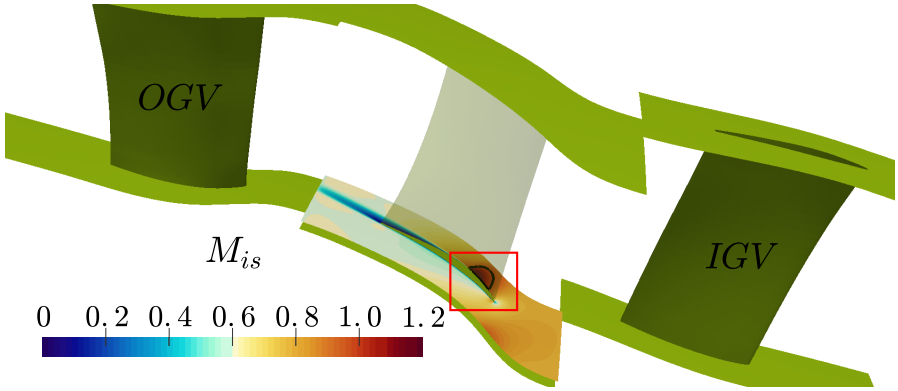

Figure 7.3: Isentropic Mach number (M_{is}) across rotor's 10%-span section (black line depicting sonic conditions).

acceleration at the suction side of highly loaded rotors implies strong pressure gradients between suction and pressure side of adjacent blades. The $3D$ resulting cross flows being responsible for a non-negligible part of the passage losses, non-axisymmetric endwall contouring has been proposed to improve the overall efficiency of highly loaded compressor stages, for example in Lepot et al., 2011; Dorfner et al., 2011; Hu et al., 2010. The joint modification of axial blade stacking and non-axisymmetric hub contouring is carried out to precisely control the spanwise mass flow distribution and the intensity and behavior of corner stall secondary flows presented in Section 2.1.1.

7.2 Design space definition

We consider here a design space associated to geometric modifications of both the blade and hub endwall of the rotating row R_1 in the booster presented on Fig. 7.2. Two independent sets of parameters are implemented. On one hand the rotor axial stacking is controlled by 2 parameters in a $3D$ in-house blade modeler allowing one slice between 30% and 70% span to move axially from 20% hub axial chord upstream up to 20% chord downstream. On the other hand, the rotor hub endwall is parametrized within the *CATIA V5R19* software. Figure 7.4 illustrates the splines (green lines) controlling the $3D$ non-axisymmetric contouring and the 17 independent parameters involved, $\mathbf{\Delta}$ representing the type of displacement allowed for each control point moving independently.

The whole design space $\mathcal{D} \subset \mathbb{R}^p$ lies in $\mathbb{R}^{19}$ and enables important modifications of the aerodynamic conditions in the passage. The radial parameters

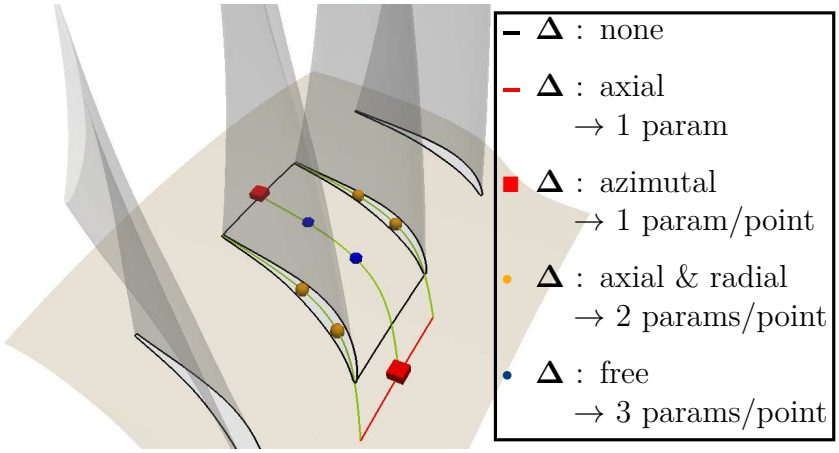

Figure 7.4: Hub contouring definition.

driving the non-axisymmetric hub endwall contouring can go up to almost 20% of the hub pitch angle (s), which yields high amplitude deformations as shown on Fig. 7.5. The described parametrization is considered as a black-box operator so that no exhaustive parameters list with their associated ranges of variation is given.

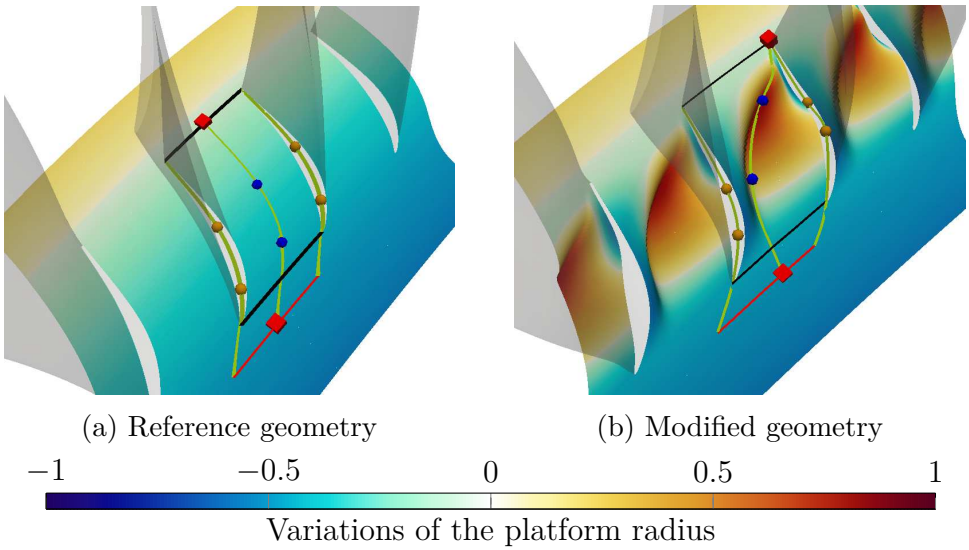

Figure 7.5: Comparison of geometries and hub elevation on the rotor.

The modification of the $3D$-hub contouring has an important impact on near-hub losses and on massflow distribution. Indeed, modifying the hub elevation tends to locally decrease or increase the velocity and has a non-negligible impact

on the transverse pressure gradient, which is the driving force behind secondary flows responsible for non-negligible efficiency losses [Reising and Schiffer, 2009] and potential hub corner stall phenomena [Lei et al., 2008]. We can observe the large deformations enabled by the described parametrization by comparing the hub geometries on Figures 7.5a (reference configuration) and 7.5b. These large deformations are responsible for non-negligible amount ($\approx$ 50%) of computation chain failures occuring either during the Computer Aided Design (CAD) generation process, the mesh generation and quality check or the flow solution convergence analysis.

Local fluctuations in the hub platform radius (R) (illustrated on Fig. 7.5), combined to the axial stacking parametrization of the rotor, allow for strongly reshaping massflow distribution and coupling between mid-span streamlines and corner stall vortices.

7.3 Flow field evaluation and multi-fidelity definition

Booster's performances are evaluated using $3D$-Reynolds Averaged Navier-Stokes (RANS) computations. The multi-block cell-centered solver *elsA v3.3p1* [Cambier et al., 2013] is used for all low- and high-fidelity simulations presented hereafter. Launder-Sharma's $k-\epsilon$ turbulence model [Launder and Sharma, 1974] without any near-wall treatment closes the RANS system of equations and is associated with an entropy corrected [Harten, 1983] second order extension of Roe's flux discretization scheme [Roe, 1981].

The multi-fidelity hierarchy is based on variable mesh refinement computations as in Kennedy and O'Hagan, 2000 or Leary et al., 2003. A first high-fidelity 3-level fully structured mesh is generated with *Autogrid v9r1.1*. The reference mesh is taken from Lepot et al., 2011 where a mesh dependence study has been performed to define the appropriate number of grid points. Leveraging the nested characteristic of the resulting mesh, the low-fidelity configuration is obtained by considering only the grid points of the 1^{st} level of coarsening (see Fig. 7.6).

The dimensionless wall distance (y^+) indicates how well the velocity gradient is captured in the boundary layer. Considering the turbulence model used in this case, it should stay below 1. One can see on Figures 7.6b and 7.6a, that the y^+ distribution is going above 1 (scale is saturated for values above 2) for the low-fidelity mesh while maintained lower in the accelerated area on the suction

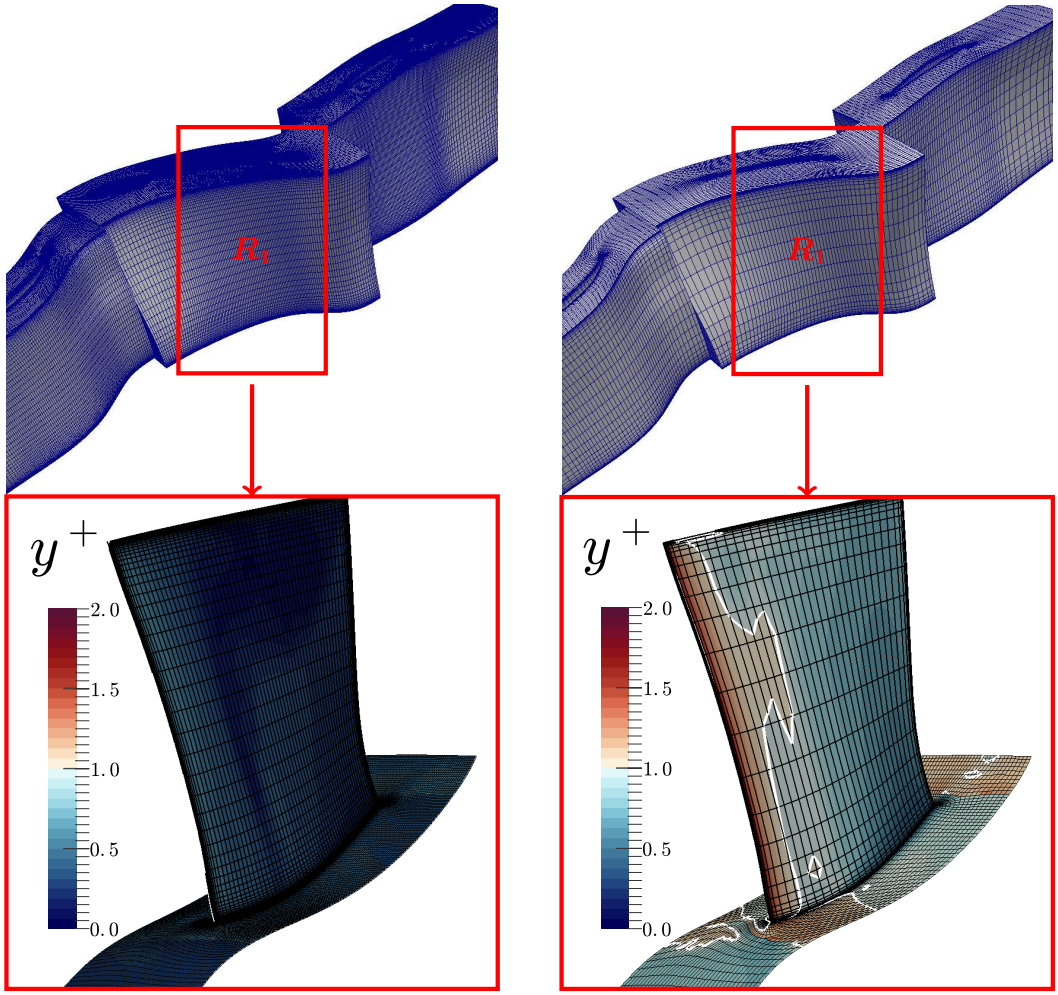

(a) High-fidelity mesh (b) Low-fidelity mesh

Figure 7.6: Comparison of low- and high-fidelity meshes (white line depicting $y^+ = 1$).

side for the high-fidelity mesh.

In addition to the increase in mesh density, high-fidelity convergence is accelerated thanks to a 2-level V-cycling multigrid. The low- and high-fidelity configurations are summarized in Table 7.1.

The impact of mesh coarsening is the dissipation of vortices in the loss-generating areas as illustrated on Figures 7.7 and 7.8.

One can see on Fig. 7.6 the impact of coarsening the mesh on y^+. Considering

	Mesh size [cells]			CPU	
	IGV	R_1	OGV	multigrid	cost [h]
LF	183,872	199,616	183,872	none	6
HF	1,470,976	1,596,928	1,470,976	V 2-level	60

Table 7.1: Mesh density and computational costs.

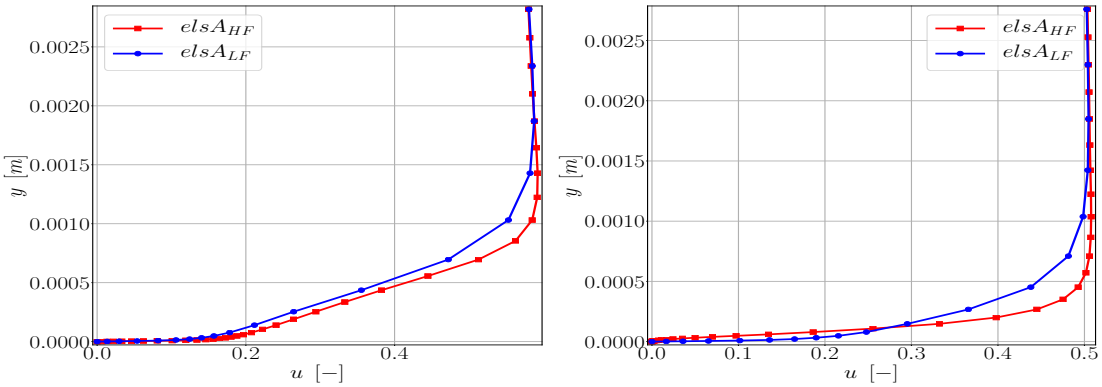

(a) Probe located at 30%-span and 80%-chord (attached boundary layer)

(b) Probe located at 75%-span and 80%-chord (reattachment area)

Figure 7.7: Skin velocity profile on the rotor blade suction side.

the skin velocity profile, the underestimation of the velocity in the viscous sublayer is verified in attached areas of the blade (see Fig. 7.7a). On the other hand, the low-fidelity solution is unable to capture the detached zones of the skin yielding the low-fidelity overestimation of the axial velocity on the blade, as illustrated on Fig. 7.7b representing the low- and high-fidelity skin velocity profiles at 75%-span and 80%-chord on the rotor blade. The rotor blade boundary layer contains between 10 and 15 mesh cells in the low-fidelity computation which is not sufficient to capture its behavior. On the opposite, the high-fidelity computations respect the recommandation for the number of mesh cells in the boundary layer to be over 20 for the type of simulations involved in this study.

As shown by highlight A on Fig. 7.8, the reference low-fidelity computation presents a weaker separation on the suction side than its high-fidelity counterpart. Coarsening the mesh provokes a rough positionning of the shock and changes the position of the shock induced boundary separation (highlight A). At the same time, a smoothing of the solution post-treated in the downstream mixing plane (highlight B) can be observed on the low-fidelity field on Fig. 7.8b with respect to Fig. 7.8a.

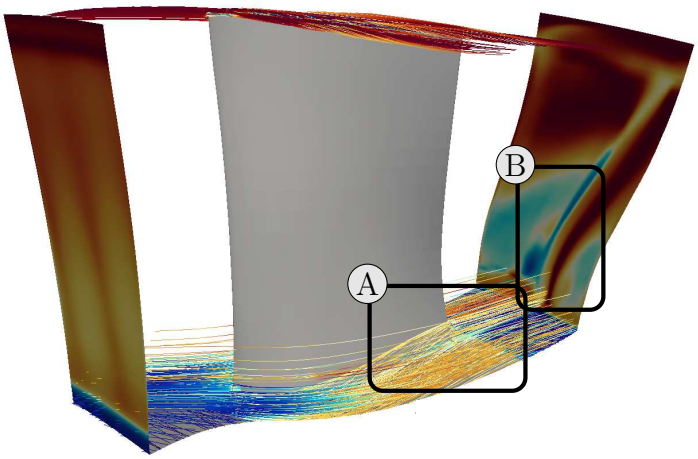

(a) High-fidelity solution

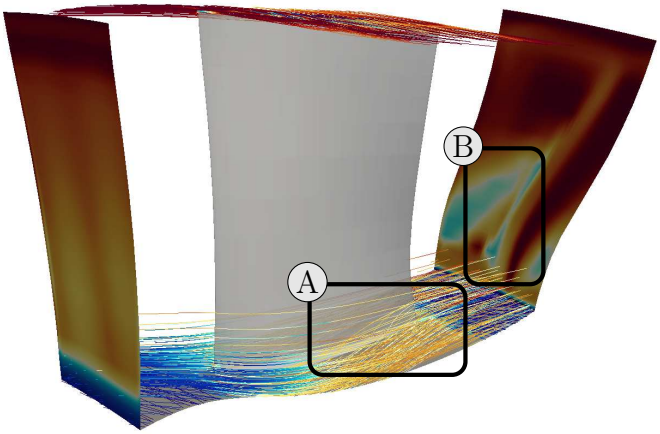

(b) Low-fidelity solution

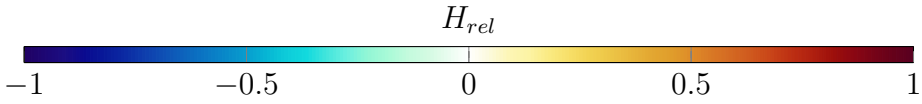

Figure 7.8: Comparison of low- and high-fidelity near endwall flow behavior and relative helicity downstream the reference rotor blade.

The aforementioned changes in conservative and derived variable distributions accross the mixing planes are responsible for a non negligible error on the η_{is} and Π_{tot}, usual objectives and constraints of a compressor optimization. In our case, these indicators are computed from the inlet and outlet states of the computational domain. One can observe on Fig. 7.9 that low-fidelity simulations are well correlated to high-fidelity results. This is a requirement for every multi-fidelity strategy to lead an optimizer towards interesting regions in the design space while

maintaining low computational costs.

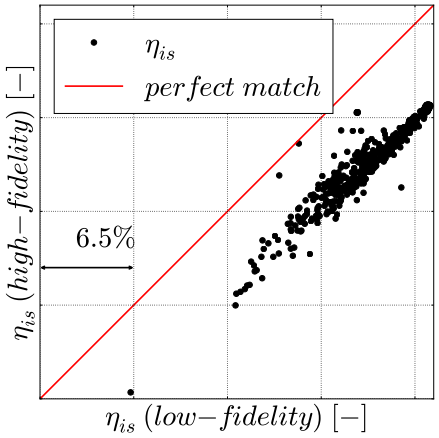

(a) Comparison of η_{is} estimated at both levels of fidelity

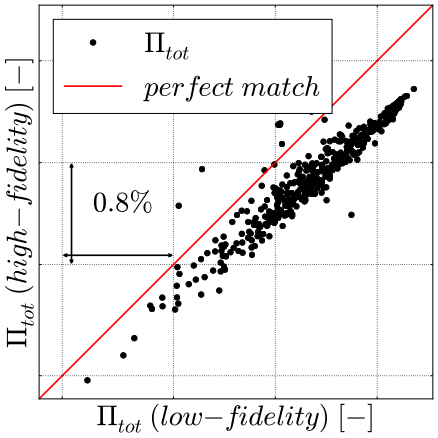

(b) Comparison of Π_{tot} estimated at both levels of fidelity

Figure 7.9: Comparison of global objective η_{is} and contraint Π_{tot} of the 1.5-stage booster at on-design configuration.

7.4 Design of Experiments

Considering the computational cost of a single high-fidelity computation in the proposed application, we propose to select "randomly" all the training databases in a fixed Design of Experiments (DoE) and validate all the surrogate models on another fixed validation DoE. A first DoE $\mathbf{\Theta}_F$ of 1000 points has been performed yielding 500 successfully computed and converged experiments (at both low- and high-fidelity levels) distributed along the 19-dimensional design space $\mathcal{D}$ according to an improvement to the Latin Hypercube Sampling (LHS) called Latinized Centroidal Voronoï Tesselation (LCVT) sampling method [Saka et al., 2007]. A second LCVT DoE $\mathbf{\Theta}_V$ containing 110 successfull high-fidelity experiments is independently generated to estimate the quality of all trained surrogate models and is therefore never used as training information for surrogates but only for validation. To assess the impact of randomness underlying the *a priori* sampling methods utilized, multiple indepedent groups of training ensembles with the following properties are built ($\$_{\frac{LF}{HF}}$ recalling the computational cost ratio between low- and high-fidelity simulations):

1. $\mathbf{\Theta}_T$: LHS DoE of $M_H + M_L$ points
2. $\mathbf{\Theta}_C$: LHS DoE of $M_H + \lceil M_L \cdot \$_{\frac{L}{H}} \rceil$ points

3. $\mathbf{\Theta}_H$: LCVT DoE of M_H points,

with $\mathbf{\Theta}_H \subset \mathbf{\Theta}_C \subset \mathbf{\Theta}_T$.

The LHS conditions of $\mathbf{\Theta}_C$ and $\mathbf{\Theta}_T$ are met by generating and enriching $\mathbf{\Theta}_H$ respectively with the LCVT sampling method [Saka et al., 2007] and the "inherited" LHS enrichment method [G. Wang, 2003]. The collision free projection illustrated (on a $2D$ toy example) on Fig. 7.10 yields pseudo-independent training ensembles $\mathbf{\Theta}_T$ while limiting the training computational time to the simulation of the first DoE $\mathbf{\Theta}_F$. It is important to keep in mind that the theoretical computational costs implied by the high-fidelity simulations of $\mathbf{\Theta}_C$ on one hand and the sum of high-fidelity simulations of $\mathbf{\Theta}_H$ and low-fidelity simulations of $\mathbf{\Theta}_T$ on the other hand are equivalent. In fact, running M_H high-fidelity and M_L low-fidelity simulations is associated to a computational cost of $M_H \cdot \$_H + M_L \cdot \$_L$. To take into account the cost associated to low-fidelity experiments utilized for training the multi-fidelity surrogate models, we compare these surrogates to mono-fidelity models trained on extended databases, this extension being represented by $\mathbf{\Theta}_C$.

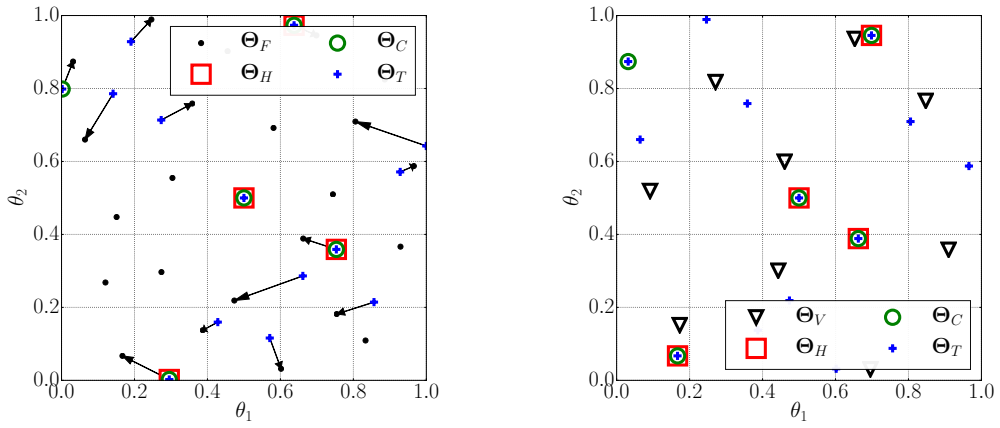

(a) Fixed DoE $\mathbf{\Theta}_F$ and collision free projection of $\mathbf{\Theta}_T$

(b) Fixed validation DoE $\mathbf{\Theta}_V$ and projected training DoE

Figure 7.10: Fixed computed and validation DoEs and Random generation of training DoEs for surrogate model construction.

This collision free process allows for taking into account a biased randomness on the predictability while both insuring a certain number of training points and restraining the CPU budget within acceptable limits.

In Chapter 8, we present a study of the the predictability of the proposed Multi-Fidelity NIPOD (MFNIPOD) surrogate models on the on-design quantities of interest for the considered booster.

Chapter 8

Surrogate model prediction of $3D$-rotor aerodynamic performances

Following the notations of Sections 4.1-4.2, and Chapter 7, this chapter evalutes the predictability of the proposed Hierarchised Multi-Fidelity NIPOD (HMFNI-POD) on the performance indicators of the studied $1.5D$-booster. Section 8.1 primarily explains the training and validation methodology applied to the study. Stressing the advantages and limitations of the proposed surrogate model w.r.t. reference models [Bishop, 1995; Kennedy and O'Hagan, 2000; Forrester, Sóbester, et al., 2007; Guénot et al., 2013; D. Xiao, Fang, et al., 2015; Shinde et al., 2016; Hamdaoui et al., 2013], single- and Multi-Fidelity POD (MFPOD) bases are compared in Section 8.2, as well as Non-Intrusive POD (NIPOD) and Multi-Fidelity NIPOD (MFNIPOD) in Section 8.3. Finally, Section 8.4 discusses choices made in order to perform optimizations of the aforementioned $1.5D$-booster.

8.1 Validation methodology and snapshot definition

We denote $\mathbf{Z}(\mathbf{\Theta})$ and $\mathbf{Y}(\mathbf{\Theta})$, the snapshot matrices obtained by computation of the points in DoE $\mathbf{\Theta}$ respectively at low- and high-fidelity, and ζ_L or ζ_H any scalar quantity of interest respectively integrated from a low- or high-fidelity full field solution of the problem at hand. To assess the quality of the proposed surrogate model, a comparison of its predictability will be made with:

- full-field models :
  - single-fidelity

1. $\mathbf{Y}(\mathbf{\Theta}_H)$ trained NIPOD
2. $\mathbf{Y}(\mathbf{\Theta}_C)$ trained NIPOD

– multi-fidelity $\mathbf{S}_M := [\mathbf{Y}(\mathbf{\Theta}_H), \mathbf{Z}(\mathbf{\Theta}_T)]$

3. $\mathbf{S}_M$ trained NIPOD (Mifsud, MacManus, et al., 2016)
4. $\mathbf{S}_M$ trained NIPOD (Sections 3.1-4.2, and Chapter 7)

- scalar models (ζ is either η_{is} or Π_{tot}) :

– single-fidelity $\boldsymbol{\zeta} := \boldsymbol{\zeta}_H$

5. $\boldsymbol{\zeta}(\mathbf{\Theta}_H)$ trained RBFN
6. $\boldsymbol{\zeta}(\mathbf{\Theta}_C)$ trained RBFN

– multi-fidelity $\boldsymbol{\zeta} := [\boldsymbol{\zeta}_H(\mathbf{\Theta}_H), \boldsymbol{\zeta}_L(\mathbf{\Theta}_T)]$

7. $\boldsymbol{\zeta}$ trained co-Kriging.

The quantities of interest (η_{is} and Π_{tot}) will be predicted by above list of reference models yielding the Pearson's correlation coefficients [Pearson, 1895; Pearson, 1896]:

$$r_k^{\eta} = \frac{\sum_{i=0}^{M_V} \left(\eta_k^{(i)} - \bar{\eta}_k^{(i)}\right)\left(\tilde{\eta}_k^{(i)} - \bar{\tilde{\eta}}_k^{(i)}\right)}{\sqrt{\sum_{i=0}^{M_V} \left(\eta_k^{(i)} - \bar{\eta}_k^{(i)}\right)^2}\sqrt{\sum_{i=0}^{M_V} \left(\tilde{\eta}_k^{(i)} - \bar{\tilde{\eta}}_k^{(i)}\right)^2}}, \tag{8.1}$$

and,

$$r_k^{\Pi} = \frac{\sum_{i=0}^{M_V} \left(\Pi_k^{(i)} - \bar{\Pi}_k^{(i)}\right)\left(\tilde{\Pi}_k^{(i)} - \bar{\tilde{\Pi}}_k^{(i)}\right)}{\sqrt{\sum_{i=0}^{M_V} \left(\Pi_k^{(i)} - \bar{\Pi}_k^{(i)}\right)^2}\sqrt{\sum_{i=0}^{M_V} \left(\tilde{\Pi}_k^{(i)} - \bar{\tilde{\Pi}}_k^{(i)}\right)^2}}, \tag{8.2}$$

where M_V is the number of points in the validation DoE $\mathbf{\Theta}_V$ and k naming a defined model type in the list above.

The NIPOD-based models will be trained for each conservative variable of the $3D$ computations and from the distributions on the coarse mesh nodes in the mixing planes, as illustrated on Fig. 8.1. The conservative variables are stored dimensionless in order to keep different physical units from changing the relative variances associated to each conservative variable. As mentioned in Kirby et al., 1990 and Jolliffe, 2002, units artificially introducing important variances (static pressure $[Pa]$ in the order of five as compared to density $[-]$ in the order of 1

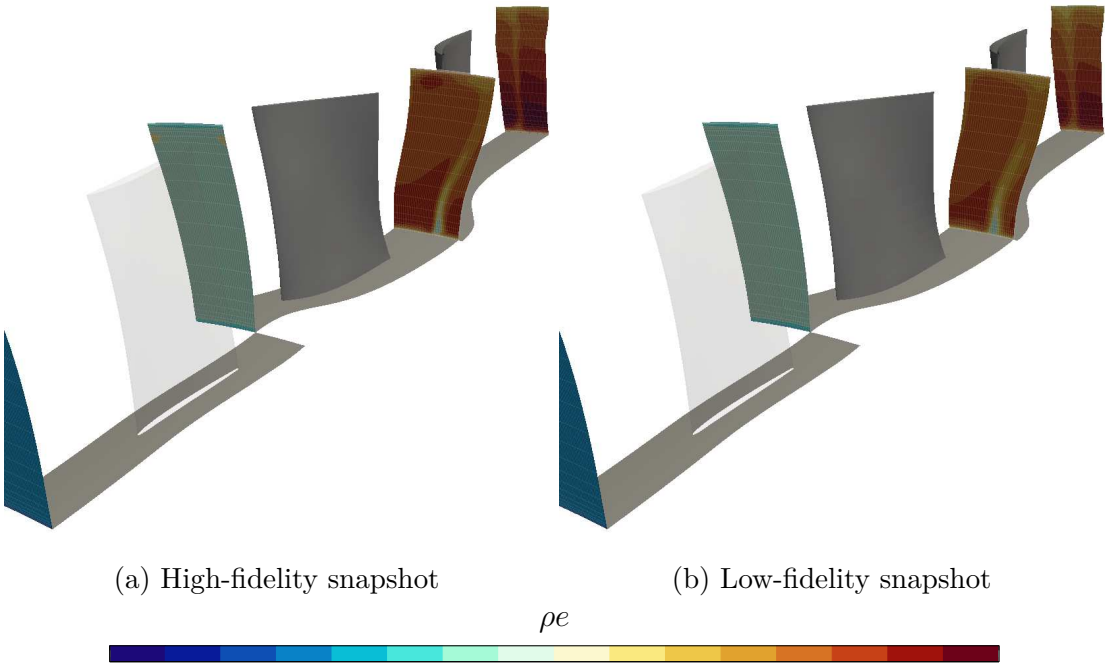

(a) High-fidelity snapshot (b) Low-fidelity snapshot

Figure 8.1: ρe distribution on coarse mesh nodes in the mixing planes (iso-range).

for example) would clearly dominate the first POD modes despite a potentially weaker link to the parametric changes.

To predict the quantities of interest η_{is} and Π_{tot}, one NIPOD model per conservative variable ρ, ρu, ρv, ρw, ρe, ρk, $\rho \epsilon$ is built in each mixing plane. This yields 28 models trained on snaphots lying in $\mathbb{R}^{1961}$.

8.2 Comparison of single- and multi-fidelity POD bases

As explained in Section 4.1.3, the proposed method tends to leverage multi-fidelity information to improve both the basis and the projection coefficient models of a NIPOD-based surrogate. To evaluate the POD basis improvement with respect to both single-fidelity [Guénot et al., 2011] and non-hierarchised multi-fidelity basis [Mifsud, MacManus, et al., 2016], we propose to compute the "ideal" representation $\mathbf{\Phi}_F$ of our problem's output space, from the whole database $\mathbf{\Theta}_F$, and quantify the lacking information of all approximate bases. In the following, we consider the comparison of the bases listed in Table 8.1 and associated to the corresponding training ensemble(s). For the sake of readability, all $\mathbf{\Phi}$, $\mathbf{\Upsilon}$ and $\mathbf{\Psi}$ bases will be respectively associated to single-fidelity POD basis training, multi-

fidelity POD construction as defined by Mifsud, MacManus, et al., 2016, and the hierarchised multi-fidelity method proposed in Section 4.1.3.

DoE	fidelity level	snapshots matrix	basis
$\mathbf{\Theta}_F$	high	$\mathbf{S}_F$	$\mathbf{\Phi}_F$
$\mathbf{\Theta}_H$	high	$\mathbf{S}_H$	$\mathbf{\Phi}_H$
$\mathbf{\Theta}_C$	high	$\mathbf{S}_C$	$\mathbf{\Phi}_C$
$\mathbf{\Theta}_T$	both	$\mathbf{S}_M$	$\mathbf{\Upsilon}_M$ [Mifsud, MacManus, et al., 2016]
$\mathbf{\Theta}_T$	both	$\mathbf{S}_M$	$\mathbf{\Psi}_M$

Table 8.1: Compared bases and associated training set

Figure 8.2 shows the energy decay of the bases $\mathbf{\Phi}_F$ associated to each POD model and built on the $\mathbf{S}_F$ snapshot matrices. As illustrated on Fig. 8.2a, the energy of the modes associated to the inlet plane of the booster is decaying very rapidly as a fixed massflow boundary condition is imposed. On the contrary, the other post-processed planes show a gentler slope for the POD modes energy decay, especially the last two planes (R_1–OGV and booster's outlet) where more than 100 modes are needed to capture 99.9% of the total energy contained in the snapshot matrices.

$\mathbf{\Phi}_F$ representing the "ideal" basis spanning the high-fidelity output spaces of pair of conservative variables in post-processing planes, we evaluate δ_i (Eq. 8.3) the "missing" relative L_2-norm of each vector $\boldsymbol{\phi}_{F_{.i}}$:

$$\delta_i = \frac{\| \left(\mathbf{I} - \mathbf{B}\mathbf{B}^\top \right) \mathbf{\Phi}_{F_{.i}} \|^2}{\| \mathbf{\Phi}_{F_{.i}} \|^2}. \tag{8.3}$$

δ_i measures the part of the vector outside the subspaces spanned by the bases $\mathbf{\Phi}_H$, $\mathbf{\Phi}_C$, $\mathbf{\Upsilon}_M$, $\mathbf{\Psi}_M$, $\mathbf{\Upsilon}_M^{99\%}$, and $\mathbf{\Psi}_M^{99\%}$, where $\times^{99\%}$ represents any basis $\mathbf{B}$ truncated at 99% of its energy $\epsilon(m)_\times = \frac{\sum_{i=1}^{m} \boldsymbol{\lambda}_i}{\sum_{i=1}^{M} \boldsymbol{\lambda}_i}$, with $\boldsymbol{\lambda}$ the vector of decreasing eigenvalues and the number of modes $m < M$ the number of training snapshots.

The bases presented on Fig. 8.3 are trained on DoE's associated to the couple $(M_H, M_L) = (38, 190)$ being respectively $2 \times dim(\mathcal{D})$ and $10 \times dim(\mathcal{D})$. Figure 8.3 shows the first interest of multi-fidelity enrichment for the POD basis construction. We can notice that the error δ is always higher for the POD basis $\mathbf{\Phi}_C$ than for the proposed basis $\mathbf{\Psi}_M$ despite equivalent training costs. Figure 8.3 also illustrates that the methodologies proposed in this work and in Mifsud, MacManus, et al., 2016 are equivalent if "un-truncated", as both curves $\mathbf{\Psi}_M$ and $\mathbf{\Upsilon}_M$ lie on top of

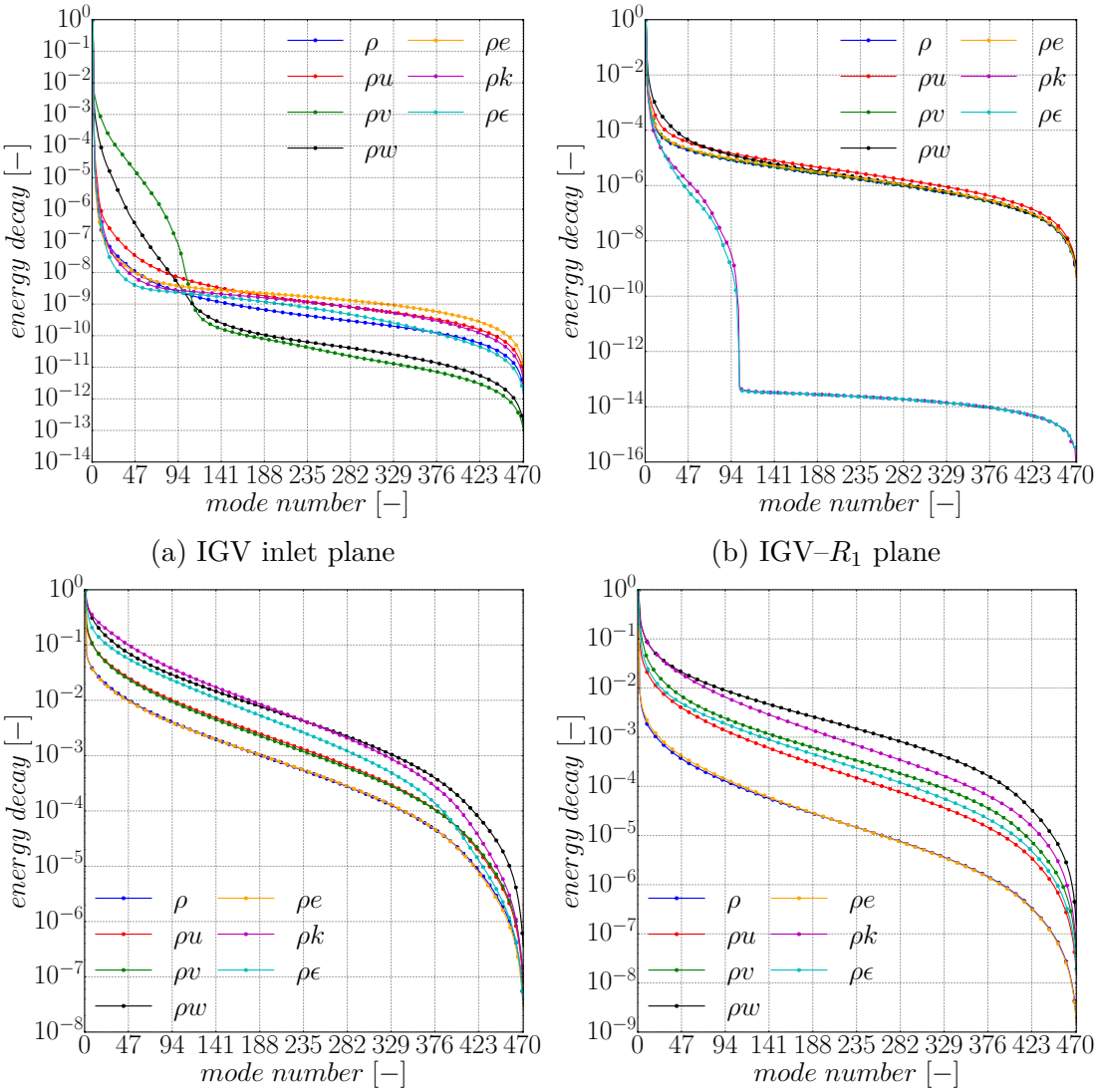

(a) IGV inlet plane

(b) IGV–R_1 plane

(c) R_1–OGV plane

(d) OGV outlet plane

Figure 8.2: Energy decay of the POD bases $\mathbf{\Phi}_F$ associated to each conservative variable.

each other. Nevertheless, truncating the POD basis brings out much broader error for the multi-fidelity POD basis $\mathbf{\Upsilon}_M^{99\%}$ with respect to $\mathbf{\Psi}_M^{99\%}$. This can be explained by the fact that all "high-fidelity" information is kept in the first modes of $\mathbf{\Psi}_M$ whereas a part of it is diffused in the last modes of $\mathbf{\Upsilon}_M$ and thus not available anymore after truncation.

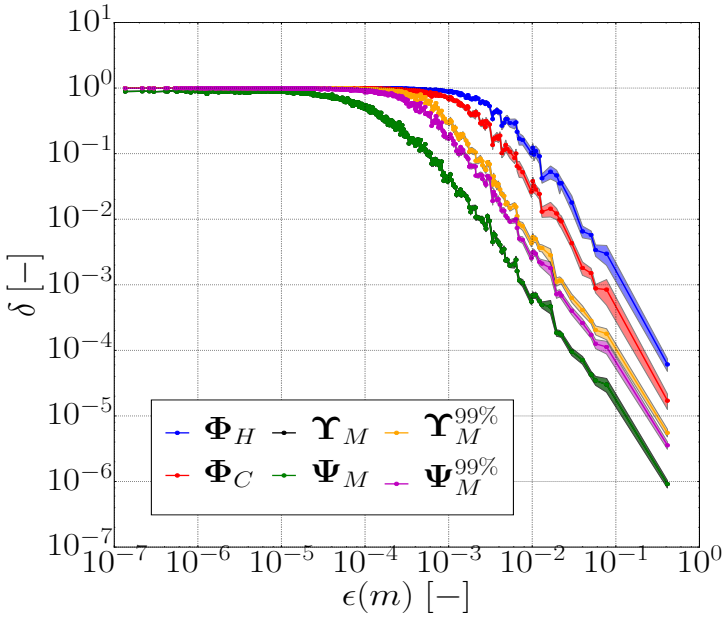

Figure 8.3: Evolution of δ for each mode of $\mathbf{\Phi}_F$ computed for ρw in the mixing plane R_1–OGV.

8.3 Comparison of surrogate models on the prediction of aerodynamic quantities

The previous section illustrated the improvement of the POD basis w.r.t. single-fidelity POD models as well as to the methodology in Mifsud, MacManus, et al., 2016. Once the surrogate models are built on the projection coefficient databases, the NIPOD prediction is available for any experiment in the design space $\mathcal{D}$. The presented results associated to NIPOD models are obtained with projection coefficients modeled by Radial Basis Function Networks (RBFN) tuned via their Leave-One-Out coefficient [Rippa, 1999]. As soon as multi-fidelity NIPOD is concerned, the projection coefficients are here modeled by additive multi-fidelity RBFN with tuned low-fidelity and bridge submodels. By applying the validation methodology in Section 8.1, the mean and standard deviation over 20 "independent" runs are computed for the Pearson's coefficient r [Pearson, 1895; Pearson, 1896] of high-fidelity versus predicted values of η_{is} and Π_{tot}. Table 8.2 presents the observed correlations for η_{is} throughout 1.5-stage of booster at on-design conditions and for different configurations (M_H, M_L).

The quality of POD bases appears clearly from the first block of numbers in Table 8.2. Considering all training ensembles yields a very good agreement (above 0.999 in mean value) between predicted and computed isentropic efficiency

k	Training configuration (M_H, M_L)					
	$(19, 95)$		$(38, 190)$		$(38, 380)$	
	$\bar{r}_\eta$	σ_{r_η}	$\bar{r}_\eta$	σ_{r_η}	$\bar{r}_\eta$	σ_{r_η}
$\boldsymbol{\Phi}_H\boldsymbol{\alpha}$	0.9987	1.0×10^{-3}	0.9998	1.2×10^{-4}	0.9998	1.3×10^{-4}
$\boldsymbol{\Phi}_C\boldsymbol{\alpha}$	0.9992	6.4×10^{-4}	1.0000	2.7×10^{-5}	1.0000	6.7×10^{-6}
$\boldsymbol{\Upsilon}_M\boldsymbol{\alpha}$	1.0000	5.4×10^{-6}	1.0000	1.2×10^{-7}	1.0000	1.2×10^{-8}
$\boldsymbol{\Psi}_M\boldsymbol{\alpha}$	1.0000	5.4×10^{-6}	1.0000	1.2×10^{-7}	1.0000	1.2×10^{-8}
$\boldsymbol{\Phi}_H\tilde{\boldsymbol{\alpha}}$	0.153	2.0×10^{-1}	0.180	2.1×10^{-1}	0.174	1.8×10^{-1}
$\boldsymbol{\Phi}_C\tilde{\boldsymbol{\alpha}}$	0.178	1.6×10^{-1}	0.250	1.1×10^{-1}	0.260	1.1×10^{-1}
$\boldsymbol{\Upsilon}_M\tilde{\boldsymbol{\alpha}}$	0.3551	2.5×10^{-2}	0.381	3.9×10^{-3}	0.462	7.2×10^{-4}
$\boldsymbol{\Psi}_M\tilde{\boldsymbol{\alpha}}$	0.3553	10.0×10^{-3}	0.392	1.6×10^{-3}	0.482	2.9×10^{-4}
$\tilde{\eta}_H^{RBF}$	0.151	1.9×10^{-1}	0.175	2.2×10^{-1}	0.168	1.8×10^{-1}
$\tilde{\eta}_C^{RBF}$	0.176	1.6×10^{-1}	0.244	1.1×10^{-1}	0.253	1.2×10^{-1}
$\tilde{\eta}_M^{CoK}$	0.196	1.7×10^{-1}	0.288	1.4×10^{-1}	0.563	9.8×10^{-4}

Table 8.2: High-fidelity to modeled isentropic efficiency correlations r_η^k over the validation DoE $\boldsymbol{\Theta}_V$

(this observation being confirmed for total-to-total pressure ratio, the associated numerical values are hidden in Table 8.3). The increase in the number of training points tends to improve the predictability of all models as shown by the increase in mean values $\bar{r}_\eta$ with couples (M_H, M_L). Despite the good quality of all POD bases, one can also observe a slight jump in mean correlations related to the proposed multi-fidelity NIPOD model w.r.t. both NIPOD based models and data fitting regressions. This trend seems stable for every couple (M_H, M_L) except for the multi-fidelity co-Kriging model able to fill in the gap with multi-fidelity NIPOD for the "richest" training ensemble, as shown on the last line of $\bar{r}_\eta^{(38,380)}$ in Table 8.2. The multi-fidelity approaches also present the smallest variances σ_{r_η} in Table 8.2, w.r.t. the 20 "independent" runs mentioned earlier.

The Table 8.3 shows that conclusions drawn from η_{is} (Table 8.2) also hold for Π_{tot}, the other quantity of interest of the problem at hand. One can see that the co-Kriging model predictivity is increasing more rapidly with the training ensemble size for Π_{tot} than for η_{is}. This situation can be explained by the relative easiness to model Π_{tot} w.r.t. η_{is}, which can also be observed from the fidelity analysis on Fig. 7.9. It is also interesting to note that multi-fidelity POD based models seem to better capture the correlations between quantities of interest. As stressed in the introduction, Data Fitting Surrogate Models (DFSMs) usually treat each

quantity of interest independently, whereas POD based models work at the full-field simulation level. Therefore, scalar quantities derived from a single POD-based model are all integrated from the same physical response, potentially yielding an increased coherency between modeled quantities. This remark is illustrated by the important difference between $\bar{r}_\Pi(\tilde{\Pi})$ and $\bar{r}_\eta(\tilde{\eta})$ with respect to differences between $\bar{r}_\Pi(\boldsymbol{\Upsilon}\tilde{\boldsymbol{\alpha}})$ and $\bar{r}_\eta(\boldsymbol{\Upsilon}\tilde{\boldsymbol{\alpha}})$ on one hand, and $\bar{r}_\Pi(\boldsymbol{\Psi}\tilde{\boldsymbol{\alpha}})$ and $\bar{r}_\eta(\boldsymbol{\Psi}\tilde{\boldsymbol{\alpha}})$ on the other hand (see Tables 8.2 and 8.3). In the case of full-field models, the predictability of all the scalar quantities of interest is correlated by their derivation from a single full-field prediction, whereas in the case of DFSMs, each scalar quantity is modeled independently.

k	Training configuration (M_H, M_L)					
	$(19, 95)$		$(38, 190)$		$(38, 380)$	
	$\bar{r}_\Pi$	σ_{r_Π}	$\bar{r}_\Pi$	σ_{r_Π}	$\bar{r}_\Pi$	σ_{r_Π}
$\boldsymbol{\Phi}_H\tilde{\boldsymbol{\alpha}}$	0.158	2.4×10^{-1}	0.206	2.1×10^{-1}	0.201	1.1×10^{-1}
$\boldsymbol{\Phi}_C\tilde{\boldsymbol{\alpha}}$	0.189	1.6×10^{-1}	0.277	4.6×10^{-2}	0.297	5.1×10^{-2}
$\boldsymbol{\Upsilon}_M\tilde{\boldsymbol{\alpha}}$	0.369	1.8×10^{-2}	0.384	4.0×10^{-3}	0.460	6.1×10^{-4}
$\boldsymbol{\Psi}_M\tilde{\boldsymbol{\alpha}}$	0.369	5.7×10^{-3}	0.391	2.0×10^{-3}	0.480	1.8×10^{-4}
$\tilde{\Pi}_H^{RBF}$	0.156	2.4×10^{-1}	0.202	2.2×10^{-1}	0.196	1.1×10^{-1}
$\tilde{\Pi}_C^{RBF}$	0.187	1.7×10^{-1}	0.270	4.9×10^{-2}	0.290	6.0×10^{-2}
$\tilde{\Pi}_M^{CoK}$	0.207	1.9×10^{-1}	0.412	3.9×10^{-2}	0.593	2.5×10^{-8}

Table 8.3: High-fidelity to modeled total-to-total pressure ratio correlations r_Π^k over the validation DoE $\boldsymbol{\Theta}_V$

Figure 8.4 illustrates the improvement of secondary flows prediction in the OGV outlet plane. It is important to note that the validation experiment on Fig. 8.4 is chosen representative of mean values in Table 8.2 at $(M_H, M_L) = (38, 190)$.

Comparing Figures 8.4b and 8.4a, we can observe that, as illustrated on Fig. 7.8, the intensity of secondary flows is reduced by mesh coarsening (highlights A, B and C). As single-fidelity NIPOD (see Fig. 8.4c) is trained only with high-fidelity snapshots, the mainstream intensity of ρw is increased (highlight B) with respect to Fig. 8.4d. Nevertheless we can see that adding low-fidelity information helps capturing new patterns as illustrated on Fig. 8.4d, where low-fidelity experiments presenting the same type of near hub behavior allow for capturing the low-ρw area in highlight C.

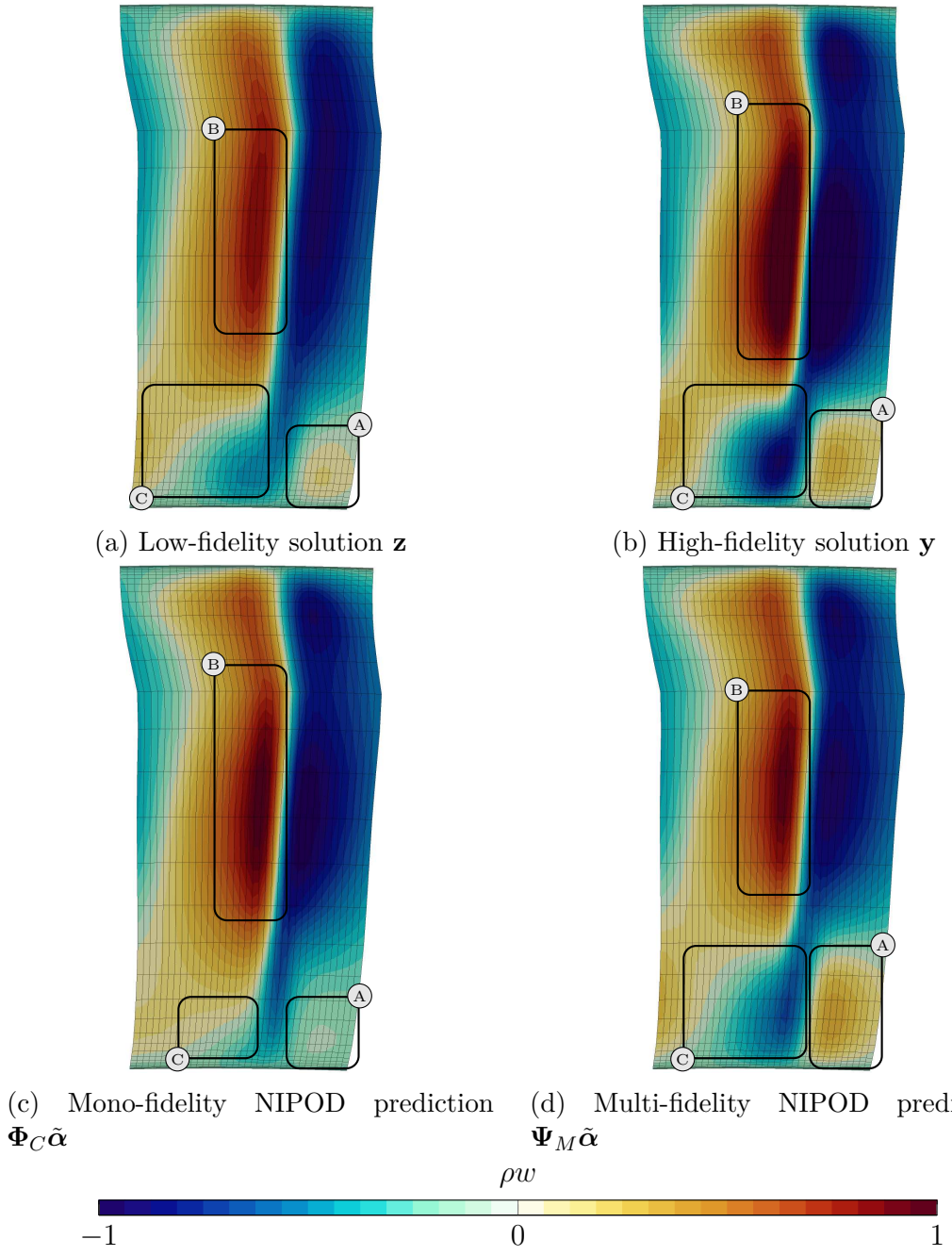

(a) Low-fidelity solution $\mathbf{z}$

(b) High-fidelity solution $\mathbf{y}$

(c) Mono-fidelity NIPOD prediction $\mathbf{\Phi}_C\tilde{\boldsymbol{\alpha}}$

(d) Multi-fidelity NIPOD prediction $\mathbf{\Psi}_M\tilde{\boldsymbol{\alpha}}$

Figure 8.4: Comparison of ρw distribution in the OGV outlet plane for one specific experiment of the validation DoE $\mathbf{\Theta}_V$.

Figure 8.5 presents the dimensionless error of relative helicity in the OGV outlet plane. Relative helicity is defined as the scalar product of velocity ($\overrightarrow{V}$)

and vorticity ($\overrightarrow{\Omega} = \nabla \times \overrightarrow{V}$), $H_{rel} = \dfrac{\overrightarrow{\Omega} \cdot \overrightarrow{V}}{|\overrightarrow{\Omega}| \cdot |\overrightarrow{V}|}$, and indicates streamwise oriented vortical motion [Colombo, 2011]. As explained in Moore et al., 1987, streamwise oriented vortices tend to dissipate kinetic energy to heat yielding an increase in stage losses.

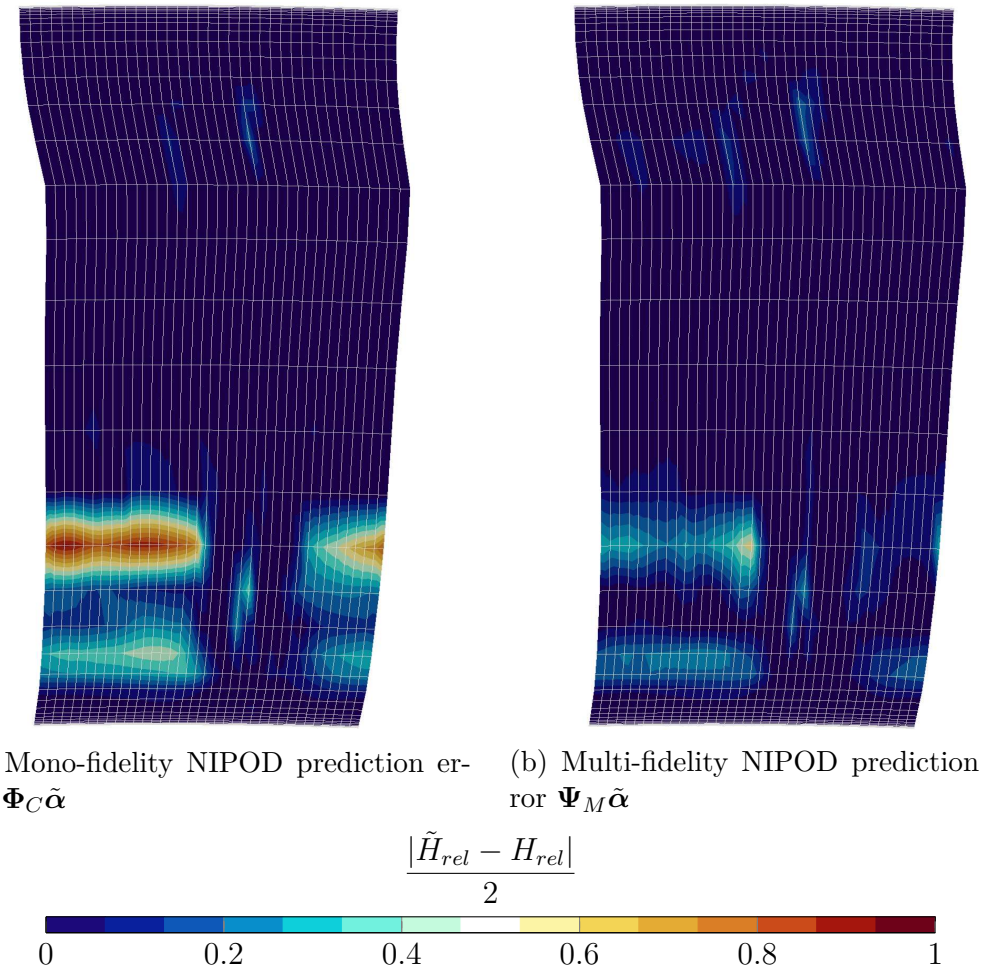

(a) Mono-fidelity NIPOD prediction error $\boldsymbol{\Phi}_C\tilde{\boldsymbol{\alpha}}$

(b) Multi-fidelity NIPOD prediction error $\boldsymbol{\Psi}_M\tilde{\boldsymbol{\alpha}}$

Figure 8.5: Comparison of adimensionalised error of relative helicity in the OGV outlet plane for one specific experiment of the validation DoE $\boldsymbol{\Theta}_V$.

Figure 8.5b shows a reduction of the relative helicity error below 30%-span with respect to Fig. 8.5a. We can speculate that the improved capture of losses generating phenomena associated to relative helicity distribution explains the increase in overall isentropic efficiency observed in Table 8.2.

8.4 Discussion and groundwork for rotor optimization

The presented results stress out the ability of the proposed methodology to reduce the prediction error w.r.t. single-fidelity DFSMs that are as demanding in terms of training computational cost. The predictability of the proposed NIPOD model is shown comparable to widely used co-Kriging models but avoids a training cost linearly increasing with the number of scalar quantities of interest, which justifies its capability to drive an EA-based optimization towards interesting designs. The presented results are obtained with very low DoE size to design space dimensionality ratios and reveal an acceptable simulated to modeled performance correlation coefficients also inciting its usage in the remainder of this chapter. Nevertheless, some properties of the snapshot definition given in Section 8 are changed in the next chapter in order to better capture the most impacting parameters for the optimization. The previous low- and high-fidelity snapshots are extracted from the mixing planes, in order to avoid any interpolation scheme for the snapshot construction. To reduce the impact of diffusion of coarse mesh cells close to the mixing planes, we move the post-treatment planes closer to the rotor blade. The impact of this diffusion can be observed by computing an ANalysis of VAriance (ANoVA) [Pearce, 1992; Sobol, 2001]. Figure 8.6 shows the increase of high order correlations when increasing the distance between the post-processed planes. The higher diffusion caused by coarser mesh cells close to the mixing planes tends to confuse the link between design parameters and outputs.

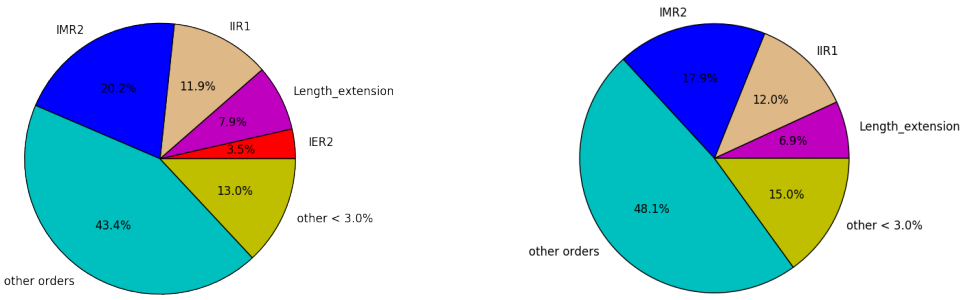

(a) ANoVA computed from interpolated planes

(b) ANoVA computed from $R1$-mixing planes

Figure 8.6: RBF based ANoVA of rotor's pressure ratio.

Figure 8.7a illustrates the difference between former and closer planes. For the previously introduced post-processing plane, no interpolation of the solution was required to extract the snapshots. In the present case, a $3D$-interpolation of the solution is needed. To keep the topology of the interpolated solution, the

extracted nodes are linearly interpolated in the initial structured grid. Once the post-processed plane is discretized linearly as illustrated on Fig. 8.7b, the solution is interpolated on the newly defined discretization thanks to the algorithm *cKDTree* [Maneewongvatana and Mount, 2001] implemented in the python library *SciPy* [E. Jones et al., 2001–].

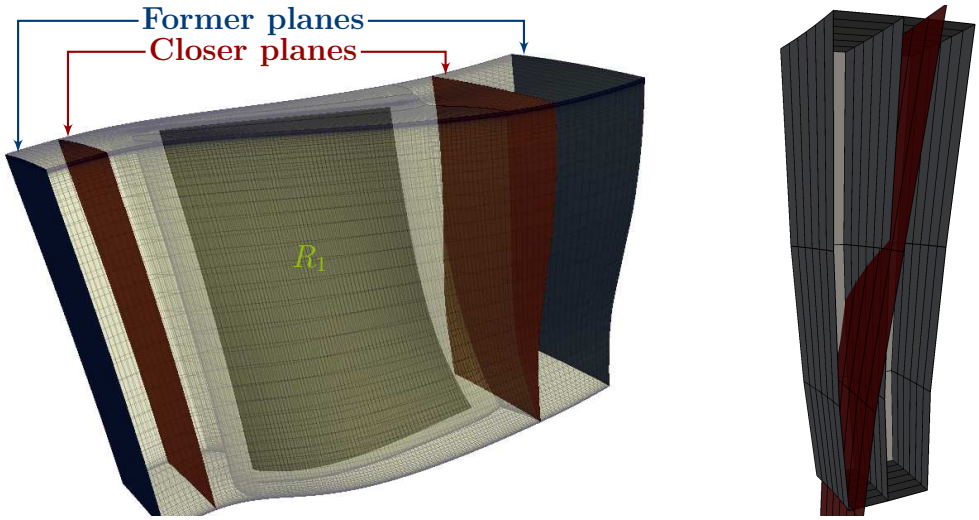

(a) R_1 surrounding blocks with former and closer post-processing planes

(b) Linear interpolation of the low-fidelity mesh on a x-fixed plane

Figure 8.7: Difference between former and new post-processing planes and interpolation procedure.

It is important to note that the discretization topology in the post-processing planes remains unchanged.

Chapter 9

$3D$-rotor optimization

This chapter gives results obtained on the design of the presented 1.5-stage booster with the Multi-Fidelity NIPOD (MFNIPOD) assisted optimization framework introduced in Chapter 6. In Section 9.1, we primarily compare the capacity given by the low- and high-fidelity levels of simulation to optimize the considered blade row and its hub endwall. Optimized geometries obtained from MFNIPOD and Radial Basis Function Networks (RBFNs) assisted optimizations are then compared in Section 9.2. Analysis of the flow features observed on both the reference and optimized geometries are given, as well as their link to the associated deformations. In order to put the presented results into perspectives, Section 9.3 compares Computational Fluid Dynamics (CFD) of the reference geometry as estimated by two different turbulence models from the literature.

Two operating points are considered, the design point and a second point close to numerical stall (hereafter called "stall" for simplicity). The optimizations tend to maximize the isentropic efficiency (η_{is}) on design while ensuring a certain total-to-total pressure ratio (Π_{tot}) both on- and off-design as well as ensuring a certain on-design inlet massflow:

- Objectives
  1. η on-design $\rightarrow$ MAXIMIZE
- Constraints
  1. on-design $\Pi_{P_t} \geq$ on-design $\Pi_{P_t}^{ref}$
  2. off-design $\Pi_{P_t} \geq$ off-design $\Pi_{P_t}^{ref}$
  3. on-design $\dot{m}_{in} \geq$ on-design $\dot{m}_{in}^{ref}$

A large DoE with high-fidelity computations is primarily evaluated to assess how intricate the problem at hand is. As expected, the parameters controlling radial deformation as well as the amplitude of axial stacking deformation for the blade are contributing the most in performances.

9.1 High- and low-fidelity driven RBFN assisted optimizations

To first evaluate the capability of the low-fidelity to drive the optimizations, two independent optimizations based on either high- or low-fidelity simulations are run. For all computed experiments during the low-fidelity driven optmization, the high-fidelity solutions of new points are also computed to be able to compare the performances attained at each iteration. The starting DoE associated to these optimizations is composed of 500 Latinized Centroidal Voronoï Tesselation (LCVT) points yielding 250 ($\approx 13 \times \text{card}(\mathcal{D})$) converged experiments.

Scalar quantity	Design point	Stall point
η	4.1×10^{-5}	9.7×10^{-5}
Π_{Pt}	9.4×10^{-6}	4.8×10^{-5}
$\dot{m}_{in}$	9.9×10^{-6}	4.9×10^{-5}

Table 9.1: Correlation coefficient (r) between low- and high-fidelity estimated performances ($1 - r$ values).

Despite very high correlation coefficients between low- and high-fidelity estimated performances, as illustrated in Table 9.1, low-fidelity cost functions would lead to degenerated optimization as shown on Fig. 9.1. It is important to keep in mind that both HF-driven and LF-driven optimizations are starting from the same DoE, meaning that the low-fidelity cost function is not able to properly rank the initial training ensemble. Indeed, rankings associated to low- and high-fidelity functions yield different best candidates. This indicates that either the low- to high-fidelity on-design isentropic efficiency transfer function is not monotonic, or that the low- and high-fidelity definitions of the constraints drive the optimizer towards different regions in the design space.

One can observe, on Figures 9.2 and 9.3, the hub profiling scaled by hub pitch angle (s) and blade axial sweep drawn respectively by LF- and HF-driven optimizations.

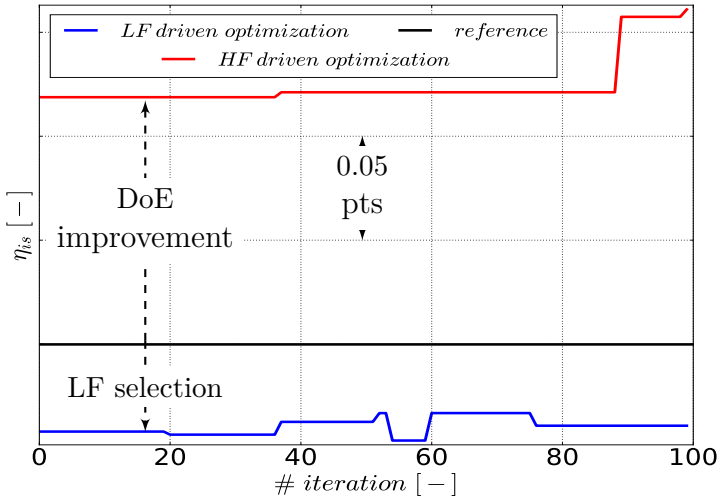

Figure 9.1: Comparison of low- and high-fidelity driver for on-design isentropic efficiency optimization.

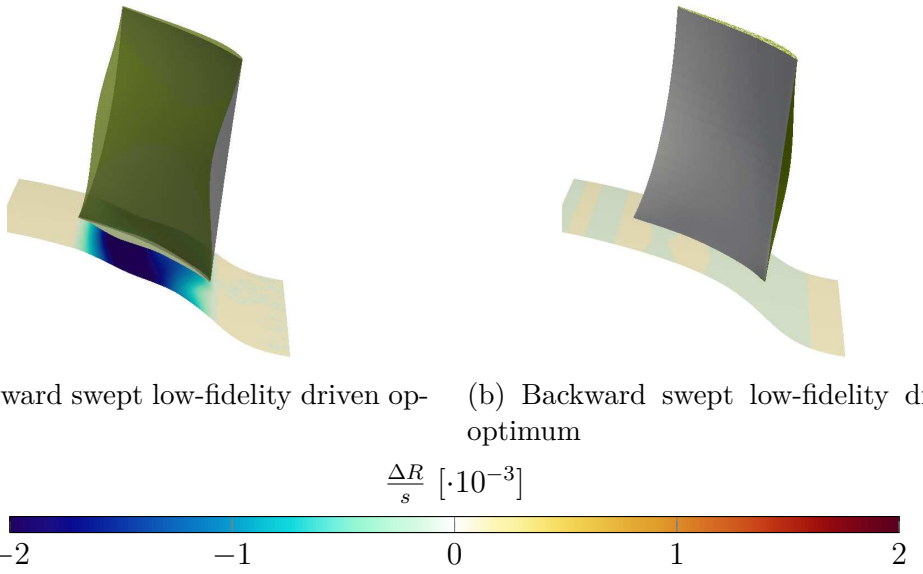

(a) Forward swept low-fidelity driven optimum

(b) Backward swept low-fidelity driven optimum

Figure 9.2: Hub profiling and blade sweep deformation of two low-driven optima (Reference blade in grey).

As expected, optimizations tend to limit the flow acceleration on the suction side by locally reducing the platform elevation in the Trailing Edge (TE) vicinity (see Fig. 9.4). The pattern observed in Lepot et al., 2011 is also present on the high-fidelity optima where a digging along the suction side in the Leading Edge (LE) vicinity and close to the rear pressure side area, and bumps appear on the

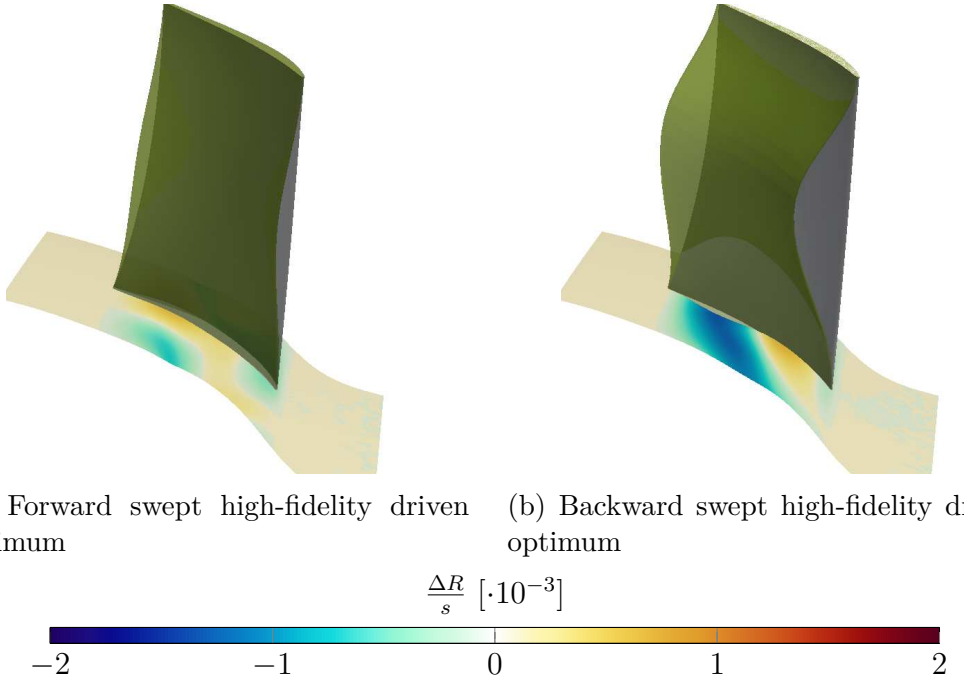

(a) Forward swept high-fidelity driven optimum

(b) Backward swept high-fidelity driven optimum

Figure 9.3: Hub profiling ($\Delta R/s$) and blade sweep deformation of two high-fidelity driven optima (Reference blade in grey).

pressure side close to the LE and at the rear part of the suction side. This pattern associated to forward sweeping is responsible for an increase in the on-design isentropic efficiency as it tends to increase the massflow rate in mid-span sections, as shown on Fig. 9.5.

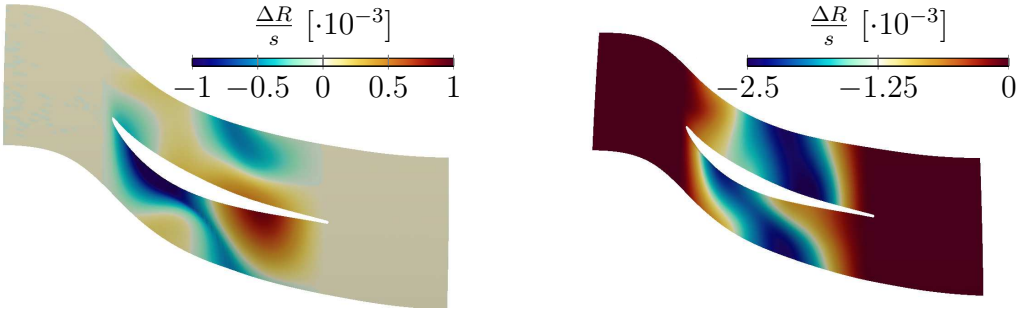

(a) Forward swept high-fidelity driven optimum

(b) Forward swept low-fidelity driven optimum

Figure 9.4: Comparison of low- and high-fidelity hub profiling patterns ($\Delta R/s$).

One can notice, from Fig. 9.4, that the low-fidelity driver tends to apply, in a crude way, the same hub profiling that is proposed by high-fidelity optimization. Keeping in mind the impact of mesh coarsening, low-fidelity simulations are made unable to properly evaluate the characteristics of the boundary layer, which is furthermore modified by the non-axisymmetric endwall contouring.

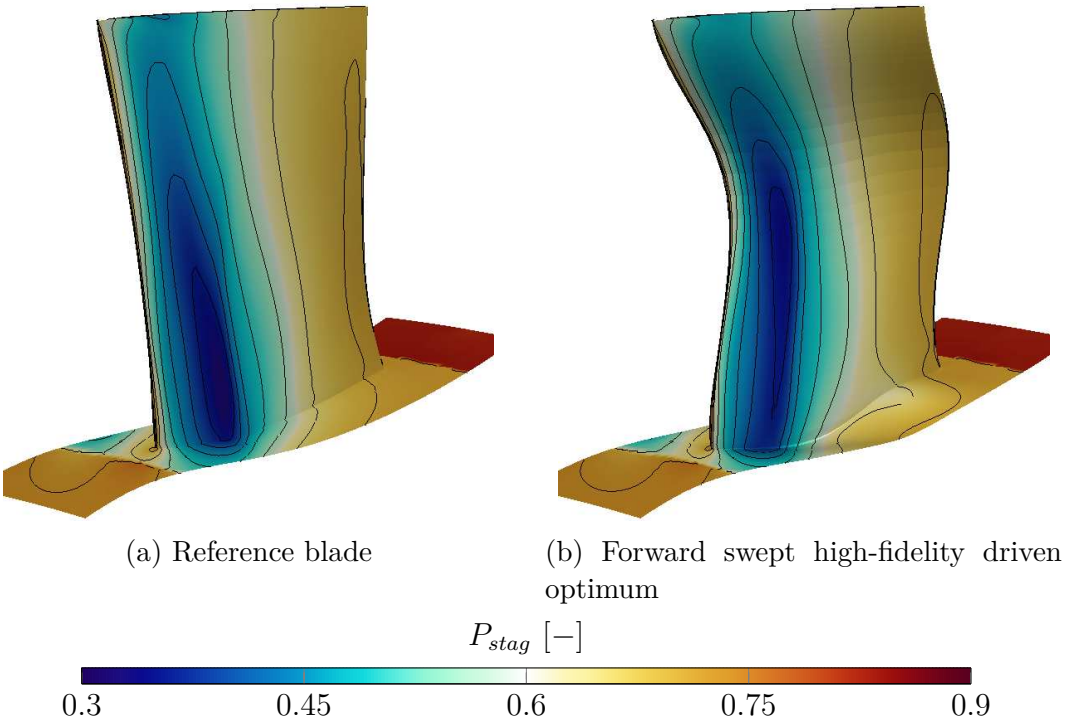

(a) Reference blade

(b) Forward swept high-fidelity driven optimum

Figure 9.5: Normalized total pressure at design point.

Even though both low- and high-fidelity evaluation chains target the capture of the same physics and despite very high low-to-high correlation factors (see Fig. 7.9), the low-fidelity information reveals itself too inaccurate to drive properly the optimizer towards the interesting zones in the design space. Any multi-fidelity optimization targets directly this kind of problems where the high-fidelity information is needed to correctly rank experiments in the design space, but its prohibitive computational cost makes the required number of evaluations for large and accurate view of the terrain shape unaffordable.

9.2 MFNIPOD assisted optimization

In this section, the surrogate model proposed in Section 4.1, primarily integrated into an Surrogate-Based Optimization (SBO) framework (as in Section 6.1), is used to the optimization of the presented booster application. As mentioned in Section 6.1, every selected enrichment location is both evaluated at low- and high-fidelity levels, as soon as multi-fidelity optimization is concerned.

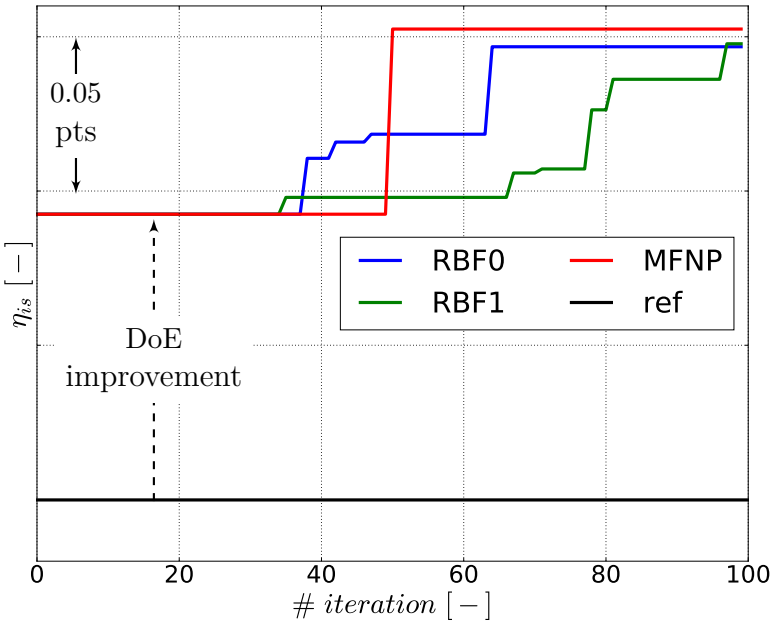

Figure 9.6: History of convergence of RBFN and MFNIPOD assisted optimizations of the on-design isentropic efficiency.

Figure 9.6 shows the convergence history of two independent RBF-assisted optimizations on one hand and a multi-fidelity non-intrusive POD-assisted optimization on the other. The single-fidelity optimizations are initialized with a high-fidelity DoE containing 240 experiments, of which 125 are successfull. The multi-fidelity optimization is associated to a multi-fidelity DoE containing 190 high-fidelity experiments, of which 100 are successfull, and 500 low-fidelity experiments, including 250 successfull computations. As previously mentioned (Section 7.4), the DoE sizes used make the single- and multi-fidelity samplings comparable in terms of computational cost. In order to reduce the bias introduced by comparing single- and multi-fidelity strategies, the best (optimization objective) point known at high-fidelity level from the DoE phase is the same for all the optimizations, as illustrated by the superimposed curves for the first

30 iterations on Fig. 9.6. With respect to RBF-assisted optimizations, the multi-fidelity non-intrusive POD-assisted optimization showed itself a bit longer to detect improved efficiency areas but spotted a highly efficient experiment after 50 iterations whereas RBF-based optimizations required at least 65 to reach a comparable level of efficiency. The optimized configurations satisfied all the aforementioned constraints, which are nevertheless responsible for the limitation of the on-design isentropic efficiency.

The optimized geometries associated to the MFNIPOD and RBF1-assisted optimizations (see Fig. 9.6) are here compared in terms of aerodynamic properties and of shape deformation. Here, the RBF1-assisted optimization is chosen as a higher efficiency is obtained after 100 iterations with respect to the RBF0-assisted optimization.

9.2.1 Flow field comparison

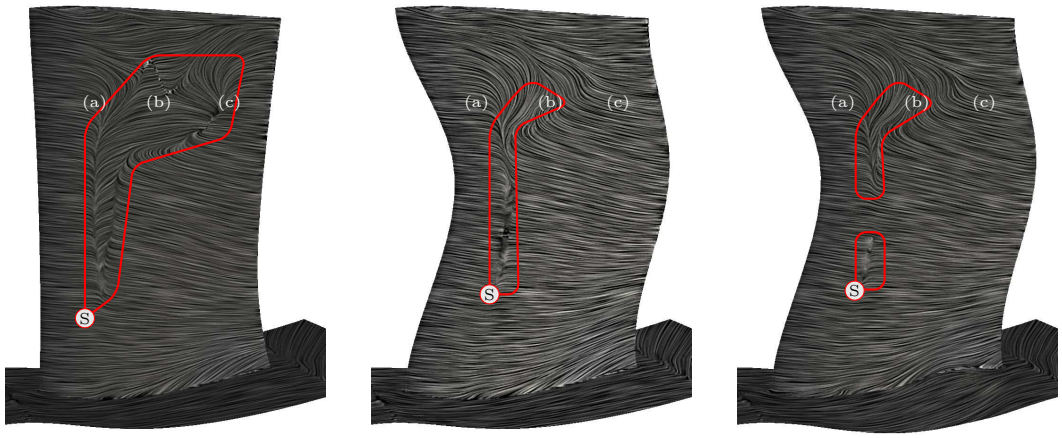

(a) Reference geometry (b) MFNIPOD-Optimized geometry (c) RBF1-Optimized geometry

Figure 9.7: Comparison of oil traces on the suction side of the rotor.

Figure 9.7 gives a comparison of the "skin motion" on the reference and optimized rotor blades. Considering viscous flows, the no-slip condition gives a cancelling velocity at a solid boundary. The oil traces are therefore computed via *line integral convolution* [Cabral and Leedom, 1993] from the friction vector on the blade. The reduction of the recirculation area at 65%-span is clearly observable on the optimized geometries. The reference geometry presents a shock-induced separation bubble stretching from 35%-span and 20%-chord to 80%-span and

60%-chord. An important loss-generating area is also visible between 60%- and 80%-span, due to the interaction between the aforementioned shock-induced separation bubble and the tip leakage flow. As shown in Shi and Fu, 2013, this interaction tends to stretch out the separation bubble and further increase the losses generated by the reference geometry; local reattachments and separations of the fluid are also probably visible at the top limit of the highlighted area (red box on Fig. 9.7a). *A contrario*, the optimized blades present reduced separated zones.

As the flow goes through the rotor passage, it is decelerated and boundary layer's kinetic energy is lowered on the blade skin. Figure 9.8 shows the skin velocity profiles at 75%-span of the rotor blade. The probe locations associated to the skin velocity profiles at 20%-, 50%-, and 80%-chord are respectively highlighted by marks (a), (b), and (c) on Fig. 9.7. One can distinguish, on Fig. 9.8c for example, the increased boundary layer thickness on the reference blade with respect to optimized geometries. One can also clearly see the reversed flow at 50%-chord on Fig. 9.8b, highlighting the aforementioned separation bubble.

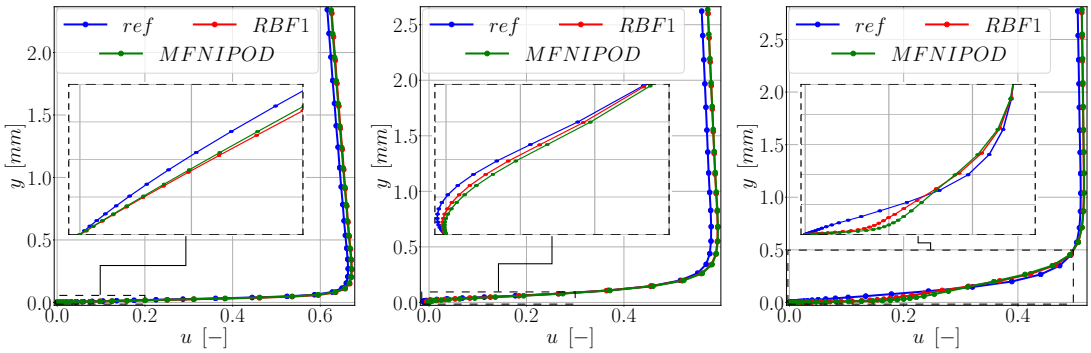

(a) 20%-chord (b) 50%-chord (c) 80%-chord

Figure 9.8: Comparison of skin velocity profiles at 75%-span on reference and optimized rotor blades.

Figure 9.9 shows the normalized streamwise vorticity $\Omega_s = \frac{\overrightarrow{\Omega} \cdot \overrightarrow{V}}{|\overrightarrow{V}|}$ as an indicator of the development of tip leakage vortices observed on the reference and optimized blades. Two colormaps are used to distinguish between negative and positive oriented vortices, the scales are saturated and the opacity is decreased for low magnitudes of streamwise vorticity in order to focus on the vortex growth. The development of tip leakage vortices appears in agreement with the insight given in Y. Wu and Chu, 2007. As illustrated in Shi and Fu, 2013, two iso-oriented

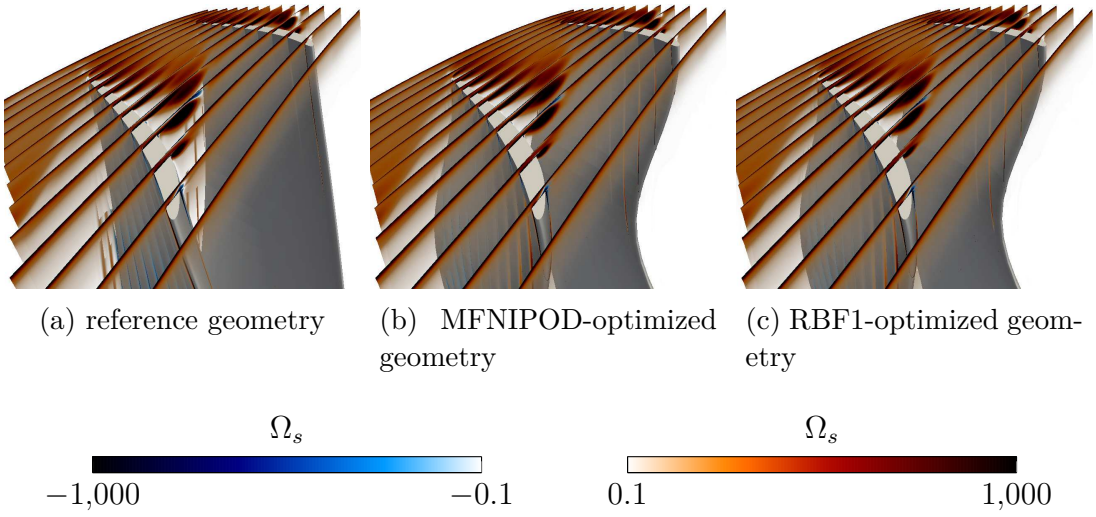

(a) reference geometry (b) MFNIPOD-optimized geometry (c) RBF1-optimized geometry

Figure 9.9: Comparison of tip leakage vortices

(orange colormap on Fig. 9.9) vortices are created in the tip leakage, the first one starts right after the leading edge and is advected and mixed with the second vortex after 70%-chord approximately. We can also see a counter-rotating vortex (blue colormap on Fig. 9.9) created around 20%-chord, due to tip leakage sheet scratching the low-momentum boundary layer on the casing endwall. This phenomenon is called interaction between the leakage flow and the annulus wall boundary layer in Lakshminarayana et al., 1995. These observations seem in accordance with the literature [Shi and Fu, 2013; Y. Wu and Chu, 2007]. We can notice from Fig. 9.9 that the rise of the tip leakage vortex core is delayed by the forward stacking deformation performed on the two optimized blades. It occurs despite the zero displacement condition applied to the extreme sections of the rotor blade.

The secondary flows primarily targeted by the utilized parametrization are the vortices located near the hub endwall of the rotor's platform as presented on Fig. 2.3b. Figure 9.10 presents a comparison of the hub corner stall observed on the reference and optimized geometries. The overturning of near hub generated streamlines explained in Section 7.1 is observable on the red stream tubes (OT mark) on Fig. 9.10. It appears clearly reduced on the optimized geometry on Fig. 9.10c as indicated by the lower normalized streamwise vorticity Ω_s. The lowering of hub sections loading is also represented by the shock onset on the suction side of the blades, which is highlighted by the normalized axial derivative of the density $\frac{1}{\rho} \cdot \frac{\partial \rho}{\partial x}$. Comparing reference and optimized geometries, one can

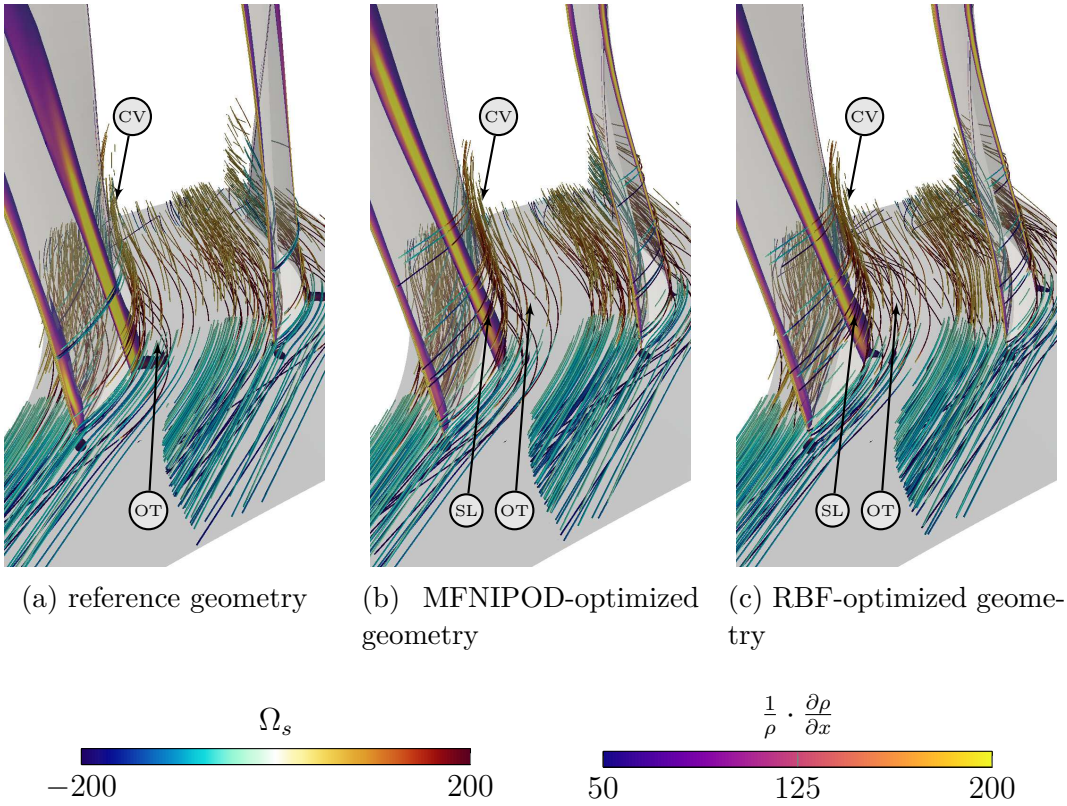

(a) reference geometry (b) MFNIPOD-optimized geometry (c) RBF-optimized geometry

Figure 9.10: Comparison of Hub Corners

observe the change in massflow distribution by the increase in the shock intensity on mid-span sections of the optimized blades, and its reduction on hub sections and endwall. The shock-induced increase in blade's boundary layer thickness is also noticeable as the normalized streamwise vorticity of streamlines on the blade brutally increases across the shock (SL mark). At the rear part of the channel, one can see the development of the corner vortex (CV mark). This phenomenon is overwhelmed on the RBF1-optimized geometry as illustrated by the CV mark on Fig. 9.7c.

9.2.2 Comparison of shape deformations

As illustrated on Figures 9.7 and 9.11, very similar forward swept configurations are here proposed by both the MFNIPOD- and RBF-assisted optimizations. As illustrated on Figures 9.7 and 9.10, this kind of deformations tends to change the spanwise massflow distribution. By decreasing the loading on hub sections, the hub-corner stall is slightly reduced as the cross-flow and skewed inlet flow effects

are attenuated by a diminished suction (see Fig. 2.3b). Figure 9.11 gives the blade shape deformation as the ratio between axial stacking deviation from the reference geometry over the mean chord length $\frac{\Delta X}{c}$. The similarity between the two optimized geometries appears clearly, as well as the amplitude of deformation with respect to the reference axial stacking shown in transparent grey on Fig. 9.11.

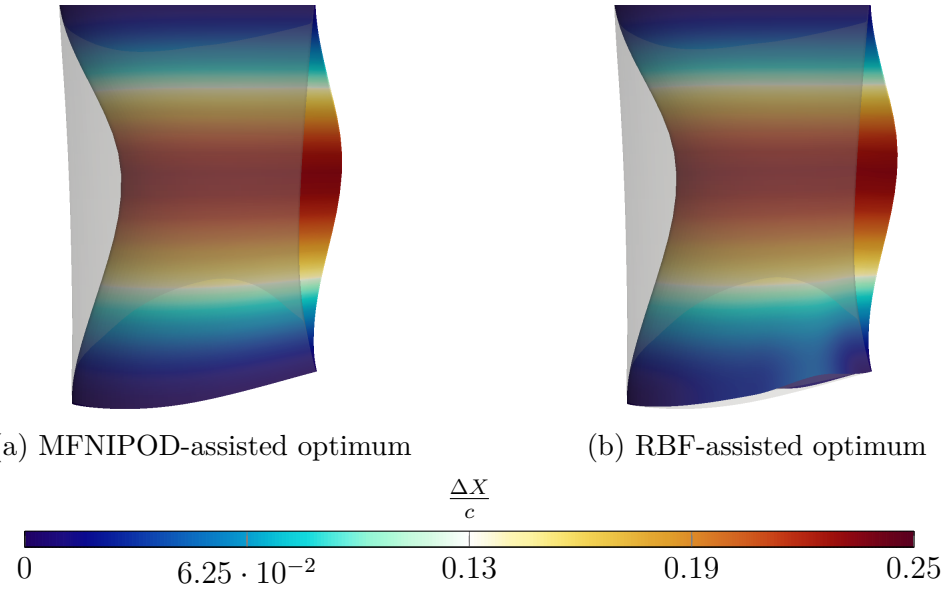

(a) MFNIPOD-assisted optimum (b) RBF-assisted optimum

Figure 9.11: Mean chord-scaled stacking deformation ($\frac{\Delta X}{c}$) w.r.t. reference blade.

Whereas the axial stacking deformation proposed by MFNIPOD- and RBF-assisted optimizations are very close to each other, the amplitude of the platform deformation is very different. Only the RBF based optimum presents a non negligible deformation as shown on Fig. 9.12.

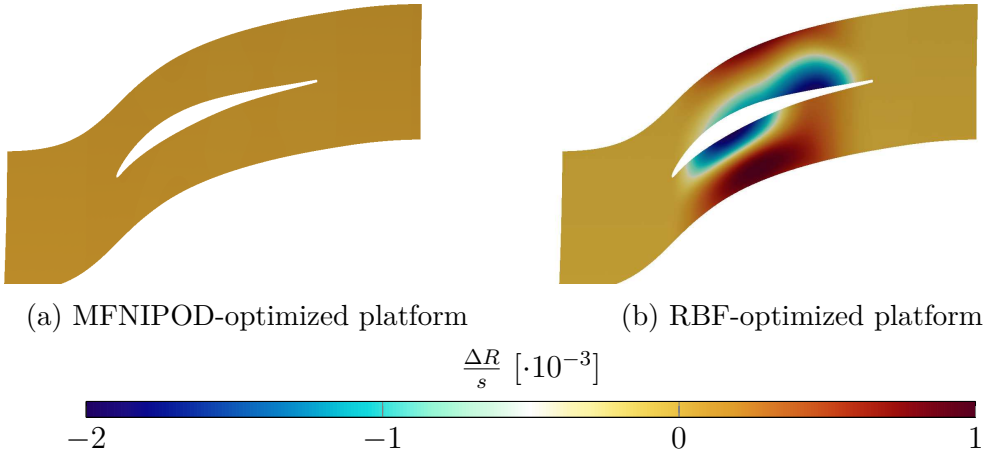

(a) MFNIPOD-optimized platform (b) RBF-optimized platform

Figure 9.12: Comparison of pitch-scaled platform deformation for MFNIPOD- and RBF-assisted optima.

9.3 Discussion on numerical results

In their study, Rodi and Scheuerer, 1986 show that the classical $k-\epsilon$ turbulence model can be seriously in error when dealing with decelerated flows. It has also been demonstrated in Chambers and Wilcox, 1977 that the curvature has no impact on the transport equation of the turbulent dissipation rate per unit energy ω, whereas it should be taken into account in the turbulent dissipation rate equation ϵ. The same difference holds when dealing with surface-roughness effects in the viscous sublayer region, where viscous damping functions are needed for the integration of the model [Wilcox, 1993]. In addition, the $k-\omega$ turbulence model is known to be able to accurately predict the defect-layer structure under all pressure gradient condition [Wilcox, 1993]. Nevertheless, one of its disadvantages is related to its sensibility to turbulent freestream conditions as demonstrated in Menter, 1992. For these reasons, and as the flow is mainly decelerated across axial compressor stages, the turbulence model proposed by Menter, 1993; Menter, 1994 has been widely used in the compressor community [Hellsten, 1998; Dragan et al., 2015].

In this section, we propose to evaluate the discrepancies of the reference geometry as simulated with the $k-\epsilon$ model from one hand and the $k-\omega$ model on the other. Figure 9.13 presents a comparison of the skin motions predicted by the two aforementioned turbulence models associated with the high-fidelity mesh. The discretization scheme is conserved as described in Section 7.3, as well as the mesh topology. The $k-\omega$ turbulence model is associated with the Shear-Stress Transport (SST) correction proposed by Menter et al., 2003.

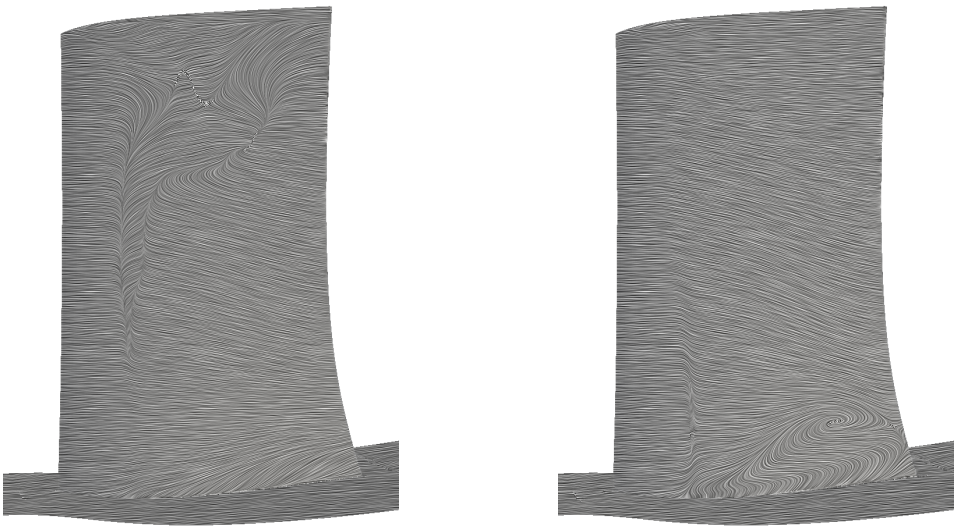

(a) Launder-Sharma's $k-\epsilon$ turbulence model [Launder and Sharma, 1974]

(b) Menter's $k-\omega$ SST turbulence model [Menter, 1994]

Figure 9.13: Comparison of oil traces on the reference geometry.

The features of the flow around the blade are totally different from one computation to the other. It appears that the massive separation on the blade skin observable on the initial simulation (Fig. 9.13a) has almost totally disappeared on the $k-\omega$ computation. This is in accordance with a commonly admitted drawback of the $k-\epsilon$ turbulence model in presence of strong adverse pressure gradient which states that this model tends to make the boundary layer separate faster in some cases. This behavior is related to the defect-layer problem and the production term of turbulent kinetic energy that should be constant in the sublayer zone, but is in the case of strong adverse pressure gradient increased by the $k-\epsilon$ model in a non-physical way. On the other hand, the relatively low intensity of the corner separation, initially observed on the $k-\epsilon$ computation, is contradicted by the $k-\omega$ SST simulation. It is important to keep in mind the parametrization involved in the optimization presented above. Targeting mostly the platform deformation and its impact on the corner stall development, the switch to the $k-\omega$ turbulence model could have strongly modified the shape of the optimized geometries. Keeping that in mind, the initial choice of the $k-\epsilon$ turbulence model is justified by the required coherency between former study in Lepot et al., 2011 that was started after a first validation of the reference computation against existing $k-\epsilon$ based technical data.

Conclusions and perspectives

This thesis develops and applies multi-fidelity optimization techniques that are broadly applicable to the design of any engineering system considering its physical behavior is assessable at different levels of fidelity. The focus is on turbomachinery applications that present complex flow features strongly impacting macro-scale indicators of the machine efficiency.

The developed methods tackled both the fusion of multi-level information and the online enrichment and Surrogate-Based Optimization (SBO) aspects. The work presented in this thesis spreads from analytical developments to industrial-scale applications, by way of efficient implementation within a pre-existing industrialized single-fidelity SBO tool.

With respect to methodologies, Part I presents the mathematical developements and justifications of the main contributions of this work in the frame of Proper Orthogonal Decomposition (POD) based modeling. The enrichment criterion proposed for Gappy-POD (GPOD) surrogate models in Chapter 5 can serve as error estimator for multi-fidelity strategies. Nevertheless, this kind of strategies hardly meets the industrial optimization needs if a low-fidelity evaluation is not instantaneous. This issue is addressed by the proposed POD based Multi-Fidelity Surrogate Model (MFSM) called Hierarchised Multi-Fidelity NIPOD (HMFNIPOD) and detailed in Chapter 4.

Part II pertains to the implementation of a Multi-Fidelity SBO (MFSBO) framework integrating the proposed HMFNIPOD surrogate models. An analytical example is given in Chapter 6 in order to benchmark futur full-field multi-fidelity methodologies on a problem we claim representative of features in turbomachinery design. The developed MFSBO is also tested on the constrained optimization of a $1.5D$-stage booster designed by $3D$-Reynolds Averaged Navier-Stokes (RANS) computations.

Chapter 8 validated the interest of the proposed methodology on an industrial-

scale problem. The predictability of the proposed surrogate model has been first evaluated on the estimation of the isentropic efficiency of a highly loaded rotor in a compressor stage, which is at the state-of-the-art in terms of daily optimization in engineering offices. The presented results, obtained from relatively low Design of Experiments (DoE) sizes, have shown a real potential for the proposed surrogate model to capture highly non-linear and localized features of the flow. The comparison of validation coefficients showed non-negligible improvements in the prediction of the isentropic efficiency over the design space.

Chapter 9 presented the optimization performed with the proposed HMFNIPOD-assisted optimization scheme introduced in Chapter 6. The increase in rotor's efficiency is shown comparable to that obtained from a more classical RBF-based optimization. By comparison with usual regressive models, the question of snapshot definition is of first importance. We showed for example a non-negligible impact of the selection of the post-treatment planes on the analysis of variances associated to the mapping between design parameters and responses. In the case presented in this chapter, the increase in the distance between the blade and the post-treatment planes makes the surrogate model more sensible to the numerical diffusion of both low- and high-fidelity models. This constraint is to be considered more carefully when dealing with POD based surrogate models as a fixed snapshot grid is usually preferred. A short analysis of the impact of the turbulence model has also been presented in this chapter in order to put the optimization results into the perspective of numerical model selection. Although this comparison is not likely to fondamentaly question the suitability of the proposed full-field MFSMs, it emphasizes the impact of the simulation tool selected for the engineering optimization, especially when dealing with physics as complex as turbulent flows.

To our best knowledge, full-field MFSMs is a relatively new field and only a very limited research proposes their use for the optimization of complex industrial systems. In order to answer more efficiently to the industrial challenges MFSBO tools have to face in the future, many potential research and developments can be carried out. The mentioned questions mainly concern the Multi-Fidelity NI-POD (MFNIPOD) framework as low-fidelity simulations in turbomachinery design are not suitable for intensive evaluation.

- No truncation has been used in the presented applications. As far as the author knows, this issue remains opened for both single and multi-fidelity POD models. In the case of MFNIPOD, this question is more stringent as the truncation of the high-fidelity basis $\mathbf{\Phi}$ should be done at the training step in order to relax the constraint on the low-fidelity enhancement.

- Classical Multi-Fidelity DFSMs (MFDFSMs) try to correct a low-fidelity surrogate with higher-fidelity information, whereas the HMFNIPOD starts capturing the physics in high-fidelity data before enhancing the basis with low-fidelity. This order of treatment could be questioned and investigated with its associated impact on the truncation strategy mentioned above.
- No fidelity level selection method is proposed for full-field MFSM. This constitutes the corner stone of a more efficient coupling between the surrogate model and the optimization algorithm composing the SBO tool.
- The proposed implementation requires the computation of the orthogonal space $\boldsymbol{Q}_2$ (Algorithm 1). In the case of fine discretizations the computational cost involved in the search of and operation on $\boldsymbol{Q}_2$ slows down the training of the surrogate model drastically.
- All the developments considered a unique design space $\mathcal{D}$ while different levels of fidelity can be associated to multiple levels of parametrization.

All these questions could greatly serve the dissemination of full-field multi-fidelity surrogate models into industrial optimization platforms and help to tackle other complex optimization problems.

Bibliography

Published References

Alexandrov, N. M., J. E. Dennis, R. M. Lewis, and V. Torczon (1998). "A trust-region framework for managing the use of approximation models in optimization". In: *Structural and Multidisciplinary Optimization* 15.1, pp. 16–23. ISSN: 1615-1488. DOI: 10.1007/BF01197433 (cit. on pp. 14, 84).

Alexandrov, N. M. and R. M. Lewis (2001). "An Overview of First-Order Model Management for Engineering Optimization". In: *Optimization and Engineering* 2.4, pp. 413–430. ISSN: 1573-2924. DOI: 10.1023/A:1016042505922 (cit. on p. 15).

Alexandrov, N. M., R. M. Lewis, C. R. Gumbert, L. L. Green, and P. A. Newman (2000). "Optimization with variable-fidelity models applied to wing design". In: *38th Aerospace Sciences Meeting and Exhibit*. American Institute of Aeronautics and Astronautics (AIAA). DOI: 10.2514/6.2000-841 (cit. on p. 17).

Alexandrov, N. M., E. Nielsen, R. M. Lewis, and W. Anderson (2000). "First-order model management with variable-fidelity physics applied to multi-element airfoil optimization". In: *8th Symposium on Multidisciplinary Analysis and Optimization*. American Institute of Aeronautics and Astronautics (AIAA). DOI: 10.2514/6.2000-4886 (cit. on p. 17).

Arsenyev, I., F. Duddeck, and A. Fischersworring-Bunk (2015). "Adaptive Surrogate-Based Multi-Disciplinary Optimization for Vane Clusters". In: *Volume 2C: Turbomachinery*. ASME International. DOI: 10.1115/gt2015-42164 (cit. on p. 22).

Audet, C. and J. E. Dennis (2006). "Mesh adaptive direct search algorithms for constrained optimization". In: *SIAM Journal on Optimization* 17.1, pp. 188–217. DOI: 10.1137/040603371 (cit. on p. 23).

Audouze, C., F. De Vuyst, and P. B. Nair (2009). "Reduced-order modeling of parameterized PDEs using time-space-parameter principal component analysis". en. In: *International Journal for Numerical Methods in Engineering* 80.8, pp. 1025–1057. ISSN: 00295981, 10970207. DOI: 10.1002/nme.2540 (cit. on p. 20).

Aulich, M. and U. Siller (2011). "High-Dimensional Constrained Multiobjective Optimization of a Fan Stage". In: *Volume 7: Turbomachinery, Parts A, B, and C*. ASME International. DOI: 10.1115/gt2011-45618 (cit. on p. 22).

Baert, L., C. Beauthier, M. Leborgne, and I. Lepot (2015). "Surrogate-Based Optimisation for a Mixed-Variable Design Space: Proof of Concept and Opportunities for Turbomachinery Applications". In: *Volume 2C: Turbomachinery*. ASME International. DOI: 10.1115/gt2015-43254 (cit. on p. 23).

Bahamonde, J. S., M. Pini, and P. Colonna (2016). "Active subspaces for the preliminary fluid dynamic design of unconventional turbomachinery". In: vol. 4, pp. 8572–8586 (cit. on pp. 15, 20).

Balabanov, V., B. Grossman, L. Watson, W. Mason, and R. T. Haftka (1998). "Multifidelity response surface model for HSCT wing bending material weight". In: Multidisciplinary Analysis Optimization Conferences. American Institute of Aeronautics and Astronautics. DOI: 10.2514/6.1998-4804 (cit. on pp. 17, 18, 39).

Bandler, J. W., R. M. Biernacki, S. H. Chen, P. A. Grobelny, and R. H. Hemmers (1994). "Space mapping technique for electromagnetic optimization". In: *IEEE Transactions on Microwave Theory and Techniques* 42.12, pp. 2536–2544. DOI: 10.1109/22.339794 (cit. on p. 19).

Bandler, J. W., Q. S. Cheng, S. A. Dakroury, A. S. Mohamed, M. H. Bakr, K. Madsen, and J. Søndergaard (2004). "Space Mapping: The State of the Art". In: *IEEE Transactions on Microwave Theory and Techniques* 52.1, pp. 337–361. DOI: 10.1109/tmtt.2003.820904 (cit. on p. 19).

Bellary, S. A. I. and A. Samad (2014). "Improvement of Efficiency by Design Optimization of a Centrifugal Pump Impeller". In: *Volume 2D: Turbomachinery*. ASME International. DOI: 10.1115/gt2014-25217 (cit. on p. 15).

Benamara, T., P. Breitkopf, I. Lepot, and C. Sainvitu (2016a). "Adaptive infill sampling criterion for multi-fidelity optimization based on Gappy-POD". In: *Structural and Multidisciplinary Optimization* 54.4, pp. 843–855. DOI: 10.1007/s00158-016-1440-3 (cit. on p. 7).

— (2016b). "Multi-fidelity extension to non-intrusive proper orthogonal decomposition based surrogates". In: *Proc. of the 7th European Congress on Computational Methods in Applied Sciences and Engineering, ECCOMAS 2016*. Vol. 2, pp. 4129–4145. DOI: 10.7712/100016.2098.9174 (cit. on p. 7).

— (2017). "LPC blade and non-axisymmetric hub profiling optimization using multi-fidelity non-intrusive POD surrogates". In: *Proc. of the ASME Turbo Expo 2017, ICOPE/GT 2017*. Vol. n.c. (accepted), n.c. DOI: n.c (cit. on p. 7).

Benamara, T., P. Breitkopf, I. Lepot, C. Sainvitu, and P. Villon (2017). "Multi-fidelity POD surrogate-assisted optimization: Concept and aero-design study".

In: *Structural and Multidisciplinary Optimization*, pp. 1–26. DOI: 10.1007/s00158-017-1730-4 (cit. on p. 7).

Biehler, J., M. W. Gee, and W. A. Wall (2015). "Towards efficient uncertainty quantification in complex and large-scale biomechanical problems based on a Bayesian multi-fidelity scheme". In: *Biomechanics and Modeling in Mechanobiology* 14.3, pp. 489–513. ISSN: 1617-7940. DOI: 10.1007/s10237-014-0618-0 (cit. on p. 19).

Bishop, C. M. (1995). *Neural Networks for Pattern Recognition*. Advanced Texts in Econometrics. Clarendon Press. ISBN: 9780198538646 (cit. on pp. 23, 29, 30, 83, 97).

Bistrian, D. A. and I. M. Navon (2016). "Randomized Dynamic Mode Decomposition for Non-Intrusive Reduced Order Modelling". In: *ArXiv e-prints*. arXiv: 1611.04884 [math.NA] (cit. on p. 20).

Booker, A. J., J. E. Dennis, P. D. Frank, D. B. Serafini, V. Torczon, and M. W. Trosset (1999). "A rigorous framework for optimization of expensive functions by surrogates". In: *Structural Optimization* (cit. on p. 15).

Bouhlel, M. A., N. Bartoli, A. Otsmane, and J. Morlier (2016). "Improving kriging surrogates of high-dimensional design models by Partial Least Squares dimension reduction". In: *Structural and Multidisciplinary Optimization* 53.5, pp. 935–952. ISSN: 1615-1488. DOI: 10.1007/s00158-015-1395-9 (cit. on p. 19).

Braconnier, T., M. Ferrier, J.-C. Jouhaud, M. Montagnac, and P. Sagaut (2011). "Towards an adaptive POD/SVD surrogate model for aeronautic design". In: *Computers & Fluids* 40.1, pp. 195–209. ISSN: 0045-7630. DOI: 10.1016/j.compfluid.2010.09.002 (cit. on pp. 61, 68).

Brand, M. (2006). "Fast low-rank modifications of the thin singular value decomposition". In: *Linear Algebra and its Applications* 415.1, pp. 20–30. ISSN: 0024-3795. DOI: 10.1016/j.laa.2005.07.021 (cit. on p. 56).

Branke, J. and C. Schmidt (2005). "Faster convergence by means of fitness estimation". In: *Soft Computing* 9.1, pp. 13–20. ISSN: 1433-7479. DOI: 10.1007/s00500-003-0329-4 (cit. on pp. 15, 16).

Breitkopf, P., G. Touzot, and P. Villon (1998). "Consistency approach and diffuse derivation in element free methods based on moving least squares approximation". In: *Computer Assisted Mechanics and Engineering Sciences* 5.4, pp. 479–501. ISSN: 2299-3649 (cit. on p. 29).

Brezillon, J., A. Ronzheimer, D. Haar, M. Abu-Zurayk, M. Lummer, W. Kruger, and F. J. Natterer (2012). "Development and application of multi-disciplinary optimization capabilities based on high-fidelity methods". In: Structures, Structural Dynamics, and Materials and Co-located Conferences. American Institute of Aeronautics and Astronautics. DOI: 10.2514/6.2012-1757 (cit. on p. 2).

Bui-Thanh, T. (2003). "Proper orthogonal decomposition extensions and their applications in steady aerodynamics". MA thesis. Ho Chi Minh City University of Technology, 107pp (cit. on pp. 20, 21, 28).

Bui-Thanh, T., M. Damodaran, and K. E. Willcox (2004). "Aerodynamic data reconstruction and inverse design using proper orthogonal decomposition". In: *AIAA Journal* 42.8, pp. 1505–1516. ISSN: 0001-1452. DOI: 10.2514/1.2159 (cit. on pp. 20, 21, 32, 34).

Bui-Thanh, T., K. E. Willcox, and O. Ghattas (2008). "Parametric Reduced-Order Models for Probabilistic Analysis of Unsteady Aerodynamic Applications". In: *AIAA Journal* 46.10, pp. 2520–2529. DOI: 10.2514/1.35850 (cit. on p. 20).

Bull, L. (1999). "On Model-Based Evolutionary Computation". In: *Soft Computing* 3.2, pp. 76–82. ISSN: 1432-7643. DOI: 10.1007/s005000050055 (cit. on p. 15).

Burton, S. A. and P. Hajela (2003). "A variable-complexity approach to second-order reliability-based optimization". In: *Structural and Multidisciplinary Optimization* 25.4, pp. 237–250. ISSN: 1615-1488. DOI: 10.1007/s00158-003-0298-3 (cit. on p. 16).

Cabral, B. and L. C. Leedom (1993). "Imaging Vector Fields Using Line Integral Convolution". In: *Proceedings of the 20th Annual Conference on Computer Graphics and Interactive Techniques*. SIGGRAPH '93. Anaheim, CA: ACM, pp. 263–270. ISBN: 0-89791-601-8. DOI: 10.1145/166117.166151 (cit. on p. 115).

Cambier, L., S. Heib, and S. Plot (2013). "The Onera elsA CFD software : input from research and feedback from industry". In: *Mechanics & Industry* 14.3, pp. 159–174. ISSN: 2257-7777, 2257-7750. DOI: 10.1051/meca/2013056 (cit. on pp. 56, 91).

Cao, B.-T., S. Freitag, and G. Meschke (2016). "A hybrid RNN-GPOD surrogate model for real-time settlement predictions in mechanised tunnelling". In: *Advanced Modeling and Simulation in Engineering Sciences* 3.1, p. 5. ISSN: 2213-7467. DOI: 10.1186/s40323-016-0057-9 (cit. on pp. 20, 28).

Chambers, T. L. and D. C. Wilcox (1977). "Critical examination of two-equation turbulence closure models for boundary layers". In: *AIAA Journal* 15.6, pp. 821–828. ISSN: 0001-1452. DOI: 10.2514/3.60713 (cit. on p. 120).

Chang, K. J., R. T. Haftka, G. L. Giles, and K. Pi-Jen (1993). "Sensitivity-based scaling for approximating structural response". In: *Journal of Aircraft* 30.2, pp. 283–288. ISSN: 0021-8669, 1533-3868. DOI: 10.2514/3.48278 (cit. on p. 17).

Chen, B. and X. Yuan (2008). "Advanced Aerodynamic Optimization System for Turbomachinery". In: *Journal of Turbomachinery* 130.2, pp. 21005-1–21005-12. ISSN: 0889-504X. DOI: 10.1115/1.2776953 (cit. on p. 3).

Chen, P. P., Q. W. Yang, S. F. A. Hashmi, P. J. Shi, and L. Zhao (2012). "Passive control of hub-corner separation/stall using axisymmetric-hub contouring". In: vol. 226. 10, pp. 1214–1224. DOI: 10.1177/0954410011421716 (cit. on p. 88).

Choi, S., J. J. Alonso, and I. M. Kroo (2005). "Multi-Fidelity Design Optimization Studies for Supersonic Jets Using Surrogate Management Frame Method". In: *23rd AIAA Applied Aerodynamics Conference*. American Institute of Aeronautics and Astronautics (AIAA). DOI: 10.2514/6.2005-5077 (cit. on p. 16).

— (2009). "Two-level multifidelity optimization studies for supersonic jets". In: *Journal of Aircraft* 46.3, pp. 776–790. DOI: 10.2514/1.34362 (cit. on p. 16).

Choi, S., J. J. Alonso, I. M. Kroo, and M. Wintzer (2008). "Multifidelity design optimization of low-boom supersonic jets". In: *Journal of Aircraft* 45.1, pp. 106–118. ISSN: 0021-8669, 1533-3868. DOI: 10.2514/1.28948 (cit. on pp. 16, 17).

Colombo, E. (2011). "Investigation on the Three-Dimensional Flow Mechanisms in Annular Axial Compressor Cascades for Aero Engines with Flow Control by Aspiration on the Hub and on the Blades". eng. PhD thesis. Lausanne: STI. DOI: 10.5075/epfl-thesis-5241 (cit. on pp. 13, 106).

Cook, P. H., M. A. McDonald, and M. C. P. Firmin (1979). "Aerofoil RAE 2822 - pressure distributions, and boundary layer and wake measurements". In: *AGARD Report AR*. Vol. 138 (cit. on pp. 56, 57).

Cortes, C. and V. Vapnik (1995). "Support-vector networks". In: *Machine Learning* 20.3, pp. 273–297. ISSN: 1573-0565. DOI: 10.1007/BF00994018 (cit. on p. 83).

Cravero, C., P. Macelloni, and G. Briasco (2012). "Three-Dimensional Design Optimization of Multistage Axial Flow Turbines Using a RSM Based Approach". In: *Volume 8: Turbomachinery, Parts A, B, and C*. ASME International. DOI: 10.1115/gt2012-68040 (cit. on p. 22).

Cremanns, K., D. Roos, S. Hecker, P. Dumstorff, H. Almstedt, and C. Musch (2016). "Efficient Multi-Objective Optimization of Labyrinth Seal Leakage in Steam Turbines Based on Hybrid Surrogate Models". In: *Volume 2C: Turbomachinery*. ASME International. DOI: 10.1115/gt2016-57457 (cit. on p. 22).

Dang, T. Q., S. V. Damle, and X. Qiu (2000). "Euler-Based Inverse Method for Turbomachine Blades, Part 2: Three-Dimensional Flows". In: *AIAA Journal* 38.11, pp. 2007–2013. ISSN: 0001-1452. DOI: 10.2514/2.879 (cit. on p. 11).

Dang, T. Q. and V. Isgro (1995). "Euler-based inverse method for turbomachine blades. I - Two-dimensional cascades". In: *AIAA Journal* 33.12, pp. 2309–2315. ISSN: 0001-1452. DOI: 10.2514/3.12985 (cit. on p. 11).

De Maesschalck, C., S. Lavagnoli, and G. Paniagua (2013). "Blade Tip Shape Optimization for Enhanced Turbine Aerothermal Performance". In: *Journal of Turbomachinery* 136.4, p. 041016. DOI: 10.1115/1.4025202 (cit. on p. 22).

Deb, K., A. Pratap, S. Agarwal, and T. Meyarivan (2002). "A fast and elitist multiobjective genetic algorithm: NSGA-II". In: *IEEE Transactions on Evolu-*

tionary Computation 6.2, pp. 182–197. DOI: 10.1109/4235.996017 (cit. on p. 22).

Deng, X., F. Guo, Y. Liu, and P. Han (2013). "Aero-Mechanical Optimization Design of a Transonic Fan Blade". In: *Volume 6B: Turbomachinery*. ASME International. DOI: 10.1115/gt2013-95357 (cit. on p. 22).

Denton, J. D. (1993). "The 1993 IGTI Scholar Lecture: Loss Mechanisms in Turbomachines". In: *Journal of Turbomachinery* 115.4, pp. 621–656. ISSN: 0889-504X. DOI: 10.1115/1.2929299 (cit. on p. 12).

Denton, J. D. and W. N. Dawes (1998). "Computational fluid dynamics for turbomachinery design". In: *Proceedings of the Institution of Mechanical Engineers, Part C: Journal of Mechanical Engineering Science* 213.2, pp. 107–124. DOI: 10.1243/0954406991522211 (cit. on p. 11).

Dorfner, C., A. Hergt, E. Nicke, and R. Moenig (2011). "Advanced nonaxisymmetric endwall contouring for axial compressors by generating and aerodynamic separator - Part I: Principal cascade design and compressor application". In: *Journal of Turbomachinery* 133.2, pp. 21–26. ISSN: 0889504X. DOI: 10.1115/1.4001223 (cit. on p. 89).

Dornberger, R., P. Stoll, D. Bueche, and A. Neu (2000). "Multidisciplinary turbomachinery blade design optimization". In: Aerospace Sciences Meetings. American Institute of Aeronautics and Astronautics. DOI: 10.2514/6.2000-838 (cit. on p. 1).

Dragan, V., I. Malael, and B. Gherman (2015). "Development of a Very High Pressure Ratio Single Stage Centrifugal Compressor". In: *International Review on Modelling and Simulations (IREMOS)* 8.3. ISSN: 1974-983X (cit. on p. 120).

Drela, M. (1989). "XFOIL: An Analysis and Design System for Low Reynolds Number Airfoils". In: *Low Reynolds Number Aerodynamics*. Ed. by T. J. Mueller. Springer Berlin Heidelberg, pp. 1–12 (cit. on p. 56).

Eldred, M. and D. Dunlavy (2006). In: Multidisciplinary Analysis Optimization Conferences. 0. American Institute of Aeronautics and Astronautics. Chap. Formulations for Surrogate-Based Optimization with Data Fit, Multifidelity, and Reduced-Order Models. DOI: 10.2514/6.2006-7117 (cit. on pp. 14, 20).

Eldred, M., A. Giunta, and S. S. Collis (2004). "Second-order corrections for surrogate-based optimization with model hierarchies". In: *Proc. 10th AIAA/ISSMO Multidisciplinary Analysis and Optimization Conference*. American Institute of Aeronautics and Astronautics. DOI: 10.2514/6.2004-4457 (cit. on p. 17).

Emmerich, M. T. M., K. C. Giannakoglou, and B. Naujoks (2006). "Single- and Multiobjective Evolutionary Optimization Assisted by Gaussian Random Field Metamodels". In: *Trans. Evol. Comp* 10.4, pp. 421–439. ISSN: 1089-778X. DOI: 10.1109/TEVC.2005.859463 (cit. on p. 16).

Escuret, J.-F., D. Nicoud, and P. Veysseyre (1998). *Recent advances in compressors aerodynamic design and analysis*. Tech. rep. RTO/NATO (cit. on p. 11).

Everson, R. and L. Sirovich (1995). "Karhunen–Loeve procedure for gappy data". In: *Journal of the Optical Society of America A* 12.8, pp. 1657–1664. ISSN: 1084-7529, 1520-8532. DOI: 10.1364/JOSAA.12.001657 (cit. on pp. 6, 21, 32).

Fang, F., C. C. Pain, I. M. Navon, G. J. Gorman, M. D. Piggott, P. A. Allison, P. E. Farrell, and A. J. H. Goddard (2009). "A POD reduced order unstructured mesh ocean modelling method for moderate Reynolds number flows". In: *Ocean Modelling* 28.1, pp. 127–136. DOI: 10.1016/j.ocemod.2008.12.006 (cit. on p. 58).

Fernández-Godino, G. M., C. Park, N. H. Kim, and R. T. Haftka (2016). "Review of multi-fidelity models". In: *ArXiv e-prints*. arXiv: 1609.07196 [stat.AP] (cit. on pp. 16–19).

Filomeno Coelho, R., P. Breitkopf, and C. Knopf-Lenoir (2008). "Model reduction for multidisciplinary optimization - application to a 2D wing". In: *Structural and Multidisciplinary Optimization* 37.1, pp. 29–48. ISSN: 1615-147X. DOI: 10.1007/s00158-007-0212-5 (cit. on pp. 23, 56).

Forrester, A. I. J. and A. J. Keane (2009). "Recent advances in surrogate-based optimization". In: *Progress in Aerospace Sciences* 45.1-3, pp. 50–79. ISSN: 0376-0421. DOI: 10.1016/j.paerosci.2008.11.001 (cit. on p. 14).

Forrester, A. I. J., A. Sóbester, and A. J. Keane (2007). "Multi-fidelity optimization via surrogate modelling". In: *Proceedings of the Royal Society A: Mathematical, Physical and Engineering Sciences*. Vol. 463, pp. 3251–3269. DOI: 10.1098/rspa.2007.1900 (cit. on pp. 14, 18, 19, 97).

— (2008). *Engineering Design via Surrogate Modelling : A Practical Guide*. John Wiley & Sons. ISBN: 978-0-470-06068-1. DOI: 10.1002/9780470770801 (cit. on pp. 14, 19, 29, 42, 73).

Gano, S. E., V. Perez, J. E. Renaud, S. Batill, and B. Sanders (2004). "Multilevel Variable Fidelity Optimization of a Morphing Unmanned Aerial Vehicle". In: *45th AIAA/ASME/ASCE/AHS/ASC Structures, Structural Dynamics & Materials Conference*. American Institute of Aeronautics and Astronautics (AIAA). DOI: 10.2514/6.2004-1763 (cit. on p. 17).

Gbadebo, S. A., N. A. Cumpsty, and T. P. Hynes (2005). "Three-dimensional separations in axial compressors". In: *Journal of Turbomachinery* 127.2, pp. 331–339. ISSN: 0889-504X. DOI: 10.1115/1.1811093 (cit. on p. 13).

Giannakoglou, K. C., D. I. Papadimitriou, and I. C. Kampolis (2006). "Aerodynamic shape design using evolutionary algorithms and new gradient-assisted metamodels". In: *Computer Methods in Applied Mechanics and Engineering* 195.44–47, pp. 6312–6329. ISSN: 0045-7825. DOI: 10.1016/j.cma.2005.12.008 (cit. on pp. 15, 23).

Giesing, J. and J.-F. Barthelemy (1998). "A summary of industry MDO applications and needs". In: Multidisciplinary Analysis Optimization Conferences. American Institute of Aeronautics and Astronautics. DOI: 10.2514/6.1998-4737 (cit. on pp. 2, 3).

Giovannini, M., M. Marconcini, F. Rubechini, A. Arnone, and F. Bertini (2016). "Scaling Three-Dimensional Low-Pressure Turbine Blades for Low-Speed Testing". In: *Journal of Turbomachinery* 138.11, p. 111001. DOI: 10.1115/1.4033259 (cit. on p. 22).

Gogu, C., R. T. Haftka, R. Le Riche, J. Molimard, and A. Vautrin (2009). "Dimensionality reduction of full fields by the principal components analysis". In: *Proc. 17th International Conference on Composite Materials (ICCM17)*, F14.7 (cit. on p. 27).

Goh, J., D. Bingham, J. P. Holloway, M. J. Grosskopf, C. C. Kuranz, and E. Rutter (2013). "Prediction and Computer Model Calibration Using Outputs From Multifidelity Simulators". In: *Technometrics* 55.4, pp. 501–512. DOI: 10.1080/00401706.2013.838910 (cit. on p. 19).

Gong, Y.-J., W.-N. Chen, Z.-H. Zhan, J. Zhang, Y. Li, Q. Zhang, and J.-J. Li (2015). "Distributed evolutionary algorithms and their models: A survey of the state-of-the-art". In: *Applied Soft Computing* 34, pp. 286–300. ISSN: 1568-4946. DOI: 10.1016/j.asoc.2015.04.061 (cit. on p. 15).

Gorla, R. S. R. and A. A. Khan (2003). *Turbomachinery Design and Theory*. First. CRC Press. ISBN: 0-8247-0980-2. DOI: 10.1201/9780203911600 (cit. on p. 9).

Goulos, I., J. Otter, T. Stankowski, D. MacManus, N. Grech, and C. Sheaf (2016). "Aerodynamic Design of Separate-Jet Exhausts for Future Civil Aeroengines—Part II: Design Space Exploration, Surrogate Modeling, and Optimization". In: *Journal of Engineering for Gas Turbines and Power* 138.8, pp. 081202-1–081202-12. DOI: 10.1115/1.4032652 (cit. on p. 23).

Greenman, R. M. and K. R. Roth (1999). "Minimizing Computational Data Requirements for Multi-Element Airfoils Using Neural Networks". In: *Journal of Aircraft* 36.5, pp. 777–784. ISSN: 0021-8669. DOI: 10.2514/2.2533 (cit. on p. 15).

Grefenstette, J. J. and J. M. Fitzpatrick (1985). "Genetic Search with Approximate Function Evaluation". In: *Proceedings of the 1st International Conference on Genetic Algorithms*. Hillsdale, NJ, USA: L. Erlbaum Associates Inc., pp. 112–120. ISBN: 0-8058-0426-9 (cit. on p. 15).

Guénot, M., I. Lepot, C. Sainvitu, J. Goblet, and R. Filomeno Coelho (2011). "Adaptive sampling strategies for non-intrusive POD-based surrogates". In: *Proc. EUROGEN 2011 Evolutionary and deterministic methods for design, optimization and control*. Capua, Italy: CIRA (cit. on pp. 20, 27, 61, 99).

— (2013). "Adaptive sampling strategies for non-intrusive POD-based surrogates". In: *Engineering Computations* 30.4, pp. 521–547. ISSN: 0264-4401. DOI: 10.1108/02644401311329352 (cit. on pp. 20, 27, 61, 62, 64, 68, 97).

Ha, K. K. and S. H. Kang (2011). "An Optimization Method for Centrifugal Compressor Design Using the Surrogate Management Framework". In: *ASME-JSME-KSME 2011 Joint Fluids Engineering Conference: Volume 1, Symposia – Parts A, B, C, and D*. ASME International. DOI: 10.1115/ajk2011-22036 (cit. on p. 22).

Haftka, R. T. (1991). "Combining global and local approximations". In: *AIAA Journal* 29.9, pp. 1523–1525. ISSN: 0001-1452. DOI: 10.2514/3.10768 (cit. on p. 17).

Hamdaoui, M., G. Le Quilliec, P. Breitkopf, and P. Villon (2013). "Surrogate POD models for parametrized sheet metal forming applications". In: *Proc. 16th ESAFORM Conference on Material Forming*. Vol. 554-557, pp. 919–927. DOI: 10.4028/www.scientific.net/KEM.554-557.919 (cit. on pp. 20, 28, 97).

Hamim, S. U. and R. P. Singh (2017). "Taguchi-based design of experiments in training POD-RBF surrogate model for inverse material modelling using nanoindentation". en. In: *Inverse Problems in Science and Engineering* 25.3, pp. 363–381. ISSN: 1741-5977, 1741-5985. DOI: 10.1080/17415977.2016.1161036 (cit. on p. 21).

Hamza, K. and K. Saitou (2012). "A co-evolutionary approach for design optimization via ensembles of surrogates with application to vehicle crashworthiness". In: *Journal of Mechanical Design* 134.1, pp. 1–10. ISSN: 1050-0472. DOI: 10.1115/1.4005439 (cit. on p. 15).

Han, Z.-H., S. Görtz, and R. Zimmermann (2013). "Improving variable-fidelity surrogate modeling via gradient-enhanced Kriging and a generalized hybrid bridge function". In: *Aerospace Science and Technology* 25.1, pp. 177–189. ISSN: 1270-9638. DOI: 10.1016/j.ast.2012.01.006 (cit. on p. 15).

Han, Z.-H., R. Zimmermann, and S. Görtz (2010). "A new cokriging method for variable-fidelity surrogate modeling of aerodynamic data". In: *Proc. 48th AIAA Aerospace Sciences Meeting Including the New Horizons Forum and Aerospace Exposition*. American Institute of Aeronautics and Astronautics. DOI: 10.2514/6.2010-1225 (cit. on p. 19).

Harten, A. (1983). "High resolution schemes for hyperbolic conservation laws". In: *Journal of Computational Physics* 49.3, pp. 357–393. ISSN: 0021-9991. DOI: 10.1016/0021-9991(83)90136-5 (cit. on p. 91).

Hellsten, A. (1998). "Some improvements in Menter's k-omega SST turbulence model". In: 0. DOI: 10.2514/6.1998-2554 (cit. on p. 120).

Heo, M.-W., S.-B. Ma, H.-S. Shim, and K.-Y. Kim (2016). "High-efficiency design optimization of a centrifugal pump". In: *Journal of Mechanical Science and Technology* 30.9, pp. 3917–3927. ISSN: 1976-3824. DOI: 10.1007/s12206-016-0803-4 (cit. on p. 23).

Hoeger, M., P. Cardamone, and L. Fottner (2002). "Influence of endwall contouring on the transonic flow in a compressor blade". In: *Proceedings of ASME TurboExpo 2002*. Amsterdam, The Netherlands: ASME, pp. 759–768. ISBN: 978-0-7918-3610-1. DOI: 10.1115/GT2002-30440 (cit. on p. 88).

Hu, S., X. Lu, H. Zhang, J. Zhu, and Q. Xu (2010). "Numerical investigation of a high-subsonic axial-flow compressor rotor with non-axisymmetric hub endwall". In: *Journal of Thermal Science* 19.1, pp. 14–20. DOI: 10.1007/s11630-010-0014-8 (cit. on p. 89).

Huang, L., Z. Gao, and D. Zhang (2013). "Research on multi-fidelity aerodynamic optimization methods". en. In: *Chinese Journal of Aeronautics* 26.2, pp. 279–286. ISSN: 1000-9361. DOI: 10.1016/j.cja.2013.02.004 (cit. on p. 19).

Jin, Y. (2005). "A comprehensive survey of fitness approximation in evolutionary computation". In: *Soft Computing* 9.1, pp. 3–12. ISSN: 1432-7643. DOI: 10.1007/s00500-003-0328-5 (cit. on p. 16).

— (2011). "Surrogate-assisted evolutionary computation: Recent advances and future challenges". In: *Swarm and Evolutionary Computation* 1.2, pp. 61–70. ISSN: 2210-6502. DOI: 10.1016/j.swevo.2011.05.001 (cit. on pp. 15, 16).

Jin, Y., M. Olhofer, and B. Sendhoff (2000). "On evolutionary optimization with approximate fitness functions". In: *Proceedings of the 2Nd Annual Conference on Genetic and Evolutionary Computation*. GECCO'00. Las Vegas, Nevada: Morgan Kaufmann Publishers Inc., pp. 786–793. ISBN: 1-55860-708-0 (cit. on p. 15).

— (2002). "A framework for evolutionary optimization with approximate fitness functions". In: *IEEE Transactions on Evolutionary Computation* 6.5, pp. 481–494. ISSN: 1089-778X. DOI: 10.1109/TEVC.2002.800884 (cit. on p. 15).

Jolliffe, I. T. (2002). *Principal Component Analysis*. Second. Springer-Verlag, p. 488. ISBN: 978-0-387-22440-4. DOI: 10.1007/b98835 (cit. on p. 98).

Jones, D. R., M. Schonlau, and W. J. Welch (1998). "Efficient global optimization of expensive black-box functions". In: *Journal of Global Optimization* 13.4, pp. 455–492. ISSN: 1573-2916. DOI: 10.1023/A:1008306431147 (cit. on p. 22).

Keane, A. J. (2012). "Cokriging for robust design optimization". In: *AIAA Journal* 50.11, pp. 2351–2364. ISSN: 0001-1452. DOI: 10.2514/1.J051391 (cit. on pp. 17, 18).

Keane, A. J. and P. B. Nair (2005). *Computational Approaches for Aerospace Design: The Prusuit of Excellence*. John Wiley & Sons. DOI: 10.1002/0470855487 (cit. on pp. 14, 17).

Kennedy, M. C. and A. O'Hagan (2000). "Predicting the output from a complex computer code when fast approximations are available". In: *Biometrika* 87.1, pp. 1–13. DOI: 10.1093/biomet/87.1.1 (cit. on pp. 18, 19, 39, 42, 91, 97).

Kerschen, G., J.-c. Golinval, A. F. Vakakis, and L. A. Bergman (2005). "The method of proper orthogonal decomposition for dynamical characterization and order reduction of mechanical systems: An overview". In: *Nonlinear Dynamics* 41.1, pp. 147–169. ISSN: 1573-269X. DOI: 10.1007/s11071-005-2803-2 (cit. on p. 20).

Keskin, A., M. Swoboda, P. M. Flassig, A. K. Dutta, and D. Bestle (2008). "Accelerated industrial blade design based on multi-objective optimization using surrogate model methodology". In: *Volume 6: Turbomachinery, Parts A, B, and C*. ASME International. DOI: 10.1115/gt2008-50506 (cit. on p. 22).

Khalfallah, S., A. Ghenaiet, E. Benini, and G. Bedon (2015). "Surrogate-based shape optimization of stall margin and efficiency of a centrifugal compressor". In: *Journal of Propulsion and Power* 31.6, pp. 1607–1620. ISSN: 0748-4658. DOI: 10.2514/1.B35543 (cit. on p. 22).

Kim, B.-S., Y.-B. Lee, and D.-H. Choi (2009). "Comparison study on the accuracy of metamodeling technique for non-convex functions". In: *Journal of Mechanical Science and Technology* 23.4, pp. 1175–1181. ISSN: 1976-3824. DOI: 10.1007/s12206-008-1201-3 (cit. on p. 19).

Kim, J.-H. and K.-Y. Kim (2012). "Analysis and optimization of a vaned diffuser in a mixed flow pump to improve hydrodynamic performance". In: *Journal of Fluids Engineering* 134.7, p. 071104. DOI: 10.1115/1.4006820 (cit. on p. 23).

Kirby, M., J. P. Boris, and L. Sirovich (1990). "A proper orthogonal decomposition of a simulated supersonic shear layer". In: *International Journal for Numerical Methods in Fluids* 10.4, pp. 411–428. DOI: 10.1002/fld.1650100405 (cit. on p. 98).

Kleijnen, J. P. (2009). "Kriging metamodeling in simulation: A review". In: *European Journal of Operational Research* 192.3, pp. 707–716. ISSN: 0377-2217. DOI: 10.1016/j.ejor.2007.10.013 (cit. on p. 18).

Kodiyalam, S. and J. S. Sobieski (2001). *Multidisciplinary aerospace systems optimization: computational aerosciences (CAS) project*. Technical Report NASA/CR-2001-211053. Sunnyvale, CA United States: Lockheed Martin Space Systems Co, pp. 1–26 (cit. on p. 23).

Koziel, S., J. W. Bandler, and K. Madsen (2006). "A space-mapping framework for engineering optimization: theory and implementation". In: *IEEE Transactions on Microwave Theory and Techniques* 54.10, pp. 3721–3730. ISSN: 0018-9480. DOI: 10.1109/TMTT.2006.882894 (cit. on p. 14).

Koziel, S. and L. Leifsson (2012). "Knowledge-based airfoil shape optimization using space mapping". In: *30th AIAA Applied Aerodynamics Conference*. Ameri-

can Institute of Aeronautics and Astronautics (AIAA). DOI: 10.2514/6.2012-3016 (cit. on p. 19).

Koziel, S. and S. Ogurtsov (2014). "Surrogate-Based Optimization". In: *Antenna Design by Simulation-Driven Optimization*. Cham: Springer International Publishing, pp. 13–24. ISBN: 978-3-319-04367-8. DOI: 10.1007/978-3-319-04367-8_3 (cit. on p. 14).

Koziel, S. and X.-S. Yang (2011). *Computational optimization, methods and algorithms*. New York: Springer. ISBN: 3642208584 (cit. on p. 14).

Krige, D. G. (1951). "A statistical approach to some basic mine valuation problems on the Witwatersrand". In: *Journal of the Chemical, Metallurgical and Mining Society of South Africa* 52.6, pp. 119–139. DOI: 10.2307/3006914 (cit. on pp. 19, 23, 83).

Kröger, G., C. Voß, E. Nicke, and C. Cornelius (2011). "Theory and application of axisymmetric endwall contouring for compressors". In: *ASME Turbo Expo 2011: Turbine Technical Conference and Exposition*. Vol. 7, pp. 125–137. DOI: 10.1115/GT2011-45624 (cit. on p. 88).

Kroo, I., S. Altus, R. Braun, P. Gage, and I. Sobieski (1994). "Multidisciplinary optimization methods for aircraft preliminary design". In: Multidisciplinary Analysis Optimization Conferences. American Institute of Aeronautics and Astronautics. DOI: 10.2514/6.1994-4325 (cit. on p. 1).

Kuya, Y., K. Takeda, X. Zhang, and A. I. J. Forrester (2011). "Multifidelity surrogate modeling of experimental and computational aerodynamic data sets". In: *AIAA Journal* 49.2, pp. 289–298. DOI: 10.2514/1.J050384 (cit. on p. 19).

Kyriacou, S. A., V. G. Asouti, and K. C. Giannakoglou (2014). "Efficient PCA-driven EAs and metamodel-assisted EAs, with applications in turbomachinery". In: *Engineering Optimization* 46.7, pp. 895–911. DOI: 10.1080/0305215X.2013.812726 (cit. on p. 20).

Lakshminarayana, B., M. Zaccaria, and B. Marathe (1995). "The structure of tip clearance flow in axial flow compressors". In: *Journal of Turbomachinery* 117.3, pp. 336–347. ISSN: 0889-504X. DOI: 10.1115/1.2835667 (cit. on p. 117).

Langston, L. (2001). "Secondary flows in axial turbines—A review". In: *Annals of the New York Academy of Sciences* 934.1, pp. 11–26. ISSN: 1749-6632. DOI: 10.1111/j.1749-6632.2001.tb05839.x (cit. on p. 12).

Launder, B. E. and B. I. Sharma (1974). "Application of the energy-dissipation model of turbulence to the calculation of flow near a spinning disc". In: *Letters in Heat and Mass Transfer* 1.2, pp. 131–137. ISSN: 0094-4548. DOI: http://dx.doi.org/10.1016/0094-4548(74)90150-7 (cit. on pp. 91, 121).

Laurenceau, J. and P. Sagaut (2008). "Building efficient response surfaces of aerodynamic functions with Kriging and Cokriging". In: *AIAA Journal* 46.2, pp. 498–507. ISSN: 0001-1452. DOI: 10.2514/1.32308 (cit. on p. 15).

Le Gratiet, L. and J. Garnier (2014). "Recursive co-Kriging model for design of computer experiments with multiple levels of fidelity". In: *International Journal for Uncertainty Quantification* 4.5, pp. 365–386. ISSN: 2152-5080,2152-5099. DOI: 10.1615/Int.J.UncertaintyQuantification.2014006914 (cit. on pp. 42, 73).

Le Quilliec, G., B. Raghavan, and P. Breitkopf (2015). "A manifold learning-based reduced order model for springback shape characterization and optimization in sheet metal forming". In: *Computer Methods in Applied Mechanics and Engineering* 285, pp. 621–638. ISSN: 0045-7825. DOI: 10.1016/j.cma.2014.11.029 (cit. on p. 20).

Leary, S. J., A. Bhaskar, and A. J. Keane (2003). "A knowledge-based approach to response surface modelling in multifidelity optimization". In: *Journal of Global Optimization* 26.3, pp. 297–319. ISSN: 0925-5001, 1573-2916. DOI: 10.1023/A:1023283917997 (cit. on pp. 19, 91).

Lee, S., S. Lee, K.-H. Kim, D.-H. Lee, Y.-S. Kang, and D.-H. Rhee (2014). "Optimization Framework Using Surrogate Model for Aerodynamically Improved 3D Turbine Blade Design". In: *Volume 2B: Turbomachinery*. ASME International. DOI: 10.1115/gt2014-26571 (cit. on p. 22).

Lei, V.-M., Z. S. Spakovsky, and E. M. Greitzer (2008). "A criterion for axial compressor hub-corner stall". In: *Journal of Turbomachinery* 130.3, p. 10. ISSN: 0889-504X. DOI: 10.1115/1.2775492 (cit. on pp. 12, 91).

Leifsson, L. T., Y. A. Tesfahunegn, and S. Koziel (2016). In: AIAA AVIATION Forum. 0. American Institute of Aeronautics and Astronautics. Chap. Aerodynamic shape optimization by variable-fidelity models and gradient-enhanced manifold mapping. DOI: 10.2514/6.2016-3865 (cit. on pp. 15, 21).

Leifsson, L. and S. Koziel (2010). "Multi-fidelity design optimization of transonic airfoils using physics-based surrogate modeling and shape-preserving response prediction". In: *Journal of Computational Science* 1.2, pp. 98–106. ISSN: 1877-7503. DOI: 10.1016/j.jocs.2010.03.007 (cit. on pp. 21, 56).

— (2015). "Surrogate modelling and optimization using shape-preserving response prediction: A review". In: *Engineering Optimization*, pp. 1–21. ISSN: 0305-215X. DOI: 10.1080/0305215X.2015.1016509 (cit. on p. 21).

Lepot, I., T. Mengistu, S. Hiernaux, and O. De Vriendt (2011). "Highly loaded LPC blade and non axisymmetric hub profiling optimization for enhanced efficiency and stability". In: *ASME Turbo Expo 2011: Turbine Technical Conference and Exposition*. Vol. 7, pp. 285–295. DOI: 10.1115/GT2011-46261 (cit. on pp. 88, 89, 91, 111, 121).

Levchenya, A. M., E. Smirnov, and V. Goryachev (2010). "RANS-based numerical simulation and visualization of the horseshoe vortex system in the leading edge endwall region of a symmetric body". In: *International Journal of*

Heat and Fluid Flow 31.6, pp. 1107–1112. ISSN: 0142-727X. DOI: 10.1016/j.ijheatfluidflow.2010.06.014 (cit. on p. 12).

Lewis, R. and S. Nash (2000). "A multigrid approach to the optimization of systems governed by differential equations". In: *Proc. 8th Symposium on Multidisciplinary Analysis and Optimization*. American Institute of Aeronautics and Astronautics. DOI: 10.2514/6.2000-4890 (cit. on p. 17).

Liang, Y. C., H. P. Lee, S. P. Lim, W. Z. Lin, K. H. Lee, and C. G. Wu (2002). "Proper orthogonal decomposition and its applications–Part I : theory". en. In: *Journal of Sound and Vibration* 252.3, pp. 527–544. ISSN: 0022460X. DOI: 10.1006/jsvi.2001.4041 (cit. on p. 29).

Lim, D., Y.-S. Ong, Y. Jin, and B. Sendhoff (2006). "Trusted evolutionary algorithm". In: *2006 IEEE International Conference on Evolutionary Computation*, pp. 149–156. DOI: 10.1109/CEC.2006.1688302 (cit. on p. 15).

Lin, Z., D. Xiao, F. Fang, C. C. Pain, and I. M. Navon (2016). "Non-intrusive reduced order modelling with least squares fitting on a sparse grid". In: *International Journal for Numerical Methods in Fluids* 83.3, pp. 291–306. DOI: 10.1002/fld.4268 (cit. on p. 20).

Lopez Peña, F., V. D. Díaz Casás, A. Gosset, and R. J. Duro (2012). "A surrogate method based on the enhancement of low fidelity computational fluid dynamics approximations by artificial neural networks". en. In: *Computers & Fluids* 58, pp. 112–119. ISSN: 0045-7930. DOI: 10.1016/j.compfluid.2012.01.008 (cit. on p. 56).

Luliano, E. and D. Quagliarella (2013). "Proper orthogonal decomposition, surrogate modelling and evolutionary optimization in aerodynamic design". In: *Computers & Fluids* 84, pp. 327–350. ISSN: 0045-7930. DOI: 10.1016/j.compfluid.2013.06.007 (cit. on p. 56).

Lumley, J. L. (1967). "The structure of inhomogeneous turbulent flows". In: *Atmospheric turbulence and radio propagation*. Ed. by A. M. Yaglom and V. I. Tatarski. Nauka, pp. 166–178 (cit. on p. 27).

Ma, S.-B., A. Afzal, K.-Y. Kim, J. Choi, and W. Lee (2016). "Optimization of a two-stage transonic axial fan to enhance aerodynamic stability". In: *Volume 2C: Turbomachinery*. ASME International. DOI: 10.1115/gt2016-56261 (cit. on p. 22).

Madsen, J. I. and M. Langthjem (2001). "Multifidelity response surface approximations for the optimum design of diffuser flows". en. In: *Optimization and Engineering* 2.4, pp. 453–468. ISSN: 1389-4420, 1573-2924. DOI: 10.1023/A:1016046606831 (cit. on p. 17).

Maneewongvatana, S. and D. M. Mount (2001). "On the efficiency of nearest neighbor searching with data clustered in lower dimensions". In: *Computational Science — ICCS 2001: International Conference San Francisco, CA, USA, May*

28–30, 2001 Proceedings, Part I. Ed. by V. N. Alexandrov, J. J. Dongarra, B. A. Juliano, R. S. Renner, and C. J. K. Tan. Berlin, Heidelberg: Springer Berlin Heidelberg, pp. 842–851. ISBN: 978-3-540-45545-5. DOI: 10.1007/3-540-45545-0_96 (cit. on p. 108).

Matheron, G. (1963). "Principles of geostatistics". In: *Economic Geology* 58.8, pp. 1246–1266. ISSN: 0361-0128. DOI: 10.2113/gsecongeo.58.8.1246 (cit. on pp. 19, 23, 83).

Meher-Homji, C. B. (2000). "The historical evolution of turbomachinery". In: *Texas A&M University - 29th turbomachinery symposium*, pp. 281–322 (cit. on p. 10).

Mehmani, A., S. Chowdhury, and A. Messac (2015). "Predictive quantification of surrogate model fidelity based on modal variations with sample density". In: *Structural and Multidisciplinary Optimization* 52.2, pp. 353–373. ISSN: 1615-1488. DOI: 10.1007/s00158-015-1234-z (cit. on p. 2).

Meng, L., P. Breitkopf, G. Le Quilliec, B. Raghavan, and P. Villon (2016). In: *Archives of Computational Methods in Engineering*, pp. 1–21. ISSN: 1886-1784. DOI: 10.1007/s11831-016-9189-9 (cit. on p. 20).

Menter, F. R. (1992). "Influence of freestream values on k-omega turbulence model predictions". In: *AIAA Journal* 30.6, pp. 1657–1659. ISSN: 0001-1452. DOI: 10.2514/3.11115 (cit. on p. 120).

— (1993). In: Fluid Dynamics and Co-located Conferences. 0. American Institute of Aeronautics and Astronautics. Chap. Zonal Two Equation k-w Turbulence Models For Aerodynamic Flows. DOI: 10.2514/6.1993-2906 (cit. on p. 120).

— (1994). "Two-equation eddy-viscosity turbulence models for engineering applications". In: *AIAA Journal* 32.8, pp. 1598–1605. ISSN: 0001-1452. DOI: 10.2514/3.12149 (cit. on pp. 120, 121).

Menter, F. R., M. Kuntz, and R. Bender (2003). In: Aerospace Sciences Meetings. 0. American Institute of Aeronautics and Astronautics. Chap. A Scale-Adaptive Simulation Model for Turbulent Flow Predictions. DOI: 10.2514/6.2003-767 (cit. on p. 120).

Mifsud, M. J. (2008). "Reduced-order modelling for high-speed aerial weapon aerodynamics". eng. PhD thesis. Cranfield: Cranfield University (cit. on pp. 4, 21, 22).

Mifsud, M. J., D. G. MacManus, and S. Shaw (2016). "A variable-fidelity aerodynamic model using proper orthogonal decomposition". In: *International Journal for Numerical Methods in Fluids* 82.10, pp. 646–663. ISSN: 1097-0363. DOI: 10.1002/fld.4234 (cit. on pp. 4, 19, 21, 52, 98–100, 102).

Mifsud, M. J., S. T. Shaw, and D. G. MacManus (2009). "A high-fidelity low-cost aerodynamic model using proper orthogonal decomposition". In: *International*

Journal for Numerical Methods in Fluids 63.4, pp. 468–494. ISSN: 1097-0363. DOI: 10.1002/fld.2085 (cit. on p. 20).

Moore, J., D. M. Shaffer, and J. G. Moore (1987). "Reynolds stresses and dissipation mechanisms downstream of a turbine cascade". In: *Journal of Turbomachinery* 109.2, pp. 258–267. ISSN: 0889-504X. DOI: 10.1115/1.3262096 (cit. on p. 106).

Moré, J. J. (1983). "Recent developments in algorithms and software for trust region methods". In: *Mathematical Programming The State of the Art: Bonn 1982*. Ed. by A. Bachem, B. Korte, and M. Grötschel. Berlin, Heidelberg: Springer Berlin Heidelberg, pp. 258–287. ISBN: 978-3-642-68874-4. DOI: 10.1007/978-3-642-68874-4_11 (cit. on p. 84).

Mueller, L., Z. Alsalihi, and T. Verstraete (2012). "Multidisciplinary Optimization of a Turbocharger Radial Turbine". In: *Journal of Turbomachinery* 135.2, p. 021022. DOI: 10.1115/1.4007507 (cit. on p. 22).

Myers, D. E. (1982). "Matrix formulation of co-kriging". In: *Journal of the International Association for Mathematical Geology* 14.3, pp. 249–257. ISSN: 1573-8868. DOI: 10.1007/BF01032887 (cit. on p. 19).

Myers, R. (2016). *Response surface methodology : process and product optimization using designed experiments*. Hoboken, New Jersey: Wiley. ISBN: 978-1-118-91601-8 (cit. on p. 23).

Nava, E., S. Pintos, and N. V. Queipo (2010). "A geostatistical perspective for the surrogate-based integration of variable fidelity models". In: *Journal of Petroleum Science and Engineering* 71.1-2, pp. 56–66. ISSN: 09204105. DOI: 10.1016/j.petrol.2010.01.005 (cit. on p. 19).

Nayroles, B., G. Touzot, and P. Villon (1992). "Generalizing the finite element method: Diffuse approximation and diffuse elements". In: *Computational Mechanics* 10.5, pp. 307–318. ISSN: 1432-0924. DOI: 10.1007/BF00364252 (cit. on p. 29).

Ong, Y. S., P. B. Nair, and A. J. Keane (2003). "Evolutionary optimization of computationally expensive problems via surrogate modeling". In: *AIAA Journal* 41.4, pp. 687–696. ISSN: 0001-1452. DOI: 10.2514/2.1999 (cit. on pp. 15, 16).

Ostrowski, Z., R. A. Białecki, and A. J. Kassab (2008). "Solving inverse heat conduction problems using trained POD-RBF network inverse method". en. In: *Inverse Problems in Science and Engineering* 16.1, pp. 39–54. ISSN: 1741-5977, 1741-5985. DOI: 10.1080/17415970701198290 (cit. on p. 21).

Page, J. H., R. Watson, Z. Ali, P. Hield, and P. G. Tucker (2015). In: AIAA SciTech Forum. American Institute of Aeronautics and Astronautics. Chap. Advances of Turbomachinery Design Optimization. DOI: 10.2514/6.2015-0629 (cit. on p. 11).

Pearce, S. C. (1992). "Introduction to Fisher (1925) Statistical Methods for Research Workers". In: *Breakthroughs in Statistics: Methodology and Distribution*. Ed. by S. Kotz and N. L. Johnson. New York, NY: Springer New York, pp. 59–65. ISBN: 978-1-4612-4380-9. DOI: 10.1007/978-1-4612-4380-9_5 (cit. on p. 107).

Pearson, K. (1895). "Note on regression and inheritance in the case of two parents". en. In: *Proceedings of the Royal Society of London* 58.347–352, pp. 240–242. ISSN: 0370-1662, DOI: 10.1098/rspl.1895.0041 (cit. on pp. 98, 102).

— (1896). "Mathematical contributions to the theory of evolution. III. regression, heredity, and panmixia". In: *Philosophical Transactions of the Royal Society of London A: Mathematical, Physical and Engineering Sciences* 187, pp. 253–318. ISSN: 0264-3952. DOI: 10.1098/rsta.1896.0007 (cit. on pp. 98, 102).

Peherstorfer, B., T. Cui, Y. Marzouk, and K. Willcox (2016). "Multifidelity importance sampling". In: *Computer Methods in Applied Mechanics and Engineering* 300, pp. 490–509. ISSN: 0045-7825. DOI: 10.1016/j.cma.2015.12.002 (cit. on p. 16).

Peoples, R. and K. E. Willcox (2006). "Value-based multi-disciplinary optimization for commercial aircraft design and business risk assessment". In: *Journal Of Aircraft* 43.4, pp. 913–921. ISSN: 0021-8669. DOI: 10.2514/1.14147 (cit. on p. 1).

Perdikaris, P., D. Venturi, J. O. Royset, and G. E. Karniadakis (2015). "Multi-fidelity modelling via recursive co-kriging and Gaussian–Markov random fields". In: *Proceedings of the Royal Society of London A: Mathematical, Physical and Engineering Sciences* 471.2179. ISSN: 1364-5021. DOI: 10.1098/rspa.2015.0018 (cit. on pp. 17, 18).

Peri, D. and F. Tinti (2012). "A multistart gradient-based algorithm with surrogate model for global optimization". In: *Communications in Applied and Industrial Mathematics* 3.1. ISSN: 2038-0909. DOI: 10.1685/journal.caim.393 (cit. on p. 15).

Pierret, S. and R. A. Van den Braembussche (1999). "Turbomachinery blade design using a Navier-Stokes solver and artificial neural network". In: *Journal of Turbomachinery* 121.2, pp. 326–332. ISSN: 0889-504X. DOI: 10.1115/1.2841318 (cit. on p. 16).

Pinto, R. N., A. Afzal, L. V. D'Souza, Z. Ansari, and M. A. D. Samee (2016). "Computational fluid dynamics in turbomachinery: A review of state of the art". In: *Archives of Computational Methods in Engineering*, pp. 1–13. ISSN: 1886-1784. DOI: 10.1007/s11831-016-9175-2 (cit. on pp. 11, 13).

Piscopo, G. (2013). "Preliminary Aerothermal Design of Axial Compressors". MA thesis. Cranfield University (cit. on p. 10).

Qian, P. Z. G. and J. C. F. Wu (2008). "Bayesian hierarchical modeling for integrating low-accuracy and high-accuracy experiments". In: *Technometrics* 50.2, pp. 192–204. DOI: 10.1198/004017008000000082 (cit. on p. 18).

Qin, N., G. Carnie, Y. Wang, and S. Shahpar (2013). "Design optimization of casing grooves using zipper layer meshing". In: *Journal of Turbomachinery* 136.3, p. 031002. DOI: 10.1115/1.4024650 (cit. on p. 23).

Quarteroni, A. and G. Rozza (2014). *Reduced Order Methods for Modeling and Computational Reduction*. Vol. 9. MS&A - Modeling, Simulation and Applications. Springer International Publishing. ISBN: 978-3-319-02089-1 (cit. on p. 58).

Queipo, N. V., R. T. Haftka, W. Shyy, T. Goel, R. Vaidyanathan, and K. P. Tucker (2005). "Surrogate-based analysis and optimization". In: *Progress in Aerospace Sciences* 41.1, pp. 1–28. ISSN: 0376-0421. DOI: 10.1016/j.paerosci.2005.02.001 (cit. on pp. 14, 23).

Raghavan, B., L. Xia, P. Breitkopf, and P. Villon (2013). "Towards simultaneous reduction of both input and output spaces for interactive simulation-based structural design". In: *Computer Methods in Applied Mechanics and Engineering* 265, pp. 174–185. ISSN: 0045-7825. DOI: 10.1016/j.cma.2013.06.010 (cit. on p. 28).

Raissi, M. (2013). "Multi-fidelity stochastic collocation methods using model reduction techniques". PhD thesis. Georges Mason University, 80pp (cit. on p. 20).

Rasmussen, C. E. and C. K. I. Williams (2006). *Gaussian Processes for Machine Learning*. MIT Press. ISBN: 026218253X (cit. on p. 29).

Ratle, A. (1998). "Accelerating the convergence of evolutionary algorithms by fitness landscape approximation". In: *Parallel Problem Solving from Nature — PPSN V: 5th International Conference Amsterdam, The Netherlands September 27–30, 1998 Proceedings*. Ed. by A. E. Eiben, T. Bäck, M. Schoenauer, and H.-P. Schwefel. Berlin, Heidelberg: Springer Berlin Heidelberg, pp. 87–96. ISBN: 978-3-540-49672-4. DOI: 10.1007/BFb0056852 (cit. on p. 15).

Redmond, J. and G. Parker (1996). "Actuator placement based on reachable set optimization for expected disturbance". In: *Journal of Optimization Theory and Applications* 90.2, pp. 279–300. ISSN: 1573-2878. DOI: 10.1007/BF02189999 (cit. on p. 15).

Reid, L. and R. D. Morre (1978). *Design and overall performance of four highly loaded, high speed inlet stages for an advanced high-pressure-ratio core compressor*. Technical Report NASA-TP-1337. Cleveland, OH, United States: NASA Lewis Research Center, pp. 1–122 (cit. on p. 22).

Reisenthel, P. H., T. T. Allen, D. J. Lesieutre, and S. H. Lee (2010). *Development of multidisciplinary, multifidelity analysis, integration, and optimization*

of aerospace vehicles. Technical Report. Defense Technical Information Center (cit. on p. 19).

Reisenthel, P. H., J. F. Love, D. J. Lesieutre, and M. F. E. Dillenius (2006). *Innovative fusion of experiment and analysis for missile design and flight simulation*. Technical Report. Defense Technical Information Center (cit. on p. 19).

Reising, S. (2011). "Steady and Unsteady Performance of a Transonic Compressor Stage with Non-axisymmetric End Walls". PhD thesis. Darmstadt: Technische Universität (cit. on p. 12).

Reising, S. and H.-P. Schiffer (2009). "Non-axisymmetric end wall profiling in transonic compressors – Part II: Design study of a transonic compressor rotor using non-axisymmetric end walls – Optimization strategies and performance". In: *ASME Turbo Expo 2009: Power for Land, Sea, and Air*. Vol. 7. DOI: 10.1115/GT2009-59134 (cit. on p. 91).

Rippa, S. (1999). "An algorithm for selecting a good value for the parameter c in radial basis function interpolation". In: *Advances in Computational Mathematics* 11.2-3, pp. 193–210. ISSN: 1019-7168, 1572-9044. DOI: 10.1023/A:1018975909870 (cit. on pp. 83, 102).

Robinson, T. D., M. S. Eldred, K. E. Willcox, and R. Haimes (2008). "Surrogate-based optimization using multifidelity models with variable parameterization and corrected space mapping". In: *AIAA Journal* 46.11, pp. 2814–2822. ISSN: 0001-1452. DOI: 10.2514/1.36043 (cit. on p. 19).

Rodi, W. and G. Scheuerer (1986). "Scrutinizing the k- Turbulence Model Under Adverse Pressure Gradient Conditions". In: *Journal of Fluids Engineering* 108.2, pp. 174–179. ISSN: 0098-2202. DOI: 10.1115/1.3242559 (cit. on p. 120).

Rodríguez, J. F., V. M. Pérez, D. Padmanabhan, and J. E. Renaud (2001). "Sequential approximate optimization using variable fidelity response surface approximations". In: *Structural and Multidisciplinary Optimization* 22.1, pp. 24–34. ISSN: 1615-1488. DOI: 10.1007/s001580100122 (cit. on p. 16).

Roe, P. L. (1981). "Approximate Riemann solvers, parameter vectors, and difference schemes". In: *Journal of Computational Physics* 43.2, pp. 357–372. ISSN: 0021-9991. DOI: 10.1016/0021-9991(81)90128-5 (cit. on p. 91).

Romero, V. J., J. V. Burkardt, M. D. Gunzburger, and J. S. Peterson (2006). "Comparison of pure and "Latinized" centroidal Voronoi tessellation against various other statistical sampling methods". In: *Reliability Engineering & System Safety* 91.10—11, pp. 1266–1280. ISSN: 0951-8320. DOI: 10.1016/j.ress.2005.11.023 (cit. on p. 58).

Rukavina, J. P. (1991). "Modification of axial-flow compressor stall margin by variation of stationary blade setting angles". en. phd. Iowa State University (cit. on p. 88).

Saka, Y., M. Gunzburger, and J. Burkardt (2007). "Latinized, improved LHS, and CVT point sets in hypercubes". In: *International Journal of Numerical Analysis and Modeling* 4.3-4, pp. 729–743. ISSN: 1705-5105 (cit. on pp. 49, 55, 58, 95, 96).

Samad, A. and K.-Y. Kim (2008). "Stacking and thickness optimization of a compressor blade using weighted average surrogate model". In: *Volume 6: Turbomachinery, Parts A, B, and C*. ASME International. DOI: 10.1115/gt2008-50262 (cit. on p. 23).

— (2009). "Surrogate based optimization techniques for aerodynamic design of turbomachinery". In: *International Journal of Fluid Machinery and Systems* 2.2, pp. 179–188. DOI: 10.5293/ijfms.2009.2.2.179 (cit. on p. 2).

Samad, A., K.-Y. Kim, T. Goel, R. T. Haftka, and W. Shyy (2006). "Shape optimization of turbomachinery blade using multiple surrogate models". In: *Volume 1: Symposia, Parts A and B*. ASME International. DOI: 10.1115/fedsm2006-98368 (cit. on p. 23).

El-Sayed, A. F. (2008). *Aircraft Propulsion and Gas Turbine Engines*. First. CRC Press. ISBN: 978-0-8493-9196-5 (cit. on p. 10).

Schnell, R., J. Yin, C. Voss, and E. Nicke (2012). "Assessment and Optimization of the Aerodynamic and Acoustic Characteristics of a Counter Rotating Open Rotor". In: *Journal of Turbomachinery* 134.6, p. 061016. DOI: 10.1115/1.4006285 (cit. on p. 22).

Shahpar, S. and S. Caloni (2013). "Aerodynamic Optimization of High-Pressure Turbines for Lean-Burn Combustion System". In: *Journal of Engineering for Gas Turbines and Power* 135.5, p. 055001. DOI: 10.1115/1.4007977 (cit. on p. 23).

Shi, K. and S. Fu (2013). "Study of shock/blade tip leakage vortex/boundary layer interaction in a transonic rotor with IDDES method". In: *Volume 6C: Turbomachinery*. ASME International. DOI: 10.1115/gt2013-95252 (cit. on pp. 116, 117).

Shinde, V., E. Longatte, F. Baj, Y. Hoarau, and M. Braza (2016). "A Galerkin-free model reduction approach for the Navier-Stokes equations". en. In: *Journal of Computational Physics* 309, pp. 148–163. ISSN: 0021-9991 (cit. on pp. 28, 97).

Siddique, M. H., K. R. Mrinal, and A. Samad (2016). "Optimization of a centrifugal pump impeller by controlling blade profile parameters". In: *Volume 2C: Turbomachinery*. ASME International. DOI: 10.1115/gt2016-56604 (cit. on p. 22).

Singh, G. and R. V. Grandhi (2010). "Mixed-variable optimization strategy employing multifidelity simulation and surrogate models". en. In: *AIAA Journal* 48.1, pp. 215–223. ISSN: 0001-1452, 1533-385X. DOI: 10.2514/1.43469 (cit. on p. 16).

Sirovich, L. (1987). *Turbulence and the Dynamics of Coherent Structures, Part1: Coherent Structures*. Vol. 45. Quarterly of Applied Mathematics 3. Brown University, Division of Applied Mathematics, pp. 561–571 (cit. on p. 29).

Smola, A. J. and B. Schölkopf (2004). "A tutorial on support vector regression". In: *Statistics and Computing* 14.3, pp. 199–222. ISSN: 1573-1375. DOI: 10.1023/B:STCO.0000035301.49549.88 (cit. on p. 29).

Sobol, I. M. (2001). "Global sensitivity indices for nonlinear mathematical models and their Monte Carlo estimates". In: *Mathematics and Computers in Simulation* 55.1–3. The Second {IMACS} Seminar on Monte Carlo Methods, pp. 271–280. ISSN: 0378-4754. DOI: 10.1016/S0378-4754(00)00270-6 (cit. on p. 107).

Song, C., Z. Han, and Y. Zhang (2016). In: AIAA AVIATION Forum. 0. American Institute of Aeronautics and Astronautics. Chap. A new formulation of gradient-enhanced surrogate model and application to aerodynamic design. DOI: 10.2514/6.2016-3869 (cit. on p. 15).

Song, L., Z. Guo, J. Li, and Z. Feng (2016). "Research on metamodel-based global design optimization and data mining methods". In: *Journal of Engineering for Gas Turbines and Power* 138.9, p. 092604. DOI: 10.1115/1.4032653 (cit. on p. 22).

Song, P., J. Sun, and K. Wang (2014). "Blade shape optimization of transonic axial flow fan in terms of sectional profiles and stacking line". In: *Volume 2B: Turbomachinery*. ASME International. DOI: 10.1115/gt2014-25816 (cit. on p. 23).

Sorensen, D. C. (1982). "Newton's method with a model trust region modification". In: *SIAM Journal on Numerical Analysis* 19.2, pp. 409–426. DOI: 10.1137/0719026 (cit. on p. 84).

Spalart, P. R. and S. R. Allmaras (1992). "A one-equation turbulence model for aerodynamic flows". In: *Proc. 30th Aerospace Sciences Meeting & Exhibit*. American Institute of Aeronautics and Astronautics. DOI: 10.2514/6.1992-439 (cit. on p. 57).

Storn, R. and K. Price (1997). "Differential Evolution – A Simple and Efficient Heuristic for global Optimization over Continuous Spaces". In: *Journal of Global Optimization* 11.4, pp. 341–359. ISSN: 1573-2916. DOI: 10.1023/A:1008202821328 (cit. on p. 22).

Taddy, M. A., R. B. Gramacy, and N. G. Polson (2011). "Dynamic trees for learning and design". In: *Journal of the American Statistical Association* 106.493, pp. 109–123. DOI: 10.1198/jasa.2011.ap09769 (cit. on p. 23).

Takeishi, K., M. Matsuura, S. Aoki, and T. Sato (1990). "An experimental study of heat transfer and film cooling on low aspect ratio turbine nozzles". In: *Journal of Turbomachinery* 112.3, pp. 488–496. ISSN: 0889-504X. DOI: 10.1115/1.2927684 (cit. on p. 12).

Talgorn, B., S. Le Digabel, and M. Kokkolaras (2014). "Statistical surrogate formulations for simulation-based design optimization". In: *Journal of Mechanical Design* 137.2, p. 021405. DOI: 10.1115/1.4028756 (cit. on p. 23).

Toal, D. J. (2014). "On the potential of a multi-fidelity G-POD based approach for optimization & uncertainty quantification". In: *ASME Turbo Expo 2014: Turbine Technical Conference and Exposition*. Vol. 2B. DOI: 10.1115/GT2014-25184 (cit. on pp. 6, 17, 21, 27, 33–35, 52–54, 68).

Toal, D. J. and A. J. Keane (2011). "Efficient multipoint aerodynamic design optimization via cokriging". en. In: *Journal of Aircraft* 48.5, pp. 1685–1695. ISSN: 0021-8669, 1533-3868. DOI: 10.2514/1.C031342 (cit. on p. 19).

Torczon, V. (1997). "On the convergence of pattern search algorithms". In: *SIAM Journal on Optimization* 7.1, pp. 1–25. DOI: 10.1137/S1052623493250780 (cit. on p. 15).

Torczon, V. and M. W. Trosset (1998). "Using approximations to accelerate engineering design optimization". In: *Proceedings of the 7th AIAA/NASA/USAF/ISSMO Symposium on Multidisciplinary Analysis and Optimization*. Vol. AIAA-98-4800 (cit. on p. 15).

Tribes, C., J.-F. Dubé, and J.-Y. Trépanier (2004). "Decomposition of multidisciplinary optimization problem: Formulations and application to a simplified wing design". In: *10th AIAA/ISSMO Multidisciplinary Analysis and Optimization Conference*. American Institute of Aeronautics and Astronautics (AIAA). DOI: 10.2514/6.2004-4544 (cit. on p. 23).

Verveld, M. J., T. Kier, N. Karcher, T. Franz, M. Abu-Zurayk, M. Ripepi, and S. Görtz (2016). "Reduced order models for aerodynamic applications, loads and MDO". In: (cit. on p. 20).

Viana, F. A. C., T. W. Simpson, V. Balabanov, and V. Toropov (2014). "Special section on multidisciplinary design optimization: Metamodeling in multidisciplinary design optimization: How far have we really come?" In: *AIAA Journal* 52.4, pp. 670–690. DOI: 10.2514/1.j052375 (cit. on p. 14).

Wagner, F., A. Kühhorn, and R. Parchem (2015). "Robust design optimization applied to a high pressure turbine blade based on surrogate modelling techniques". In: *Volume 7A: Structures and Dynamics*. ASME International. DOI: 10.1115/gt2015-42365 (cit. on p. 22).

Wang, F. and Q.-J. Zhang (1997). "Knowledge-based neural models for microwave design". In: *IEEE Transactions on Microwave Theory and Techniques* 45.12, pp. 2333–2343. ISSN: 0018-9480. DOI: 10.1109/22.643839 (cit. on p. 19).

Wang, G. (2003). "Adaptive response surface method using inherited latin hypercube design points". In: *Journal of Mechanical Design* 125.2, pp. 210–220. ISSN: 1050-0472. DOI: 10.1115/1.1561044 (cit. on p. 96).

Wang, H., X. Zhu, Z. Du, and H. Yang (2010). "Aerodynamic optimization system development for low pressure exhaust hood of steam turbine". In: *Volume 7: Turbomachinery, Parts A, B, and C*. ASME International. DOI: 10.1115/gt2010-22280 (cit. on p. 22).

Wang, X. D. (2010). "CFD simulation of complex flows in turbomachinery and robust optimization of blade design". PhD thesis. Vrije Universiteit Brussel, 231pp (cit. on pp. 10, 11).

Wilcox, D. C. (1993). "Comparison of two-equation turbulence models for boundary layers with pressure gradient". In: *AIAA Journal* 31.8, pp. 1414–1421. ISSN: 0001-1452. DOI: 10.2514/3.11790 (cit. on p. 120).

Wu, Y. and W. Chu (2007). "Behaviour of tip-leakage flow in an axial flow compressor rotor". In: *Proceedings of the Institution of Mechanical Engineers, Part A: Journal of Power and Energy* 221.1, pp. 99–110. DOI: 10.1243/09576509JPE329 (cit. on pp. 116, 117).

Xiao, D., F. Fang, A. G. Buchan, C. C. Pain, I. M. Navon, and A. Muggeridge (2015). "Non-intrusive reduced order modelling of the Navier-Stokes equations". In: *Computer Methods in Applied Mechanics and Engineering* 293, pp. 522–541. ISSN: 0045-7825. DOI: 10.1016/j.cma.2015.05.015 (cit. on pp. 20, 27, 39, 97).

Xiao, D., P. Yang, F. Fang, J. Xiang, C. C. Pain, and I. M. Navon (2016). "Non-intrusive reduced order modelling of fluid–structure interactions". In: *Computer Methods in Applied Mechanics and Engineering* 303, pp. 35–54. ISSN: 0045-7825. DOI: http://dx.doi.org/10.1016/j.cma.2015.12.029 (cit. on p. 20).

Xiao, D., P. Yang, F. Fang, J. Xiang, C. C. Pain, I. M. Navon, and M. Chen (2017). "A non-intrusive reduced-order model for compressible fluid and fractured solid coupling and its application to blasting". In: *Journal of Computational Physics* 330, pp. 221–244. DOI: 10.1016/j.jcp.2016.10.068 (cit. on p. 20).

Xiao, M., P. Breitkopf, R. Filomeno Coelho, C. Knopf-Lenoir, M. Sidorkiewicz, and P. Villon (2010). "Model reduction by CPOD and Kriging". In: *Structural and Multidisciplinary Optimization* 41.4, pp. 555–574. ISSN: 1615-147X. DOI: 10.1007/s00158-009-0434-9 (cit. on pp. 27, 31).

Xiao, M., P. Breitkopf, R. Filomeno Coelho, C. Knopf-Lenoir, P. Villon, and W. Zhang (2013). "Constrained Proper Orthogonal Decomposition based on QR-factorization for aerodynamical shape optimization". In: *Applied Mathematics and Computation* 223.0, pp. 254–263. ISSN: 0096-3003. DOI: 10.1016/j.amc.2013.07.086 (cit. on pp. 27, 31, 39).

Xiao, M., P. Breitkopf, R. Filomeno Coelho, P. Villon, and W. Zhang (2014). "Proper orthogonal decomposition with high number of linear constraints for aerodynamical shape optimization". In: *Applied Mathematics and Computation*

247.0, pp. 1096–1112. ISSN: 0096-3003. DOI: 10.1016/j.amc.2014.09.068 (cit. on pp. 27, 39).

Zimmermann, R. (2013). "Gradient-enhanced surrogate modeling based on proper orthogonal decomposition". en. In: *Journal of Computational and Applied Mathematics* 237.1, pp. 403–418. ISSN: 0377-0427. DOI: 10.1016/j.cam.2012.06.010 (cit. on p. 15).

Zimmermann, R. and Z.-H. Han (2010). "Simplified cross-correlation estimation for multi-fidelity surrogate cokriging models". en. In: *Advances and Applications in Mathematical Sciences* 7.2, pp. 181–202. ISSN: 0974-6803 (cit. on p. 19).

Online References

Jones, E., T. Oliphant, P. Peterson, et al. (2001–). *SciPy: Open source scientific tools for Python*. [Online; accessed 2017-01-28]. URL: http://www.scipy.org/ (cit. on p. 108).

Safran Aero Boosters,
bibinitperiod (2016). *Low Pressure Compressor*. URL: https://www.safran-aero-boosters.com/propulsion/techspace-aero-low-pressure-compressor-expert (visited on 04/04/2017) (cit. on pp. 87, 88).

Safran Aircraft Engines (2017). *Safran Aircraft Engines - A world leader in aircraft engines*. URL: https://www.safran-group.com/company/safran-aircraft-engines (visited on 04/09/2017) (cit. on p. 1).